Multi-scale investigation of the subsurface structure at the InSight landing site, on Mars, using single-station seismology

Inaugural-Dissertation

zur Erlangung des Doktorgrades
der Mathematisch-Naturwissenschaftlichen Fakultät
der Universität zu Köln

vorgelegt von

Alejandro Sebastián Carrasco Morales

aus Pichilemu, Chile

Köln, 2023

1. Gutachter: Dr. B. Knapmeyer-Endrun
2. Gutachter: Prof. Dr. B. Tezkan
3. Gutachter: Prof. Dr. T. Meier

Tag der mündlichen Prüfung: 08.03.2024

Abstract

The internal structure of a planet provides constraints for understanding its evolution and dynamics. To this end, seismological data is of great relevance since seismic waves can map its interior at different scales, from meters to kilometers deep. In November 2018, the InSight spacecraft landed on Mars and deployed a set of geophysical instruments, including one seismological station. In this work, the subsurface structure at the InSight landing site (ILS) is explored, from the shallow subsurface to crustal depths, by applying single-station seismological techniques (SST) on Martian ambient vibrations and seismic events data.

The shallow subsurface at the ILS, in the order of meters, is investigated using the horizontal-to-vertical spectral ratios (HVSR) technique under the diffuse field assumption (DFA). After assessing the recordings, the ambient vibrations of the first Martian year of the mission are discouraged for HVSR analysis due to (i) the likely recording of the instrumental self-noise at low wind periods and (ii) the strong influence of wind-lander interaction on the recordings as the wind speed increases. Instead, the characteristic HVSR for the ILS, between 0.4 and 10 Hz, is derived from the coda of seismic events (eHV). The eHV presents a strong peak around 8 Hz, a rapid decay towards low frequencies and a narrow trough around 2.4 Hz. Assuming a full-wavefield DFA, a nonlinear inversion using the conditional Neighbourhood Algorithm (NA) allowed to map the shallow subsurface at the ILS. Due to the non-uniqueness problem, different sets of models are retrieved. The 8 Hz peak can be explained by a Rayleigh wave resonance due to a shallow high-velocity layer, while the 2.4 Hz trough is explained by a P-wave resonance due to a buried low-velocity layer.

The kilometer-scale subsurface was constrained by Rayleigh wave ellipticity measurements from large martian seismic events. The open-source Python-based tool *Rellipy* was developed for ellipticity extraction. The ellipticity measurements (0.03-0.07 Hz) were jointly inverted with P-to-s Receiver Functions and P-wave lag times from autocorrelations, to provide a subsurface model for the martian crust at the ILS. The joint inversion using NA allowed the unveiling of a new shallow layer at the ILS, unreported by previous models inverting seismological data. The HVSR in the 0.06-0.5 Hz frequency range from

the coda of S1222a, the largest event ever recorded on Mars, suggests a gradual transition from shallow to crustal depths and consolidates the shallow subsurface models with large shear-wave velocities as the most compatible with the crustal structure.

A comprehensive multi-scale model of the ILS subsurface is proposed. The ILS is characterized by the emplacement of a low-velocity regolith/coarse ejecta layer over a high-velocity Amazonian fractured lava flow (∼2 km/s, ∼30 m thick). A buried Late Hesperian-Amazonian sedimentary layer is deposited below (∼450 m/s, ∼30 m thick), underlain by a heavily weathered Early Hesperian lava flow. The latter overlays a thick, likely Noachian sedimentary layer that extends to a depth of 2-3 km. This shallow structure forms the first crustal layer derived from the joint inversion. Deeper crustal layers are consistent with other reported ILS models, with intracrustal discontinuities at 8-12 km and 18-23 km depth. The Moho depth at the ILS is found at 35-45 km depth. Shear-wave velocities above ∼20 km depth are lower than 2.5 km/s, slower than in other regions of Mars, suggesting a higher alteration due to local processes or a different origin of the upper crust at the ILS. The proposed model is consistent with the geologic history of Mars and other independent observations, confirming the great potential of SST for multi-scale investigation of, e.g., other planetary bodies or understudied regions on Earth.

Kurzzusammenfassung

Die innere Struktur eines Planeten liefert Anhaltspunkte für das Verständnis seiner Entwicklung und Dynamik. Zu diesem Zweck sind seismologische Daten von großer Bedeutung, da seismische Wellen das Innere des Planeten in verschiedenen Maßstäben abbilden können, von Metern bis zu Kilometern Tiefe. Im November 2018 landete die Raumsonde InSight auf dem Mars und setzte eine Reihe von geophysikalischen Instrumenten ein, darunter eine seismologische Station. In dieser Arbeit wird die Struktur des Untergrunds an der InSight-Landestelle (ILS) erforscht, vom flachen Untergrund bis in die Tiefe der Kruste, indem seismologische Einzelstationsverfahren (SST) auf die Daten der Umgebungsvibrationen und seismischen Ereignisse auf dem Mars angewendet werden.

Der flache Untergrund am ILS, in der Größenordnung von einigen Metern, wird mit der Technik der horizontal-vertikalen Spektralverhältnisse (HVSR) unter der Annahme eines diffusen Feldes (DFA) untersucht. Nach der Auswertung der Aufzeichnungen werden die Umgebungsvibrationen des ersten Marsjahres der Mission für die HVSR-Analyse nicht berücksichtigt, da (i) die Aufzeichnung des instrumentellen Eigenrauschens bei geringen Windperioden wahrscheinlich ist und (ii) die Aufzeichnungen bei zunehmender Windgeschwindigkeit stark von der Wind-Lander-Interaktion beeinflusst werden. Stattdessen wird die charakteristische HVSR für das ILS, zwischen 0,4 und 10 Hz, aus der Koda seismischer Ereignisse (eHV) abgeleitet. Die eHV zeigt eine starke Spitze um 8 Hz, einen schnellen Abfall zu niedrigen Frequenzen und einen schmalen Tiefpunkt um 2,4 Hz. Unter der Annahme eines Vollwellenfeldes DFA ermöglichte eine nichtlineare Inversion unter Verwendung des bedingten Nachbarschaftsalgorithmus (NA) die Abbildung des flachen Untergrundes am ILS. Aufgrund des Nicht-Eindeutigkeitsproblems wurden verschiedene Modellsätze ermittelt. Die gemeinsamen Muster deuten darauf hin, dass die 8-Hz-Spitze durch eine Rayleigh-Wellenresonanz aufgrund einer flachen Schicht mit hoher Geschwindigkeit erklärt werden kann, während der 2,4-Hz-Trog durch eine P-Wellenresonanz aufgrund einer vergrabenen Schicht mit niedriger Geschwindigkeit erklärt wird.

Der kilometergroße Untergrund wurde durch Rayleigh-Wellen-Elliptizitätsmessungen aus großen seismischen Ereignissen auf dem Mars eingegrenzt. Für die Extraktion der

Elliptizität wurde das Open-Source-Programm *Rellipy* auf Python-Basis entwickelt. Die Elliptizitätsmessungen (0,03-0,07 Hz) wurden gemeinsam mit P-to-s-Empfangsfunktionen und P-Wellen-Verzögerungszeiten aus Autokorrelationen invertiert, um ein Untergrundmodell für die Marskruste am ILS zu erstellen. Die gemeinsame Inversion unter Verwendung von NA ermöglichte die Enthüllung einer neuen flachen Schicht am ILS, die von früheren Modellen, die seismologische Daten invertierten, nicht erfasst wurde. Die HVSR im Frequenzbereich von 0,06-0,5 Hz aus der Coda von S1222a, dem größten jemals auf dem Mars aufgezeichneten Ereignis, deutet auf einen allmählichen Übergang von flachen zu krustalen Tiefen hin und konsolidiert die flachen Untergrundmodelle mit großen Scherwellengeschwindigkeiten als die mit der Krustenstruktur am besten kompatiblen.

Es wird ein umfassendes Multiskalenmodell des ILS-Untergrunds vorgeschlagen. Der ILS ist durch die Einlagerung einer Regolith-/Grobejekta-Schicht mit niedriger Geschwindigkeit über einem zerklüfteten Lavastrom mit hoher Geschwindigkeit (∼2 km/s, ∼30 m dick) aus der Amazonischen Periode gekennzeichnet. Darunter wird eine vergrabene Sedimentschicht aus dem späten Hesperian-Amazonian abgelagert (∼450 m/s, ∼30 m dick), die von einem stark verwitterten Lavastrom aus dem frühen Hesperian unterlagert wird. Letzterer überlagert eine dicke, wahrscheinlich noachische Sedimentschicht, die sich bis in eine Tiefe von 2-3 km erstreckt. Diese flache Struktur bildet die erste Krustenschicht, die sich aus der gemeinsamen Inversion ergibt. Tiefer liegende Krustenschichten stimmen mit anderen berichteten ILS-Modellen überein, mit intrakrustalen Diskontinuitäten in 8-12 km und 18-23 km Tiefe. Die Moho-Tiefe am ILS befindet sich in 35-45 km Tiefe. Die Scherwellengeschwindigkeiten oberhalb von 20 km Tiefe sind niedriger als 2,5 km/s und damit langsamer als in anderen Regionen des Mars, was auf eine stärkere Alteration aufgrund lokaler Prozesse oder einen anderen Ursprung der oberen Kruste am ILS hindeutet. Das vorgeschlagene Modell stimmt mit der geologischen Geschichte des Mars und anderen unabhängigen Beobachtungen überein und bestätigt das große Potenzial von SST für die multiskalige Untersuchung von z.B. anderen planetaren Körpern oder unerforschten Regionen auf der Erde.

Contents

List of Figures ix

List of Tables xiii

1 Introduction 1
1.1 Structure of the thesis . . . 2

2 Scientific framework 5
2.1 Mars exploration and the InSight mission . . . 5
2.1.1 Mars, the Red Planet . . . 5
2.1.2 The Martian crust . . . 7
2.1.3 Planetary and extraterrestrial seismology . . . 9
2.1.4 Seismology on Mars . . . 10
2.1.5 The InSight mission . . . 11
2.1.6 Geological setting at the InSight landing site . . . 16
2.1.7 Martian seismic activity . . . 19
2.2 Single-station seismology for mapping the subsurface structure . . . 22
2.2.1 Fundamentals of seismology . . . 22
2.2.2 The horizontal-to-vertical spectral ratios (HVSR) technique . . . 24
2.2.3 HVSR under the Diffuse Field Assumption (DFA) . . . 26
2.2.4 HVSR on diffuse coda waves . . . 29
2.2.5 Limitations of the HVSR method . . . 30
2.2.6 Ellipticity of direct Rayleigh waves . . . 30
2.3 Summary and concluding remarks . . . 31

3 Data and Methods 33
3.1 The InSight seismological data . . . 33
3.1.1 The ambient vibrations and non-seismic signals . . . 34
3.1.2 The Martian seismic events . . . 38
3.2 Data processing and methods . . . 41
3.2.1 Polarization analysis . . . 41
3.2.2 Horizontal-to-vertical spectral ratios (HVSR) . . . 43
3.3 Inversion scheme . . . 47
3.3.1 The Neighborhood algorithm (NA) . . . 47

4 HVSR from Martian ambient vibrations 51
4.1 Considerations on the data processing . . . 52
4.1.1 Effect of donks . . . 52

4.1.2 Effect of glitches . . . 54
4.2 Variability of the ambient vibrations HVSR over a sol . . . 55
4.2.1 Low-noise period . . . 63
4.2.2 Mid-noise period . . . 67
4.2.3 High-noise period . . . 69
4.3 Variability of the ambient vibrations HVSR over a Martian year . . . 71
4.4 Influence of environmental conditions and the lander modes . . . 74
4.5 Summary and concluding remarks . . . 80

5 Shallow subsurface from Martian seismic events HVSR 81
5.1 HVSR from the coda of Martian seismic events (eHV) . . . 82
5.1.1 The Martian seismic events . . . 82
5.1.2 Diffuse coda waves on Mars . . . 83
5.1.3 *eHV* determination . . . 83
5.1.4 Comparison between *nHV* and *eHV* . . . 87
5.2 Non-linear inversion of *eHV* . . . 89
5.2.1 HVSR forward modeling under DFA . . . 90
5.2.2 Inversion algorithm and parametrization . . . 90
5.3 Implications for the subsurface structure . . . 93
5.3.1 Models from *fHV* inversion . . . 93
5.3.2 Alternative model without 2.4 Hz trough . . . 96
5.4 Compatibility with compliance observations . . . 98
5.5 Implications for the seismological recordings . . . 99
5.6 Summary and concluding remarks . . . 101

6 Martian crustal structure at the InSight site 103
6.1 Introduction . . . 104
6.2 Large seismic events on Mars . . . 106
6.2.1 Back-azimuth determination for S1222a . . . 107
6.3 *Rellipy*: a python tool for extracting Rayleigh-wave ellipticity . . . 108
6.4 Ellipticity and phase-shift measurements . . . 111
6.4.1 Ellipticity analysis on Martian seismic events . . . 111
6.4.2 Comparative analysis of ellipticity data on Earth . . . 113
6.5 Joint inversion of ellipticity, P-to-s RFs and T_a . . . 116
6.5.1 Local-scale measurements . . . 116
6.5.2 Joint inversion settings and parameterization . . . 119
6.5.3 Initial inversions for local crustal structure . . . 121
6.5.4 Local crustal structure at the InSight landing site . . . 123
6.6 Summary and concluding remarks . . . 126

7 Towards a consolidated model at the ILS 127
7.1 The ILS subsurface structure at intermediate depths . . . 127
7.1.1 HVSR from S1222a coda . . . 128
7.1.2 Forward modeling of possible models . . . 129
7.2 A consolidated subsurface structure at the ILS . . . 133
7.2.1 The shallow subsurface . . . 133
7.2.2 The crustal scale . . . 137

7.3 Summary and concluding remarks . . . 142

8 Conclusions and Outlook **143**

Bibliography **147**

Appendix **173**
A1 SEIS instrument responses . . . 175
A1.1 Comparison of VBB raw and deglitched data . . . 178
A1.2 Comparison between SP and VBB . . . 179
A1.3 Instruments self-noise . . . 180
A2 Evolution of spectral and polarization features . . . 181
A2.1 Variation throughout a martian year . . . 181
A2.2 Influence of temperature . . . 182
A2.3 Influence of the wind speed . . . 182
A3 Ground compliance inversion . . . 190
A4 Additional joint-inversion runs . . . 191
A4.1 3LOH cases . . . 191
A4.2 4LOH cases . . . 194
A5 Density assessment . . . 197
A6 Comparison against further observations . . . 198

Acknowledgments **199**

List of Figures

2.1 MOLA Topographic map of Mars . . . 8
2.2 InSight lander setup . . . 13
2.3 Schematic view of SEIS components . . . 15
2.4 InSight geological map . . . 17
2.5 InSight local-scale context . . . 18
2.6 Topographic features around the InSight landing site . . . 20
2.7 Estimated crustal thickness around the InSight landing site . . . 20
2.8 Estimates of size-frequency distribution of seismic events . . . 21
2.9 Basic concepts for single-station seismology . . . 23
2.10 Multiple scattering sketch . . . 28

3.1 Availability of main InSight data used by MQS . . . 34
3.2 Seismic and environmental data recorded during sol 419 . . . 35
3.3 Non-seismic signals recorded by SEIS . . . 37
3.4 Martian seismicity in the first 1011 sols of InSight . . . 39
3.5 Sketch to illustrate polarization angles Θ_H and Θ_V . . . 42
3.6 Stratified model used for DFA . . . 45
3.7 Comparison *gpell* and DFA . . . 46
3.8 Illustration of the Neighborhood Algorithm (NA) . . . 48

4.1 Effect of donks in HVSR calculation . . . 53
4.2 Effect of glitches in H/V calculation . . . 55
4.3 Z-spectrogram of Martian ambient vibrations over Sol 422 . . . 57
4.4 H-spectrogram of Martian ambient vibrations over Sol 422 . . . 58
4.5 HV-gram of Martian ambient vibrations over Sol 422 . . . 59
4.6 DOP-gram of Martian ambient vibrations over Sol 422 . . . 60
4.7 Θ_V-gram of Martian ambient vibrations over Sol 422 . . . 61
4.8 Θ_H-gram of Martian ambient vibrations over Sol 422 . . . 62
4.9 Spectral and polarization attributes of the low-noise period . . . 64
4.10 Time-domain cross-correlations between SP and VBB . . . 66
4.11 Spectral and polarization attributes of the mid-noise period . . . 68
4.12 Spectral and polarization attributes of the high-noise period . . . 70
4.13 Seasonal HVgram of Martian ambient vibrations during local evening . . . 72
4.14 Variation of spectral features over a Martian year during local evening . . . 73
4.15 HVgram as a function of wind speed . . . 75
4.16 Influence of wind speed on spectral features . . . 76
4.17 Effect of compliance in seismic recordings . . . 77
4.18 Characteristic horizontal spectral amplitudes over a sol . . . 78

5.1 Spectral and polarization attributes of the S0794a event . . . 84
5.2 Spectral characteristics of Martian seismic events . . . 85
5.3 VF events and environmental conditions . . . 86
5.4 Summary of events HVSR (*eHV*) . . . 87
5.5 Summary of HVSR curves . . . 88
5.6 SML1 models from *fHV* inversion . . . 92
5.7 Theoretical H/V curves for two exemplary models obtained from the SML1 inversion results . . . 94
5.8 SML2 models from *fHV* inversion . . . 97
5.9 Synthetic modeling HVSR and left flank . . . 97
5.10 HVSR inversion models and synthetic ground compliance . . . 98
5.11 Site effect at the InSight landing site . . . 100

6.1 Epicentral locations of large seismic events on Mars . . . 106
6.2 Determination of S1222a back-azimuth . . . 108
6.3 *Rellipy* processing steps . . . 109
6.4 Rayleigh wave ellipticity and phase shift results . . . 111
6.5 Phase shifts for different BAZ for S1222a . . . 112
6.6 Ellipticity and phase shifts for station DREG (Earth, Germany) . . . 113
6.7 Variation of single events with respect to median ellipticity . . . 114
6.8 Examples of low phase shifts on Earth . . . 115
6.9 Phase shift for normal-faulting Mexico earthquake . . . 115
6.10 Receiver Functions sketch . . . 117
6.11 Seismic interferometry sketch . . . 118
6.12 Ellipticity-only inversion using different parameterization spaces . . . 121
6.13 Joint inversion using 3LOH . . . 122
6.14 Synthetic modeling of a shallow layer with lower velocities . . . 122
6.15 Joint-inversion results and resulting Martian crustal models using a 4LOH parameter space . . . 124

7.1 Spectral features and HVSR of S1222a . . . 128
7.2 Consolidated ILS subsurface model using a homogeneous intermediate layer and representative M2 model . . . 130
7.3 Consolidated ILS subsurface model using a homogeneous intermediate layer and representative L2 model . . . 130
7.4 Consolidated ILS subsurface model using an intermediate layer with power-law velocity increase and representative M2 model . . . 132
7.5 Consolidated ILS subsurface model using an intermediate layer with power-law velocity increase and representative L2 model . . . 132
7.6 Schematic profile of subsurface structure at the ILS . . . 134
7.7 Comparison of available crustal structures on Mars . . . 138
7.8 S1222a path and Martian crustal structure . . . 141

A1.1 Instrument response of VBB@100 sps . . . 175
A1.2 Instrument response of VBB@20 sps . . . 176
A1.3 Instrument response of SP@100 sps . . . 176
A1.4 Instrument response of SP@20 sps . . . 177
A1.5 Comparison of VBB data (20 vs 100 sps) . . . 178

A1.6 Comparison between raw and deglitched VBB@20 sps . . . 178
A1.7 Comparison of spectral features from VBB and SP data . . . 179
A1.8 Determination of SP self-noise . . . 180
A2.1 Variation of spectral features over a martian year during local night . . . 181
A2.2 Variation of spectral features over a martian year during local day . . . 182
A2.3 Horizontal spectral amplitudes and air temperature . . . 183
A2.4 Wind speed and DOP . . . 184
A2.5 Wind speed and Vertical spectral amplitude . . . 185
A2.6 Wind speed and Horizontal spectral amplitude . . . 186
A2.7 Wind speed and Ellipticity . . . 187
A2.8 Wind speed and Planarity . . . 188
A2.9 Wind speed and Rectilinearity . . . 189
A3.10 Discrete subsurface structure models from ground compliance inversion including a shallow high-velocity layer . . . 190
A4.1 3LOH inversion run - RF only . . . 192
A4.2 3LOH inversion run - RF and ellipticity . . . 193
A4.3 3LOH inversion run - RF, ε and T_a . . . 193
A4.4 3LOH inversion run - RF and T_a . . . 195
A4.5 3LOH inversion run - RF (0.30), ε (0.60) and T_a (0.10) . . . 195
A4.6 3LOH inversion run - RF (0.60), ε (0.30) and T_a (0.10) . . . 196
A5.7 Effect of scaling density on ellipticity and RFs . . . 197
A5.8 Sensitivity of ellipticity and P-to-s RFs to density . . . 197
A6.9 Proposed crustal models and further observations . . . 198

List of Tables

2.1 Orbital and physical properties of Mars 6
2.2 Surface missions successfully landed on Mars before InSight 11

3.1 Classification of events detected by MQS according to spectral content . . . 40
3.2 Classification of events detected by MQS based on signal clarity 40

5.1 Summary of Martian seismic events used for HVSR computation 82
5.2 Parameter spaces explored for the *fHV* inversion 91

6.1 Existing crustal structure models for the ILS 105
6.2 Predicted times of P-wave reflections from representative crustal models . . 105
6.3 Parameter space 3LOH 120
6.4 Parameter space 4LOH 123

A1 Weights for 3LOH inversion runs 191
A2 Weights for 4LOH inversion runs 194

CHAPTER 1

Introduction

Mars, the so-called *red planet*, is the fourth planet from the Sun and the second closest to Earth. Like Mercury, Venus and the Earth, Mars is also a rocky planet. They are composed primarily of rocks or metals, unlike the gaseous planets, such as Jupiter or Neptune, composed mainly of volatiles. The rocky planets and planetary bodies differentiate into three main compositional layers: a dense core, an intermediate density mantle and an external crust at the surface (e.g., MacDonald, 1962; Elkins-Tanton, 2011). Among them, the Earth is the only planet whose inner structure and dynamics have been intensely studied, even though the interior of the Moon, a planetary body, has also been explored but in lesser detail. The study of Mars's inner structure and dynamics is of great interest to gain information on the geological processes that took place there, which can give insights into how the planet has evolved. Furthermore, knowing the interior and dynamics of Mars can serve as a point of comparison for the general study of the formation and evolution of planetary bodies. Comparing their internal structures is crucial to understanding their past, their present and hypothesizing possible future scenarios.

Because of this, among other reasons, Mars has been one of the most studied planets for many years. In this regard, the study of Mars's interior has implemented different methodologies such as telescopic observations, analysis of Martian meteorites, the use of *orbiters* (spacecraft orbiting the planet), *landers* (spacecraft fixed at one specific location) and *rovers* (vehicles moving around the planet's surface). Most available information about Mars comes from measurements or observations made in one of these ways, mainly including sidereal information, gravity, topography data and satellite images of its surface. Although rough ideas about its internal structure and dynamics can be derived from these measurements, further details will provide a more refined understanding and a better perspective of *the red planet*.

Among the different geophysical techniques for planetary exploration, seismology plays a relevant role by studying the propagation of seismic waves through the planet. In

this sense, seismological techniques offer one of the most direct ways to study a planet's internal structure and mechanical properties at different scales. On Earth, seismology has allowed the characterization of the planet's interior in great detail, from the inner core to near-surface structures. On Mars, the Viking missions in the 1970s carried out the only seismological experiment so far, but it did not provide conclusive information about its internal structure and dynamics.

In this context, on 5 May 2018, NASA[1] launched the InSight[2] mission to Mars, which brought a robotic lander that deployed a new seismological station on the Martian surface. This seismological station is planned to record ground-motion data for over two terrestrial years and, supported by other geophysical experiments, aims to answer long-lived questions about the interior and dynamics of Mars like: How frequent is the Martian seismic activity? Where are the Martian seismic events occurring? What are the characteristics of the near-surface structure? What is the internal structure of the Martian crust? How large is the core? Among other questions, including those that may arise during the mission.

Throughout this work, two of these possible questions are sought to be answered: *What are the characteristics of the near-surface structure at the InSight landing site?* and *What is the internal structure of the Martian crust?*. For this purpose, the seismological data recorded by the InSight mission will be used to characterize the local subsurface structure at shallow and crustal scales, ranging from the order of meters to kilometers, respectively. Unlike Earth, data from only one seismological station is available on Mars and, therefore, the single-station seismological techniques must be exploited. In order to achieve a multi-scale investigation and accomplish the goals of this research, different well-established single-station seismological techniques on Earth are utilized. The shallow subsurface structure is studied using the recordings of ambient vibrations and Martian seismic events by performing horizontal-to-vertical spectral ratios (HVSR) analysis. After, the ellipticity of Rayleigh waves is investigated and inverted, together with P-to-s Receiver Functions and P-wave lag times from autocorrelations, to derive the characteristics of the crustal structure at the InSight landing site. A detailed structure of this manuscript is presented below whereas further details on the data set and techniques are presented in the following chapters.

1.1 Structure of the thesis

This work has been carried out in parallel to the course of the InSight mission on Mars, so it has been shaped by the availability of data and discussions within the InSight Science Team. In this context, this doctoral research is presented as follows:

Chapter 2 presents the scientific framework in which the InSight mission and this work are based. An overview of Mars's characteristics is given, including its main planetary features and geological structures. In the context of interplanetary missions, a brief summary of past seismological experiments out of the Earth is provided. Then, details of

[1]Short for **N**ational **A**eronautics and **S**pace **A**dministration

[2]Short for **I**nterior Explorati**o**n using **S**eismic **I**nvestigations, **G**eodesy and **H**eat **T**ransport

the InSight mission, as well as the local and regional characteristics of the landing site are also given to better contextualize the study region. An overview of key seismological concepts and the background of the horizontal-to-vertical spectral ratios (HVSR) technique under the diffuse field approach is also provided.

An overview of the data and methods utilized throughout this work is presented in Chapter 3. Here, the main characteristics of the InSight data are provided, together with a first presentation of the recorded signals, including seismic events and non-seismic signals. The methods section presents more details on the techniques and algorithms utilized for the data processing and analysis. In the end, the non-linear inversion procedure to derive the subsurface structure using the Neighbourhood Algorithm is provided.

In Chapter 4, as little information was known at the beginning of the mission, a first assessment of the ambient vibrations recordings is conducted. For this, the spectral and polarization features of the Martian ambient vibrations, as well as their temporal evolution and dependence on environmental variables are investigated, in order to assess the use of the HVSR technique on this InSight data set. After characterizing the different features observed and the possible origin of the ambient vibrations, a final assessment of the HVSR measurements is provided.

Chapter 5 presents the HVSR analysis using the coda of Martian seismic events. After comparing against the HVSR from ambient vibrations, a characteristic HVSR curve is defined for the InSight landing site. This HVSR curve is inverted, in the high-frequency range (0.4-10 Hz), to map the shallow subsurface structure in the order of meters deep beneath the InSight lander. The reliability of the derived models under two different scenarios and the possible geological causes, as well as the implications for the ground motions recorded by SEIS, are discussed in this chapter.

In Chapter 6, the crustal-scale subsurface structure at the ILS is investigated by jointly inverting local-scale seismological observations. These include the Rayleigh-waves ellipticity from large Martian seismic events at low frequencies (0.03-0.07 Hz), the P-wave lag times from autocorrelations of ambient vibrations data and the P-to-s Receiver Functions from Martian seismic events. The developed Python tools for the extraction of ellipticity data from Martian and terrestrial seismic events are presented, including examples for an Earth case as a benchmark. A set of models explaining these observations is presented and their main characteristics are discussed.

To harmonize the results at different scales, Chapter 7 presents a possible subsurface model for the InSight landing site that could simultaneously explain the meters-scale and kilometers-scale measurements. In order to link the shallow to the crustal subsurface structure, the transition depths were investigated by studying the intermediate frequency range 0.06-0.5 Hz. For this, the HVSR of the coda of the largest seismic event ever recorded on Mars was investigated. Forward modeling is performed to assess the feasibility of certain models. A consolidated model is proposed, from shallow to crustal depths, which is discussed against the geological history of Mars, as well as recent and independent works that cover other Martian regions.

Finally, Chapter 8 presents a summary of the main findings of this work, their implications for the understanding of Mars interior and dynamics, and the opportunities for future work using a single station, either on Earth, Mars or any other planetary body.

CHAPTER 2

Scientific framework

The research carried out throughout this work is based, in part, on the advances achieved through the various space missions that have explored Mars, the technological improvements in seismological instrumentation and the development of techniques that allow characterizing the subsurface using a single station. This chapter presents the scientific framework in which the InSight mission and, particularly, this doctoral research are conducted, which includes information on the *state-of-the-art* of Mars exploration and the use of single-station seismological techniques for subsurface mapping. The information provided here is based mainly on works and findings available before the InSight landing and/or roughly around the time of starting this work.

2.1 Mars exploration and the InSight mission

2.1.1 Mars, the Red Planet

Besides Earth, Mars is one of the planets in the Solar System that has been most extensively studied. Conditions similar to some places on Earth, the more accessible exploration compared to Venus hostile surface (e.g., Taylor et al., 2018), the presence of water and the possibilities of habitability are some of the reasons that have driven research on Mars. For these purposes, knowledge of its internal structure and dynamics has been crucial to comprehensively understanding the Red Planet. Over the years of diligent observations and exploration of Mars, various research endeavors and space missions have contributed significant insights into the Martian interior. These findings form the foundation of our current understanding and the state-of-the-art of the planet.

As a first overview, a comparison between Mars and Earth's orbital and physical parameters is presented in Table 2.1. Mars is about nine times less massive and around seven times smaller than the Earth. Its mean density is slightly lower than that of our

	Mars	**Earth**
Mass [10^{24} kg]	0.64199	5.9722
Volume [10^{10} km^3]	16.312	108.321
Mean radius [km]	3389.5	6371.0
Mean density [kg/m^3]	3934	5513
Mean Surface gravity [m/s^2]	3.73	9.82
Mean Surface pressure [mbar]	6.36	1013.25
Solar day [h]	24.6597 h (1 sol)	24 h (1 day)
Sidereal orbit period [days]	686.98	365.256

Table 2.1: Orbital and physical properties of Mars. Values are taken from Williams (2004).

planet, whereas the mean surface gravity is almost a third of the terrestrial case. One of the main characteristics of Mars is its rather thin atmosphere, generating an average low surface pressure of 6.36 mbar, compared to the Earth's. A solar day on Mars, also known as *sol*, lasts 24 hours, 37 minutes and 22.66 seconds (∼24.66 h), which is slightly longer than the Earth's solar day (24 h). Respectively, its orbital period around the Sun (a Martian year) is about 687 Earth's days, i.e., around 669 sols. Throughout this work, "sols" refers to the Martian solar day and "days" to the Earth's solar day.

Different measurement data sets have helped to gain information on Mars's internal structure throughout the years. Two-way Doppler radio tracking data from early missions to Mars allowed determining the gravitational field and global geodetic parameters such as its polar Moment of Inertia (MoI), spin-axis precession rate, obliquity and other orbital parameters (e.g., Lorell et al., 1972; Reasenberg et al., 1975; Kaula, 1979; Folkner et al., 1997; Yoder and Standish, 1997). Further investigations using data from the orbiters Mars Global Surveyor (MGS, Smith et al., 1999a; Zuber et al., 2000; Lemoine et al., 2001) and Mars Reconnaissance Orbiter (MRO, Zuber et al., 2007; Konopliv et al., 2011) refined these and further parameters, like the tidal potential Love number k_2 (Yoder et al., 2003; Konopliv et al., 2011, 2016), which is related to the gravity signal generated by the Sun tide. These geophysical measurements, together with geochemical data from Martian meteorites (Dreibus and Wanke, 1985; McSween Jr and Keil, 2000), allowed determining that the Martian core is iron-rich, is mostly in a liquid state and has a radius ranging between 1700 and 1900 km (e.g., Rivoldini et al., 2011; Khan et al., 2018; Bagheri et al., 2019).

The Martian core is surrounded by a less dense silicate mantle, whose characteristics come mainly from analyzing Martian meteorites and geochemical and geophysical modeling. The mantle is primarily composed of olivine, pyroxene and garnet (Bertka and Fei, 1997) and has been proposed to have a higher content of volatile elements and to be more iron-rich than the Earth's (Dreibus and Wanke, 1985; Wänke and Dreibus, 1994). An Earth-like upper and lower mantle structure for Mars is unclear because it largely depends on the presence of bridgmanite, which strongly depends on the temperature and pressure at the core-mantle-boundary (CMB), the size of the core and the iron content (Khan et al., 2018). As these parameters have a high uncertainty, the presence of bridgmanite is not clear.

2.1.2 The Martian crust

The crust overlays the mantle as on any rocky planet. Diverse studies have investigated the Martian crust using Martian meteorites and data from different missions to Mars. In particular, the global topography of Mars and its gravitational field have been key observations to characterize its crust. Extensive global mapping was performed by the Mars Orbiter Laser Altimeter (MOLA, Smith et al., 1999b, 2001), an instrument aboard MGS, using a high-accuracy laser altimetry technique. A brief overview of the main topographical features on Mars is presented below.

As shown in Fig. 2.1, the so-called *dichotomy boundary* is a remarkable topographical feature that demarks a sharp contrast between the southern and northern hemispheres. The southern hemisphere, also known as *highlands*, is about 1-3 km higher and has more impact craters than the northern *lowlands*, which presents a relatively smooth topography and where impact craters have been buried by a combination of sedimentation and volcanism (Smrekar et al., 2019). Several extended low-lying plain areas are observed in the northern hemisphere, like Utopia, Elysium or Amazonis Planitia. Based on the density of impact craters and stratigraphic relationships, the history of Mars can be divided into three main epochs: the Noachian epoch, older than ∼3.7 billion years ago (Ga), the Hesperian (∼3.7 to ∼3 Ga) and Amazonian (∼3 Ga to present) (e.g., Carr and Head, 2010). Another prominent topographic feature is the Tharsis rise, a volcanic plateau around the equator, between 60°W and 130°W, located west of Valles Marineris, a vast canyon system stretching over 4000 km near the Martian equator. In the Tharsis region lie the Tharsis Montes, a set of three high volcanic edifices, only surpassed by Olympus Mons, the tallest volcano on the planet (and the Solar System), whose summit is at 21.287 km elevation. The elevation range on Mars is about 30 km, with the lowest point reaching -8.180 km elevation at the Hellas basin (Smith et al., 2001). Other basins, like Argyre (50°S, 40°W) and Isidis (10°N, 80°E), are also clearly seen from the topographic view.

Gravitational data has been obtained by analyzing Doppler radio tracking data from orbiters exploring Mars over the last decades. For this, the measured travel times of radio signals sent from Earth to the orbiters are compared to a theoretical model where the gravity field of Mars is one of the modeling parameters. As more measurements have been made, the Martian gravitational field has been continuously refined over the years (e.g., Smith et al., 1999a; Lemoine et al., 2001; Konopliv et al., 2011). The most recent models have been derived from tracking data of MGS, MRO and Mars Oddyssey (ODY) and have a maximum spatial resolution of ∼105 km in the south pole (Genova et al., 2016; Konopliv et al., 2016).

The Martian crust's thickness (also called the Moho depth) and density have been studied mainly by modeling the relationship between topography and gravity data. Different approaches can be used for this purpose, as summarized by Wieczorek and Zuber (2004) and Smrekar et al. (2019). Zuber et al. (2000) did the first reliable determination of the Martian crustal structure using MOLA topography data and gravity data from MGS. They performed a global crustal thickness inversion, for which a constraint on the thickness of the crust at a specific value is required (an *anchor-point*, either at a specific location or as a minimum/maximum permitted). In this case, the minimum crustal thickness was arbitrarily set to 3 km, which was found to occur beneath the Isidis basin. By assuming uniform crustal and mantle densities of 2900 and 3500 kg/m^3, respectively, a

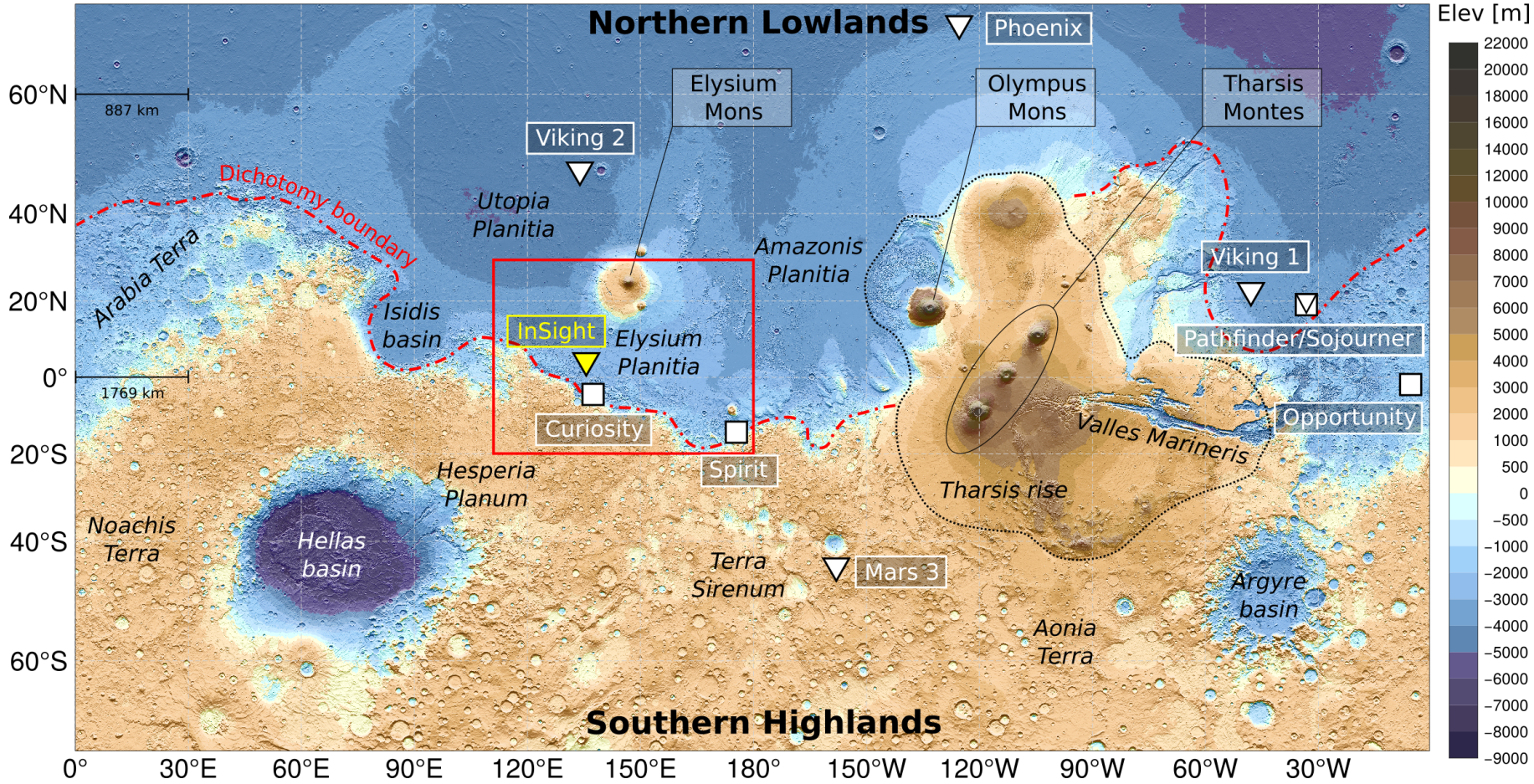


Figure 2.1: Topographic map of Mars, based on Mars Orbiter Laser Altimeter data (MOLA, Smith et al., 2001), using Mercator projection between 70°S and 65°N. The zero elevation corresponds to the equipotential surface whose average value at the equator is equal to the mean radius as determined by MOLA. The main geomorphological features on Mars are highlighted (*italics*). The dichotomy boundary is illustrated as a red dash-dotted line, following the concept of Tanaka et al. (2014). A black dotted line denotes the Tharsis rise/region. The landing sites of rovers (square) and landers (inverted triangle) that successfully landed on Mars are illustrated. The landing site of the InSight spacecraft is also plotted (yellow inverted triangle). The red box outlines the context map shown in Fig. 2.6 and 2.7. The nomenclature of the regions follows the convention of the International Astronomical Union (IAU).

global mean crustal thickness of ∼50 km was derived. A relatively uniform crustal thickness of about 35 km thick was found for other northern lowlands. Later, Wieczorek and Zuber (2004) proposed an average crustal thickness of 33 to 81 km, by using the geoid-to-topography ratios, assuming Airy isostasy and a range of crustal densities between 2700 and 3100 kg/m^3. Under the idea that crustal density is laterally heterogeneous, Neumann et al. (2004) applied corrections for the anomalous densities of the polar caps and major volcanoes and performed a non-linear inversion for Moho relief. Their results suggest that a single-layered crust of 45 km global mean thickness can explain the measured Bouguer anomaly and is consistent with Mars's geological and thermal history. Besides, crustal thicknesses of 32 and 58 km were obtained for the northern and southern hemispheres, respectively. Other studies have proposed average thickness of the Martian crust in the ranges 49-87 km (Plesa et al., 2018b), 37-79 km (Rivoldini et al., 2011) and 55-80 km (Khan et al., 2018). Further details on the expected local geology and crustal structure at the site where InSight landed are provided in Section 2.1.5.

A strong trade-off between the crust's density and thickness is evident from the different studies. In this regard, Baratoux et al. (2014) proposed crustal density values larger than 3100 kg/m^3, based on a review of the major element chemistry of Martian meteorites and the density of igneous rocks on the Martian surface. Although these values might not be representative of the whole crust, it would mean an average crustal thickness of ∼100 km. Recently, Goossens et al. (2017) found evidence for average bulk density for the Martian crust ranging between 2400 and 2800 kg/m^3. Similar low values had been proposed by Nimmo (2002) and even lower for Martian sedimentary formations (∼1760 kg/m^3, Ojha and Lewis, 2018).

One way to overcome this problem is to determine the crustal thickness with seismological techniques, thus constraining the range of acceptable densities. In addition, the local crustal structure at the InSight landing site can be used as an anchor point for studying the global crustal thickness of Mars. Here is where seismology plays a relevant role, allowing for a more detailed characterization of the Martian crust, from the shallow subsurface to the crustal bottom.

2.1.3 Planetary and extraterrestrial seismology

Some ideas about a planetary body's interior can be inferred by looking at the geomorphological features on its surface, like the absence of fault system traces on the lunar surface or the huge volcanoes on Mars suggesting no or low tectonic activity, respectively. Nevertheless, further details on the physical properties and internal structure, especially at large depths, must be derived from geophysical observations, as shown above for Mars. Among other approaches, seismology allows for determining the mechanical properties and structural characteristics of such a body by studying the propagation of seismic waves through it. On Earth, since Ernst von Rebeur-Paschwitz identified the arrival of teleseismic phases at the Potsdam and Willhelmshaven Observatories in 1889, the study of the Earth's interior has successfully evolved. From the determination of inner discontinuities (e.g., Oldham, 1906; Mohorovicic, 1910; Gutenberg, 1914) or the discovery of a solid inner core by Lehman (1936), to the thousands of detailed and complex models of

local subsurface structures, the seismological recordings have been an essential piece in learning more about our planet.

Similarly, the study of the interior of other planetary bodies has pursued the idea of using seismology as an elementary tool. As on Earth, using seismometers to record the surface ground motions is one of the most direct ways to map their interiors. Nevertheless, seismological instrumentation has been brought only to the Moon, Venus and Mars, with different levels of success in each case. In the first case, five stations were deployed on the surface of the Moon between 1969 and 1977, as part of the Apollo program carried out by NASA. These stations successfully recorded ground-motion data that has allowed characterizing its seismic activity (e.g., Oberst and Nakamura, 1987; Nakamura, 2005; Lognonné, 2005) and determining local and global properties of the internal structure (e.g., Toksőz et al., 1972; Vinnik et al., 2001; Weber et al., 2011; Dal Moro, 2015). Secondly, a data set of only two hours of seismic data is available for Venus, which was recorded by the uni-axial seismometer brought by the missions Venera 13 and 14 in 1982. However, it is unclear whether the recorded signals are related to natural seismic activity or other phenomena (Ksanfomaliti et al., 1982; Stevenson et al., 2015). Lastly, the seismological exploration of Mars has provided more data than in the Venus case, but its results are less clear than in the lunar case, as detailed below.

2.1.4 Seismology on Mars

The seismological exploration of Mars began with the Viking program by NASA, between 1976 and 1978. On that occasion, the Viking Lander 1 (VL1) and Viking Lander 2 (VL2) were equipped with one three-axis short-period seismometer. Unfortunately, the seismometer on VL1 failed to uncage and therefore, only one seismic station operated on Mars, at the landing site location of VL2, in the Utopia Planitia region (Anderson et al., 1977). Regarding sensitivity, the operative seismometer on Mars was ten times better than the Apollo sensors for frequencies above 1 Hz (Lognonné and Pike, 2015). Nevertheless, to minimize the weight and complexity of the mission, the seismometer was not deployed on the Martian surface but stayed mounted on the lander. The seismological recordings were thus contaminated by increased noise generated by wind and lander activities.

Despite these and other difficulties, the seismometer operated almost continuously for nearly 19 months and provided the first Martian seismological data set. Most quake-like event signals were associated with sudden wind gusts, as confirmed by the meteorological experiment carried out at the same location (Anderson et al., 1977). Only one event was suspected to be a Martian seismic event caused by tectonic activity (hereafter marsquake). It occurred during the Martian night-time, when wind activity was typically low, but no simultaneous meteorological data was available to confirm or discard a meteorological event. Lorenz et al. (2017) recently reviewed the Viking seismological and meteorological data and proposed that a gust origin of this event is unlikely, although it cannot be completely discarded. In any case, an early assessment by Goins and Lazarewicz (1979) suggested that zero to one event would be detected by this seismic station. Consequently, although this upper limit constraint, it was impossible further to characterize the Martian seismic activity or its internal structure.

Mission	Landing date	Period of operation
Mars 3/Prop-M	2 December 1971	20 seconds
Viking 1	20 July 1976	2307 days (2245 Sols)
Viking 2	3 September 1976	1316 days (1281 Sols)
Mars Pathfinder/Sojourner*	4 July 1997	85 days (83 Sols)
Mars Exploration Rover Spirit*	4 January 2004	2269 days (2208 Sols)
Mars Exploration Rover Opportunity*	25 January 2004	5498 days (5352 Sols)
Phoenix	25 May 2008	161 days (157 Sols)
Mars Science Laboratory Curiosity*	6 August 2012	Still operational

Table 2.2: Surface missions (lander or rover) that have successfully landed on Mars before the InSight mission and their period of operation. Rovers are marked with a star (*).

After the Viking mission, a new attempt to deploy seismological instrumentation on Mars came in 1996 with the Mars 96 mission by the Russian Space Forces. The plan was to bring two small surface stations, each equipped with one 0.1-1 Hz vertical seismometer (OPTIMISM experiment, Lognonné et al. (1998)), besides two very short-period vertical seismometers. Unluckily, the mission failed shortly after launch, so nothing of this could be achieved. In the meantime, further international efforts were underway for an eventual return to Mars, such as the InterMarsNet (Chicarro et al., 1994; Lognonné et al., 1996) or NetLander (Lognonné et al., 2000; Dehant et al., 2004) projects. Besides, other non-seismological missions successfully landed on Mars and have explored its surface and atmosphere for years, as presented in Table 2.2. However, scientists had to wait almost four decades after the Viking mission to bring a new seismological experiment to Mars, with NASA's selection of the InSight project (Banerdt et al., 2012).

2.1.5 The InSight mission

InSight (**In**terior Exploration using **S**eismic **I**nvestigations, **G**eodesy and **H**eat **T**ransport) is an interplanetary mission selected by NASA in 2012, as part of the Discovery program, for development and launch to explore the internal structure and dynamics of Mars. It is an interdisciplinary effort among different worldwide institutions mainly led by JPL (Jet Propulsion Laboratory, USA), IPG Paris (Institut de Physique du Globe de Paris, France), ETH Zürich (Switzerland), UCL (University College London, United Kingdom) and DLR (Deutsches Zentrum für Luft- und Raumfahrt, Germany), where scientists of the University of Cologne are also directly involved.

By mapping the interior of Mars, InSight aims to help understand terrestrial bodies' formation and evolution. For this purpose, six science objectives are planned to be accomplished (Banerdt et al., 2013; Smrekar et al., 2019):

1. Determine the size, composition and physical state of the core.
2. Determine the thickness and structure of the crust.
3. Determine the composition and structure of the mantle.

4. Determine the thermal state of the interior of the planet
5. Measure the rate and geographical distribution of Mars' internal seismic activity.
6. Measure the rate of impacts on the surface.

Pursuing these objectives, the InSight spacecraft was launched on May 5, 2018, and successfully landed in western Elysium Planitia, on November 26, 2018. Throughout this work, the exact location where the InSight spacecraft landed on Mars is known as the InSight landing site (also called ILS). The planned ILS was scouted before launch and selected after thoroughly assessing the potential landing sites. In this assessment, the engineering constraints had more influence on the final selection than the science objectives. As stated by Golombek et al. (2017), the engineering constraints are the technical aspects that allow a successful Entry, Descent and Landing (EDL) and adequate performance of the spacecraft, lander and instruments. These included the elevation of the site (sufficiently low to have a thick atmosphere to slow down the entry and descent of the lander), the latitude (for solar power and thermal management of the spacecraft) and the characteristics of the load-bearing surface (to enable a successful touchdown and deployment of instruments), among others. Under these constraints, the selected ILS was an ellipsoidal area in western Elysium Planitia, of 130 km × 27 km around ∼4.5°N/∼135.9°E, which exceeded the 99% probability of success (Golombek et al., 2017).

After a successful EDL, the InSight spacecraft landed in the plains of western Elysium Planitia on 26 November 2018 (Banerdt et al., 2020). A post-landing assessment of the ILS, by Golombek et al. (2020c), determined its location at 4.502384°N, 135.623447°E, at an elevation of -2613.426 m with respect to the MOLA geoid (see Fig. 2.1). Even though other missions like Curiosity and Spirit landed in nearby regions, this is the first mission to land in the plains of Elysium Planitia. The InSight lander finally settled at the ILS to deploy the first seismological experiment on the Martian surface.

The InSight lander

To achieve the goals of the mission, the InSight lander (once the spacecraft landed and rested on the Martian surface) is equipped with a set of geophysical instruments to perform the following primary experiments:

- **RISE** (**R**otation and **I**nterior **S**tructure **E**xperiment): uses two X-band antennas to track the lander location and determine the rotation, precession and nutation of Mars (Folkner et al., 2018).
- **SEIS** (**S**eismic **E**xperiment for **I**nterior **S**tructure): a single seismological station to monitor the Martian ground motion and investigate the propagation of seismic waves through Mars interior (Lognonné and Pike, 2015).
- **HP^3** (**H**eat Flow and **P**hysical **P**roperties **P**ackage): a self-hammering mole with embedded sensors to measure temperature profile to a depth of 3 - 5 m. Surface temperature variations and conductivity measurements are also performed (Spohn et al., 2018).

Figure 2.2a shows a schematic view of the lander setup. Two of these geophysical experiments (HP^3 and SEIS) were deployed on the Martian surface by a robotic arm (IDA

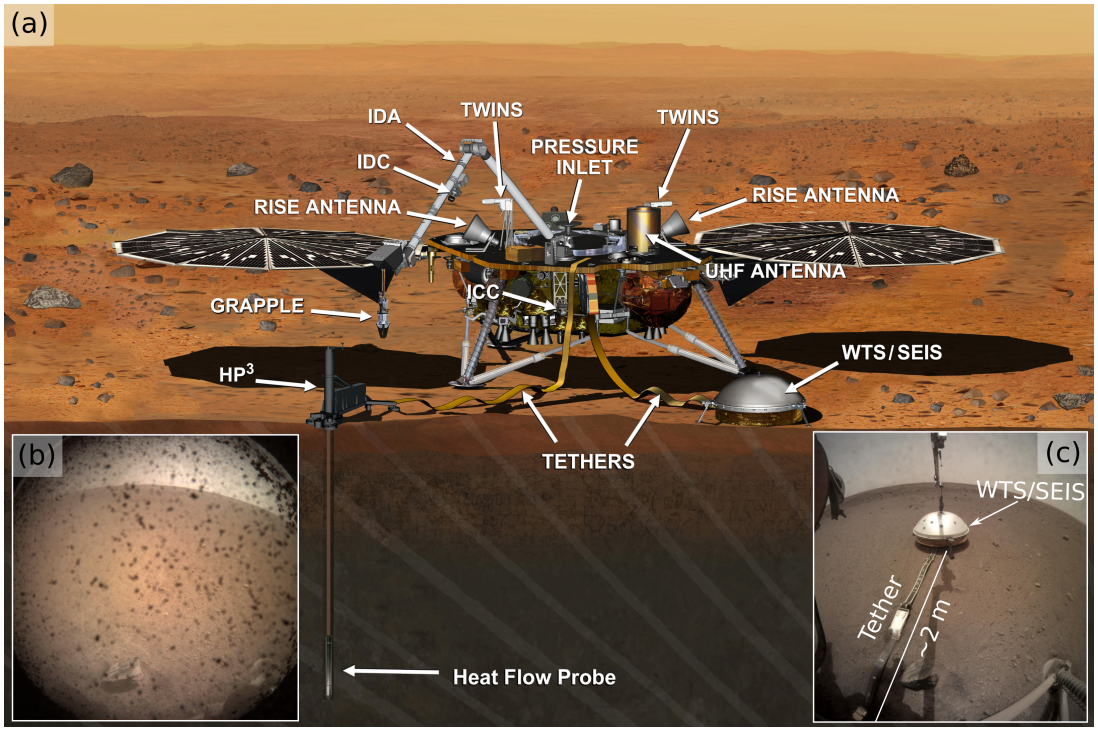


Figure 2.2: InSight lander setup. **(a)** Artist's concept of the InSight lander setup on Mars after instrumentation deployment. RISE antennas are on the lander's deck. SEIS and HP^3 are deployed on the Martian surface and connected to the lander via tethers. Other instruments are: IDC - Instrument Deployment Camera, a pointable medium-resolution camera; IDC - Instrument Context Camera, a fixed wide-angle camera; IDA - Instrument Deployment Arm; Pressure Inlet - Wind-shielded opening for pressure sensor; TWINS - Temperature and Winds for InSight; UHF Antenna - Antenna used for communication with orbital relay spacecraft; WTS - Wind and Thermal Shield protecting the seismometer from the environment. **(b)** First picture of the InSight landing site, taken by ICC shortly after landing. **(c)** Deployment of WTS. Credits to: NASA/JPL-Caltech.

- Instrument Deployment Arm, Trebi-Ollennu et al., 2018), with the aid of two cameras to image the deployment zone (Maki et al., 2018), and are connected to the lander via a tether. RISE is mounted on the deck of the lander. In addition, sensors to measure environmental variables, also known as APSS (Auxiliary Payload Sensor Suite), are also mounted on the lander. These include a 3-axis magnetometer, TWINS (Temperature and Wind for INSight) and pressure sensors, which are used to decorrelate seismic signals from atmospheric effects or lander magnetic field variations (Banfield et al., 2019). Solar arrays power the lander by producing about 4 kWh of energy per sol (Lam et al., 2016).

Shortly after landing, a first view of the ILS was obtained (Fig. 2.2b), whereas the deployment of instruments started with SEIS, 22 sols after landing. After leveling and initial noise assessment, SEIS was covered with the Wind and Thermal Shield (WTS) on Sol 66, the 66th sol after landing (2 February 2019), as shown in Fig. 2.2c, to reduce noise due to atmospheric perturbations (Lognonné et al., 2020). Calibration and tuning of SEIS finished around Sol 85, when it started to record seismic data at full performance (Banerdt et al., 2020). The deployment of HP^3 started a few days later, on 4 February 2019, whereas the hammering jobs to dig the heat flow probe (see Fig. 2.2a) started on 28

February 2019. With this configuration, InSight is initially expected to operate for two terrestrial years on Mars[3].

Among all the experiments and instruments, SEIS is the most interesting for this work as it will record the Martian ground motion, which brings information about the subsurface structure. Thus, a brief overview of the instrument's specifications is provided below. For further details on the components and performance of SEIS, the reader is referred to Lognonné et al. (2019), on which the following subsection is primarily based.

Characteristics of SEIS

SEIS consists of one seismological station deployed at the ILS, around $\sim$ 2 m away from the deck of the InSight lander (Fig. 2.2c). It is the first seismological instrumentation deployed on the Martian surface, as the instrument carried by Viking 2 stayed on the lander. Figure 2.3 presents a schematic overview of SEIS components for better contextualization.

SEIS comprises six seismological sensors: three Very Broadband (VBB) and three short-period (SP) sensors, which form the VBB and SP seismometers, respectively. The VBB sensors are a trio of oblique identical inverted pendulums tuned for Mars gravity, in a non-Galperin configuration, tilted by $\sim$30° with respect to the ground horizontal and oriented along directions 120° away from each other (see Fig. 2.3b). Each VBB sensor measures ground motion along one axis of a UVW coordinate system, so the final vertical and horizontal ground-motion components are obtained by combining the output of these three channels. This differs from SP, whose vertical component (SP1) is measured independently from the mutually orthogonal horizontal components (SP2 and SP3).

The VBB seismometer was especially designed for monitoring the 0.01 - 5 Hz frequency bandwidth, with natural and corner frequencies of 0.5 and 0.0625 Hz, respectively. On the other hand, the SP covers the 0.1 - 50 Hz bandwidth, with natural and corner frequencies at 6 and 0.0286 Hz, correspondingly. Because of this, VBB performs better at long periods than SP and is the main instrument to detect distant Martian seismic events, whereas SP can be used for more local to regional-scale phenomena.

The SEIS seismometers are designed to mechanically couple to the Martian ground while hermetically, thermally and mechanically isolated from the surrounding Mars's atmospheric and thermal environment. For this, the SEIS instrumentation is protected with different insulating layers. First, the VBB is placed in a highly evacuated titanium sphere, also known as the Evacuated Container (EC), where the components are kept under vacuum conditions. The EC is then placed on the SEIS Leveling System (LVL), a common structure that acts as a rigid link to the ground and allows leveling the seismometers with three electrically motorized legs (Fayon et al., 2018). The LVL is the main structure of the Sensor Assembly (SA), where heaters (to face cold temperatures in winter), temperature sensors and the SPs, among other electronics, are also mounted (see Fig. 2.3b). The SA is then protected by the RWEB (Remote Warm Enclosure Box), a thermal blanket to protect against thermal noise. The outermost layer is the WTS, which protects against wind and temperature variations.

[3]At the time of submitting this manuscript, InSight has ceased operations as of 15 December 2022 due to the lack of power caused by dust accumulation on the solar arrays.

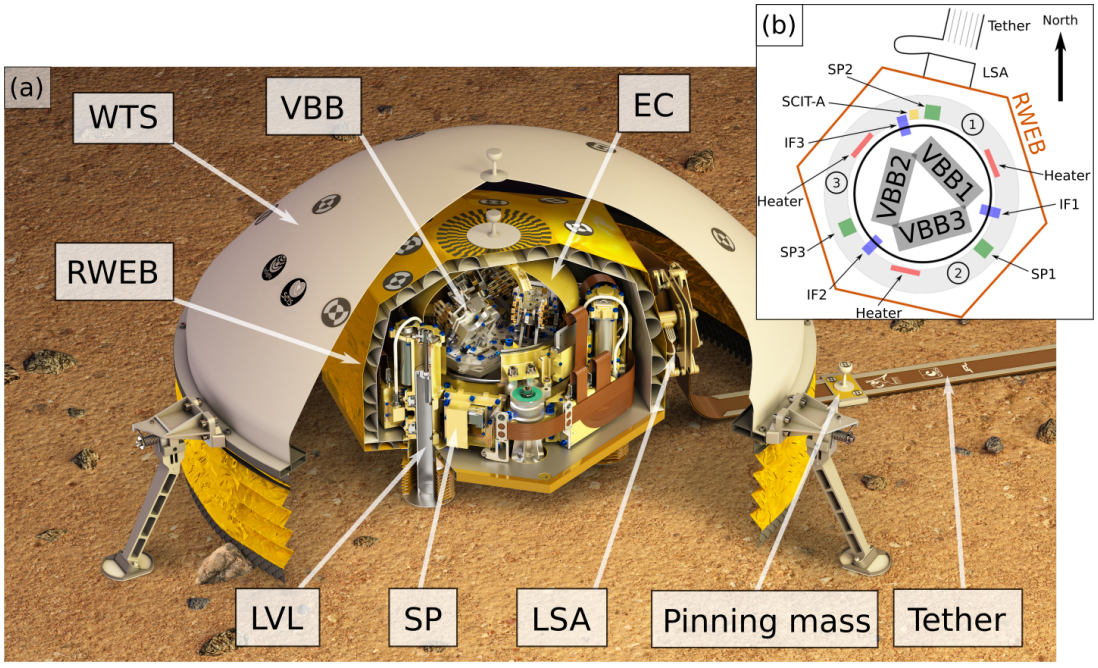


Figure 2.3: Schematic view of SEIS components. **(a)** Cut-through view of SEIS, including the Wind and Thermal Shield (WTS). The main components of SEIS are labeled. RWEB: Remote Warm Enclosure Box, EC: Evacuated Container, LVL: Levelling System, SP: Short-Period sensor, LSA: Load Shunt Assembly, VBB: Very Broadband sensors. **(b)** Plan view of SEIS, modified from Scholz et al. (2020). The gray ring is the Sensor Assembly (SA) support structure carrying the SP sensors, heaters, and the SCIT-A (scientific temperature A) sensor. IF1–IF3: mounting bolts connecting the EC of the VBB sensors with the ring structure. Numbers 1–3: electronic legs of LVL. The three VBB (VBB1, VBB2 and VBB3) sensors are oriented according to the actual configuration utilized.

The main part of the electronics for SEIS is contained in the Electronic Box (EBox), which stays on the lander deck. The EBox sends power and exchanges electronic signals (including the ground-motion data) with the SA via the Tether, a semi-rigid flat cable between the SA and the lander (see Fig. 2.2c and 2.3). As noise coming from the lander could reach the SA through the Tether, a decoupling system (LSA - Load Shunt Assembly) is also included. It consists of one plate fixed to the SA and one free plate connected to the Tether. After deployment, the LSA is "opened" by separating these two plates, emulating the loop around the sensor done on Earth installations, to enable thermoelastic and mechanic isolation of the SA. This isolation is boosted by a pinning mass in the Tether, which can also help to adjust the geometry of the LSA.

Once fully deployed, SEIS recorded ground-motion data continuously, unless operational reasons prevented it. VBB had a preferential sampling acquisition rate of 20 samples per second (sps), although 100 sps data was also retrieved. The recorded data is stored in a flash memory in the EBOX before being decimated and transmitted to SISMOC (SEIS on Mars Operations Center). The Marsquake Service (MQS) is the official service within the InSight mission in charge of routine monitoring of InSight data for the detection and location of Martian seismic events, in order to create and curate a catalog of seismicity on Mars during the course of the mission (Clinton et al., 2018). To this end, different methodologies, single-station approaches and preliminary models have been developed for determining the source location of the events and their magnitude (e.g., Panning et al., 2015; Khan et al., 2016; Böse et al., 2017). Following international

seismological standards, the InSight seismological station has been named as *ELYSE* and network code *XB*. The seismological data and metadata are publicly available through IPGP and IRIS Data Centers (InSight Mars SEIS Data Service, 2019).

2.1.6 Geological setting at the InSight landing site

Proper knowledge and understanding of the geological setting is needed to investigate further the characteristics of the Martian subsurface structure. At the InSight landing site, information about the geological features at local (tens of meters) and regional (tens of kilometers) scales was available before the mission's launch and shortly after landing. This information is fundamental to correctly interpreting the seismological recordings collected by SEIS and their outcomes and is presented below to better contextualize the scope of this work and the open questions about the ILS subsurface structure.

Local geology at the landing site

The InSight spacecraft landed in western Elysium Planitia, a broad plain region around the Martian equator (Fig. 2.1). As presented in Fig. 2.4, the ILS has been mapped by Tanaka et al. (2014) as either volcanic or sedimentary Early Hesperian Transition unit (eHt), surrounded by younger Hesperian and Amazonian lavas from Elysium Mons (AHv), to the north, and very young Late Amazonian lavas from Cerberus Fossae (lAv), about 1500 km to the east (Vaucher et al., 2009).

Further properties of the shallow subsurface structure beneath the ILS have been derived before and shortly after landing by analyzing surface geology and orbital imagery from HiRISE (High Resolution Imaging Science Experiment, McEwen et al., 2007), CTX (Context Camera, Malin et al., 2007) and CRISM (Compact Reconnaissance Imaging Spectrometer for Mars, Murchie et al., 2007) images from MRO.

Various observations support the plains of the ILS to be of volcanic origin, as summarized by different authors (e.g., Golombek et al., 2017; Knapmeyer-Endrun et al., 2017; Grant et al., 2020). Some of the arguments are:

1. The number of 10 to 100-m diameter impact craters showing ejected rocks with a low albedo, which is consistent with a strong competent layer underneath (Golombek et al., 2017; Warner et al., 2017).
2. The absence of any observable sedimentary structures in rocks at the landing site (Grant et al., 2020).
3. Smooth Early Amazonian to Late Hesperian lava flows up to 200 m thick south of the landing site (Golombek et al., 2017).
4. The presence of rocks with a uniform fine-grained aphanitic texture, consistent with a basaltic origin (Golombek et al., 2020b).

Particularly, the ILS is located within the so-called Homestead hollow (Fig. 2.5a), an impact crater of 27 m diameter and 0.3 m deep that has been heavily degraded by eolian, lesser impacts and mass-wasting processes (Golombek et al., 2020b; Grant et al., 2020; Warner et al., 2020). The InSight lander is placed on the western rocky side of the

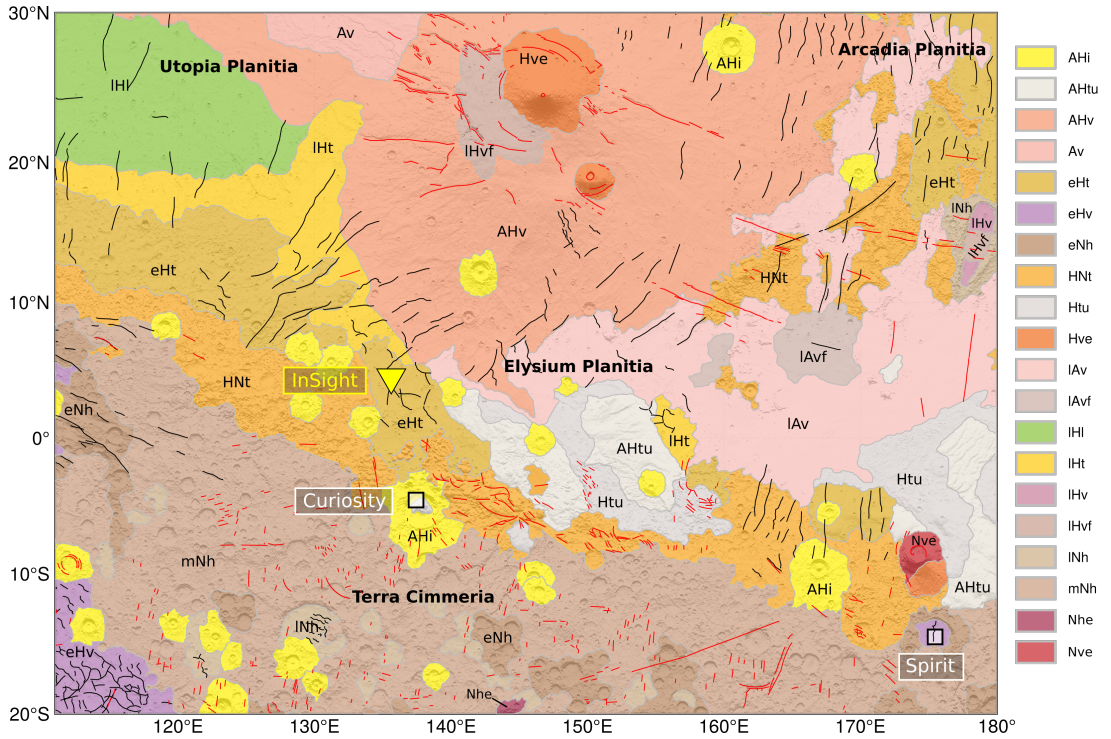


Figure 2.4: Geological map in the surrounding region around the InSight landing site. The following geological units, identified by Tanaka et al. (2014), are present in this region: **AHi** (Amazonian and Hesperian impact unit), **AHtu** (Amazonian and Hesperian transition undivided unit), **AHv** (Amazonian and Hesperian volcanic unit), **Av** (Amazonian volcanic unit), **eHt** (Early Hesperian transition unit), **eHv** (Early Hesperian volcanic unit), **eHv** (Early Hesperian volcanic unit), **eNh** (Early Noachian highland unit), **HNt** (Hesperian and Noachian transition unit), **Htu** (Hesperian transition undivided unit), **Hve** (Hesperian volcanic edifice unit), **lAv** (Late Amazonian volcanic unit), **lAvf** (Late Amazonian volcanic field unit), **lHl** (Late Hesperian lowland unit), **lHt** (Late Hesperian transition unit), **lHv** (Late Hesperian volcanic unit), **lHvf** (Late Hesperian volcanic field unit), **lNh** (Late Noachian highland unit), **lNh** (Late Noachian highland unit), mNh (Middle Noachian highland unit), **Nhe** (Noachian highland edifice unit), **Nve** (Noachian volcanic edifice unit). Background topography is from MOLA data (Smith et al., 2001). The compression and extension structures, compiled by Knapmeyer et al. (2006) and Knapmeyer et al. (2008), are plotted as black and red lines, respectively.

hollow, in a rather flat ground with slopes between $2-4^{\circ}$ ($<1^{\circ}$) in the surrounding 1-5 m (100 m) length scale (Golombek et al., 2020a).

The topmost layer of the Martian subsurface is known as the regolith, a sandy fine-grained unit that has been greatly fractured by impacts and aeolian processes. The top ∼5-10 cm of this layer is known as the duricrust, a layer of small rocks and pebbles cemented in a finer-grained matrix (Golombek et al., 2020b; Warner et al., 2020). One of the mission's requirements was to land where the regolith was >3 m thick to facilitate the deployment of HP^3 (Golombek et al., 2017). Thus, during the ILS selection process, the regolith thickness was estimated between ∼3 and 18 m by analyzing the size and distribution of the impact craters in the expected landing area, including rocky and non-rocky ejecta craters (Warner et al., 2017). Here, a rocky ejecta crater (REC) is understood as an impact crater with rocky ejecta material (boulders ejected from the rocky unit beneath the regolith) on the surface around its rim. Conversely, a non-REC is an impact crater without ejecta material on the surface. A post-landing assessment, considering craters in a close area around the actual ILS, suggests a regolith thickness ∼2.5-4 m

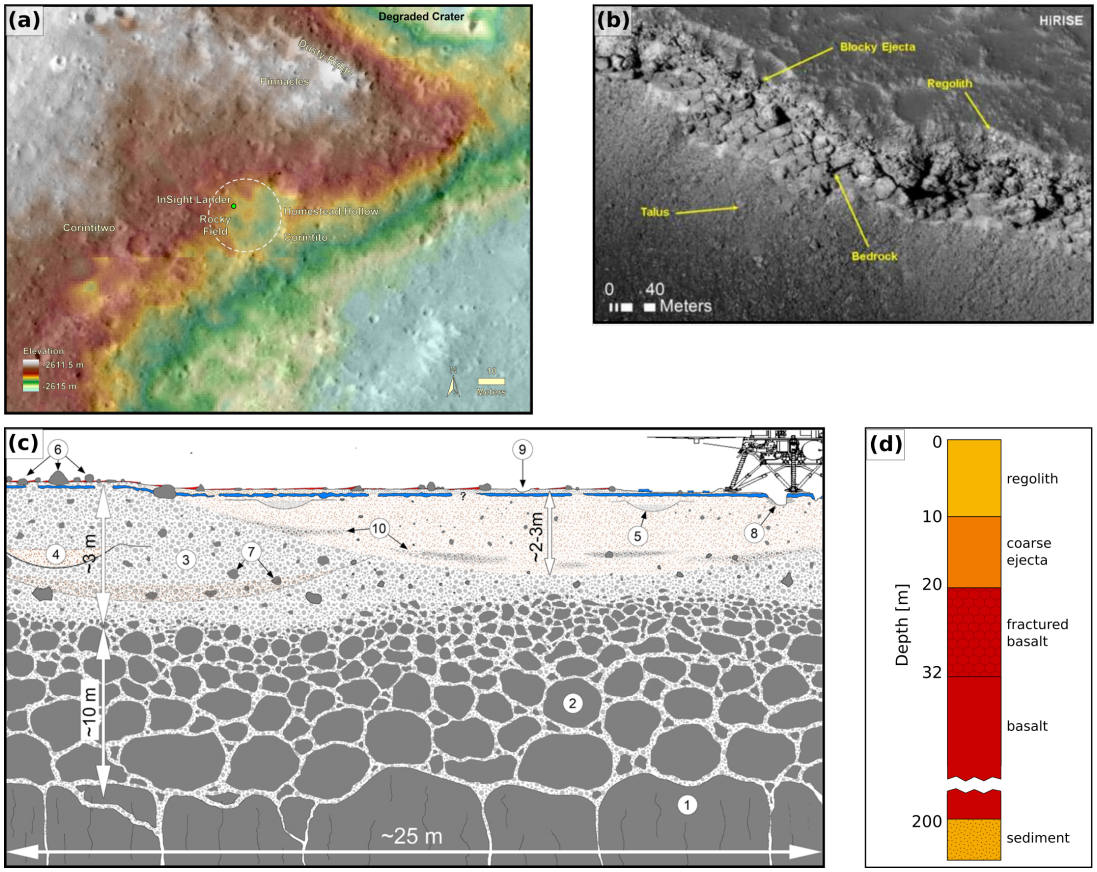


Figure 2.5: InSight local-scale context. **(a)** Topographic map overlain on a HiRISE image of the area around InSight. The Homestead hollow is remarked by segmented white line. Two secondary craters (Corintito and Corintitwo) are in view of the lander. Note craters in widely varying states of degradation from very fresh (Corinto secondaries) to highly degraded Homestead hollow. Digital elevation model (color) from stereo HiRISE images from Fergason et al. (2017) (taken from Golombek et al., 2020c). **(b)** Portion of Hephaestus Fossae in southern Utopia Planitia at 21.9°N, 122.0°E showing thick, fine-grained regolith, that grades into coarse, blocky ejecta that overlies strong, jointed bedrock. (taken from Knapmeyer-Endrun et al., 2017). **(c)** Interpretative cross-section of the shallow subsurface beneath the InSight lander illustrating the fine-grained impact-generated regolith (3), blocky ejecta (2) and the fractured basalt flows (1). For further details in the numbering, the reader is referred to Golombek et al. (2020b), from where this figure is taken. **(d)** Pre-landing model for the InSight landing site, as proposed by Knapmeyer-Endrun et al. (2017).

(Golombek et al., 2020a), which agrees with the estimated fill beneath the lander from degradation analysis of the Homestead hollow (Warner et al., 2020).

The geological units beneath the regolith are expected to be Hesperian to Early Amazonian basaltic lava flows. In this sense, terrains with similar surface geology and age as the ILS region (i.e., lava plains and Early Amazonian to Hesperian) are expected to have a similar subsurface structure (Warner et al., 2017; Golombek et al., 2017). Hephaestus Fossae, a fracture system located ∼900 km to the northwest of the ILS (see Fig. 2.6), meets these criteria and is used to infer the structures beneath the ILS. Three different units can be identified from HiRISE imagery over an exposed escarpment nearby Hephaestus Fossae (Fig. 2.5b), corresponding to: (1) a fine-grained regolith ∼5 m thick, (2) a coarse, boulder-rich brecciated unit underlain by (3) a massive, strong fractured unit (Warner et al., 2017; Golombek et al., 2017). The brecciated material beneath the regolith can

be understood as a lava flow or other competent bedrock broken into boulder-sized clasts through impact weathering. This layer lies on top of a more massive fractured unit, both being the transition units between the fine-grained regolith and a deeper consolidated bedrock (Warner et al., 2017). This sedimentary pattern is expected for regolith formation contexts where the number of small impacts, which penetrate shallow depths, is larger than large impacts (e.g., Hartmann et al., 2001; Wilcox et al., 2005). A sketch of the near-surface stratigraphy around the ILS, from orbital imagery and surface observations, is presented in Fig. 2.5c, where the main units: regolith, blocky-ejecta and fractured basalt are illustrated. The basalt lava flows have been proposed to extend to 200 m depth after analyzing large craters in the surrounding ILS area. In particular, HiRISE and CTX imagery across the region revealed that few rocks are observed in the ejecta of > 2 km-sized craters, which is interpreted as the impact did not excavate a rocky unit (Golombek et al., 2017; Warner et al., 2017).

With this information and material properties inferred from laboratory or field measurements in analog Earth materials, Knapmeyer-Endrun et al. (2017) proposed a preliminary shallow subsurface model for the ILS, known as the pre-landing model (Fig. 2.5d). The model proposes a shallow regolith layer (10 m thick), followed by a coarse ejecta layer (10 m thick), underlain by a fractured basalt unit (12 m thick) and deeper pristine basalt unit, which extends down to 200 m depth, where a sedimentary unit is expected. This model is used as a reference for this study.

Regional features in Elysium Planitia

On a regional scale (in the order of tens to hundreds of kilometers), the ILS is surrounded by remarkable geomorphological features, such as the dichotomy boundary to the south and southwest, Elysium Mons to the north, Hephaestus Fossae to the northwest and Cerberus Fossae to the northeast (Fig. 2.6). As inferred from the topography data, the ILS is located in a slight topographical depression along a SW-NE direction delimited by the Elysium Mons, to the north, and the southern highlands, to the south.

Various studies have proposed different crustal models for Mars, including the western Elysium Planitia region (e.g., Plesa et al., 2018b). As a reference, by studying the correlation between topography and gravity and assuming an average crustal thickness of 42 km, Goossens et al. (2017) proposed that the bulk crustal density in Mars is 2582 ± 209 kg m^{-3}. Under these considerations, and using a larger density for volcanic complexes, the crustal thickness (H_c) in the 500 km around the InSight lander would range between 30 and 40 km (Fig. 2.7). However, it is relevant to highlight that lower bulk crustal densities result in smoother changes in the crustal thickness as compared to larger densities, for which sharper transitions are observed. Other works propose similar crustal thickness for the ILS region, but the trade-off between crustal density and thickness remains.

2.1.7 Martian seismic activity

The Martian seismic events, either due to a tectonic origin or other phenomena, will also be used throughout this work to investigate the subsurface structure at the ILS. Before the InSight mission, little was known about the seismic activity on Mars. The evidence of

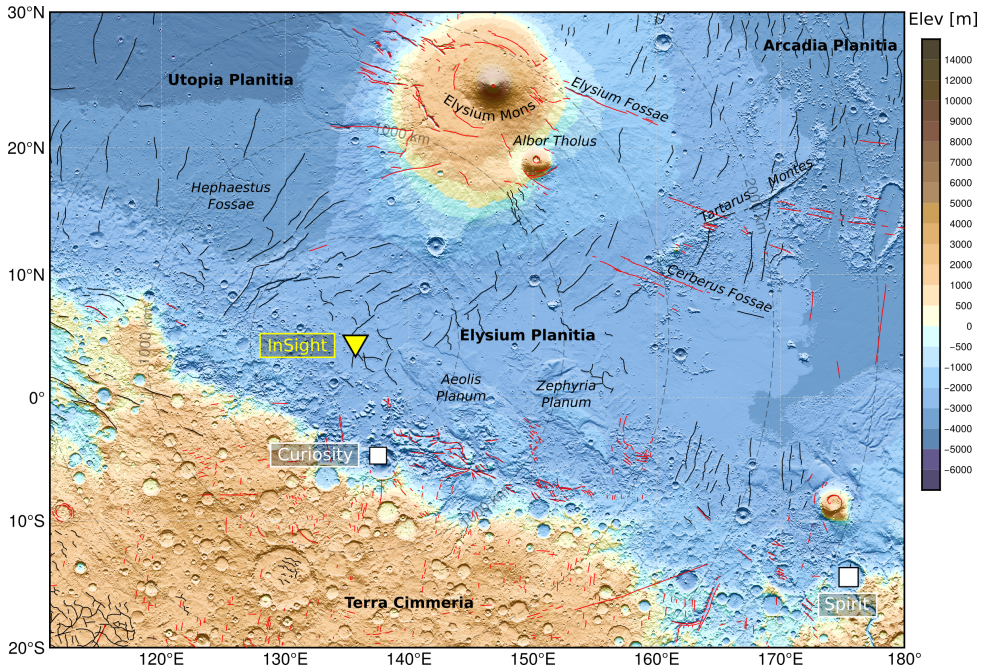


Figure 2.6: Topographic features around the InSight landing site. The color scale of the background map is given by the elevation with respect to the MOLA geoid (Smith et al., 1999b). The compression and extension structures, compiled by Knapmeyer et al. (2006) and Knapmeyer et al. (2008), are plotted as black and red lines, respectively. The landing sites of InSight (inverted yellow triangle), Curiosity and Spirit (white squares) are also illustrated. Distance isolines from the InSight landing site are plotted every 500 km (dashed lines).

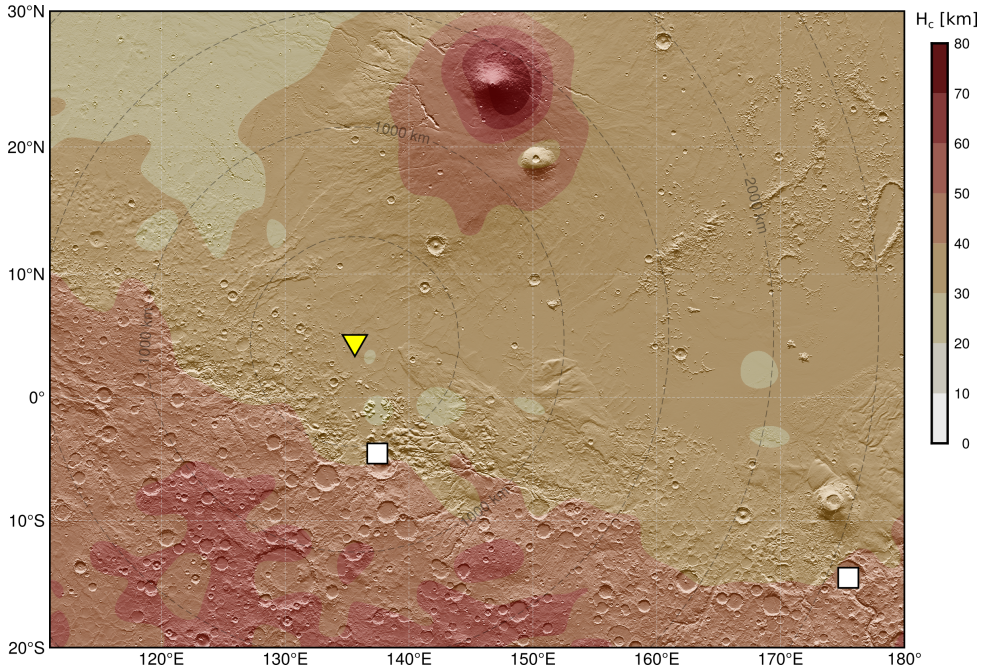


Figure 2.7: Estimated crustal thickness around the InSight landing site. The color scale indicates the range for the crustal thickness (H_c) in the region around the ILS, as modeled by Goossens et al. (2017). Mission landing sites and isolines plotted in Fig. 2.6 are also shown.

volcanic and tectonic activity from orbital imagery suggests that Mars might have been tectonically active during its evolution, although ambiguous in some cases (Carr, 2007). In current times, the Red Planet is covered by a single plate, also called a stagnant lid, and does not present active Earth-like plate tectonics (Barlow, 2008).

As stated in section 2.1.3, the recordings of the Viking 2 seismometer are unclear and do not confirm the occurrence of a seismic event. This was one of the reasons to propose that Mars was less active than the Earth (Anderson et al., 1977). Further theoretical studies on the level of seismicity of Mars have also proposed low seismic activity based on the geological evaluation of surface structures (e.g., Golombek et al., 1992; Golombek, 2002) or geodynamic modeling (Phillips, 1991; Knapmeyer et al., 2006; Plesa et al., 2018a). Based on these studies, a total of 1-10 events with moment magnitude M_w>5.3 and many more smaller events would be detected within the two years of the mission duration (Panning et al., 2015).

The Martian seismic activity is thus expected to be less than the global seismicity on Earth, likely less than the intraplate terrestrial activity and higher than the shallow seismicity on the Moon (Fig. 2.8). The Cerberus Fossae region has been proposed as a tectonically active area around the InSight landing site, based on evidence of fresh bolder trails that had been originated from tectonic Martian seismic events, also known as *marsquakes* (Roberts et al., 2012). Other potential seismic sources are the impacts of meteorites on the Martian surface, for which the epicentral location could be constrained by their identification in orbital imagery.

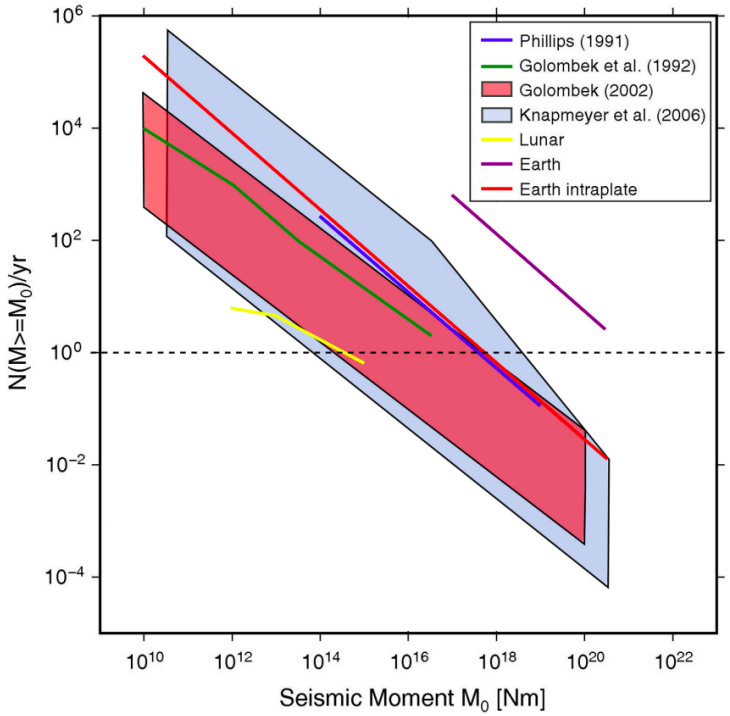


Figure 2.8: Estimates of the size-frequency distribution of seismic events on Mars, the Earth and the Moon (adapted and compiled from Knapmeyer et al. (2006) and Panning et al. (2015)). The dashed horizontal line indicates the level above which events would be expected to be detected by SEIS (Panning et al., 2015). Figure taken from Becker (2018).

2.2 Single-station seismology for mapping the subsurface structure

Unlike Earth, where thousands of seismological stations can be used for studying the planet, only one station is available for exploring Mars interior. Therefore, single-station seismological techniques must be exploited. These techniques require data from one station only to obtain information about the seismic sources, the subsurface structure where the station is located or the path between the seismic sources and the station. Particularly, this work aims to map the subsurface structure at the ILS at different scales, for which different single-station techniques have been proposed (e.g., autocorrelations, horizontal-to-vertical spectral ratios, P-to-s Receiver Functions). The primary technique utilized throughout this work is the horizontal-to-vertical spectral ratios (HVSR), for the shallow subsurface, and the Rayleigh-waves ellipticity, for the crustal scale. This section provides a brief overview of general seismological concepts and the theoretical background of HVSR. Most of the explanations provided in the first subsection are based on Shearer (2019), whereas the second subsection strongly follows Lunedei and Malischewsky (2015).

2.2.1 Fundamentals of seismology

A seismic source generates two main types of waves, P and S waves, known as body waves. The interaction of the body waves with the medium can generate Love and Rayleigh waves, also known as surface waves. Some of the differences among them rely on their velocity of propagation and particle motion (i.e., the motion of a particle when passing the wave), as shown in Fig. 2.9a, and highlighted below:

- **P waves:** or primary waves, are the fastest seismic waves, traveling with velocity V_p, and so arrive first at a specific recording station. Their particle motion is parallel to the direction of wave propagation.
- **S waves:** secondary or shear waves, are slower than P-waves, traveling with velocity V_s, and thus arrive later than the P wave. Their particle motion is perpendicular to the direction of wave propagation.
- **Love waves:** travel with a lower velocity than the S-wave. Their particle motion is perpendicular to the direction of wave propagation and parallel to the free surface.
- **Rayleigh waves:** travel with typically a lower velocity than the Love waves. The generated ground motion is both parallel to the wave propagation direction and perpendicular to the surface. The vertical ground motion is theoretically delayed 90° from the horizontal ground motion, thus generating an elliptical particle motion.

Another relevant characteristic is that, unlike the body waves, the surface waves are dispersive, so that different wavelengths travel at different velocities and, thus, a train of Love or Rayleigh waves is observed in a certain time window rather than a single arrival.

The phenomenon generating body waves is a seismic event, which might be due to, e.g., a meteorite impact or natural tectonic forces. When a seismic event occurs, it will generate body waves, and potentially surface waves, that will produce ground motion upon the arrival at the seismological station. Depending on the amplitude of the ground

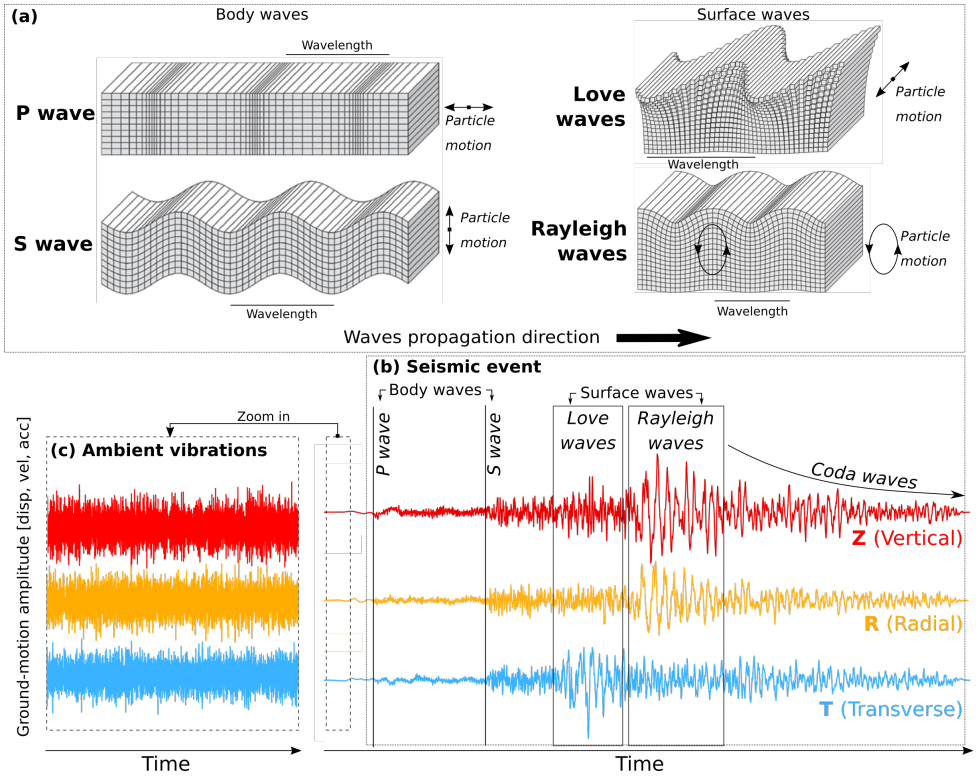


Figure 2.9: Basic concepts for single-station seismology. (a) Particle motion of body (P and S) and surface (Love and Rayleigh) waves. Modified from Shearer (2019). **(b)** Arrivals and recordings of body, surface and coda waves generated by a seismic event at a specific station, displayed in the ZRT coordinate system (Vertical, Radial and Transverse). **(c)** Example of ambient vibrations before the arrival of seismic waves related to a seismic event, illustrating the seismic signals apparently unrelated to any specific seismic source. Ground-motion amplitudes are typically described in displacement, velocity or acceleration units.

motion and the detection limit of the instrument at the recording site (also known as the *noise floor*), the ground motion generated by the arrival of these waves might be visible in the seismological recordings. The recording of a seismic event is thus characterized by the ground motion generated by some (or all) of these waves, as shown in Fig. 2.9b. The ground motions are typically recorded in an orthogonal three-component coordinates system like ZNE (Vertical, North and East). If the source location is known, the back-azimuth, i.e., the angle of the great-circle path from the station to the source, can be used to rotate into the ZRT coordinate system (Vertical, Radial and Transverse). The radial component would correspond to the direction of wave propagation and thus the visualization of the different waves is clearer, as in Fig. 2.9b.

Besides these main seismic waves, possible reverberations and the interference of converted and reflected waves at and around the station are also recorded. Due to conversions at the layer discontinuities, some secondary phases may be clearly seen in the recordings, depending on the subsurface structure. After the arrival of the body and surface waves (if any), the ground motion decays from large amplitudes until reaching the level of ground-motion amplitudes before the P-wave arrival. This time window is known as the *coda* of the seismic event and is composed of diffuse waves scattered by small-scale heterogeneities in the subsurface structure (Aki, 1969; Aki and Chouet, 1975; Margerin et al., 1999), also known as coda waves (Fig. 2.9b).

The seismic energy recorded out of the seismic event window (or basically everything that cannot be attributed to a discrete seismic event) is known as *ambient vibrations*, *ambient noise* or also *seismic noise* (Fig. 2.9c), which are originated from sources distributed in space and time. On Earth, the ambient vibrations are the result of seismic waves generated primarily by wind and cultural noise at high frequencies (>1 Hz) and ocean waves and atmospheric effects at longer periods. The term *seismic noise* has been used because it interferes in the study of seismic events, which have long been the main source for investigating the Earth's interior. Nevertheless, recent studies have shown that continuous *noise* recordings can be the main source as they can be used to illuminate the subsurface structure.

Throughout this work, different features of the seismological recordings are used to map the subsurface structure. In the first part, the ambient vibrations and coda of seismic events are investigated in the high-frequency range (>0.4 Hz) in order to map the shallow subsurface structure. In the second part, a strong focus is put on Rayleigh waves at long periods (>10 s) to get constraints for the crustal structure at the InSight landing site. Here, the horizontal-to-vertical spectral ratios (HVSR) are the main single-station technique used for mapping the shallow interior of Mars, for which further details are provided below.

2.2.2 The horizontal-to-vertical spectral ratios (HVSR) technique

The horizontal-to-vertical spectral ratios (HVSR or H/V) is a well-consolidated single-station seismological technique that has been widely used for a long time on Earth. It only requires the three components of the ground motion (two horizontals and one vertical). The ratio between the spectral amplitudes of the horizontal over the vertical ground motion is called the H/V (or HVSR) curve, which is a function of the frequency. This technique, first introduced by Nogoshi and Igarashi (1971) and popularized by Nakamura (1989), allows the estimation of the fundamental resonance frequency, ground-motion amplification and elastic properties of the shallow structure by using seismic recordings of either ambient vibrations or earthquake motions.

Even though this method has become popular in recent decades, the discussion on its strengths and limitations is still due to the absence of a clear theoretical basis (Bonnefoy-Claudet et al., 2008). The theory and physical interpretation behind the HVSR are unclear, as well as the nature of the ambient vibrations wavefield. In fact, the relation between the observed HVSR curve and the subsurface structure has been under discussion for a long time. Regarding the ambient vibrations, there are three main approaches to understanding the physical meaning of the HVSR, as briefly described below.

The body-waves approach

One theoretical explanation for the HVSR was formulated by Nakamura (1989), who assumed that the ambient vibrations wavefield is composed of S and Rayleigh waves. He considered that the effect of the latter can be neglected when considering the HVSR at the surface, for which it was assumed that the vertical component of the ground motion is not amplified due to the underground structure and the H/V is 1 at the bedrock. This HVSR

curve would directly correspond to the amplification phenomena affecting the horizontal ground motion.

After criticism, Nakamura et al. (2000) modified the HVSR interpretation by considering the ambient-vibration wavefield as a combination of vertically incident P and S waves along with Rayleigh waves, given by the following equation:

$$HVSR(\omega) = \frac{A^{BW}_{H,bedrock}(\omega)}{A^{BW}_{V,bedrock}(\omega)} \frac{T_H(\omega) + \frac{A^{SW}_{H,surface}(\omega)}{A^{BW}_{H,bedrock}(\omega)}}{T_V(\omega) + \frac{A^{SW}_{V,surface}(\omega)}{A^{BW}_{V,bedrock}(\omega)}} \tag{2.1}$$

which the author calls "quasi transfer spectrum" (QTS). Here, $A^{\gamma}_{\delta,\sigma}(\omega)$ are the spectral amplitudes at certain angular frequency ω, for the component $\delta = H$ (horizontal) or V (vertical), at the bedrock or at the surface (σ) and using $\gamma = BW$ (body waves) or SW (surface waves). T_H and T_V are the horizontal and vertical transfer functions. Assuming that the body-waves amplitude ratio at the bedrock is close to 1, then, when the surface-waves contribution is neglectable, the HVSR curve is close to T_H/T_V.

As vertically incident body waves are considered only, the vertical and horizontal ground motions are related to the P and S waves. Due to its larger velocities, P-wave amplifications are not expected near the S-wave resonance frequency. The HVSR curve should thus approximate the S-wave transfer function around its peak frequency. In definitive, the author states that the HVSR peak (maximum of the HVSR curve) represents the site S-wave resonance frequency and its relative amplification factor, irrespective of Rayleigh waves.

This idea was reaffirmed in Nakamura (2008) and made the HVSR technique popular for quick subsurface mapping. This approach has succeeded in explaining the correspondence between HVSR frequency peak and the S-wave resonance frequency but failed in predicting the amplification factor (Lunedei and Malischewsky, 2015). Besides, this approach is only valid for explaining the HVSR curve around the main frequency peak, and any extension to the whole HVSR curve requires further assumptions (Bard et al., 1999).

The surface-waves approach

Although the body waves approach can explain some features of the HVSR curve, it is well-accepted within the seismological community that the ambient vibrations are composed of all the seismic phases and not only body waves. The key element here is the relative contribution of each of these waves to the full wavefield (e.g., SESAME, 2004).

Nogoshi and Igarashi (1971) first showed that the HVSR computed from ambient vibrations is comparable to the frequency-dependent ellipticity curve of the Rayleigh wave fundamental mode, concluding that this seismic wave plays a big role in the ambient vibrations. Subsequently, several authors agree with this observation (e.g., Lachet and Bard, 1994; Lermo and Chávez-García, 1994; Konno and Ohmachi, 1998; Fäh et al., 2001; Malischewsky and Scherbaum, 2004), which is justified by the energetic predominance of Rayleigh waves. It can be understood as a phenomenon where the ellipticity peak is related

to a spectral minimum of the vertical component and, in some cases, in a change in the sense of motion of the Rayleigh-wave fundamental mode, from retrograde to prograde or vice versa, in the presence of a large impedance contrast (Malischewsky and Scherbaum, 2004; Bonnefoy-Claudet et al., 2008).

Many studies have used the Rayleigh-wave ellipticity approach to successfully invert the HVSR from ambient vibrations for layered subsurface models (e.g., Yamanaka et al., 1994; Scherbaum et al., 2003; Wathelet et al., 2004). Nevertheless, some studies have shown that higher modes are needed to explain, for instance, the presence of low-velocity zones (Arai and Tokimatsu, 2004; Parolai et al., 2005; Rivet et al., 2015). Similarly, other subsurface structures with high impedance contrasts can be explained only by the coupling of the fundamental mode of the Rayleigh wave with the Airy phase of the Love wave fundamental mode (e.g., Bonnefoy-Claudet et al., 2008; Konno and Ohmachi, 1998; Lunedei and Albarello, 2010). In fact, the relative contribution of Love or Rayleigh waves to the full-wavefield ambient vibrations is not equal and may vary from site to site, with frequency and time (e.g., Köhler et al., 2007; Endrun, 2011).

In any case, the peak of the HVSR curve has been shown to be close to the S-wave resonance frequency, but the shape is closely related to the fundamental mode Rayleigh-wave ellipticity (Lachet and Bard, 1994; Arai and Tokimatsu, 2000), which suggests that the HVSR curve is due to a combined effect of body and surface waves.

The full-wavefield approach

The studies presented above suggest that the ambient vibrations can be explained by the contribution of all types of waves and the higher modes of the surface waves. Indeed, Bonnefoy-Claudet et al. (2008) showed that HVSR from ambient vibrations can be explained by different combinations of waves, depending on the impedance contrast. Field and Jacob (1993) proposed a theoretical model to relate the ambient vibration displacements to the Green's functions of the underground structure, by assuming that they are generated by an infinitude of uncorrelated point-like sources uniformly located on the surface. This model was later extended by Lunedei and Albarello (2010) to include all seismic phases, which was termed Distributed Surface Sources (DSS). One of the limitations of this model is that, because the sources are only superficial, it does not consider the presence of deep scattering. The inversion of the HVSR requires the knowledge of the specific sources acting at a site, making it a complex approach.

In this context, Sánchez-Sesma et al. (2011) proposed that the ambient vibrations can be represented as a diffuse wavefield containing all types of body and surface waves. This diffuse field assumption (DFA) has a strong theoretical background based on the principle of energy equipartition (Weaver, 1982; Margerin, 2017). This approach is used throughout this work and is explained in more detail in the next subsection.

2.2.3 HVSR under the Diffuse Field Assumption (DFA)

As shown above, even though the HVSR method is widely utilized on Earth, there is a lack of theoretical background to explain all the features of the spectral curve, especially considering that the ambient vibrations are a composition of all the types of waves.

The pioneering work of Shapiro and Campillo (2004) showed that the averaged time-domain cross-correlation of the ambient vibrations recorded in two stations allowed retrieving the approximate Green's Functions of the medium between them. This has been shown to be possible due to the condition of having a diffuse wavefield (e.g., Sánchez-Sesma and Campillo, 2006; Sánchez-Sesma et al., 2008), implying that the ambient vibrations can be understood as a diffuse field.

Ambient vibrations as a diffuse field

A diffuse field can be understood as the result of isotropic illumination of random waves, which is usually attributable to multiple scattering (e.g., Sato and Fehler, 1998; Margerin et al., 2009). In this case, the ambient noise sources are randomly distributed and the generated seismic waves suffer multiple diffractions during the propagation due to the medium heterogeneities (Campillo, 2006), as illustrated in Fig. 2.10. Therefore, rather than depending on the source locations, the characteristics of the diffuse field are controlled by the multiple scattering and the heterogeneities of the studied region (Sánchez-Sesma, 2017). According to Shapiro et al. (2000), a diffusive regime is reached when the distribution of seismic energy is almost isotropic and the phase is random as a result of multiple scattering. To some extent, the diffuse field can be understood as there are no preferred directions of the incoming energy.

The concept to describe this isotropic illumination is known as the principle of energy equipartition, first discussed by Weaver (1982) for elastic waves in a solid body. When the medium becomes completely randomized, all the modes of propagation are excited statistically at the same level, i.e., all the components of the Green's functions are excited. For each point of the medium in vibration, the diffuse field can be represented as an isotropic and random superposition of plane waves, which have amplitudes that slowly vary over time and with a random phase (Shapiro et al., 2000).

Despite the clear theoretical background, the difficult task is to prove that the ambient vibrations are in the diffuse regime. On Earth, different studies have found that the ambient vibrations field is not fully diffuse (e.g., Weaver et al., 2009; Mulargia, 2012). Particularly, Mulargia (2012), using single-station approaches, showed that the ambient vibrations are usually polarized and thus energy equipartition is not secured. On the other hand, Piña-Flores et al. (2021), using a 50 m square array, showed evidence of seismic energy equipartition in ambient noise recordings in Mexico. Although it is difficult to observe energy equipartition explicitly (Sánchez-Sesma et al., 2011), the full-wavefield DFA has been successfully used to explain the HVSR features and has been demonstrated to be a robust approach (e.g. Lontsi et al., 2015; Piña-Flores et al., 2016; Spica et al., 2018; Bora et al., 2020).

In any case, studying the nature of the ambient vibrations is still a key element for the subsequent HVSR analysis. Although strictly determining energy equipartition would require measuring spatial variations of the wavefield (e.g., Shapiro et al., 2000; Piña-Flores et al., 2021), an assessment and identification of potential non-natural sources is relevant for later interpretation (Dal Moro, 2020).

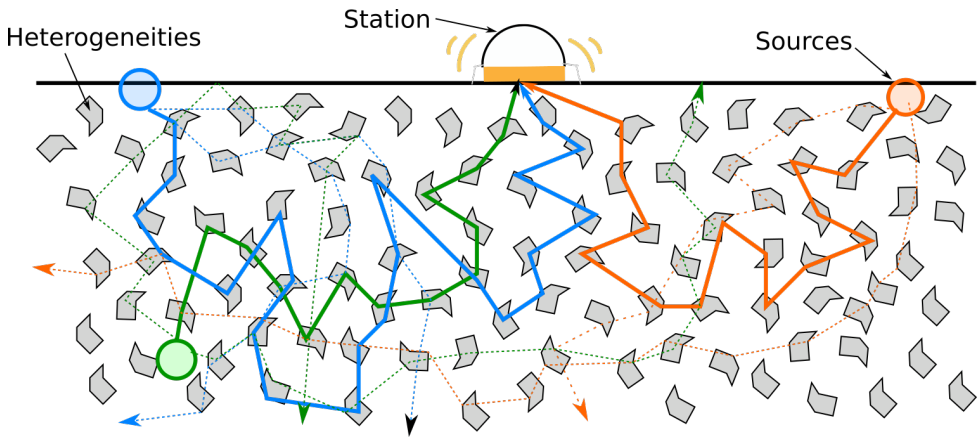


Figure 2.10: Multiple scattering sketch. Representation of the multiple scattering phenomenon, where sources (colored circles) randomly distributed around a station generate seismic waves (colored lines), which are diffracted by multiple heterogeneities in the medium (gray polygons). Solid-colored lines represent the waves arriving at the recording station, whereas dashed lines go somewhere else.

HVSR and the medium Green's Functions

In definitive, under the DFA, the Green's functions can be retrieved from averaging cross-correlations of the recorded ground motions of such diffuse field (e.g., Lobkis and Weaver, 2001; Campillo and Paul, 2003; Wapenaar, 2004). Assuming energy equipartition, Perton et al. (2009) demonstrated that the imaginary part of the Green's function between two sites is proportional to the average cross-correlations of the corresponding displacements:

$$\langle u_i(\mathbf{x}_\mathrm{A},\omega)u_j^*(\mathbf{x}_\mathrm{B},\omega)\rangle \propto Im[G_{ij}(\mathbf{x}_\mathrm{B},\mathbf{x}_\mathrm{A};\omega)], \tag{2.2}$$

with $\omega = 2\pi f$ the angular frequency, $u_i(\mathbf{x}_\mathrm{A},\omega)$ is the displacement field component in i direction at point $\mathbf{x}_\mathrm{A}$, the Green's function $G_{ij}(\mathbf{x}_\mathrm{B},\mathbf{x}_\mathrm{A};\omega)$ is defined as the displacement in the direction i at point $\mathbf{x}_\mathrm{B}$ due to the application of a unit harmonic point force in the direction j at point $\mathbf{x}_\mathrm{A}$. The asterisk (*) corresponds to the complex conjugate. The product in the frequency domain, as stated in Eq. 2.3, is equivalent to the correlation operation in the time domain.

If the source and receiver are at the same place, i.e., the sites $\mathbf{x}_\mathrm{A}$ and $\mathbf{x}_\mathrm{B}$ are the same, and the components i and j are also the same, then the average of the autocorrelation corresponds to the directional energy density $E_i(\mathbf{x},\omega)$ at point $\mathbf{x}$ (Sánchez-Sesma et al., 2008; Perton et al., 2009). Given Eq. 2.3, $E_i(\mathbf{x},\omega)$ is then proportional to the imaginary component of the Green's function, such that:

$$E_i(\mathbf{x},\omega) = \rho\omega^2\langle||u_i(\mathbf{x},\omega)||^2\rangle \propto Im[G_{ii}(\mathbf{x},\mathbf{x};\omega)], \tag{2.3}$$

where ρ is the mass density. Thus, the HVSR in a diffuse field, defined as the square root of the ratio between the horizontal and the vertical energies (Arai and Tokimatsu, 2004), is equivalent to the square root of the ratio between the imaginary parts of the corresponding Green's functions, i.e.:

$$HVSR = \frac{H}{V}(\mathbf{x},\omega) = \sqrt{\frac{\langle||u_1(\mathbf{x},\omega)||^2\rangle + \langle||u_2(\mathbf{x},\omega)||^2\rangle}{\langle||u_3(\mathbf{x},\omega)||^2\rangle}}, \tag{2.4}$$

$$= \sqrt{\frac{Im[G_{11}(\mathbf{x},\mathbf{x};\omega)] + Im[G_{22}(\mathbf{x},\mathbf{x};\omega)]}{Im[G_{33}(\mathbf{x},\mathbf{x};\omega)]}}, \tag{2.5}$$

where $i = 1, 2$ are the horizontal components and $i = 3$ is the vertical component.

Equation 2.3 provides a robust theoretical formulation to calculate the H/V spectral ratio. The way to model the HVSR consists of determining the diagonal elements (G_{11}, G_{22} and G_{33}) of the elastodynamic Green's tensor (Green's functions), which are associated to the geometry of the subsurface structure and the material properties. In conclusion, using a proper approach for the Green's functions calculation, the theoretical HVSR obtained from ambient vibrations can be modeled by defining a subsurface structure model with certain properties. Correspondingly, the observed HVSR can be inverted to derive the subsurface structure and properties.

2.2.4 HVSR on diffuse coda waves

The diffuse field regime can also be extended to the seismic events recordings. In this regard, Shapiro et al. (2000) first showed that the coda of local seismic events, in this case in Guerrero (Mexico), is under the diffuse regime. Since then, other field experiments have interpreted the coda waves as presenting signatures of energy equipartition (e.g., Hennino et al., 2001; Hong and Menke, 2008; Margerin et al., 2009; Galluzzo et al., 2015). In fact, the energy properties of the coda waves are well described by the radiative transfer equation and the diffuse approximation (e.g., Hoshiba, 1991; Margerin et al., 1999).

The interpretation of coda waves as being in a diffuse regime is based on the fact that they are the by-product of multiple scattering in the medium (Aki, 1969). In the coda waves, multiple scattering can be inferred by measuring the time between the onset of a phase arrival and the maximum amplitude, known as the delay-time t_d (Sato, 1982; Saito et al., 2002), or the shape of the temporal decay, known as the coda quality factor Q_c (Aki and Chouet, 1975). It can also be assessed by evaluating the fitting of the observations with the predicted coda decay assuming an elastic radiative transfer theory (Margerin et al., 1999). Therefore, coda waves could be readily assumed to be in the diffuse regime due to their nature, so the calculated HVSR can be modeled under the DFA. Although not part of this work, further confirmation could potentially secure this assumption.

In summary, considering the wavefield in the coda is equipartitioned, the DFA can be applied to model the HVSR curve from this data window. Therefore, the HVSR curve can be computed from the ambient vibrations and the seismic events coda. In both cases, the HVSR can be explained by the Green's functions of a subsurface structure with given material properties.

2.2.5 Limitations of the HVSR method

In spite of its practicality and cost-efficiency, the HVSR method has its own technical limitations. One of them is the well-documented non-uniqueness problem when inverting the HVSR measurements for the subsurface structure (e.g., Scherbaum et al., 2003; Piña-Flores et al., 2016). This means there are a set of different models, including scaled models, which provide the same or highly similar HVSR curves. Different approaches can help to reduce this problem, like joint inversion with independent similar-scale measurements (e.g., dispersion curves, active seismics) or *a-priori* information on the properties of the subsurface (e.g., expected range of velocities, number of layers). In definitive, without clear constraints on the absolute values, the HVSR curve provides the relative variations of the layer properties (mainly shear-wave velocity) along the subsurface structure.

Besides, the minimum (z_{min}) and maximum (z_{max}) depths of investigation (i.e., the depth range where the models can be resolved) are hard to constrain without knowing the range of shear-wave velocities of the medium and the specific frequency range. Under the full-wavefield DFA, the observed HVSR is a combined effect of body and surface waves, which can map the subsurface structure at different depths depending on the frequency of interest. As a reference, when considering the surface-waves approach only, z_{min} and z_{max} can be estimated as a quarter of the minimum and maximum wavelengths of the waves mapping the structure, respectively (e.g., Mulargia and Castellaro, 2016). As the shear-wave velocity is the main parameter resolved by the HVSR technique and in the presence of a clear HVSR peak related to a sharp discontinuity, the minimum and maximum depths of investigation can be estimated as:

$$z_{min} = < v_s >^a \lambda_{min} = \frac{< v_s >^a}{4 f_{max}} \tag{2.6}$$

$$z_{max} = < v_s >^m \lambda_{max} = \frac{< v_s >^m}{4 f_{min}} \tag{2.7}$$

with f_{min} and f_{max} the minimum and maximum frequencies where the HVSR has been measured, respectively. $< v_s >^a$ is the average shear-wave velocity above the sharp discontinuity related to the HVSR peak at the highest frequency, whereas $< v_s >^m$ is the average shear-wave velocity above the last discontinuity of the model. It is also important to note that layers with low impedance might be not detected and resolved by this method.

2.2.6 Ellipticity of direct Rayleigh waves

The Rayleigh-wave ellipticity can be considered a particular case of the HVSR analysis, where the horizontal and vertical ground motions are measured on Rayleigh waves generated by seismic events. In this case, knowing the back-azimuth of the seismic event, the radial and vertical components of the Rayleigh-wave ground motion can be obtained. The Rayleigh-wave ellipticity is then calculated as the quotient between the radial and vertical components of the ground motion at different frequencies.

Indeed, for a smooth, laterally heterogeneous and transversely isotropic planet, the HVSR of fundamental Rayleigh waves is determined by the local structure beneath the station (Woodhouse, 1974; Ferreira and Woodhouse, 2007b,a). Due to the low-frequency

content of the direct Rayleigh waves, this technique has been successfully used on Earth for mapping the local-crust structure at the vicinity of a recording station (e.g., Sexton et al., 1977; Munirova and Yanovskaya, 2001). In particular, it has been demonstrated to be a powerful tool when combined with other approaches that map similar depth ranges, like Receiver Functions or dispersion curves (e.g., Lin et al., 2012; Chong et al., 2016).

Using this approach, the ellipticity of direct Rayleigh waves at low frequencies (<0.1 Hz) will be investigated in order to perform a joint inversion with other local-scale observations. Further details are discussed in Chapter 6.

2.3 Summary and concluding remarks

The scientific background here provided is the basis on which this research is carried out. As shown above, although some rough ideas can be inferred from regional observations, measurements and modeling, the subsurface structure at the InSight landing site (ILS), at shallow and crustal scales, is still an open question. Knowing the characteristics of the ILS is a key element for better understanding the seismological recordings and the geological processes that have occurred at the local and eventually global scale. The pre-landing model proposed by Knapmeyer-Endrun et al. (2017) for the ILS has velocities close to the surface of about 150 m/s, related to the regolith, and average velocities around 1000 m/s above the expected basalt unit. If the HVSR curve is analyzed between 0.5 and 10 Hz, for this range of velocities, the subsurface could be explored between 3 m to 500 m depth.

The HVSR can be understood as the natural way the media vibrates, given its mechanical properties. The way the horizontal ground motion is amplified with respect to the vertical at a certain frequency depends on the subsurface structure. In this context, the diffuse field assumption (DFA) has the potential to explain the features of the HVSR curve obtained either from Martian ambient vibrations or the coda of seismic event recordings, which are most likely composed of the superposition of all the types of waves. This full-wavefield approach can help to retrieve the shallow structure by inverting the HVSR observations, but some preliminary investigation must be made first in order to support or discard the diffuse nature of the recordings, particularly because lander resonances are expected to interfere with the recordings (e.g., Knapmeyer-Endrun et al., 2018). For this, the variation of spectral and polarization features of the ambient vibrations, as well as knowing the properties of the coda of seismic events, can act as a supporting tool for further analysis.

Besides, the recordings of direct Rayleigh waves generated by Martian seismic events can help to map the crustal structure. In this case, and depending on the source, large events are expected to generate Rayleigh waves, whose ellipticity can be measured and combined with other crustal-scale observations like P-to-s receiver functions and P-wave lag times from autocorrelations. The focus of this work will be mainly on the Rayleigh-wave ellipticity.

In any case, knowing the characteristics of the InSight data, as well as utilizing the right tools for data processing and analysis, is key to the development of this research. These two aspects are presented in the next chapter.

CHAPTER 3

Data and Methods

This chapter presents an initial overview on the characteristics of the InSight data utilized throughout this work, which was conducted while the station was operational, so clarity on these features became known during the course of the mission. Besides, the background of the main methods for data analysis (Polarization features), forward modeling (Horizontal-to-Vertical Spectral Ratio and Rayleigh-wave Ellipticity) and inversion (Neighbourhood Algorithm) of the observations is presented.

3.1 The InSight seismological data

SEIS recorded the Martian ground motion at the InSight landing site using one seismological station. The VBB and SP seismometers transmit data at different sampling rates, depending on the requirements of the scientific team and operational restrictions. This data is initially inspected and analyzed by the Marsquake Service (MQS), whose products can serve as input for other researchers of the InSight team (or externals). The main product of the MQS is the catalog of Martian seismicity during the course of the mission. Martian seismicity has been shown to be low (Giardini et al., 2020) and thus the most abundant data are the ambient vibrations, which include non-seismic signals. This section provides an overview of these data features, which is strongly based on Clinton et al. (2021) and Ceylan et al. (2021), unless otherwise indicated.

The first part of this work investigated the ambient vibrations and Martian seismic events recorded roughly during the first Martian year of the mission. For this, together with the seismological data (VBB and SP instruments), environmental data was also transmitted to Earth and they were archived as separated channels of the *XB.ELYSE* station. Due to the different sampling rates, gains, instruments and operating modes, InSight uses an extended version of the SEED data format (IRIS, 2012) for different data streams. A summary of data stream availability of the most used InSight data by MQS

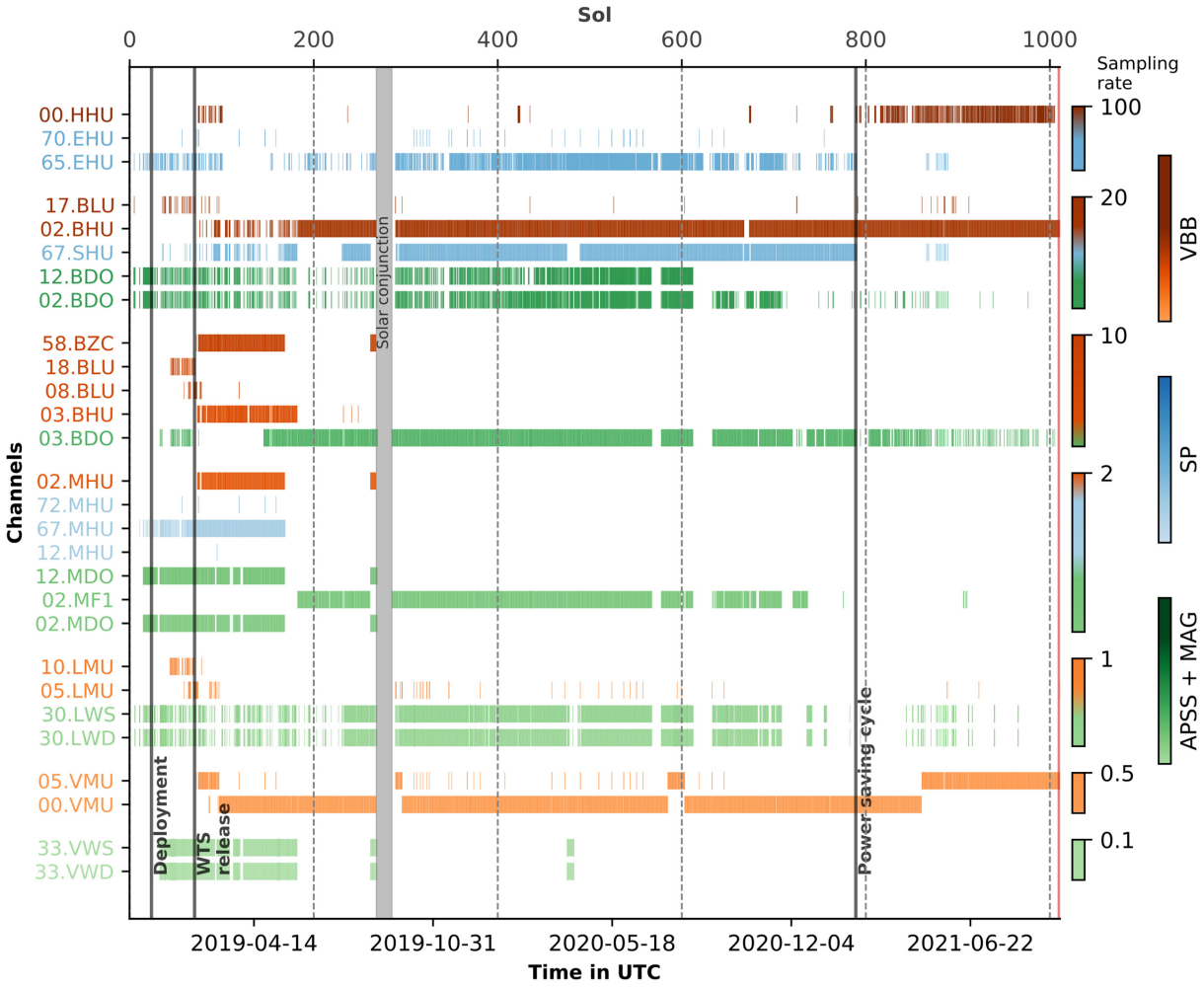


Figure 3.1: Availability summary of main InSight data used by MQS between sols 0-1011. For simplicity, only one of the channels for 3-component sensors is shown. The colors represent instrument types (VBB, SP or APSS+MAG). Channels are grouped by sampling rate and shown by the color intensity. VBB and SP are the seismic sensors. APSS includes the wind and pressure channels, and MAG is the magnetometer. Continuous SP operation stopped on sol 789 due to power saving cycle as labeled. This date and the deployment and WTS release are marked as vertical gray lines. Solar conjunction time, when no data could be transmitted, is denoted as a gray area. Figure is taken from Ceylan et al. (2022).

during the first 1011 sols of the mission is shown in Fig. 3.1, as presented by Ceylan et al. (2022). Only the streams of interest for this work are described below, so the reader is referred to Ceylan et al. (2021) for the nomenclature of all the stream codes.

3.1.1 The ambient vibrations and non-seismic signals

The SEIS seismological recordings have been shown to be composed of mainly ambient vibrations (Giardini et al., 2020; Lognonné et al., 2020). Although just a few hours of recordings might be enough for performing the analyses aimed at this work, longer time windows can help to understand possible variations and to have a more comprehensive perspective of the recordings. As shown in Fig. 3.1, the 20 sps VBB streams (02.BH) are the most abundant and continuous data, particularly since around the sol 190 of the mission (June 2019). VBB at 100 sps data (00.HH) was available for certain time

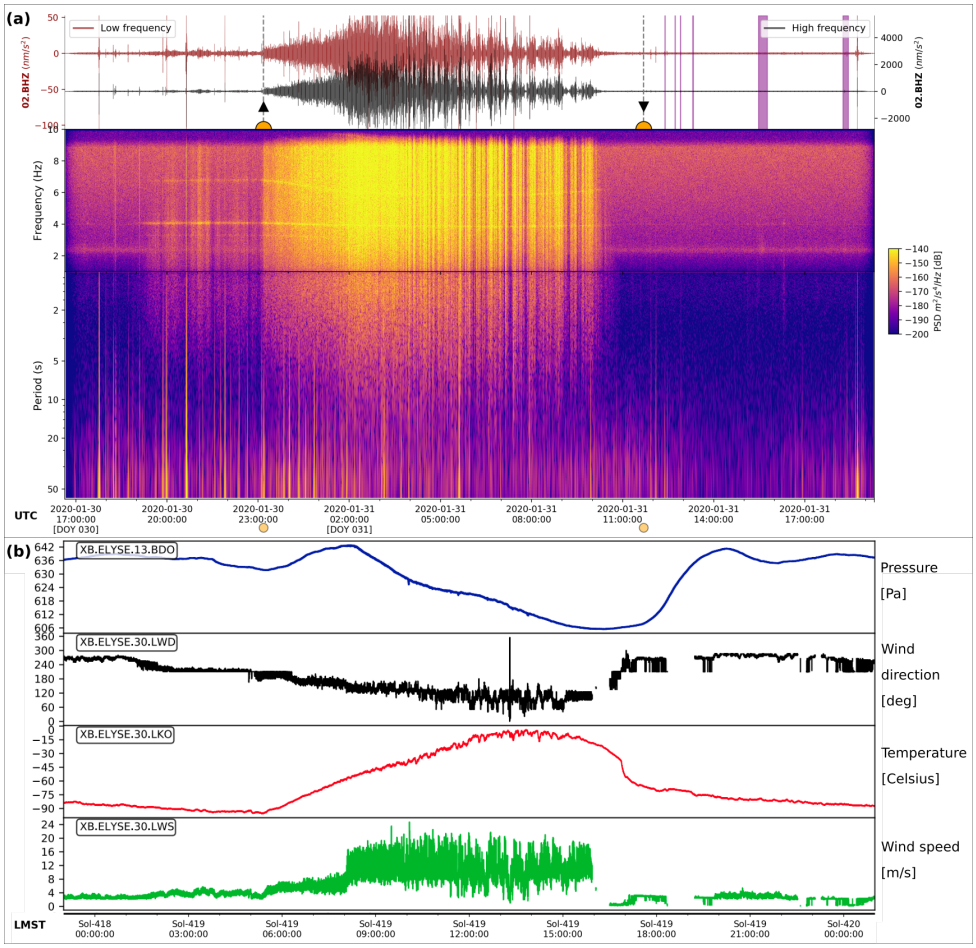


Figure 3.2: Seismic and environmental data recorded during sol 419. **(a)** Vertical component of the seismic data recorded by VBB at 20 sps (02.BH stream). The top panel shows the waveforms of the ground motion in acceleration units, below (low frequency) and above 1 Hz (high frequency). The sunrise and sunset times are marked dashed vertical lines with arrows pointing up and down, respectively. The bottom panel shows the spectrogram of the presented waveforms on top, ranging from 0.02 to 10 Hz, colored by the amplitudes given in dB. The figure is courtesy of MQS. **(b)** Environmental data over sol 419. The horizontal time axis is in Local Mean Solar Time (LMST), matching the time period of the seismic data in (a).

windows only, mostly upon scientific request and depending on operational restrictions. The SP instrument also transmitted 20 sps data (67.SH) in a continuous manner until sol 789, when the continuous transmission of this stream was stopped in order to save power for future operations. Between sols 190 and 800, a considerable amount of SP data at 100 sps (65.EH) was transmitted. Besides the seismological data, environmental data is available, especially between sols 190 and 800, including wind speed (30.LWS and 33.LWS), wind direction (30.LWD and 33.LWD), pressure (MDO and BDO streams) and ambient temperature (LKO streams, not present in Fig. 3.1 but mostly simultaneous to wind streams, as part of TWINS). Simultaneous recordings by both VBB and SP at 100 sps spanning longer than one Martian Sol are available only for two time periods: from Sol 422 to Sol 423, during the summer in the northern Martian hemisphere, and from Sol 762 to Sol 763, during the northern winter. In order to also compare the performance of the two instruments, the recordings of sols 422 and 423 are also analyzed in Chapter 4.

The initial analyses of the InSight data by MQS and the InSight team allowed to have a first overview on the main characteristics of the data (Giardini et al., 2020; Lognonné et al., 2020). A typical sol of seismic data on Mars can be separated into three main periods based on the amplitude of the ambient vibrations and the environmental conditions. These different periods can be identified in Fig. 3.2, where the vertical component of the ground-motion data and the environmental data recorded on Sol 419 are presented. A first period starts from early morning to the sunrise, from 02:00 to 06:00 Local Mean Solar Time (LMST) in this case, where the ground-motion amplitudes are in the range -170 and -160 dB in acceleration (Fig. 3.2a). In this period, steady weak laminar winds and low temperatures are recorded (Banfield et al., 2020). After sunrise, the ground-motion amplitudes start to increase as the wind speed increases with strong fluctuations, leading to strong turbulent winds (Banfield et al., 2020; Lognonné et al., 2020), reaching the largest amplitudes recorded over a Sol, particularly at high frequencies (>1 Hz). This *noisy* period stays until the sunset, when the temperature and wind speeds drop. During the evening, SEIS records the lowest amplitudes over the sol (Fig. 3.2a). Indeed, the ground-motion amplitudes during this period are ∼500 times lower than on Earth, reaching -200 dB in acceleration at night (Stutzmann et al., 2021). These observations indicate that the SEIS recordings seem affected by the environmental conditions at the InSight landing site (ILS), despite being covered by the WTS. Further investigation on the spectral features of the ambient vibrations has been part of this work and is presented in Chapter 4.

The attributes of the seismic ambient vibrations below 1 Hz have been previously investigated by Stutzmann et al. (2021). They showed the day-time ground motion between 0.3 and 1 Hz can be partially explained by pressure waves propagating along the planet's surface and acoustic waves coming from the atmosphere. On the other hand, the ground motion recorded during the Martian evening is azimuthally isotropic and polarized in the horizontal plane. The authors proposed this time period of each sol to be the only candidate for recording the propagation of seismic wave background noise.

Non-seismic signals in the SEIS recordings

Specific signals have been identified in the recordings, which could not be related to tectonic events or impact meteorites and thus have been cataloged as non-seismic signals. The correct identification of these signals is relevant for the analysis and interpretation of the SEIS data. A description of the main classes of these signals is provided below and they are shown in Fig. 3.3. Further details can be found in Ceylan et al. (2021) and Kim et al. (2021a).

- **1 Hz mode:** also referred to as the *tick-noise*. It is a very narrow resonance peak observed on both sensors SP and VBB at 1 Hz and with decreasing amplitudes at its harmonics at 2 Hz, 3 Hz, etc. It is an artifact generated by the electrical cross-talk on the tether, and possibly within the sensor assembly, from temperature signals of the EBOX measurement system. It is recorded permanently. Different procedures have been proposed for its removal (Compaire et al., 2021) and Zweifel et al. (2021).
- **Lander modes:** a set of modes identified early during the mission (Giardini et al., 2020; Lognonné et al., 2020), excited at various frequencies (e.g., 3.3 Hz, 4 Hz, 7

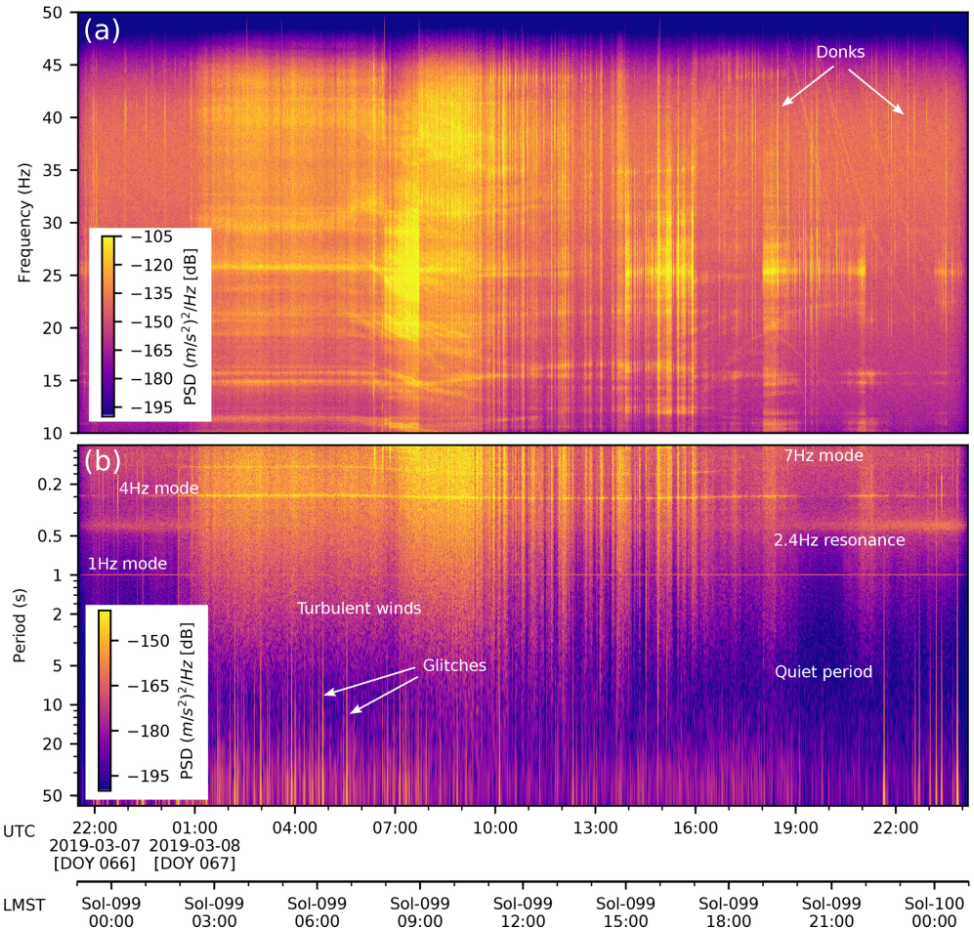


Figure 3.3: Non-seismic signals recorded by SEIS on sol 99. Acceleration spectrograms of the vertical component of 100 sps VBB (00.HH channel). (a) Spectrogram between 10 and 50 Hz, with the frequency axis in linear scale. (b) Spectrogram between 0.02 and 10 Hz, with the frequency axis in log scale. Earth and Mars time are shown in the horizontal axis. Note the different color scales for the ground-motion amplitudes between (a) and (b). Figure is taken from Ceylan et al. (2021).

Hz). They are mostly observed during the early morning and daytime, when the wind speeds are higher. Their amplitudes and resonance modes are likely driven by the wind speed and temperature conditions at the ILS (Dahmen et al., 2021b).

- **2.4 Hz resonance:** it is a resonance observed around 2.4 Hz, mainly in the vertical component of the ground-motion recordings. Its amplitude and orientation vary during the day and it is excited by ground motion produced by seismic events. Unlike the lander resonances, its amplitude does not seem to be dependent on the wind speeds. It is mainly observed during the local evening and has been proposed to be related to a subsurface structure (Hobiger et al., 2021).

- **Donks:** short duration pulses (<10 s) of high-frequency energy bursts, typically above 12 Hz. This signal is recorded on all three components of both SP and VBB. They are thought to be transient energy associated with stress release from temperature cycling on the lander, tether, or SEIS. They can be observed over the whole sol.

- **Glitches:** single and multi-component one-sided pulses, most frequently observed on the 20 sps VBB streams. They have a time duration of about ∼25-30 s independent of their amplitudes and have been modeled as the instrument response convolved with a step in the recorded acceleration (Scholz et al., 2020). They are observed as broadband energy from very low frequencies, usually up to 1 Hz, and over the whole sol.

The lander modes and the 2.4 Hz resonance are in the frequency range of interest to investigate the shallow subsurface structure with the horizontal-to-vertical spectral planned in this work. Furthermore, Hurst et al. (2021) also showed there are a number of expected resonances at about 2.86, 5.3, 9.5, 12, 14 and 23-28 Hz related to the Load Shunt Assembly. Other signals not related to seismic events are those caused by lander activity (e.g., arm motion, calibration) or atmospheric changes. Among the latter, the evening rumbles are long-duration low-frequency signals due to long period change in atmospheric pressure occurring at the beginning of the evening. They can resemble the spectral energy of some seismic events. Besides, the recordings of pressure drops have been proposed as another way for mapping the subsurface structure. To this end, the pressure and seismic recordings are combined to determine the so-called compliance, i.e., the ground deformations caused by transient atmospheric pressure variations (Kenda et al., 2020; Lognonné et al., 2020). These measurements can be used to compare against the results obtained with the approach of this work.

3.1.2 The Martian seismic events

Besides the ambient vibrations, the Martian seismic events reported by MQS will also be used to map the subsurface structure. Given the variation of ground-motion amplitudes over a Sol, the Martian seismic events were mainly recorded during the quiet evening and night times, when the noise level was the lowest, as shown in Fig. 3.4.

As of September 30th 2021 (Sol 1011), the MQS has reported more than 900 potential seismic events (MQS catalog Version 9, reported by Ceylan et al., 2022). The origin and nature of these events are still under investigation, but a classification based on their spectral content can be made. These events are classified into two main groups: the low frequency (LF) and high frequency (HF) families. The low-frequency family events are characterized by long-period energy below 1 Hz. These events can be cataloged as Low Frequency (LF) events, which do not excite the 2.4 Hz mode, and the Broadband (BB) events, which do excite this mode (Clinton et al., 2021). On the other hand, the events of the high-frequency family are characterized by the excitation of frequencies mainly above 1 Hz. The HF family comprises three types of events: the 2.4 Hz events, which excite the 2.4 Hz mode and frequencies up to 4 Hz; the High Frequency (HF) events, exciting the 2.4 Hz mode and higher frequencies up to about 10 Hz; and the Very High Frequency (VF) events, which show a strong excitation of the horizontal components at frequencies above 5 Hz, up to even 35 Hz (Clinton et al., 2021). In addition, Dahmen et al. (2021a) identified a new type of events, so-called Super High Frequency (SF) events, which excite frequencies above 5 Hz with a stronger excitation of the horizontal than the vertical component, as in the VF events, but with a very short duration (∼20 s) and no identifiable seismic phases. A summary is shown in Table 3.1 and their temporal distribution can be seen in Fig. 3.4.

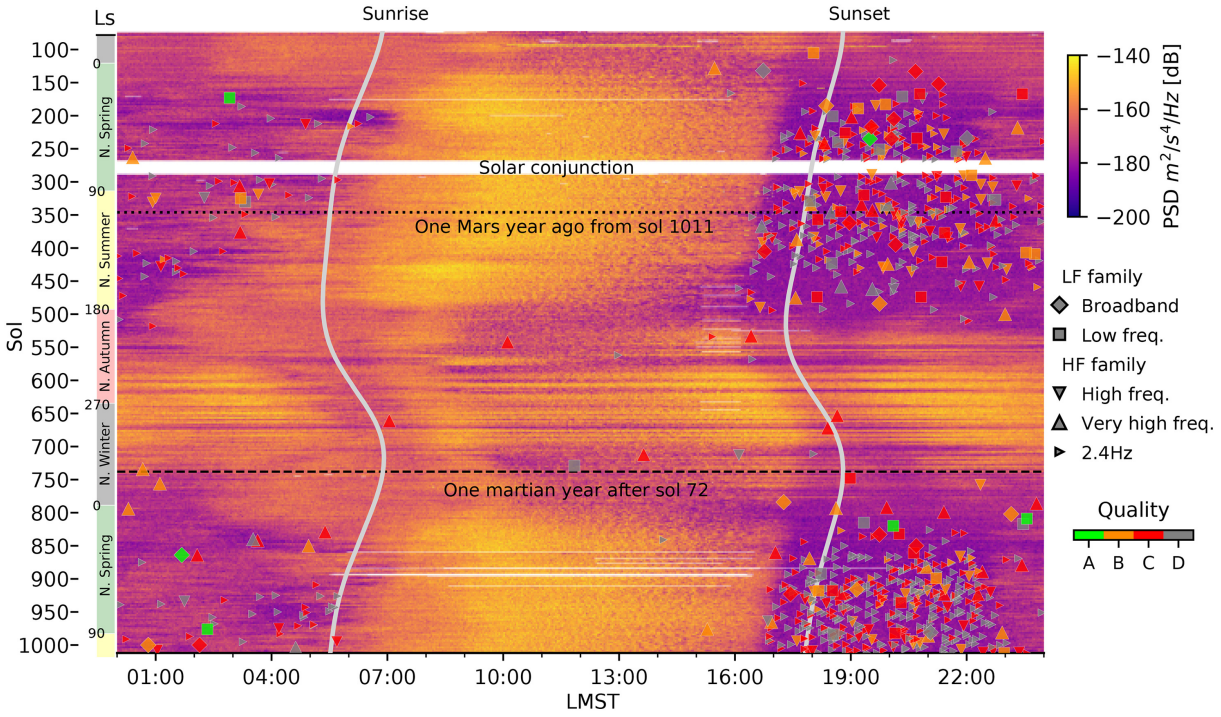


Figure 3.4: Martian seismicity in the first 1011 sols of InSight. The background image is a stack of sol-long acceleration spectrograms for frequencies 0.05-4 Hz, colored by the spectral acceleration. The sol since InSight landed and the solar longitude (Ls), defining the local Martian season in the northern hemisphere, are shown in the y-axis (recent times are at the bottom). The x-axis shows the Local Mean Solar Time (LMST). Each marker corresponds to one seismic event, where the symbol indicates the event family and the color denotes its quality. The plot covers the period from Sol 72, shortly before the WTS was placed and SEIS started continuous recording, up to Sol 1011. The sunrise and sunset times at the ILS over the mission are also plotted as white curves. Figure taken from Ceylan et al. (2022).

Among other characteristics, the LF family events are similar to teleseismic events observed on Earth, where P and S waves are often identified. The HF family events include phases identified as Pg and Sg, interpreted as crustal guided waves, and a slowly decaying coda (Giardini et al., 2020; van Driel et al., 2021). In the MQS V9 catalog (InSight Marsquake Service, 2022), 882 HF and 69 LF family events are reported, with the 2.4 Hz as the most detected type of event (731). However, 1062 SF events were reported but treated separately due to their likely thermal-driven origin (Dahmen et al., 2021a). This is the typical seismicity pattern detected throughout the first Martian year of the InSight mission. The duration of the events, i.e., the time between the first arrival and until the spectral energy returns to the pre-event level, varies depending on the event distance, but quality A or B events have durations of 10-30 min (Ceylan et al., 2022).

Along with this classification based on the spectral energy content, the seismic events also have assigned a quality index based on the signal strength and the ability to identify and interpret the phase arrivals (Clinton et al., 2021). Therefore, the quality index can be either A (*high*), B (*medium*), C (*low*) or D (*suspicious*), where a quality A event has multiple clear and identifiable phases whereas a quality D event is a weak signal and may not be attributable to an internal seismic phenomenon. Table 3.2 summarizes this classification.

Event type	Description
Low Frequency (LF)	Energy in three components, all below 2.4 Hz.
Broadband (BB)	Energy in three components, predominantly below 2.4 Hz but with some possible excitation of the 2.4 Hz resonance.
2.4 Hz	Energy in three components centered around the 2.4 Hz resonance, with limited excitation above or below.
High Frequency (HF)	Energy in three components, predominantly at and above 2.4 Hz.
Very High Frequency (VF)	Energy in all three components, with horizontal significantly larger than vertical energy at higher frequencies (>5 Hz).
Super High Frequency (SF)	Very short duration high-frequency events with energy predominantly in the range 5-10 Hz.

Table 3.1: Classification of events detected by MQS according to spectral content.

Label	Quality	Description
A	High	Multiple clear, identifiable phases and clear polarization that allow determining the back-azimuth and distance.
B	Medium	Multiple clear and identifiable phases, but no polarization, i.e., distance is derived but no back-azimuth.
C	Low	Signal is clearly observed but no clear phases can be identified, only a single phase is clearly identifiable or multiple phases are identifiable but no clear P- or S-phase picks.
D	Suspicious	Signal only weakly observed or signal is likely not attributable to a seismic event.

Table 3.2: Classification of events detected by MQS, based on signal clarity.

Each event is named after the sol when it was recorded, followed by a letter (a, b, c, etc.). The largest events in the MQS catalog V9 occurred on the same sol: the LF event S0976a and the VF event S0976b. The magnitude of the events is determined based on the distance and a Mars-calibrated moment magnitude (M_w^{Ma}) following Böse et al. (2021). In this case, S0976a had a magnitude M_w^{Ma} ~4.2 whereas S0976b reached M_w^{Ma} ~4.1, making them the largest LF and VF events recorded by then, respectively. S0976a is also the most distant event recorded by SEIS, located in the Valles Marineris region, 146°±7° away from the InSight lander. The second furthest event reported is S1000a, which occurred at a distance of 116°±9° and has the longest duration of about 94 min (Horleston et al., 2022). The smallest events reported by MQS have a magnitude around 1.0 and are located in the closest 10° around the ILS.

Most of the seismicity reported in the MQS catalog V9 is located between 25°-35° epicentral distance and due east (Ceylan et al., 2022), suggesting that the most likely tectonic source is the Cerberus Fossae graben system (Perrin et al., 2022). The VF events are equidistributed between 0° and 40°, so they have been proposed to be suitable candidates for impact events (Ceylan et al., 2022).

3.2 Data processing and methods

The steps taken for the analysis of ambient vibrations, coda waves of seismic events and direct Rayleigh waves are explained in more detail in Chapter 4, Chapter 5 and Chapter 6, respectively, but some common steps and approaches are explained below. Particularly, the inversion approach to retrieve the subsurface structure is the same for the shallow and crustal case (Chapters 5 and 6), so it is explained here. In this section, background information and definitions are provided in order to further understand the results.

For each instrument, SP and VBB, the ground-motion recordings were pre-processed by correcting for the instrument response, high-pass filtering at 0.01 Hz and rotating from the sensor orientations (U, V, W) to the geographic coordinate system (Z, N, E). The ground motions in the ZNE system are the basis of the next steps.

3.2.1 Polarization analysis

In order to better assess and characterize any potential resonances caused by the subsurface structure or the lander, the spectral polarization attributes of both the ambient vibrations and the seismic events were studied using a similar approach as presented by Park et al. (1987), which is based on the work of Samson (1983). For each data window, the calculation of the polarization features relies on the eigen-decomposition of the spectral covariance matrix ($\mathbf{S}$) of the three-component ground motion data $\mathbf{x}(t) = (x^1(t), x^2(t), x^3(t))$ (in this case, ZNE). The spectral covariance matrix is composed of the convolution of the spectra of all the components, i.e.:

$$\mathbf{S} = \mathbf{S}_{jk}(f) = y^j(f) * y^k(f), \tag{3.1}$$

where y^j and y^k are the Fourier spectra of components j and k. The approach of Park et al. (1987) includes using a multitaper algorithm to smooth the spectra and avoid spectral leakage. This is done by applying a set of K Discrete Prolate Spheroidal Sequences (DPSS, Slepian, 1978). The covariance matrix $\mathbf{S}_{jk}(f)$ is calculated after smoothing the spectra. The polarization angles are obtained from the eigenstructure of $\mathbf{S}_{jk}(f)$, investigated through singular value decomposition. The largest eigenvalue and the corresponding eigenvector $\hat{\mathbf{z}}$ of $\mathbf{S}$ represent the polarization of the seismic signal (either ambient vibrations or events coda) during the given time window, for each frequency. The directional attributes of this polarization are obtained from the components of the largest eigenvector $\hat{\mathbf{z}} = (z_1, z_2, z_3)$, with z_1 is perpendicular to the surface, as shown in Fig. 3.5. Given a coordinate system, the horizontal incidence angle θ_{H} is measured in degrees clockwise from North, using the horizontal component z_H of $\hat{\mathbf{z}}$, defined by z_2 and z_3. The vertical incidence angle θ_{V} is defined by the vertical and horizontal components of $\hat{\mathbf{z}}$, z_1 and z_H, respectively. θ_{V} is restricted to lie between 0° (vertical incidence, perpendicular to the ground surface) and 90° (horizontal, parallel to the ground surface), as shown in Fig. 3.5.

With the directional attributes, the degree of polarization (*dop*) was also computed, as proposed by Samson and Olson (1980). The *dop* measures how polarized the seismic signal is so that it can be described by fewer than three degrees of freedom. In this case, for a three-component ground motion record, the degree of polarization is defined as

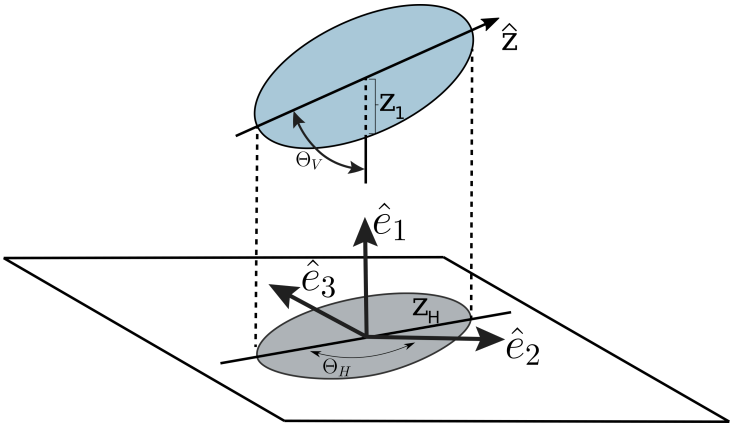


Figure 3.5: Sketch to illustrate polarization angles Θ_H and Θ_V. The azimuth Θ_H is restricted to (0°, 360°) and is measured counterclockwise from $\hat{e}_2$. The angle is chosen by determining the maximum horizontal displacement of the particle motion for which Θ_V will fall in the range $0° \leq \Theta_V \leq 90°$. Based on Park et al. (1987).

$$dop = \frac{3\mathrm{tr}(\mathbf{S}^2) - [\mathrm{tr}(\mathbf{S})]^2}{2[\mathrm{tr}(\mathbf{S})]^2}, \tag{3.2}$$

where tr is the trace and $\mathbf{S}$ is the spectral covariance matrix of the ground-motion data. This parameter ranges from 0, when the signal is fully depolarized, to 1, when a single non-zero eigenvalue exists and the signal is completely polarized in the direction of the corresponding eigenvector. In this regard, high values of *dop* correspond to a polarized signal with a particle motion that can be either linear or elliptical.

As the three eigenvalues of $\mathbf{S}$ are available, $\lambda_1 \geq \lambda_2 \geq \lambda_3$, the planarity and rectilinearity, according to Jurkevics (1988), and the ellipticity, following the concept of Vidale (1986), were also calculated. They are defined as:

$$\text{Planarity:} \quad P = 1 - \frac{2\lambda_3}{\lambda_1 + \lambda_2} \tag{3.3}$$

$$\text{Rectilinearity:} \quad R = 1 - \frac{\lambda_3 + \lambda_2}{2\lambda_1} \tag{3.4}$$

$$\text{Ellipticity:} \quad E = \frac{\sqrt{1 - X^2}}{X}, \quad \textit{with} \tag{3.5}$$

$$X = \sqrt{(\mathrm{Re}(x_1 \mathrm{cis}\alpha))^2 + (\mathrm{Re}(x_2 \mathrm{cis}\alpha))^2 + (\mathrm{Re}(x_3 \mathrm{cis}\alpha))^2} \tag{3.6}$$

where α is the angle between 0° and 180° that maximizes X, the length of the real component of the eigenvector. The term $\mathrm{cis}\alpha = \cos\alpha + i \sin\alpha$ and $\mathrm{Re}(x)$ is the real part of x. (x_1, x_2, x_3) are the components of the eigenvector related to the largest eigenvalue.

All these values vary between 0 and 1. The rectilinearity (R) is 1.0 when there is only one nonzero eigenvalue, as for pure body waves. Planarity is close to one for waves having ground motion in two directions (e.g., Rayleigh waves). The ellipticity is 0 for linearly polarized motion and 1.0 for circularly polarized motion.

3.2.2 Horizontal-to-vertical spectral ratios (HVSR)

Empirical HVSR

The empirical horizontal-to-vertical spectral ratios (HVSR) were computed from both the ambient vibrations data (nHV) and the coda of the seismic events (eHV).

The HVSR of the ambient vibrations was calculated using the classical approach. A continuous recording was divided into shorter time windows (usually 120 s, see Chapter 4 for details). For each time window, the spectral amplitudes of the Z, N and E components were calculated. Taking advantage of the calculation of the polarization features, the spectral amplitudes were obtained from there. For simplicity, due to the large amount of data, the HVSR is calculated following the classical *Nakamura's* approach as:

$$HVSR(\omega) = \sqrt{\frac{N^2(\omega) + E^2(\omega)}{Z^2(\omega)}}, \tag{3.7}$$

where N^2, E^2 and Z^2 are the squared spectral amplitudes calculated from the polarization analysis. No smoothing was applied in order to detect possible resonant frequencies and avoid their contamination towards neighboring frequencies (e.g., the 1 Hz tick noise or lander modes). After calculating the HVSR for a number of time windows, the final HVSR curve is estimated as the median of all the selected time windows, i.e., the statistics are performed after the HVSR calculation. This approach is slightly different from the diffuse field HVSR, which calculates a single HVSR curve from the average of each horizontal component ground motions and the average of the vertical ground motions (Eq. 2.4), i.e., the statistics are performed before the HVSR calculation. Despite the differences, it has been shown that these two approaches provide the same resonant frequencies and the amplitude differences are in the 5% error range (e.g., Spica et al., 2015). Based on this, both approaches are considered to be equally valid.

The diffuse HVSR calculation is followed for the HVSR of the seismic events coda, following the equation 2.4. Because of the per-component average, in order to have the same contribution from each time window, spectral whitening was applied to normalize the signals by the source energies computed in each time window and across several frequency bands. This is done to avoid that time windows with larger ground-motion amplitudes rule the final result. After the spectral whitening, the normalized ground motion corresponds to:

$$\hat{u}_i(\mathbf{x}, \omega) = \frac{u_i(\mathbf{x}, \omega)}{\sqrt{\sum_{i=1}^{3} |u_i(\mathbf{x}, \Delta\omega)|^2}}, \tag{3.8}$$

where the denominator is a normalization term, given by the total power in a certain bandwidth $\Delta\omega$. In this work, $\Delta\omega = 50$ Hz was used here to normalize by the power of the total spectrum. This way, the final HVSR is computed as in Equation 2.4 but replacing u_i by the normalized ground motion $\hat{u}_i$.

Theoretical HVSR (Forward modeling)

The theoretical HVSR was calculated assuming the recordings correspond to contributions of all types of waves (full wavefield) under the diffuse field assumption (DFA), as explained in Chapter 2. Under the DFA, the HVSR is taken as the ratio between the horizontal and vertical energies, which can be rewritten in terms of the Green's functions of the media, as in Eq. 2.5. Based on this equation, the HVSR under the DFA can be calculated by directly computing the Green's function of a given media, as the code proposed by García-Jerez et al. (2016) using suitable contour integrals in the complex wavenumber plane.

A slightly different approach was proposed by Margerin (2009) and Margerin et al. (2009), who developed the theory for calculating generalized eigenfunctions of a stratified media, assuming a diffuse field, for each component and for the full wavefield. This approach is used in this work. This method does not compute the Green's functions or their imaginary part but rather calculates the normalized horizontal and vertical energies directly. A brief explanation is given here but the reader is referred to Margerin (2009) and Margerin et al. (2009) for further theoretical details and more background on the numerical solutions.

Given an elastic layered media with n layers with density ρ_i, P-wave c_i^p and S-wave velocities c_i^s, over a half-space with corresponding ρ_∞, c_∞^p and c_∞^s, as shown in Fig. 3.6, Margerin (2009) determined the eigenfunctions of the elastic wave equation satisfying the continuity of displacements and reactions across each interface z=0, ..., z_{n-1} and the traction-free condition at the surface of the medium.

Following Margerin (2009), the displacement field for a semi-infinite 3D layered elastic body, like the structure in Fig. 3.6, can be written as:

$$\begin{aligned} u(\mathbf{x},t) &= \sum_{n,R,L} \int\int_{\omega_n \in B} \frac{dp_x dp_y}{2\pi} \left(A_n^{R,L}(p_x,p_y)\psi_n^{R,L}(z) e^{i(p_x x + p_y y)} e^{-i\omega_n^{R,L}(p_x,p_y)t} \right) \\ &+ \int_{p_z<0} dp_z \sum_{P,S} \int\int_{\omega \in B} \frac{dp_x dp_y}{2\pi} \left(A^{P,S}(p_x,p_y,p_z)\psi_{p_z}^{P,S}(z) e^{i(p_x x + p_y y)} e^{-i\omega^{P,S}(p_x,p_y,p_z)t} \right) \end{aligned} \tag{3.9}$$

where $\psi_n^{R,L}$ indicate the eigenfunctions of the nth-mode of Love (L) and Rayleigh (R) waves, $\psi_{p_z}^{P,S}$ are the generalized P and S (SH-SV) eigenfunctions. B is the frequency band of the signal and u is the complex analytic signal, whose real part is the measured displacement vector. Under the diffuse field assumption, the amplitudes $A_n^{R,L}$ and $A^{P,S}$ are assumed to be white-noise processes:

$$< A_n^{R,L} A^{P,S} > = 0 \tag{3.10}$$

$$< A_n^{R,L}(p_x,p_y) A_m^{R,L}(p_x',p_y')^* > = \sigma^2 \delta^{R,L} \delta_{nm} \delta(p_x - p_x') \delta(p_y - p_y') \tag{3.11}$$

$$< A^{P,S}(p_x,p_y,p_z) A^{P,S}(p_x',p_y',p_z')^* > = \sigma^2 \delta^{P,S} \delta(p_x - p_x') \delta(p_y - p_y') \delta(p_z - p_z') \tag{3.12}$$

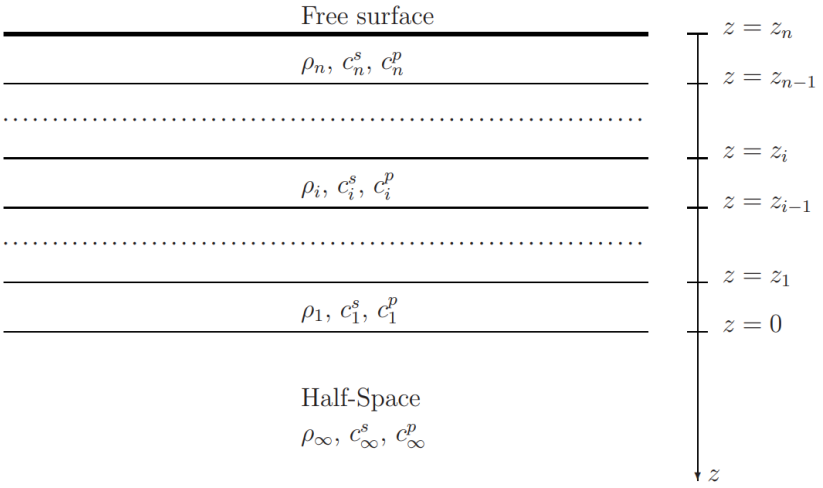


Figure 3.6: Stratified media with n elastic layers bounded by a free surface at $z = z_n$ and overlying a homogeneous half-space (z>0). The elastic properties of layer i are defined by the density ρ_i, the shear and compressional wave speeds, c_i^s and c_i^p, respectively. Taken from Margerin (2009).

where the brackets denote an ensemble average. In Eq. 3.11 and 3.12, $\delta^{L,R}$ and $\delta^{P,S}$ equals 1 for surface waves and body waves of the same type, respectively, and 0 otherwise. These equations are the mathematical representation of the equipartition principle.

The horizontal and vertical kinetic energies can be calculated from these equations. In particular, the vertical kinetic energy densities at central frequency ω_0 can be obtained by means of a Wigner distribution of the complex analytic wavefield u:

$$E_z(t,\tau,\mathbf{x}) = \frac{1}{2}\rho(z) < \frac{\partial u_z(t+\tau/2,\mathbf{x})}{\partial t}\frac{\partial u_z(t-\tau/2,\mathbf{x})}{\partial t}^* >, \tag{3.13}$$

a similar expression is used for the horizontal energy using components x and y. The next steps involve inserting the expression for the complex displacement (Eq. 3.9) into the Wigner distribution (Eq. 3.13), applying the equipartition principle (Eq. 3.10-3.12), taking a Fourier transform with respect to the time variable τ and converting into a spherical coordinates representation. By doing this, the following expressions can be derived:

$$\begin{aligned} E_z(\omega_0,z) &= \sum_{n,R}\frac{\rho(z)\omega_0^3\sigma^2}{4\pi c_n^R u_n^R}\left|\psi_{n,z}^R(z)\right|^2 \\ &\quad + \sum_{P,SV}\frac{\rho(z)\omega_0^4\sigma^2}{4\pi v_\infty^{p,s3}}\int_{\pi/2}^{\pi} d\theta\sin\theta\left|\psi_{p_z,z}^{P,SV}(z)\right|^2\Big|_{p_z=(\omega_0/v_\infty^{p,s})\cos\theta} \end{aligned} \tag{3.14}$$

$$\begin{aligned} E_h(\omega_0,z) &= \sum_{n,R,L}\frac{\rho(z)\omega_0^3\sigma^2}{4\pi c_n^{R,L} u_n^{R,L}}\left|\psi_{n,h}^{R,L}(z)\right|^2 \\ &\quad + \sum_{P,SV,SH}\frac{\rho(z)\omega_0^4\sigma^2}{4\pi v_\infty^{p,s3}}\int_{\pi/2}^{\pi} d\theta\sin\theta\left|\psi_{p_z,h}^{P,SV,SH}(z)\right|^2\Big|_{p_z=(\omega_0/v_\infty^{p,s})\cos\theta} \end{aligned} \tag{3.15}$$

These equations correspond to the full-wavefield vertical (Eq. 3.14) and horizontal (Eq. 3.15) energies under the diffuse field assumption. Some of the terms involved are the phase (c_n) and group (u_n) velocities of the nth surface wave mode. The subscript h corresponds to the horizontal component of the wavefunction measured in the plane of polarization, ω_0 is the angular frequency of the corresponding wave. Note that Love waves and SH eigenfunctions only contribute to the horizontal kinetic energy. The code slows down as more layers are added because the continuity of traction and displacements at all interfaces must be ensured, so this restricts the parameterizations to explore.

The forward modeling code utilized in this work, available from L. Margerin upon request, performs the calculation of the eigenfunctions ($\psi^{P,SV,SH,R,L}$), the sum and integrals numerically. It has been shown to be numerically faster and, to some extent, more reliable than the classical locked-mode technique (Margerin et al., 2009). Due to the calculation of the eigenfunctions for each type of wave, it is also possible to retrieve the horizontal and vertical energies for each of them and, consequently, the HVSR of the corresponding type of waves can be calculated.

Rayleigh-wave ellipticity calculation

The HVSR under the DFA using the generalized eigenfunctions is a relatively expensive calculation because it involves the numerical solution of the eigenfunctions, sums and integrals. Nevertheless, the computation of the HVSR of the fundamental mode Rayleigh wave (better known as the ellipticity), a particular step in the full DFA, can be performed using a relatively faster approximation, as shown by Wathelet et al. (2004). The forward modeling tool for this calculation is *gpell* and is available from the website `https://www.geopsy.org/`. A comparison between the two approaches is shown in Fig. 3.7, evidencing that *gpell* is perfectly compatible with the diffuse field approximation. Because of this and the faster computation, *gpell* will be used in the joint inversion carried out in Chapter 6.

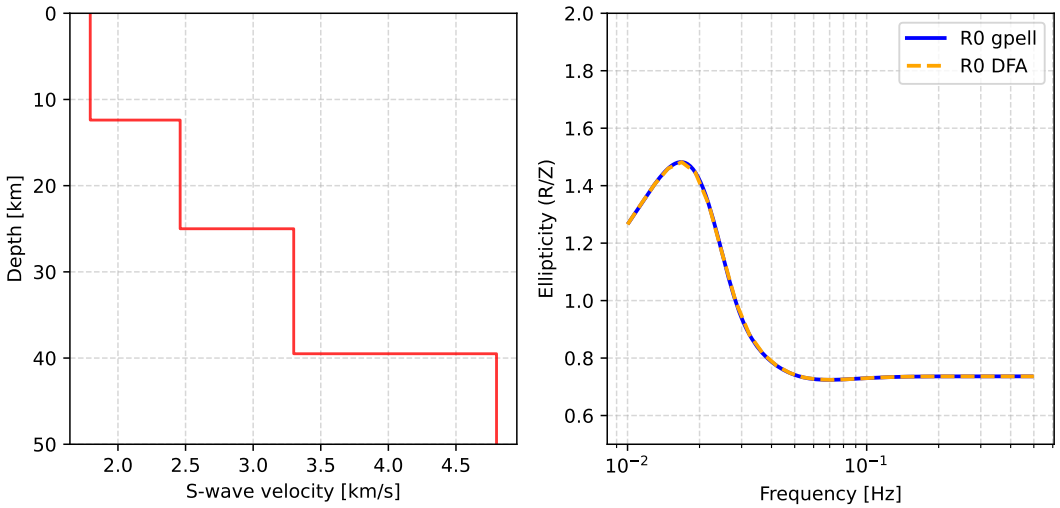


Figure 3.7: Comparison between DFA and *gpell*. **Left**: synthetic model to test. **Right**: synthetic ellipticity curve in the frequency range 0.01-0.5 Hz as calculated by *gpell* (solid blue) and the DFA approach used in this work (dashed yellow).

3.3 Inversion scheme

In order to find the best subsurface models explaining the measurements, a nonlinear inversion scheme was implemented. The inversion technique utilized here is the so-called Conditional Neighbourhood Algorithm (Wathelet, 2008), a modification of the initial Neighbourhood Algorithm (NA) developed by Sambridge (1999). In the following, and throughout this work, the conditional Neighbourhood Algorithm and its current implementation is simply referred to as the Neighborhood Algorithm.

3.3.1 The Neighborhood algorithm (NA)

The Neighborhood Algorithm (NA) is a stochastic, derivate-free, direct search method to sample a given parameter space and used for non-linear geophysical inverse problems. Given a set of models $\mathbf{m}_i$ and observations $\mathbf{d}_o$, for which a forward modeling operator $\mathbf{F}$ allows calculating the theoretical prediction $\mathbf{d}_m$, the NA performs a random search of the best minimum-misfit model, according to a custom misfit function $\phi(\mathbf{m}_i, \mathbf{d}_o)$.

The steps to perform this search are exemplified in Fig. 3.8, an example taken from (Gosselin et al., 2022). This is a 2D example where the models are defined by the parameters X and Y, which are allowed to take values in a certain range. In this case, each parameter ranges between -0.5 and 1.5. The parameter space is defined by all the parameter ranges, which generate a set of possible combinations that define a model. The goal is to find the model providing the lowest misfit. The *synthetic* misfits are given in this case by the Rastrigin function, a non-convex function with multiple local minima, as shown in Fig. 3.8a. The NA starts with a population of N_{s0} random models distributed over the parameter space (e.g., 20 colored circles, given by the misfit value, in Fig. 3.8b). Based on the "location" of these initial models (generator points or models), the parameter space is divided into Voronoi cells, i.e., the points in the cell are closer to the generator point than to any other model in the parameter space. Each generator point has a misfit value, which is assigned to the corresponding generated Voronoi cell. This leads to a nearest-neighbor interpolation of the misfit function. The 20 Voronoi cells of the initial population are shown in Fig. 3.8b).

The next step is to select the N_r Voronoi cells with the lowest misfits. Inside these best N_r Voronoi cells, N_s new models are generated, as shown by the open circles in Fig. 3.8b, using $N_r = 10$ and $N_s = 10$. These 10 new models generate 10 new Voronoi cells, which are added to the initial ones. Therefore, 30 models have been evaluated at this point (colored circles in Fig. 3.8c) and the parameter space is correspondingly divided into 30 Voronoi cells (also shown in Fig. 3.8c).

The previous step is repeated: N_r Voronoi cells with the lowest misfits are selected, where N_s new models are generated (open circles in Fig. 3.8c). These new models generate N_s Voronoi cells, which redefine the tesselation of the parameter space (Fig. 3.8d). This process is repeated until it converges to an optimal solution (with the lowest misfit).

Some of the advantages of the NA, compared to other nonlinear approaches, is that it can quickly escape from a local minima region, as shown by Sambridge (1999), and has a relatively simple tunning scheme, given by the parameters N_{s0}, N_s and N_r. The latter

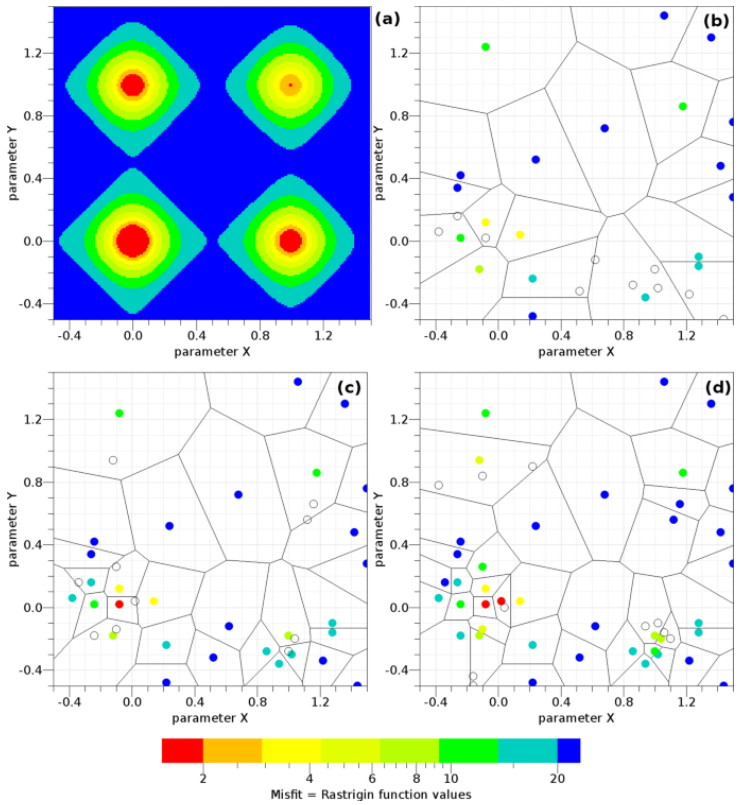


Figure 3.8: Illustration of the NA for a 2D parameter space corresponding to the Rastrigin function. **(a)** Dense sampling of the Rastrigin function showing four minima. **(b)** 20 random models of an initial population (colored circles) and the corresponding Voronoi geometry (solid lines). Ns = 10 new models (open circles) are generated randomly inside the Nr = 10 cells with the lowest misfit. **(c)** The new models are integrated into the Voronoi geometry and their misfits are computed, leading to a total population of 30 models (colored circles). **(d)** This process is repeated to obtain 40 models. Taken from Gosselin et al. (2022).

two parameters control the exploration (N_s, more models to explore) and the optimization (N_r, more lowest-misfit Voronoi cells to explore).

The NA version utilized in this work is the so-called conditional Neighbourhood Algorithm (Wathelet, 2008), an improved version of the original NA. This version allows imposing conditions between different parameters, like constraining Poisson's ratio (which links P- to S-wave), and implemented a dynamic parameter axis scaling to optimize the mapping of less sensitive parameters, like deeper layers, among other improvements.

The conditional Neighbourhood Algorithm is implemented through the *dinver* tool from the Geopsy software (Wathelet et al., 2020). Specifically through *dinverext*, as it allows implementing custom forward calculation. Here, the following parameters can be tuned:

N_{s0}: initial number of models generated with a Monte-Carlo technique.

N_r: number of best Voronoi cells where new models will be generated. A higher N_r makes the inversion more explorative.

N_s^*: total number of models generated by the Neighbourhood Algorithm, excluding the initial N_{s0} models. This is different from the parameter N_s specified above.

N_w: number of random walks before generating a new model. A common value of 2 is accepted. To generate a new model inside a cell, a Gibbs

GU: percentage of bad generated models (e.g., providing NaN values or synthetic calculation fails) after which a best model is abandoned. A value of 90 is recommended and fixed.

The same NA is utilized for the inversion of the shallow (Chapter 5) and crustal (Chapter 6) subsurface structure. The misfit definition, tuning parameters and the parameter space utilized in each case are provided in each chapter, respectively.

The NA does not provide a single best model by itself, but a set of models with their misfits (model ensemble). The obtained models must be evaluated to check the fitting between the theoretical predictions and the observations or a specific maximum misfit threshold needs to be set. Performing statistical analysis on the model ensemble generated by the NA inversion is biased because it will depend on the number of models explored. If the number of models is large enough, the dispersion around the best-fitting model will decrease because of the nature of the NA. Therefore, estimating uncertainties from the NA is not a direct outcome and must be assessed properly. In this case, for each inversion, the uncertainty is roughly assessed by checking the parameter ranges of models with a misfit lower than a certain threshold, as specified in each chapter.

CHAPTER 4

HVSR from Martian ambient vibrations

Is it the same to perform classical one-station seismological techniques on Earth as on Mars? Which challenges are faced when applying these techniques on the Martian data? This chapter analyses the horizontal-to-vertical spectral ratios (HVSR or H/V) and other polarization attributes calculated from the Martian ambient vibrations, in order to assess their stability and use for HVSR inversion under the diffuse field approach (DFA). These analyses are supported by a thorough characterization of the observed features, including their temporal variability and phenomenology, providing a comprehensive perspective for their interpretation and subsequent inversion. Some of these observations, analyses and results have been published as part of the following articles:

1. **Carrasco, S.**, Knapmeyer-Endrun, B., Margerin, L., Schmelzbach, C., Onodera, K., Pan, L. *et al.* (2023). *Empirical H/V spectral ratios at the InSight landing site and implications for the Martian subsurface structure.* Geophysical Journal International, 232(2), 1293–1310. doi:10.1093/gji/ggac391.

2. Hobiger, M., Hallo, M., Schmelzbach, C., Stähler, S. C., Fäh, D., Giardini, ..., **Carrasco, S.** *et al.* (2021). *The shallow structure of Mars at the InSight landing site from inversion of ambient vibrations.* Nature Communications, 12(6756), 1–13. doi:10.1038/s41467-021-26957-7.

4.1 Considerations on the data processing

The horizontal-to-vertical spectral ratios (HVSR) analysis was first carried out on the ambient vibrations recordings, which are initially expected to provide information about the subsurface structure underneath the InSight lander. The spectral and polarization features were initially investigated using the data recorded during sols 422 (the 422nd *Martian day* since landing), 423 and 424, but the analysis was extended for the range between July 1st, 2019 and July 1st, 2021 (sols 210 to 922). This latter time range corresponds to about one Martian year, during which enough data has been collected under different environmental conditions and seasonal variations can be investigated.

This study initially aims to investigate the HVSR features in the frequency range between 0.2 and 30 Hz, which is suitable for exploring subsurface characteristics in the order of meters. For this, the noise features were computed for the available VBB and SP data recorded at 100 and 20 sps (depending on data availability). Initially, the seismic recordings were divided into data windows of 120 seconds each, which were windowed with three Discrete Prolate Spheroidal Sequences (DPSS) of half bandwidth $bw = 2$ to reduce spectral leakage during spectral computation. Due to the large number of data windows resulting from the time range of this study, and to optimize the use of computational resources, no overlapping was implemented to calculate the features. Furthermore, given the presence of predicted lander modes and the fact that spectral smoothing can make it difficult to identify them, no smoothing was applied to the spectra. Instead, the final HVSR curve smoothing is obtained by statistical means.

Some considerations must be taken into account before processing the data. As mentioned in Chapter 3, different special signals have been identified in the recordings. Among these, the so-called donks and glitches are the most recurrent signals and may affect the spectral and HVSR analysis. Other special signals, such as pressure drops or seismic event signals, are not expected to affect the final HVSR as they are less frequent. Thus, to assess the data processing and interpretation of the results, a preliminary evaluation of the effect of the donks and glitches on the spectral curves was conducted.

4.1.1 Effect of donks

For the evaluation of the donks, a data window of 120 s (as initially proposed) was divided into smaller segments of 5 s, the typical duration of the donk signals (Fig. 4.1a). The vertical and horizontal spectra were calculated for each of these 5 s segments as well as for the full 120 s data window (Fig. 4.1b and c). Here, the data segments without the donk present similar spectral amplitudes between them. Given its high-frequency nature, larger amplitudes at frequencies above 10 Hz are observed for the data window including the donk (red box and curves in Fig. 4.1). The spectra of the full 120 s data window also show large amplitudes at high frequencies, which are related to the effect of the short donk signal contained in this longer data window. Otherwise, if no donk would be present, the spectral curves of the 120 s data window would look like the without-donk data segments. Consequently, the effect of the donk is observed in the HVSR curve above 10 Hz, where the with-donk and the full 120 s data windows present larger H/V amplitudes than the donk-free data segments (Fig. 4.1d). Below 10 Hz, some spectral differences are observed

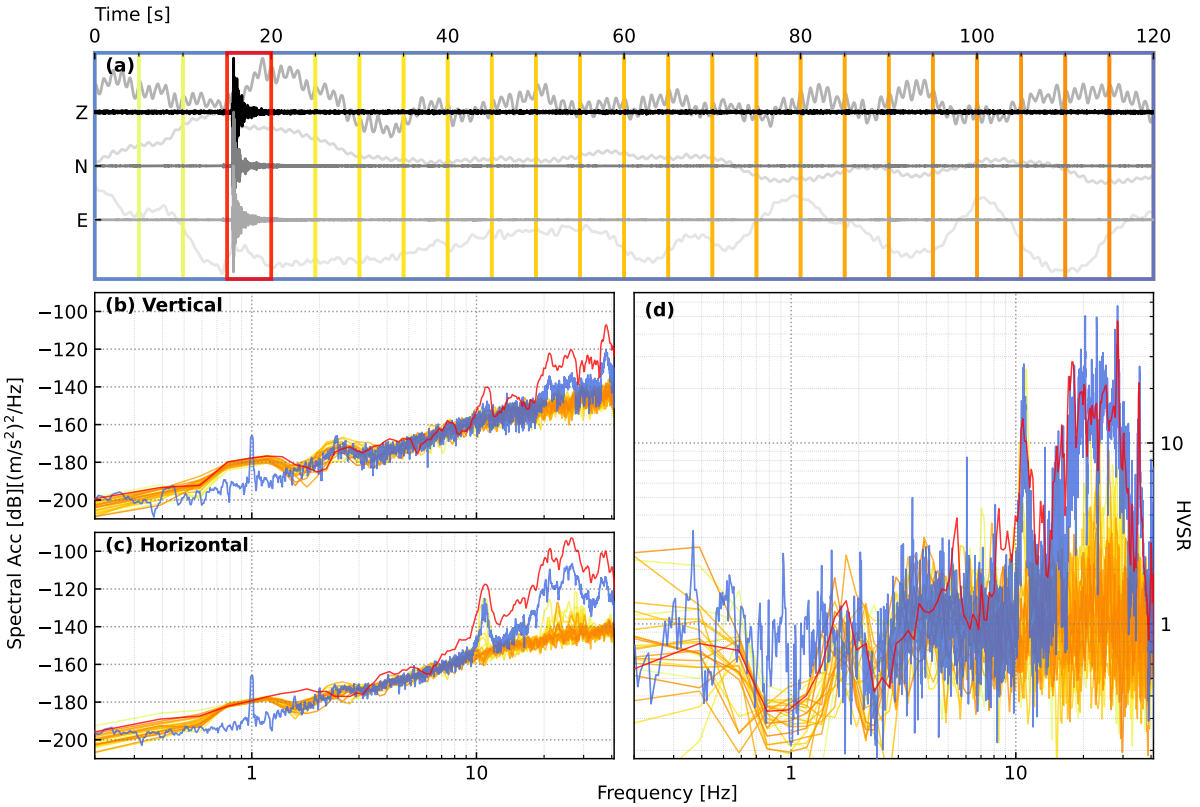


Figure 4.1: Effect of donks in HVSR calculation. **(a)** Waveforms of the components of ground motion normalized by its corresponding maximum amplitude. Main clear waveforms are high-pass filtered above 1 Hz. Less clear waveforms in the background are low-pass filtered below 1 Hz. Colored boxes denote the time windows utilized for the spectral calculation (5 s long). The red box shows the time window where a donk is registered. The blue box corresponds to the 120s time window initially utilized. **(b)** Vertical and **(c)** Horizontal spectral acceleration of the ground-motion waveforms shown in (a). The color of the curves correlate with the color of the time windows in (a). **(d)** HVSR calculated for each time window shown in (a).

between the data segments with and without donk. However, these differences disappear as longer data windows are used.

Given these observations, only data windows without donks are considered to avoid contamination by these signals and potential misinterpretations. For this purpose, a simple donk detector was constructed by applying an STA/LTA (short time average/long time average) algorithm to the time series of the absolute horizontal component, defined as $H(t) = |N(t)| + |E(t)|$, filtered between 20 and 30 Hz. For the STA/LTA algorithm, the duration of the short-term and long-term windows is 1 s and 20 s, respectively. The on and off thresholds, i.e. the STA/LTA values at which the detector is activated and deactivated, are set to 4 and 1.5, respectively. Once the data windows with donks have been detected and discarded, the remaining recordings without donks are divided into 20 s data segments, which are used to calculate the spectral features at high frequencies (>2 Hz). In this case, the 20 s duration was preferred to 120 s because it is less likely to find a donk in shorter time windows.

4.1.2 Effect of glitches

Glitches are another special signal to consider when calculating spectral attributes and HVSR. As presented in Chapter 3, they are observed as low-frequency disturbances in either one, two or three components of the ground-motion recordings. Therefore, their spectral characteristics are not always the same, but a quick assessment can be made using one of these cases as an example. A new 120 s data window containing a glitch is used to illustrate its effect on the spectra characteristics, as shown in Fig. 4.2a. In this case, the glitch is observed mainly in the horizontal components, between 65 and 80 s. As expected, no clear effect of the glitch is observed in the vertical spectrum (Fig. 4.2b). Regardless, the glitch effect is observed in the horizontal spectra, where the with-glitch data window presents larger spectral amplitudes below 3 Hz than the data segments without it (Fig. 4.2c). Similarly, the horizontal spectrum of the full 120 s data also has larger spectral amplitudes than the glitch-free windows, particularly below 1 Hz. As previously shown, some donks in these recordings also affect the high-frequency part of the spectrum. Given the spectral content, the glitch and the full 120 s window have larger H/V amplitudes at low frequencies (< 1 Hz) than the glitch-free windows. Therefore, the glitches might have an important effect on the low-frequency part of the HVSR curve.

One way to get rid of this problem is by removing the glitches from the raw data. In this case, the deglitched data, obtained after applying the UCLA deglitching method presented in Scholz et al. (2020), is used. This method correlates the raw UVW velocity recordings with the instrument's response to a step in acceleration (understood as the Green's functions of the glitch), which is then removed from the recordings. Further details can be found in Scholz et al. (2020).

The raw data is affected by the deglitching process. Due to the different time stamps of the raw data samples and the deglitching algorithm acting in the low frequencies, the deglitched data is interpolated along a common time array to synchronize the different components. This interpolation step acts as a low-pass filter which, in the case of the VBB@20 sps data, affects the recordings mainly above 3 Hz. Figure A1.5 in the Appendix shows the difference between the deglitched and un-deglitched data is more significant at such high frequencies. This is also evident in the UVW waveforms, where the short-period signals of the deglitched data have lower amplitudes than the raw un-deglitched waveforms (Fig. A1.6 in the Appendix). Therefore, special care must be taken when analyzing spectral features above 3 Hz obtained from deglitched VBB@20 sps data.

In light of the considerations above, the following steps were taken for the analysis. The high-frequency part of the SP and VBB spectra (roughly above 2 Hz) is studied by using 20 s data windows from the raw un-deglitched SP and VBB@100 sps recordings, after filtering the donks out. The low-frequency features of VBB data are investigated by using 120 s data windows from the deglitched VBB@20 sps data, after applying the UCLA method. As the number of glitches observed on SP is much less than in VBB, and given its poor sensitivity to long periods, the low frequencies of the SP instrument are studied by using 120 s data windows from raw un-deglitched SP@100 sps data.

Once the essential aspects of the data processing have been considered, the following step is to examine the stability of the HVSR over a sol (the Martian day) and over the Martian year (around 668 sols, 687 Earth days). This way, it is possible to have an

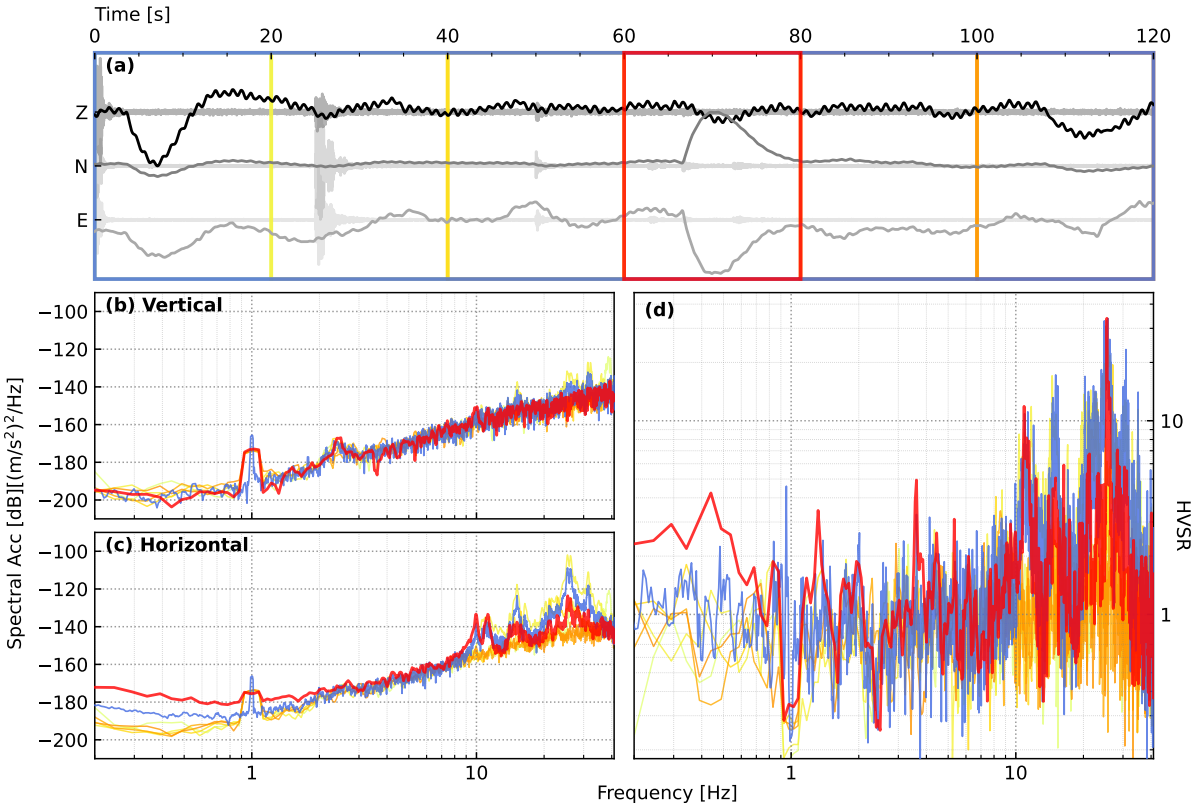


Figure 4.2: Effect of glitches in H/V calculation. **(a)** Waveforms of the components of ground motion normalized by its corresponding maximum amplitude. Main clear waveforms are low-pass filtered below 1 Hz. Less clear waveforms in the background are high-pass filtered above 1 Hz. Colored boxes denote the time windows utilized for the spectral calculation (20 s long). The red box shows the time window where a glitch is registered. The blue box corresponds to the 120 s time window initially utilized. **(b)** Vertical and **(c)** Horizontal spectral acceleration of the ground-motion waveforms shown in (a). The color of the curves correlates with the color of the time windows in (a). **(d)** HVSR calculated for each time window shown in (a).

overview of the possible factors affecting the spectral and polarization features of the ambient vibrations, in order to confirm or discard the usability of the resulting HVSR curve under the DFA.

4.2 Variability of the ambient vibrations HVSR over a sol

Since the VBB and SP sensors are expected to have different performances at low and high frequencies, the variability of the spectral features is investigated in both instruments. This analysis was conducted over the sols 422, 423 and 424, as these are some of the few consecutive sols with the most VBB and SP data at 100 and 20 sps simultaneously available, as well as environmental TWINS data.

To have a first overview of the data, the vertical spectral amplitudes of the VBB and SP instruments illustrate the noise level variation over sol 422 (Fig. 4.3b and f). Sol 422 spans February 2nd and 3rd, 2020, in the middle of the northern Martian summer.

The environmental conditions during this sol are illustrated by using the TWINS data recorded during sols 422, 423 and 424, in order to cover data gaps between different sols (Fig. 4.3a).

The spectral amplitudes of the ambient noise vibrations seem to correlate to the environmental conditions throughout a sol. As shown in Fig. 4.3a, the wind speed and air temperature reach their highest levels during the daytime, mainly between 08:00 and 16:00 Local Mean Solar Time (LMST), when the wind direction is roughly N100°E. During this period of the sol, the VBB and SP instruments record their largest vertical spectral amplitudes (Fig. 4.3b and f). On the contrary, the lowest ground-motion spectral amplitudes are reached during the local evening, mainly between 18:00 and 23:00 LMST. In this time range, the wind speed suddenly decreases until reaching its lowest level of about 3 m/s, which is close to the lowest reliable measurement (∼2.8 m/s, Banfield et al., 2020), so the actual wind speed can be even lower. As the wind direction is derived from the measured wind speed, there is also low reliability of this parameter during this time. The air temperature has a first fast drop around 16:00 LMST and then steadily decreases from the moment the sun has set over the horizon, ranging from ∼210 to ∼190 K close to the local midnight. Nevertheless, the lowest temperatures are observed during the early morning, roughly between 00:00 and 05:00 LMST. During this time, the wind speed slightly increases as well as the spectral ground-motion amplitudes. After this period, once the sun has risen over the horizon, both wind speed and temperature increase until reaching their daily peak and the pattern continues. Thus, based on the recorded ground-motion amplitudes, the sol can be divided into three distinct periods: a *low-noise* period (during the local evening, ∼17:00-00:00 LMST), a *mid-noise* period (early morning, ∼00:00-05:00 LMST) and a *high-noise* period (day, ∼08:00 and 16:00 LMST).

Given these different periods of the sol, a proper characterization of the noise features can be obtained by taking the spectra recorded during part of these periods between sols 422 and 424. In particular, the low, mid and high-noise periods are characterized by the spectra obtained between 19:00-23:00, 00:00-04:00 and 12:00-16:00 LMST, respectively. For these different periods, a normalized density distribution of the vertical spectral amplitudes is shown in Fig. 4.3c-e, for VBB, and Fig. 4.3g-i, for SP. Here, the number of occurrences of each spectral bin is divided by the total number of observations for that frequency. Analogously, the same overview is presented for the HVSR (Fig. 4.5), the degree of polarization (DOP, Fig. 4.6), the vertical Θ_V (Fig. 4.7) and the horizontal incidence angle Θ_H (Fig. 4.8) of the recorded signals. The following analysis aims to understand the nature of the noise wavefield and determine similarities and/or differences between SP and VBB. For this purpose, the median value of the observations is preferred, especially for comparing the spectral amplitudes, but the distribution mode is considered for a better assessment of the polarization features.

The following pages present the overview of these features, which are then discussed in terms of the different noise periods over a sol.

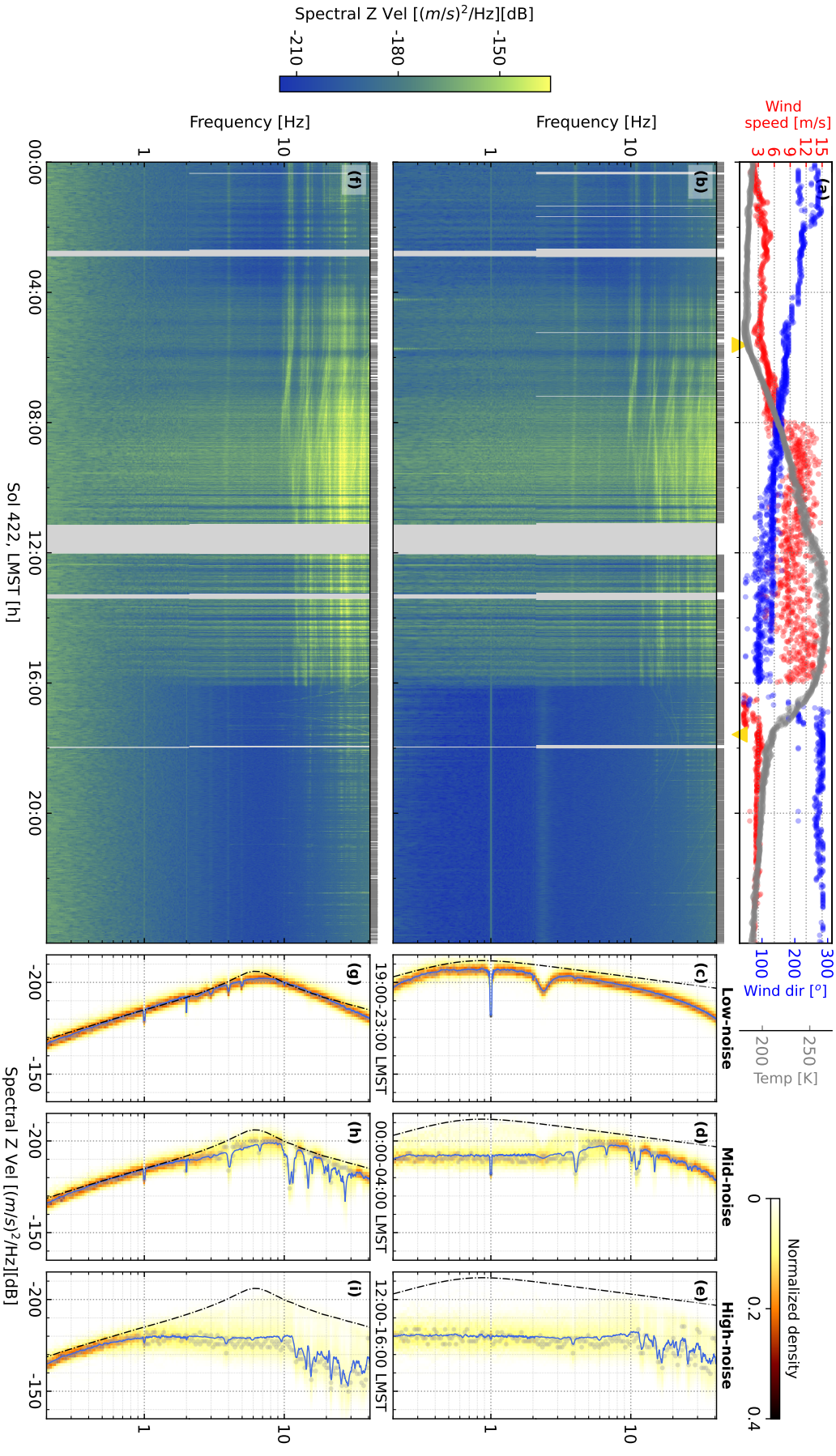


Figure 4.3: Spectrogram of the vertical component of the Martian ground-motion over a characteristic sol, as recorded by VBB and SP at 100 and 20 sps. **(a)** Wind speed (red circles), wind direction (blue circles) and air temperature (gray circles) as a function of time. Data from sols 422, 423 and 424 are used to cover TWINS data gaps. **(b)** Spectrogram of the vertical velocity component recorded by VBB at 100 sps. Deglitched data is used for frequencies below 2.1 Hz. Vertical gray lines on top denote the time of occurrence of donks. **(c)-(e)** The normalized density of vertical spectral amplitudes recorded during sols 422, 423 and 424 computed for **(c)** low-noise (19:00 - 23:00 LMST), **(d)** mid-noise (00:00 - 04:00 LMST) and **(e)** high-noise (12:00 - 16:00 LMST) periods. The distribution mode is plotted as gray circles whereas the blue curve denotes the median. Subplots **(f)**, **(g)**, **(h)** and **(i)** are analogous figures for SP 100 sps data.

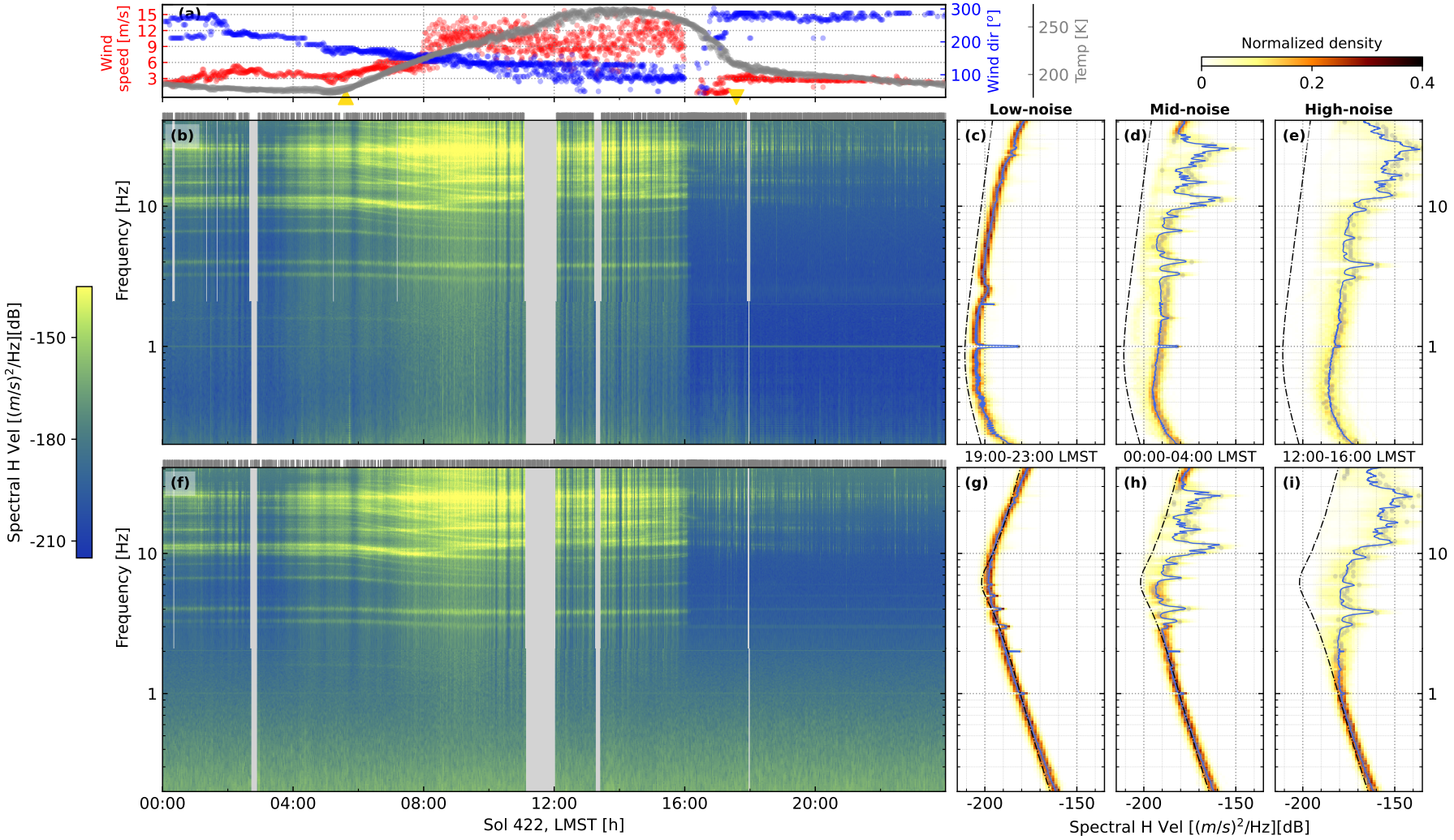


Figure 4.4: Spectrogram of the horizontal component of the Martian ground-motion over a characteristic sol, as recorded by VBB and SP at 100 and 20 sps. **(a)** Wind speed (red circles), wind direction (blue circles) and air temperature (gray circles) as a function of time. Data from sols 422, 423 and 424 are used to cover TWINS data gaps. **(b)** Spectrogram of the horizontal velocity component recorded by VBB at 100 sps. Deglitched data is used for frequencies below 2.1 Hz. Vertical gray lines on top denote the time of occurrence of donks. **(c)-(e)** The normalized density of horizontal spectral amplitudes recorded during sols 422, 423 and 424 computed for **(c)** low-noise (19:00 - 23:00 LMST), **(d)** mid-noise (00:00 - 04:00 LMST) and **(e)** high-noise (12:00 - 16:00 LMST) periods. The distribution mode is plotted as gray circles whereas the blue curve denotes the median. Subplots **(f)**, **(g)**, **(h)** and **(i)** are analogous figures for SP 100 sps data.

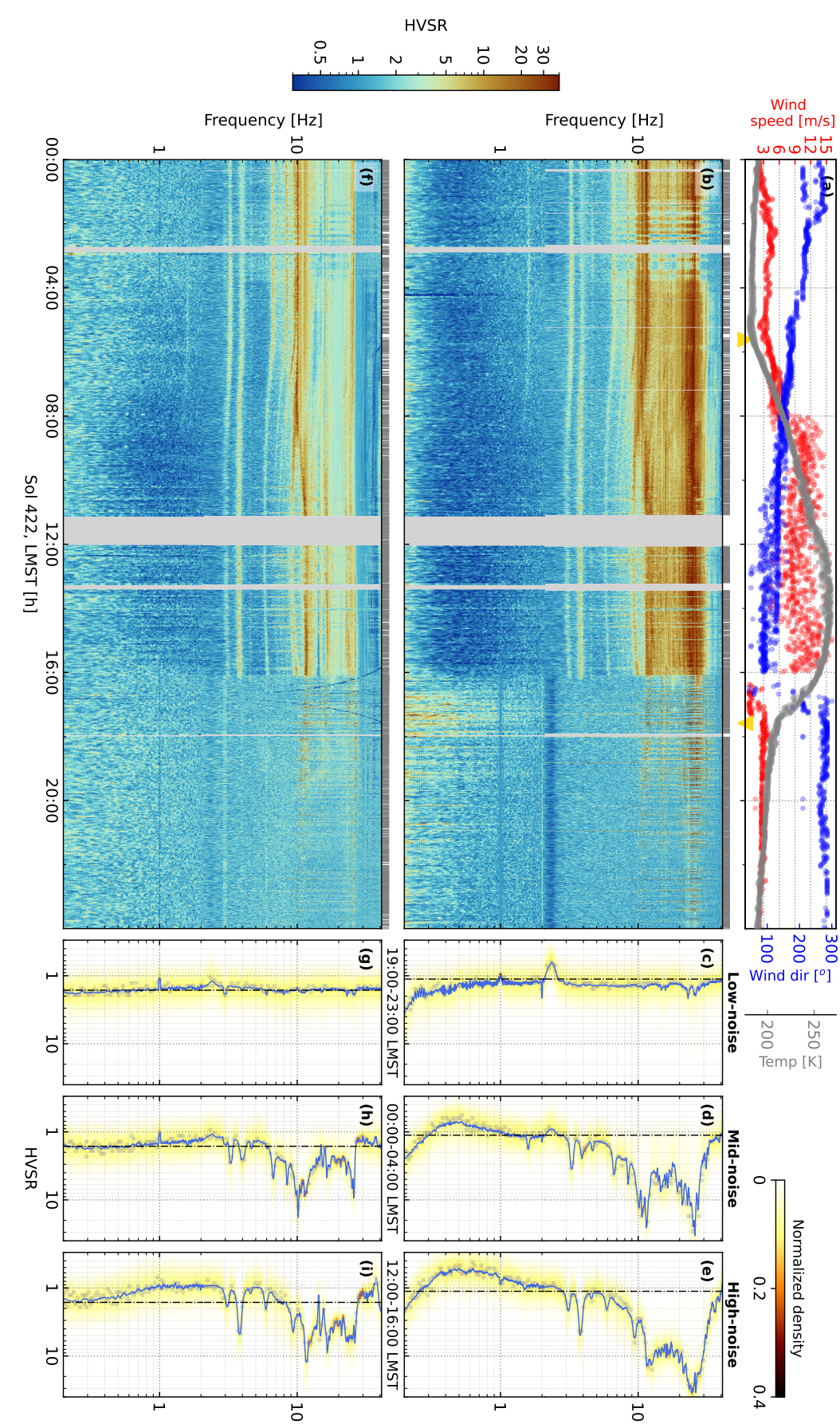


Figure 4.5: Temporal evolution of Martian ground-motion HVSR over a characteristic sol, as recorded by VBB and SP at 100 sps and 20 sps. **(a)** Wind speed (red circles), wind direction (blue circles) and air temperature (gray circles) as a function of time. Data from sols 422, 423 and 424 are used to cover TWINS data gaps. **(b)** Time-frequency evolution of the HVSR as recorded by VBB at 100 sps. Deglitched data is used for frequencies below 2.1 Hz. Vertical gray lines on top denote the time of occurrence of donks. **(c)-(e)** The normalized density of HVSR spectral amplitudes obtained from sols 422, 423 and 424 are computed **(c)** low-noise (19:00 - 23:00 LMST), **(d)** mid-noise (00:00 - 04:00 LMST) and **(e)** high-noise (12:00 - 16:00 LMST) periods. The distribution mode is plotted as gray circles whereas the blue curve denotes the median. Subplots **(f)**, **(g)**, **(h)** and **(i)** are analogous figures for SP 100 sps data.

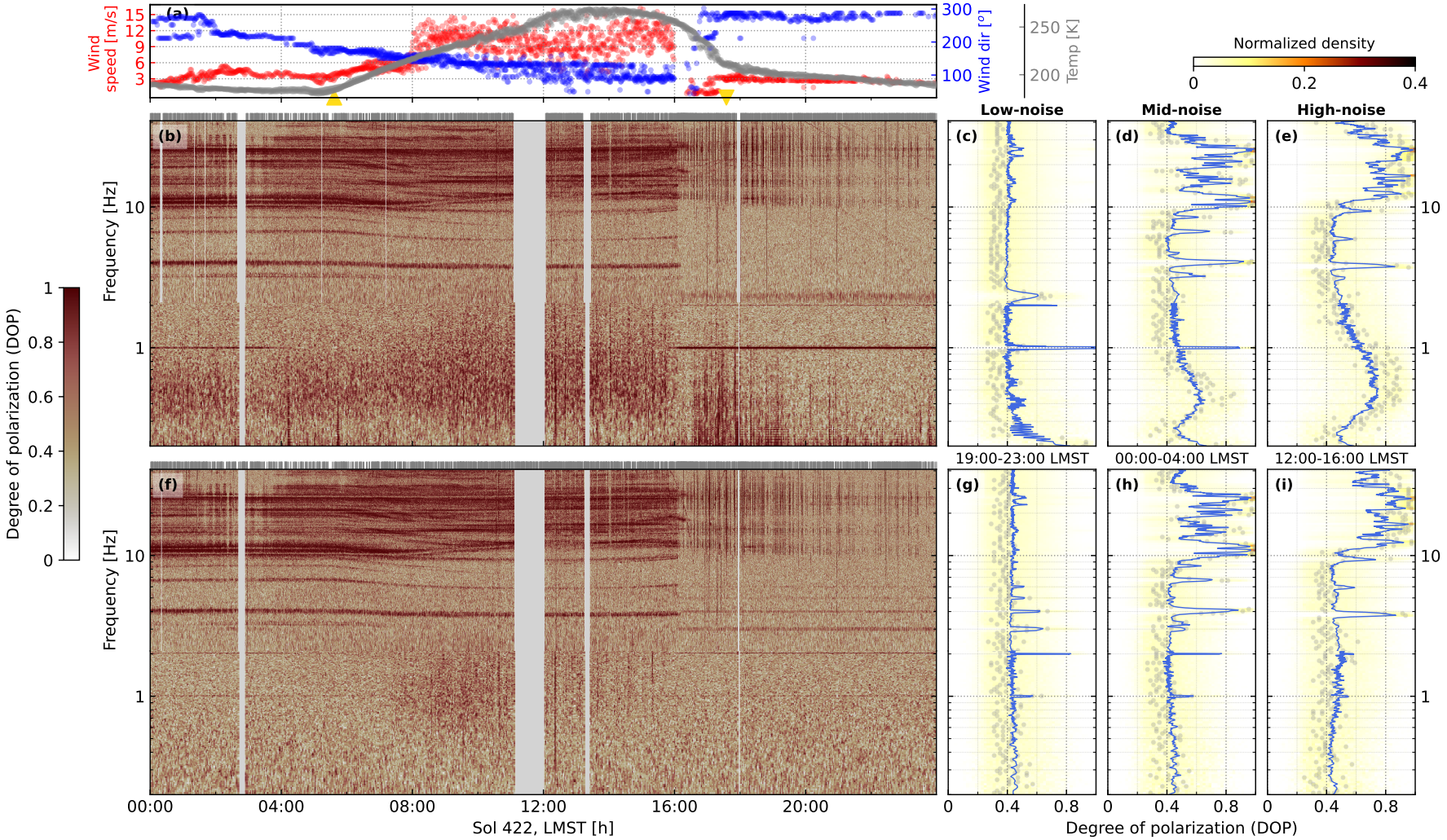


Figure 4.6: Temporal evolution of the *degree of polarization* (DOP) of the Martian ground-motion over a characteristic sol, as recorded by VBB and SP at 100 sps and 20 sps. **(a)** Wind speed (red circles), wind direction (blue circles) and air temperature (gray circles) as a function of time. Data from sols 422, 423 and 424 are used to cover TWINS data gaps. **(b)** Time-frequency evolution of the degree of polarization (DOP) as recorded by VBB at 100 sps. Deglitched data is used for frequencies below 2.1 Hz. Vertical gray lines on top denote the time of occurrence of donks. **(c)-(e)** The normalized density of HVSR spectral amplitudes obtained from sols 422, 423 and 424 are computed **(c)** low-noise (19:00 - 23:00 LMST), **(d)** mid-noise (00:00 - 04:00 LMST) and **(e)** high-noise (12:00 - 16:00 LMST) periods. The distribution mode is plotted as gray circles whereas the blue curve denotes the median. Subplots **(f)**, **(g)**, **(h)** and **(i)** are analogous figures for SP 100 sps data.

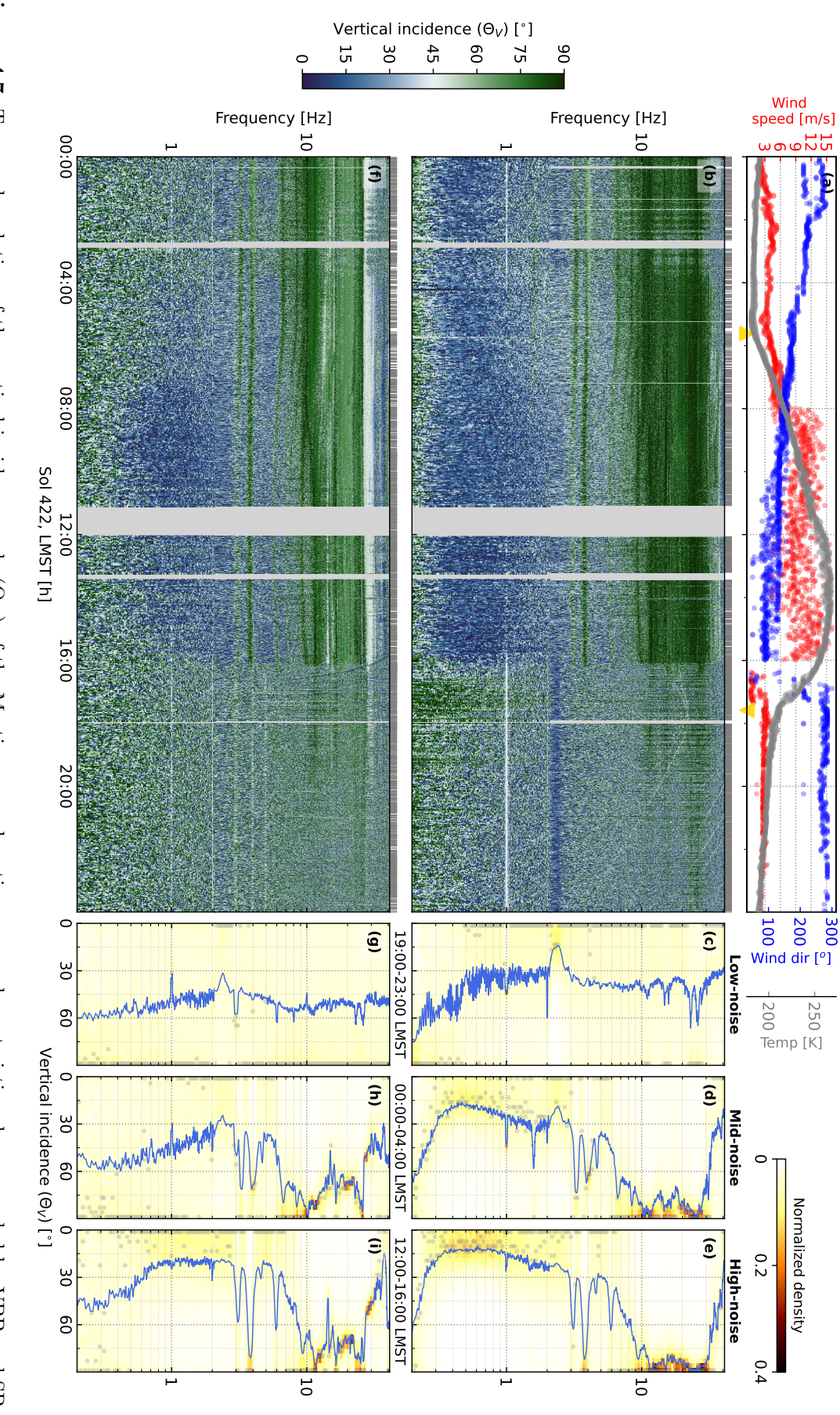


Figure 4.7: Temporal evolution of the vertical incidence angle (Θ_V) of the Martian ground-motion over a characteristic sol, as recorded by VBB and SP at 100 sps and 20 sps. **(a)** Wind speed (red circles), wind direction (blue circles) and air temperature (gray circles) as a function of time. Data from sols 422, 423 and 424 are used to cover TWINS data gaps. **(b)** Time-frequency evolution of the vertical incidence angle Θ_V as recorded by VBB at 100 sps. Deglitched data is used for frequencies below 2.1 Hz. Vertical gray lines on top denote the time of occurrence of donks. **(c)-(e)** The normalized density of HVSR spectral amplitudes obtained from sols 422, 423 and 424 are computed **(c)** low-noise (19:00 - 23:00 LMST), **(d)** mid-noise (00:00 - 04:00 LMST) and **(e)** high-noise (12:00 - 16:00 LMST) periods. The distribution mode is plotted as gray circles whereas the blue curve denotes the median. Subplots **(f)**, **(g)**, **(h)** and **(i)** are analogous figures for SP 100 sps data.

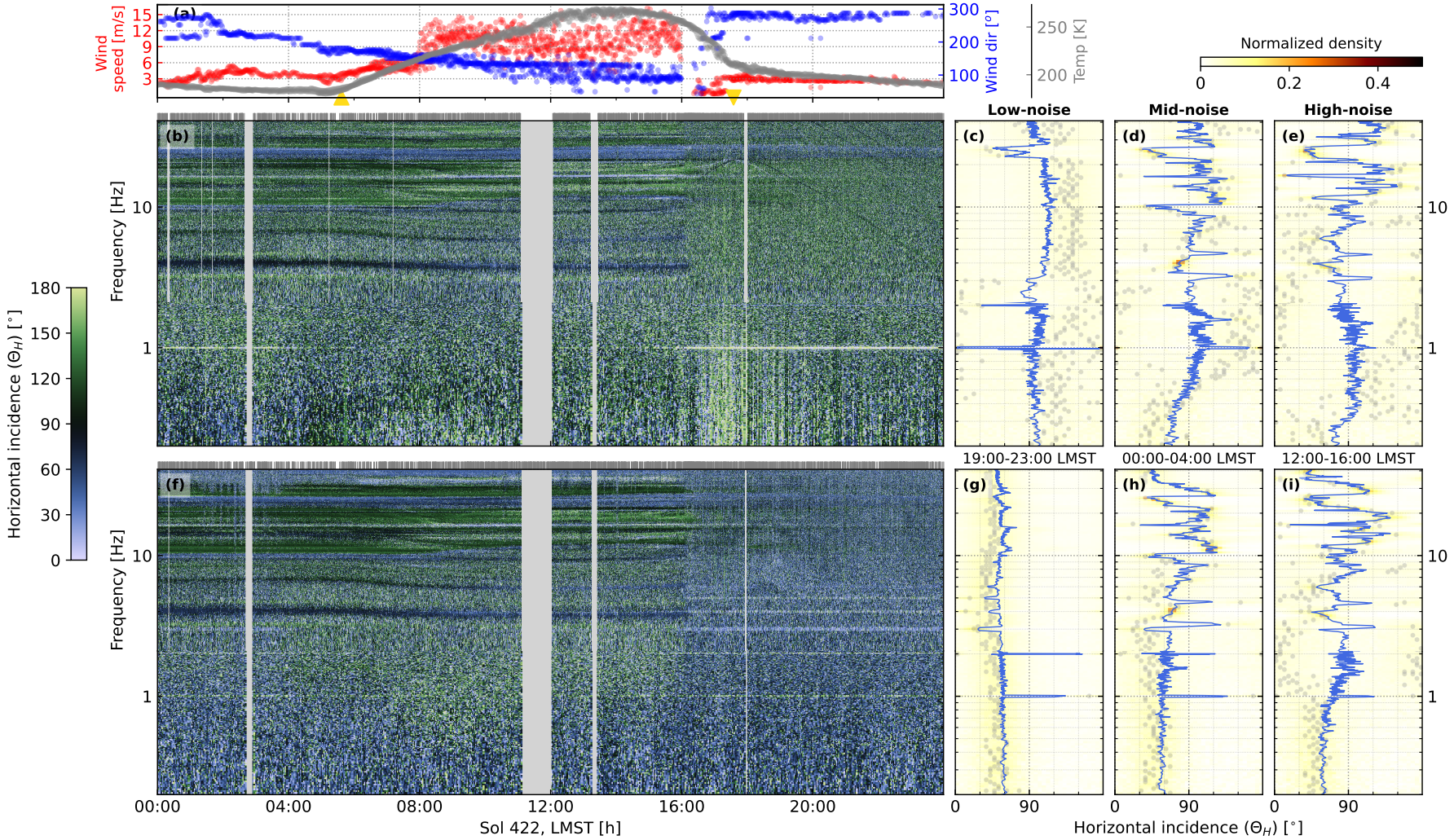


Figure 4.8: Temporal evolution of the horizontal incidence angle (Θ_H) of the Martian ground-motion over a characteristic sol, as recorded by VBB and SP at 100 sps and 20 sps. **(a)** Wind speed (red circles), wind direction (blue circles) and air temperature (gray circles) as a function of time. Data from sols 422, 423 and 424 are used to cover TWINS data gaps. **(b)** Time-frequency evolution of the horizontal incidence angle Θ_H as recorded by VBB at 100 sps. Deglitched data is used for frequencies below 2.1 Hz. Vertical gray lines on top denote the time of occurrence of donks. **(c)-(e)** The normalized density of HVSR spectral amplitudes obtained from sols 422, 423 and 424 are computed **(c)** low-noise (19:00 - 23:00 LMST), **(d)** mid-noise (00:00 - 04:00 LMST) and **(e)** high-noise (12:00 - 16:00 LMST) periods. The distribution mode is plotted as gray circles whereas the blue curve denotes the median. Subplots **(f)**, **(g)**, **(h)** and **(i)** are analogous figures for SP 100 sps data.

4.2.1 Low-noise period

The low-noise period is one of the most interesting time windows of the sol. During this time, the environmental conditions are stable enough not to generate large disturbances and the wind speed reaches its lowest values (although undeterminable). As the ground vibrations caused by the wind-lander interaction strongly depend on the wind speed (Murdoch et al., 2017; Mimoun et al., 2017), low winds are expected to generate little or no contamination on the recorded signals.

Thus, one of the most distinctive features during this time is the tick noise, a set of clear and narrow peaks observed on the vertical and horizontal components of VBB and SP (Fig. 4.9a, b). It is observed at 1 Hz, where it reaches its largest amplitude, and with lower amplitudes at its higher harmonic modes. It is well visible up to 6 Hz, especially on the SP recordings, but some higher harmonics are also visible at 9 and 10 Hz and higher frequencies (Fig. 4.9a). As no spectral smoothing has been applied, their presence in the HVSR curve can be clearly identified as narrow spikes and be discarded (Fig. 4.9c). The tick noise is understood as an electronic noise due to the interference of signals coming from temperature measurements and, therefore, are highly polarized compared to the surrounding frequencies (Fig. 4.9).

Low spectral amplitudes and the instrumental self-noise

The vertical and horizontal spectral amplitudes have similar shapes and are close to the theoretical instrument self-noise (ISN), as shown in Fig. 4.9a and b. In particular, the theoretical ISN spectral curves of SPZ and SPH fit well within the measured median and its uncertainty (Fig. 4.9a). This suggests that, during the low-noise period, at least the SP recordings correspond to the ISN instead of actual Martian ground motion. A similar comparison can be performed using the SP recordings during the cruise stage, i.e., while the InSight spacecraft traveled from Earth to Mars, as shown in Fig. A1.8. In this case, the ISN can be expected to be recorded because the noise sources are minimized as long as no maneuvers are performed (e.g., Santoli et al., 2020). Nevertheless, only the ISN of the horizontal components (SPV and SPW) could be properly recorded because the vertical SP sensor requires gravity for correct functioning.

Assuming the SP spectral amplitudes correspond to the ISN, some characteristics can be derived from the polarization attributes. The median DOP is stable around 0.43 but most often around 0.33 (Fig. 4.9d). These values might indicate that the amplitudes along the preferred direction of motion are up to 5-6 times the other two and are understood as weakly polarized signals. Figures 4.9e and 4.9f show the incidence angle of the different frequencies. Despite the weak polarization, the vertical angle of incidence (Θ_V) is larger than 45° and often close to 90°, suggesting a nearly horizontal incidence of the signals, which would have an incidence direction of $\Theta_H \sim 45°$ (NW-SE orientation). Even though it cannot be confirmed, these values are likely obtained due to the configuration of the SP sensors. Particularly, because only one sensor records the vertical wavefield (SPU) whereas two record the horizontal ground motion (SPV and SPW). The latter two sensors have azimuths of 110° and 345°, respectively, which can generate a virtual $\sim$ 45° incidence if each sensor records similar amplitudes.

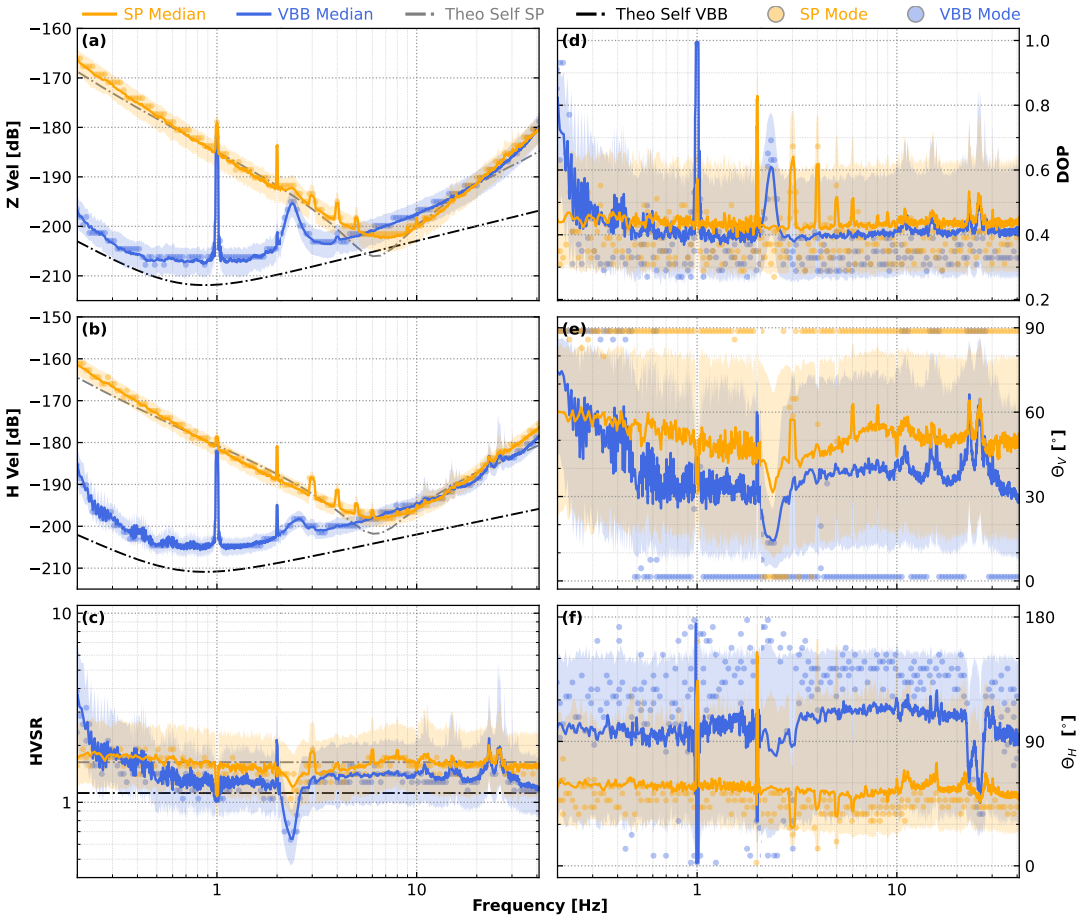


Figure 4.9: Spectral and polarization features of low-noise period. Summary of observations obtained between 19:00 and 23:00 LMST during sols 422, 423 and 424. **(a)** Vertical spectra, **(b)** Horizontal spectra, **(c)** HVSR, **(d)** degree of polarization (DOP), **(e)** vertical incidence angle Θ_V (with respect to the vertical) and **(f)** horizontal incidence angle Θ_H (clockwise from the North direction). For each feature, the median (solid line) and mode (circles) of the distribution are presented for VBB (blue) and SP (orange). The theoretical vertical and horizontal instrument self-noise spectra and the theoretical H/V are shown as dot-dashed lines for VBB (black) and SP (gray).

In fact, by comparing the SP and VBB spectral curves, it is clear that the SP recordings correspond to the ISN at least up to ~ 5 Hz, where the SP and VBB spectra start to show similar amplitudes. Otherwise, if the SP recordings (at frequencies below 5 Hz) were actual ground motion, similar spectral amplitudes and shape should be recorded by both VBB and SP due to the lower sensitivity of VBB at low frequencies, which is not the case.

On the other hand, the VBB recorded spectra also seem related to the ISN. For example, similar low DOP values suggest weakly polarized signals, even though these can be related to other sources and not necessarily ISN. A large dispersion is also observed for the vertical incidence angle, which is closer to the vertical ($\Theta_V < 45°$) and almost purely vertical incidence angles (90°) are typically recorded. Recording almost purely horizontal, as for the SP case, and vertical incidence angles over a wide range of frequencies are assumed to be related to non-natural sources, such as the corresponding ISN. Although the VBB signals are more vertically polarized, the horizontal incidence, particularly above 3 Hz, ranges between 120 and 150 degrees, which can be understood as a virtual incidence

direction given by instrument noise recorded at the VBB sensors (UVW), given their azimuths of 135°, 345° and 255°, respectively.

Another observation to further assess the nature of the recordings during the low-noise period is the difference in spectral amplitude, more clearly observed between 7 and 9 Hz, between SPZ and VBBZ (Fig. 4.9a). In this frequency range, the VBBZ spectral amplitudes are larger than those recorded by SP. Assuming that the recorded SPZ amplitudes correspond to the SP ISN, as discussed above, this observation implies that the recorded VBBZ amplitudes would correspond to the VBB ISN. Otherwise, if the VBBZ amplitudes were due to actual ground motions, then SP would record these signals and the amplitude difference would be much smaller. In another case, if the SPZ amplitudes correspond to actual ground motion, then the VBBZ amplitudes would definitively be the ISN level as VBB is not capable of measuring lower amplitudes.

In any of these two cases, the gains of the instruments are assumed to be well-calibrated. If not, even if the amplitudes might differ, the shapes of the signals are expected to be similar. In order to test this hypothesis, a cross-correlation analysis was performed in the time domain between ZNE SP and VBB signals filtered between 7 and 8.5 Hz and recorded during the same 30 s time windows at different wind/noise levels (Fig. 4.10). The cross-correlation factors between the SP and VBB signals recorded during a high-noise period, i.e., when the wind level is high, indicate a high cross-correlation for all the components (Fig. 4.10a-c). This is expected as the recorded spectral amplitudes are well above the theoretical ISN and correspond to the same actual ground motion (see further discussion in the next subsection). The similar amplitudes also prove that the gains are well-calibrated. On the contrary, the signals recorded during a low-noise period have cross-correlation factors mostly below 0.5 (Fig. 4.10d-f), suggesting that the recorded ground-motion amplitudes do not correspond to the same signal. This low cross-correlation confirms that the VBB recordings, at least in the 7-8.5 Hz frequency range, correspond to the ISN level. Figures 4.10g-i present a similar example at higher frequencies that will be discussed in the subsection on the high-noise period below.

Other features of the HVSR curve

Besides the tick noise and the ISN, other significant features can be identified during the low-noise period. A clear resonance at around 2.4 Hz is observed, especially on the VBB recordings, from which a large DOP is derived, suggesting a strong polarization. It is vertically polarized ($\Theta_V < 20°$) and, because of this, it is difficult to define the horizontal incidence angle Θ_H, even though the results suggest a N-S direction of incidence. The 2.4 Hz resonance is visible on the HVSR as a trough, where it reaches its lowest amplitude. The origin of this resonance is unclear but, given its vertical incidence, it might be related to the subsurface structure. Further details on the variability and characteristics of this resonance are provided in Section 4.4. The VBB data reveal another distinctive feature below 0.5 Hz. Here, the DOP is slightly larger than in the higher frequencies and the recorded signals have a horizontal rather than vertical incidence angle ($\Theta_V > 60°$). The direction of horizontal incidence is $\Theta_H \sim 120°$, which is slightly different from the horizontal incidence angle of the higher frequencies (between 120° and 150°), assumed to be related to the ISN. Because of these differences, the signals recorded by VBB below 0.5 Hz might be related to a phenomenon other than ISN. Particularly, these attributes can

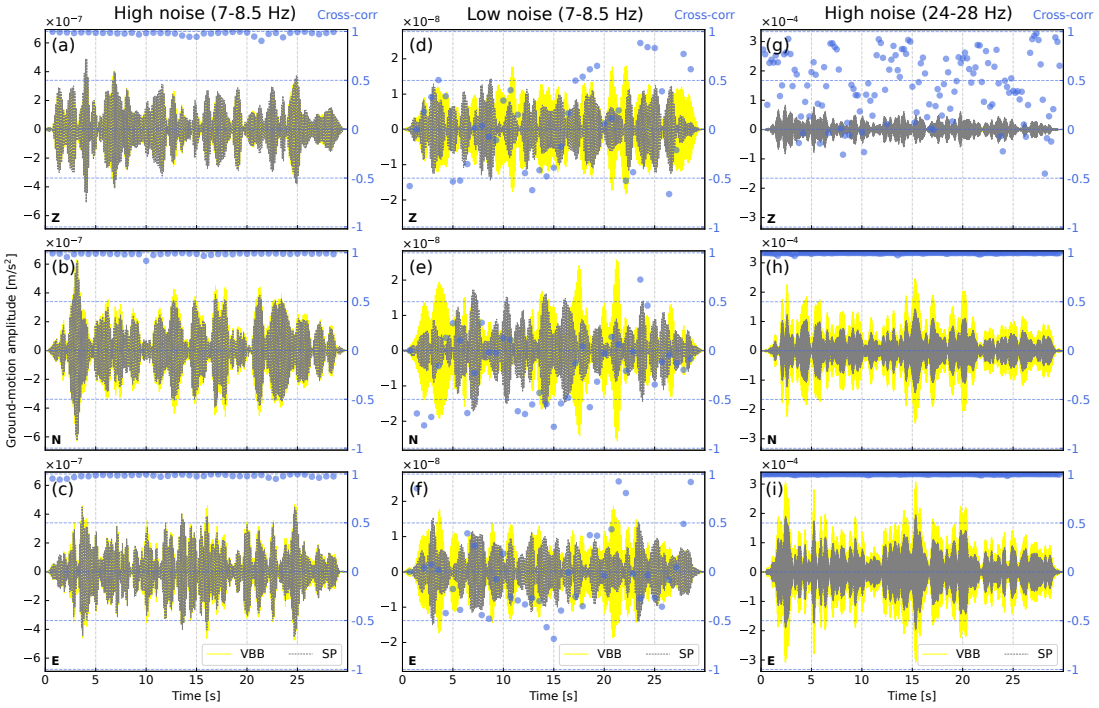


Figure 4.10: Time-domain cross-correlations between SP and VBB for different frequency bands and noise levels. From top to bottom: ground-motion components Z, N and E. Cross-correlations of SP and VBB signals **(a)-(c)** filtered between 7 and 8.5 Hz during a high-noise period, **(d)-(f)** filtered between 7 and 8.5 Hz during a low-noise period, and **(g)-(i)** filtered between 24 and 28 Hz during a high-noise period.

be related to pressure waves propagating at low wind speeds. Following Sorrells (1971), these pressure waves generate an elliptical ground motion with larger horizontal than vertical ground motion when the wind speed is low, leading to a slight increase of the HVSR at low frequencies, as observed in Fig. 4.9c (and as shown in Figure 14 of Stutzmann et al., 2021). Some other minor peaks observed around 11, 15 and 25 Hz are related to low-amplitude donks that were not filtered out after the processing due to the thresholds and STA/LTA parameters utilized.

Once all the relevant signals have been described, the HVSR curve can be appropriately evaluated. In this case, assuming the amplitudes recorded by SP correspond to the ISN, the resulting HVSR curve cannot be used for inversion of the subsurface structure as it is not based on actual ground motions. On the other hand, below 0.5 Hz, the HVSR curve from VBB recordings is affected by propagating pressure waves that follow a different physical approach not included in this work, so it can be left out of the analysis. It is unclear whether the frequency range $\sim 0.5 - 2$ Hz is affected by the VBB ISN or might correspond to the actual wavefield. If the latter is true, this frequency range could be considered for later analysis and inversion for the subsurface structure. Otherwise, it should be discarded. Similarly, the HVSR between 2 and 3 Hz is affected by the 2.4 Hz resonance, which might be related to the subsurface structure. If this is the case, it can be included in subsequent analyses. It is unclear whether the spectral amplitudes between 3 and 5 Hz correspond to ISN, but the shape of the curve and proximity to the theoretical ISN are suspicious. In any case, the HVSR above 5 Hz seems to correspond to the VBB and SP ISN, so discarding the higher frequencies for future analyses is suggested.

4.2.2 Mid-noise period

The mid-noise period is understood as a transition stage between the low-noise and high-noise periods. During this time, the wind speeds range between 3 and 6 m/s, being not as low as in the low-noise period and not as high as in the high-noise period. Besides, these wind speeds are relatively stable over time compared to the high-noise period, when more turbulent and larger wind variations are measured. This wind speed stability is difficult to compare against the low-noise period because, during this time, actual winds are below the resolution and reliability limit of the wind sensors.

Following the analysis given above, similar observations can be derived from this period. The SP vertical and horizontal amplitudes, at least between 0.2 and ∼2 Hz, still correspond to the ISN level, with similar polarization attributes as during the low-noise period (Fig. 4.11a and b), which lead to HVSR values that match the theoretical H/V (Fig. 4.11c). In the same frequency range, the amplitudes of the vertical and horizontal VBB are notably larger than those of the quiet period, suggesting that VBB records actual ground motion during this time. The polarization attributes of this frequency range suggest a polarized signal with close-to-vertical incidence ($\Theta_V < 20°$, Fig. 4.11e), which generates a general deflection of the HVSR curve (Fig. 4.11c). Similarly to the low-noise case, the origin of these features is related to pressure waves that propagate at a larger (wind) speed through the surface. As shown by Stutzmann et al. (2021), the H/V generated by such pressure waves increases towards low frequencies when the wind speeds are low but, as the wind speed increases, the vertical ground motion starts to increase faster than the horizontals, generating a broad trough in the HVSR. As the theory behind this phenomenon is not considered in this investigation, leaving this segment out of further analysis is suggested.

Between 1 and 10 Hz, the SP and VBB spectra show similar amplitudes, especially along the horizontal component, suggesting the recordings correspond to actual ground motion and not to ISN. The 2.4 Hz resonance is not as clear as during the low-noise period, but still visible on the VBB spectra and from the polarization attributes. Instead, other narrow peaks are observed at specific frequencies, strongly polarized with relatively large DOPs (Fig. 4.11d) and a nearly horizontal angle of incidence ($\Theta_V > 45°$, Fig. 4.11e). These peaks are most clearly observed on the horizontal spectra (Fig. 4.11b), particularly around the following frequencies: 1.6 Hz, 3.2 Hz, 4.1 Hz, 4.6 Hz, 6.7 Hz and 8.3 Hz. These frequencies are referred to as resonances and, given their strong polarization, nearly horizontal incidence and *a priori* dependence on environmental conditions, they can be related to the interaction between the lander and wind. Further details on their variability are shown in Section 4.4. These resonances are identifiable on the HVSR obtained from SP and VBB data. Indeed, both HVSR curves are nearly identical in this frequency range, which implies that the recordings correspond to actual ground motions. Nevertheless, these ground motions are not the natural vibrations of the subsurface but correspond to a much more complex phenomenon involving the lander, the wind conditions and also the subsurface structure, which is out of the scope of this work. Because of this, this frequency range (1-10 Hz) during the mid-noise period is useless for further study of the subsurface structure based on the HVSR technique.

The spectral curves above 10 Hz are even more contaminated by frequency peaks, which dominate and shape the spectra. The polarization attributes of these peaks indi-

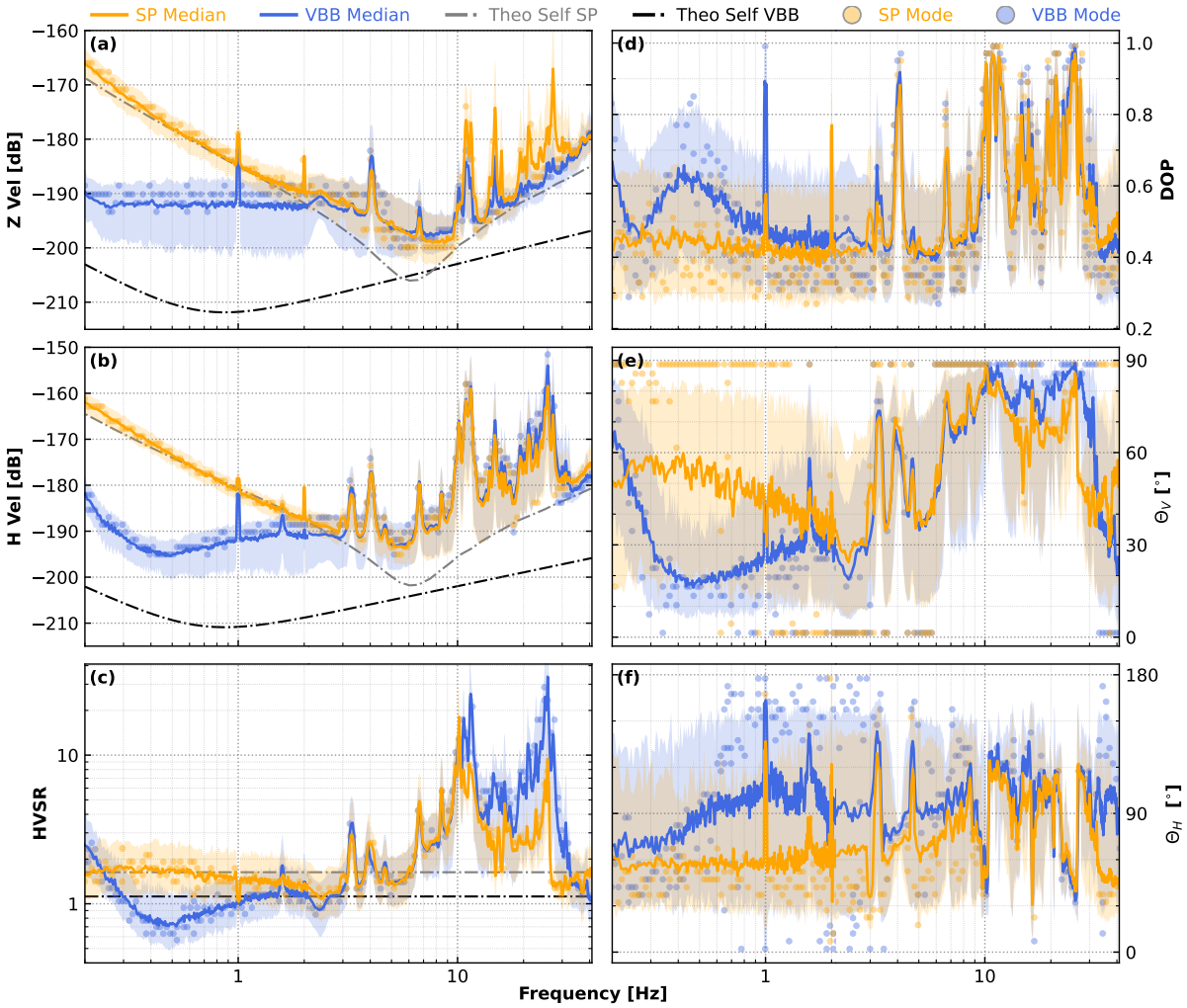


Figure 4.11: Spectral and polarization attributes of the mid-noise period. Summary of observations obtained between 00:00 and 04:00 LMST during sols 422, 423 and 424. **(a)** Vertical spectra, **(b)** Horizontal spectra, **(c)** HVSR, **(d)** degree of polarization (DOP), **(e)** vertical incidence angle Θ_V (with respect to the vertical) and **(f)** horizontal incidence angle Θ_H (clockwise from the North direction). For each feature, the median (solid line) and mode (circles) of the distribution are presented for VBB (blue) and SP (orange). The theoretical vertical and horizontal self-noise spectra, as well as the theoretical H/V, are shown as dot-dashed lines for VBB (black) and SP (gray).

cate even more polarized signals with nearly horizontal incidence angles, similar to the resonances between 1 and 10 Hz, suggesting that these high-frequency peaks are also related to resonances due to the lander. Interestingly, while the horizontal amplitudes of these spectral peaks are similar between SP and VBB recordings, the vertical amplitudes differ by orders of magnitude (tens of dB) in some cases. These differences lead to different HVSR amplitudes at frequencies larger than 10 Hz. As this phenomenon is observed when the wind speeds are higher, further discussion about this is given when analyzing the high-noise period.

4.2.3 High-noise period

Lastly, the outcomes from the high-noise period (Fig. 4.12) present some clearer features that can help to understand better the observations during the low and mid-noise stages and to have a better overview of the different HVSR curves that can be obtained from the ambient vibrations measurements.

In general, the largest horizontal and vertical amplitudes are recorded during this period, which can be understood as actual ground motion being recorded by both SP and VBB instruments over the whole range of frequencies of interest. Nevertheless, this is not always the case because, roughly below 1 Hz, the SP spectral amplitudes still correspond to the ISN as the actual ground-motion amplitudes are below this level. Similar to the mid-noise case, the pressure waves propagating at even larger speeds generate a broad trough on the HVSR curve at low frequencies (< 1 Hz), as recorded by VBB. Because of these two phenomena, the HVSR below 1 Hz is unusable in the context of this study.

Between 1 and 10 Hz, the so-called lander modes have larger amplitudes than any other moment of the sol, likely due to the larger wind speeds recorded during this time. The presence of these resonances therefore contaminates the HVSR curve. Furthermore, a nearly vertical incidence angle is derived for frequencies up to ~ 3 Hz, suggesting that the pressure waves propagating at large speeds also affect the frequency range between 1 and 3 Hz.

Similar to the lander modes, and as already observed during the mid-noise period, the frequencies above 10 Hz are strongly polarized with a nearly horizontal incidence angle and even larger amplitudes during this noisy period. Nevertheless, the vertical amplitudes recorded by VBB and SP are not the same, leading to different HVSR curves (Fig. 4.12c). In particular, the vertical amplitudes recorded by SP are larger than those recorded by VBB at all frequencies above 10 Hz (Fig. 4.12a). The SPH amplitudes are more similar to SPZ than VBBH to VBBZ. Besides, the shape of the SPZ and VBBZ spectra also differs slightly, suggesting that the origin of the difference is not only due to potential gain miscalibration but another process might also be involved. It is however difficult to decide whether SPZ or VBBZ is correct as the nature and phenomenology of the resonances are unclear.

As done for the low-noise period in the frequency range 7-8.5 Hz, a time-domain cross-correlation analysis was performed at one of these high-frequency ranges, between 24 and 28 Hz, during a high-noise period with high wind speeds (see Fig. 4.10g-i). If the amplitude differences would be only a matter of gain miscalibration, then the cross-correlation factor should still be close to 1. This might be the case for the horizontal components (N and E), for which slightly larger amplitudes are recorded by VBB. Still, the cross-correlation factor is almost 1 for the whole time window, suggesting that both instruments record the same signal. On the other hand, the vertical components have lower cross-correlation factors, between 0 and 1 (and just a few cases with negative cross-correlation), which suggests that different signals are being recorded by VBBZ and SPZ. These dissimilar signals can be due to the distinct locations of the VBBZ and SPZ measurements. As shown in Fig. 2.3b, the VBB and SP sensors are installed in different places inside the SEIS container. Hence, given their configuration, the three VBBs recompose the vertical motion in the center of the LVL while the vertical SP sensor records

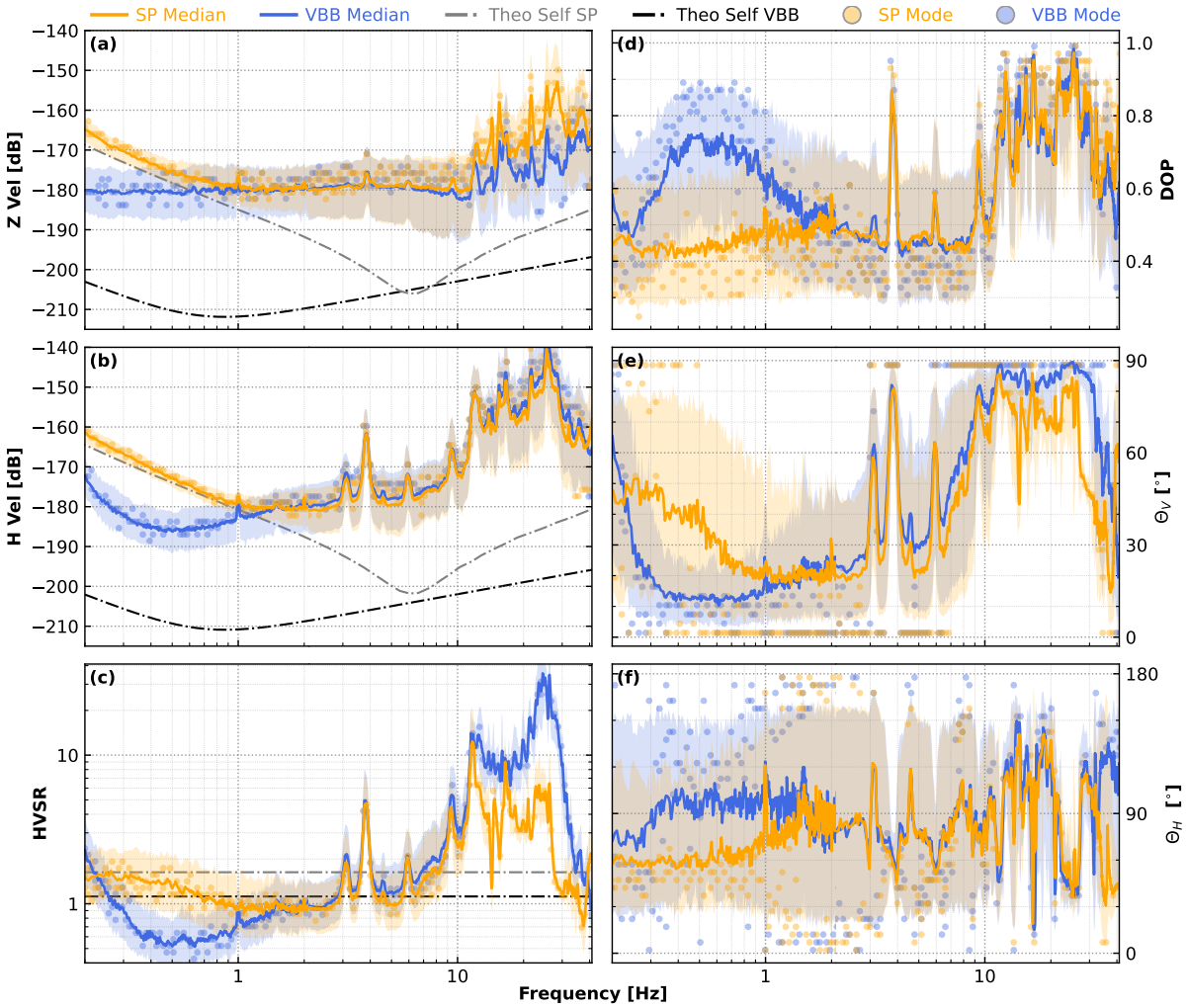


Figure 4.12: Spectral and polarization attributes of the high-noise period. Summary of observations obtained between 00:00 and 04:00 LMST during sols 422, 423 and 424. **(a)** Vertical spectra, **(b)** Horizontal spectra, **(c)** HVSR, **(d)** degree of polarization (DOP), **(e)** vertical incidence angle Θ_V (with respect to the vertical) and **(f)** horizontal incidence angle Θ_H (clockwise from the North direction). For each feature, the median (solid line) and mode (circles) of the distribution are presented for VBB (blue) and SP (orange). The theoretical vertical and horizontal self-noise spectra, as well as the theoretical H/V, are shown as dot-dashed lines for VBB (black) and SP (gray).

the ground motion on the ring of the LVL, where it is installed. In any case, Fayon et al. (2018) showed that both VBB and SP instruments might be affected by rotational motions, especially at high frequencies. Due to the incompatibility between VBBZ and SPZ recordings at high frequencies (> 10 Hz), and also the abundant presence of resonances disturbing the recordings, using the H/V curves above 10 Hz is dismissed for any further analysis.

Given the patterns observed during different environmental conditions, further analysis of the spectral and polarization attributes between 0.2 and 10 Hz was performed using the VBB data recorded during a full Martian year. Considering that the amplitude of the background seismic wavefield might vary over the year and eventually excite the subsurface resonances, seasonal variations of the HVSR can also be explored.

4.3 Variability of the ambient vibrations HVSR over a Martian year

As shown above, the lowest noise spectral amplitudes tend to occur during the local evening at the ILS, and they can be interpreted as being (or having a relevant contribution from) the instrument self-noise. Following this idea, the actual ground-motion amplitudes are lower than this spectral level (particularly below VBB self-noise) and the HVSR curve can thus not be related to the subsurface structure. Namely, the amplitudes of the background wavefield must be larger than the instrument self-noise for the recorded HVSR to be associated with the local structure. On Earth, it has been shown that the amplitude of the background seismic wavefield can vary over a terrestrial year due to natural activity (e.g., Hillers et al., 2015; Rigo et al., 2021) or even due to anthropogenic behavior (e.g., Lecocq et al., 2020; Poli et al., 2020). In the Martian case, variations of the seismic wavefield due to anthropogenic causes can be discarded but seasonal changes over the Martian year cannot be ruled out.

The spectral amplitude variations during the evening time (low-noise period) were investigated over about one Martian year, roughly between sol 211 and 921. The spectral amplitudes during the night and day time of the northern summer (as shown in the previous section for sols 422-424) are assumed to be the lowest levels that can be reached during those periods of the sol over the Martian year, so they were not investigated. This way, the amplitudes of the background seismic wavefield are inspected, expecting they can exceed the instrument self-noise level and map the natural HVSR of the site.

The seasonal variation of HVSR shows that the spectral curves during the expected low-noise period (evening time) are unstable over the Martian year. As shown in Fig. 4.13, different HVSR amplitudes and shapes are obtained for different Martian seasons. Similar to the daily pattern shown in Section 4.2, these different HVSR curves are due to the different local environmental conditions at the ILS. In fact, Fig. 4.13 shows that the wind speed levels during the northern autumn and winter evenings ($\sim$ 5 m/s) are higher than in the summer and spring evenings ($<$ 3 m/s). Because of this, the obtained HVSR curves during autumn and winter evenings are similar to those of the night-time during the northern summer (mid-noise, as represented by sols 422-424), where steady and not-so-turbulent winds are recorded.

A summary of the different spectral features (Fig. 4.14) shows that similar HVSR curves are obtained during summer and spring, and separately during autumn and winter, mainly driven by similar wind conditions. Unfortunately, meteorological data is available until around Sol 750, but the slightly higher spectral amplitudes suggest that wind speeds are slightly higher during northern autumn than winter (Fig. 4.13). In any case, the spectral amplitudes during autumn and winter, although higher than in summer and spring and thus above the self-noise level, are highly influenced by wind forces and, therefore, are also not useful for retrieving the HVSR curve related to the subsurface structure. Even if the natural background wavefield is higher than in summer/spring, this is hidden by the noise generated by the local winds. As expected, higher spectral amplitudes influenced by the local winds were recorded during the night and day times (moderate and high-noise periods) over the whole Martian year, as shown in Fig. A2.1 and A2.2, and therefore those HVSR curves can be discarded for further analysis as well.

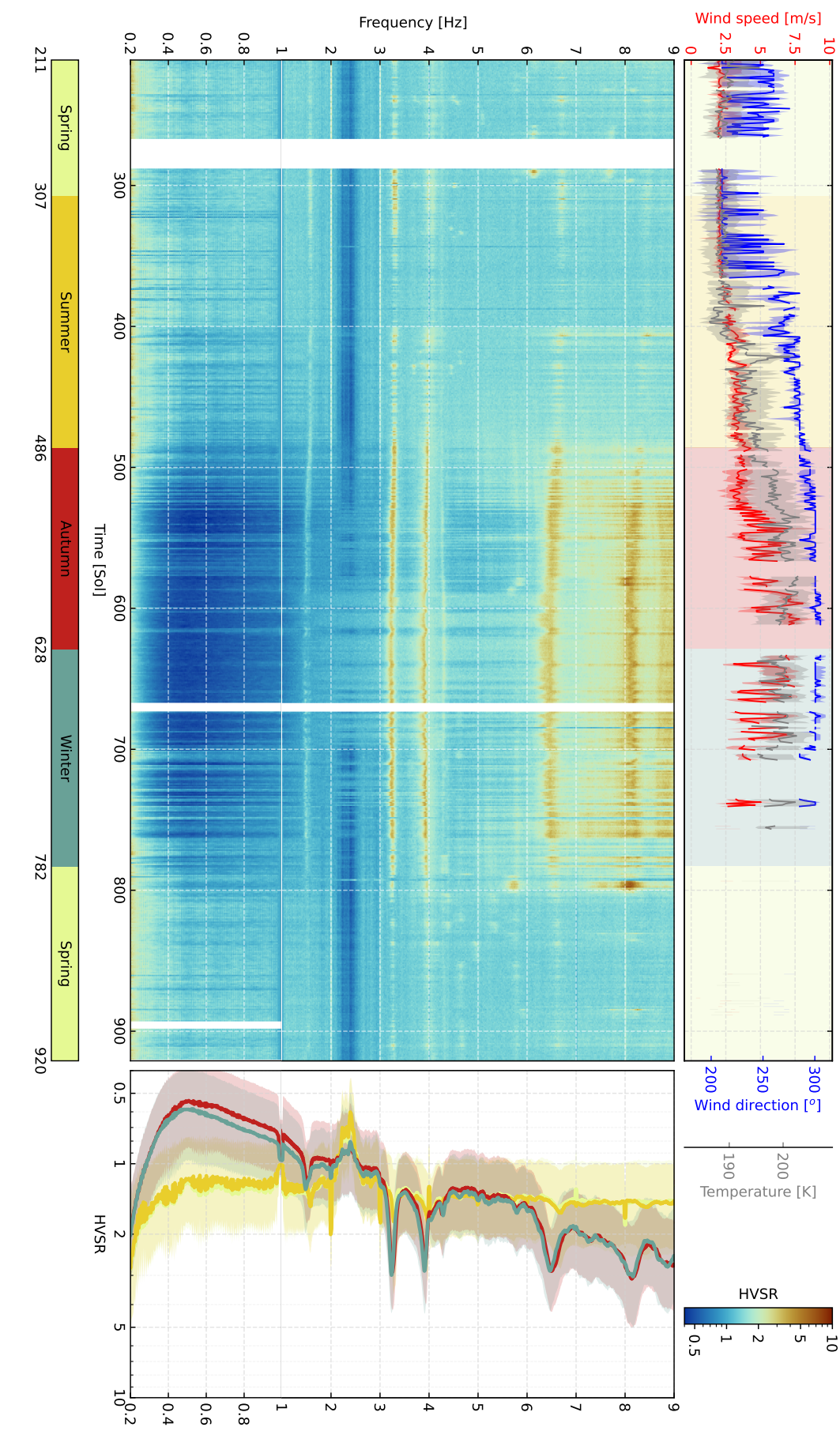


Figure 4.13: Seasonal *HVgram* of Martian ambient vibrations recorded by VBB at 20 sps during the local evening (19:00-23:00 LMST), over a Martian year (sols 210 to 922). **Top**: variation of wind speed (red), wind direction (blue) and temperature (gray) over the Martian year during evening time. **Middle left**: variation of HVSR during evening time between sols 210 and 922, colored by HVSR amplitude. **Middle right**: median HVSR curves for different seasons of the Martian year (see color bar at the bottom).

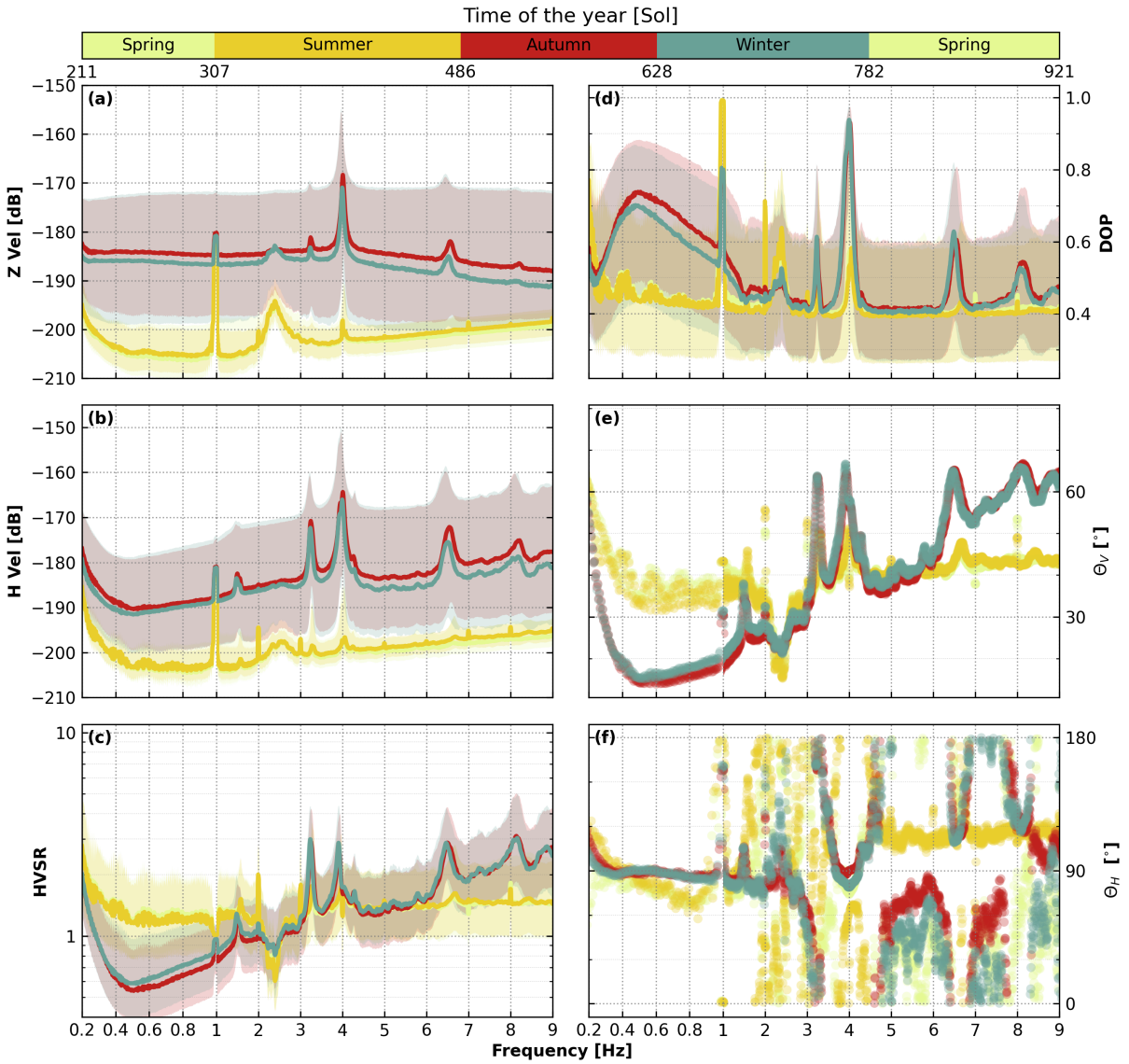


Figure 4.14: Variation of spectral features over a Martian year during local evening (low-noise period, 19:00 - 23:00 LMST). **(a)** Vertical spectra, **(b)** Horizontal spectra, **(c)** HVSR, **(d)** degree of polarization (DOP), **(e)** vertical incidence angle Θ_V (with respect to the vertical) and **(f)** horizontal incidence angle Θ_H (clockwise from the north direction). The median values are shown in each case. The color code is given by the season of the Martian year (color bar at the top).

4.4 Influence of environmental conditions and the lander modes

As suggested above, the wind speed is the primary variable controlling the HVSR curves over the sol and the Martian year. Due to this, the variation of spectral features and HVSR curves under different wind speed levels were analyzed using the VBB data and the available wind data from TWINS (until roughly sol 750). For this, the HVSR curves recorded at a certain wind speed are averaged within 0.25 m/s bins. The variation of HVSR with wind speed is shown in Figure 4.15, where different HVSR amplitudes are obtained for different wind speed levels, indicating the strong influence of the wind on the recordings. The variation of other polarization features is shown in the Appendix A2.3.

By taking different wind speed levels, the overview of spectral features in Fig. 4.16 shows that, for all the frequencies, the vertical and horizontal spectral amplitudes of the Martian ground motion increase as the wind speed increases. As expected, the HVSR curves from different noise levels over a sol, as shown in Section 4.2, can also be associated with different wind speed levels (Fig. 4.16c).

In the low-frequency range (< 1 Hz), the HVSR curve varies from a relatively stable level (at low wind speeds) to a broad trough at high wind speeds. During the low wind speed case (< 2.5 m/s, below the resolution limit of TWINS), the HVSR amplitudes are stable between 0.5 and 1 Hz but start to slowly increase below $\sim$ 0.5 Hz. This slight increase can be related to the larger tilt generated at low frequencies due to the propagation of pressure waves at low wind speeds, according to Sorrells' theory (Sorrells, 1971; Kenda et al., 2017). As shown in Fig. 4.17a for a synthetic subsurface model (see caption for details), at low wind speeds ~ 2 m/s, the tilt due to the propagation of pressure waves is larger than the generated horizontal and vertical ground-motion below ~ 0.4 Hz. Because of this, the HVSR amplitudes would steadily increase towards low frequencies, similar to what is observed from the data (Fig. 4.16). The broad trough observed from the data at high wind speeds between 0.2 and 1 Hz can be explained by the joint effect of the tilt, the horizontal and vertical ground motion at such high wind speeds (Fig. 4.17b). In all these cases, either low or high wind speeds, the tilt is the main contributor to the horizontal motion at low frequencies and thus generating the high HVSR amplitudes.

In the high-frequency range (>1 Hz), the HVSR curve shows different behavior during the different wind levels, characterized by the presence of narrow-band peaks at various frequencies. Such peaks have been identified before, while analyzing the variation of the HVSR over a sol, and have been related to resonances due to the interaction between the lander and the subsurface structure. They have been shown to have a high degree of polarization, to be horizontally polarized and to have larger amplitudes on the horizontal than in the vertical component of the ground motion (Fig. 4.16a, b). In this frequency range, narrow-band peaks around 1.6, 3.2, 4.0, 6.0, 6.8 and 8.5 Hz can be identified. Their horizontal spectral amplitude increase as the wind speed increases but at different rates as the background spectral amplitude. This is, e.g., the case of the resonance at ~ 1.6 Hz, which is clearer at low than high wind speeds (Fig. 4.16b). Or the resonance around 3.2 Hz, which is more distinguishable from the background noise level at low wind speeds (~ 3 m/s) than high wind speeds (> 12 m/s). In any case, the ground motion related to these peaks increase with wind speed, suggesting a non-natural origin.

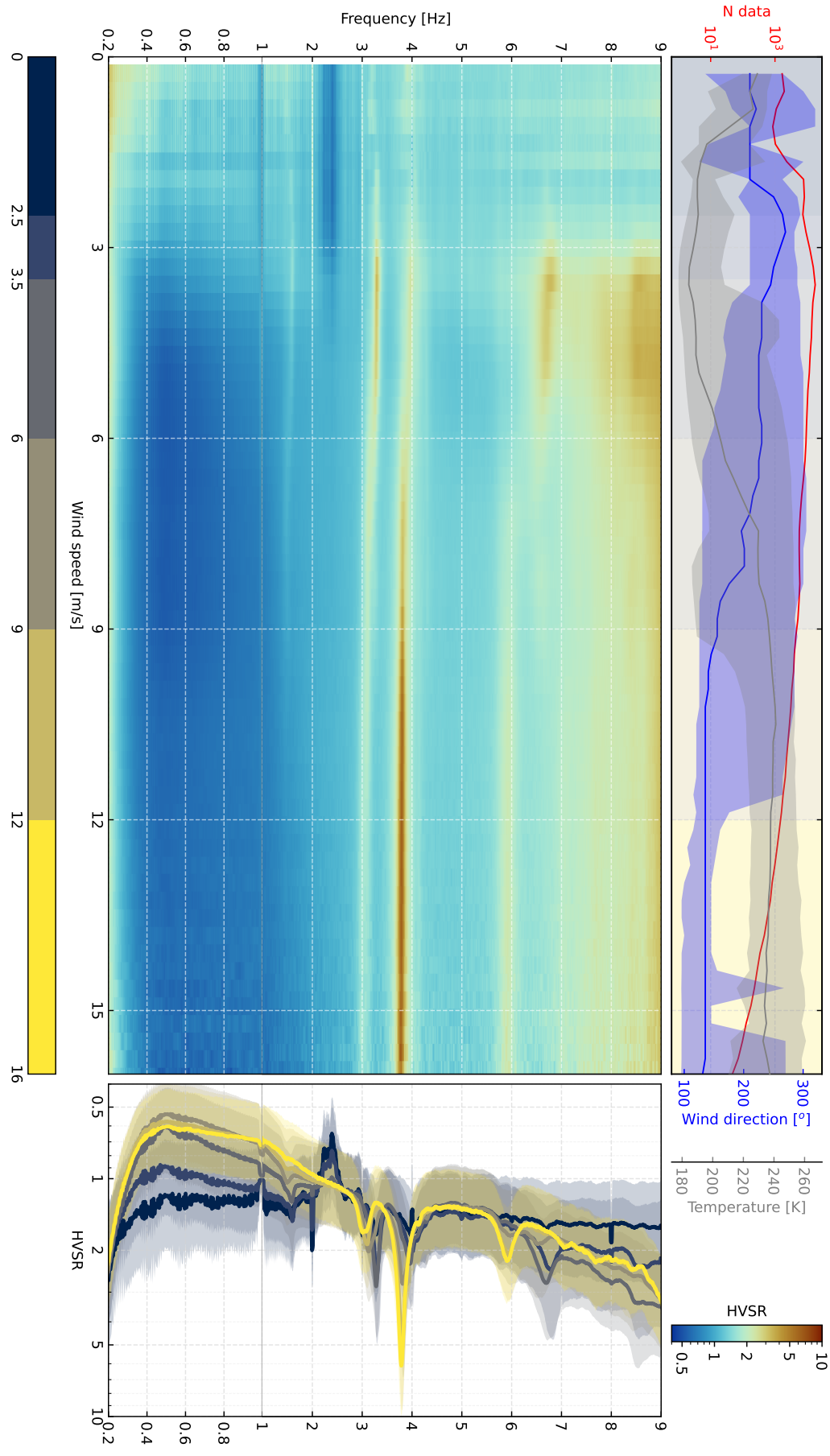


Figure 4.15: *HVgram* of Martian ambient vibrations recorded by VBB at 20 sps as a function of wind speed. **Top**: number of wind speed measurements (red), average wind direction (blue) and average temperature (gray) for given wind speed. **Middle left**: variation of HVSR with wind speed. **Middle right**: median HVSR curves for different wind speed levels (see color bar at the bottom).

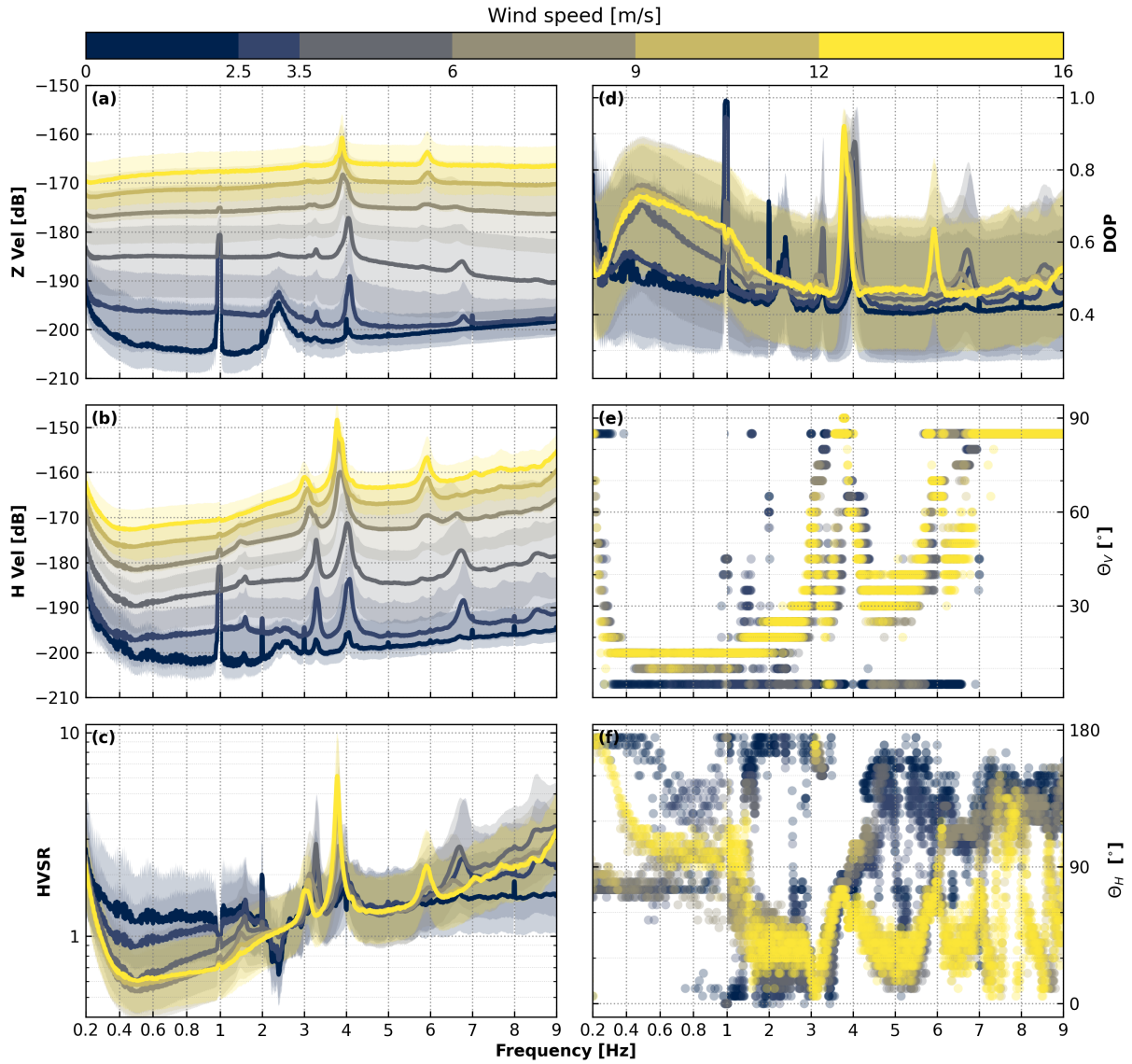


Figure 4.16: Influence of wind speed on spectral features. **(a)** Vertical spectra, **(b)** Horizontal spectra, **(c)** HVSR, **(d)** degree of polarization (DOP), **(e)** vertical incidence angle Θ_V (with respect to the vertical) and **(f)** horizontal incidence angle Θ_H (clockwise from the North direction). The median values are shown in (a)-(d) whereas the modes are shown in (e)-(f). The color code is given by the different wind speed levels (color bar at the top).

Furthermore, different frequency peaks can be seen in the HVSR at certain wind speed levels while not in others (Fig. 4.16c). For example, a clear peak around 5.8 Hz is observed for wind speeds above 12 m/s, which is not observed for wind speeds between 3.5 and 6 m/s. In this latter wind speed range, a peak around 6.8 Hz is observed instead. These different peaks are interpreted as the same lander-related resonant mechanism, whose resonance frequency is shifted due to a temperature effect. This thermal phenomenon can be inferred from the variation of the horizontal spectral amplitudes over a sol, as calculated during the northern autumn and winter (sols 478 to 776), when high enough wind speeds are recorded, so the lander modes are excited over the whole sol (Fig. 4.18b). Here, in a certain frequency range, the maximum spectral amplitudes are recorded at frequencies varying with a similar pattern as the temperature changes over the sol (Fig. 4.18a),

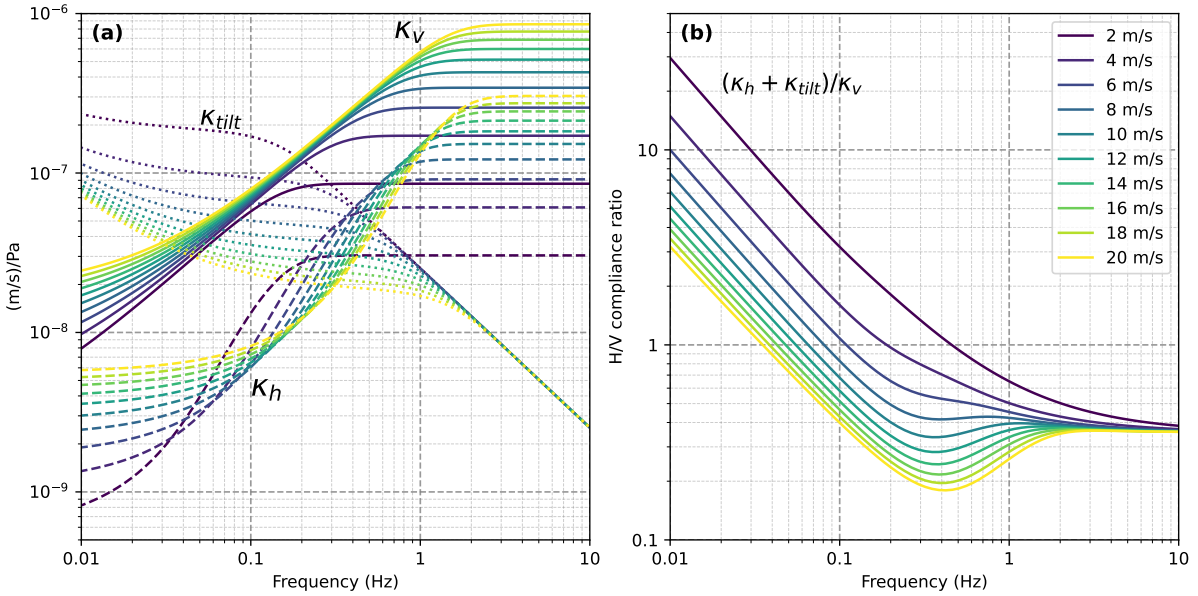


Figure 4.17: Effect of compliance in seismic recordings. **(a)** Compliance (spectral amplitudes normalized by pressure) of vertical, horizontal and tilt ground-motion, following Sorrells (1971) and Kenda et al. (2017). **(b)** Theoretical H/V spectral ratios due to compliance at different wind speeds, considering the effect of the tilt on the horizontal component. For this, a simple model was used consisting of one layer (5 m thick) over a half-space. The P-wave, S-wave velocity and density are 198 m/s, 118 m/s and 1300 kg/m^3, for the top layer, and 926 m/s, 512 m/s and 3000 kg/m^3 for the half-space.

as shown in Fig. 4.18b where the maximum horizontal spectral amplitudes are tracked using the reversed temperature pattern. Similarly, this frequency shift is also revealed by the close-to-linear relation between air temperature for certain frequency ranges, as shown in Fig. A2.3. From these figures, it can be inferred that the frequency of the resonant mechanism decreases as the environmental temperature increases. Nevertheless, this close-to-linear relation reaches a limit where there is no further variation of the resonant frequency with increasing temperature, as revealed by the mismatching between maximum spectral amplitudes and temperature pattern between 12:00 and 16:00 LMST in Fig. 4.18b, for instance, around 6 Hz, or for high temperatures (>240 K) in Fig. A2.3b.

Hence, five resonant mechanisms can be related to the lander, covering the following frequency ranges: (i) 1.45-1.7 Hz, (ii) 3.1 - 3.3 Hz, (iii) 3.8 - 4.1 Hz, (i) 5.8 - 6.7 Hz and (v) 6.7 - 8.5 Hz. The excitation of these non-natural resonances contaminates the HVSR curves due to their mechanical origin and thus do not represent the local subsurface structure. In addition, the steady increase of HVSR amplitude for frequencies above ∼6 Hz can be understood as the mechanical noise generated by the interaction of high Martian winds with the InSight lander and the WTS, as proposed by Murdoch et al. (2017). In this case, the horizontal ground response to the wind is expected to be greater than the vertical one due to propagation of shear stress (Naderyan et al., 2016; Lott et al., 2017). This broadband HVSR shape is not directly related to the subsurface structure. Indeed, Mucciarelli et al. (2005) showed that high wind speeds enhance the horizontal components, likely explained by flow rotation near the soil and the instrument, leading to unreliable H/V peaks at high frequencies. No lander modes have been identified for frequencies below 1 Hz, where the effect of propagating pressure waves is dominant.

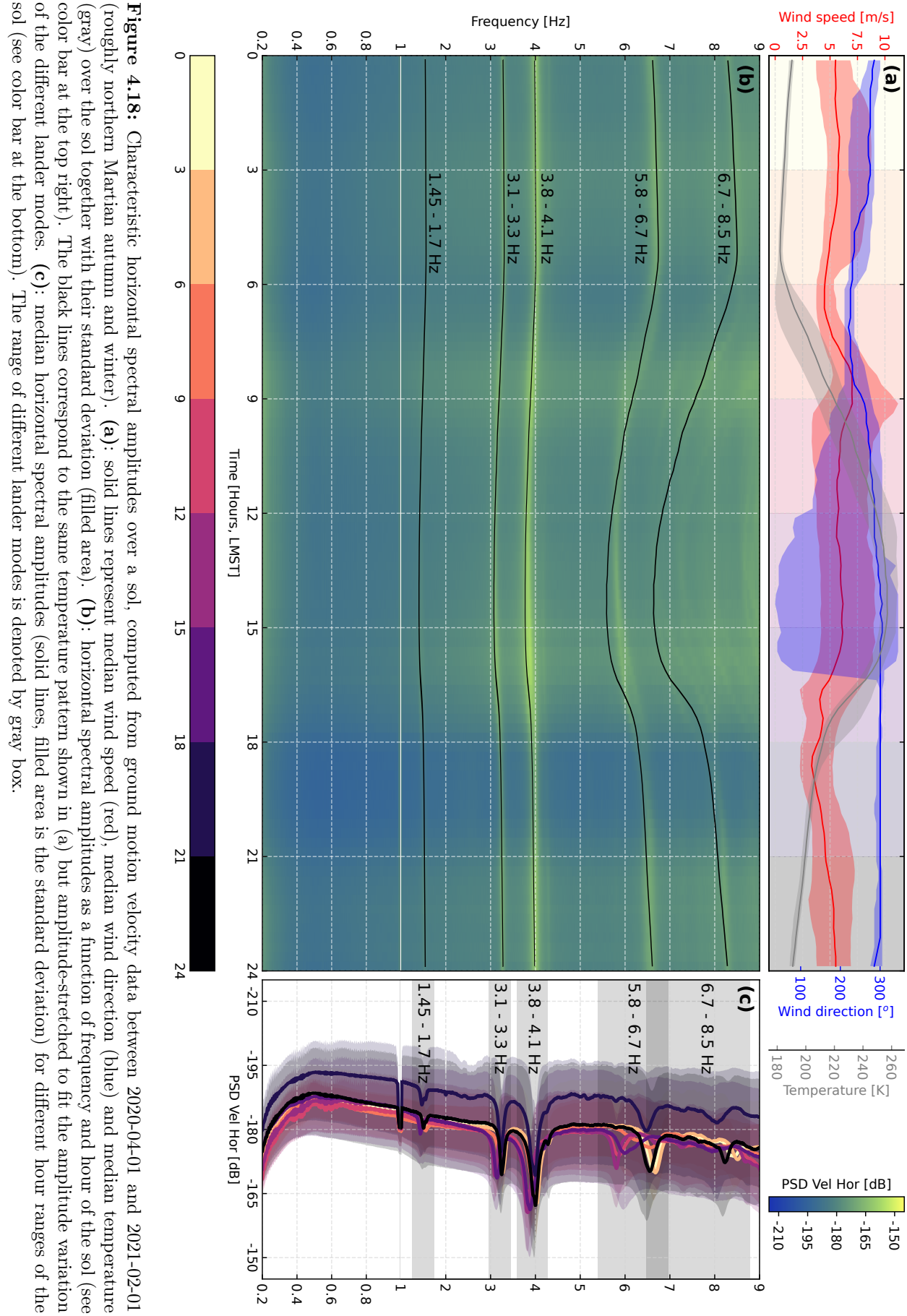


Figure 4.18: Characteristic horizontal spectral amplitudes over a sol, computed from ground motion velocity data between 2020-04-01 and 2021-02-01 (roughly northern Martian autumn and winter). **(a)**: solid lines represent median wind speed (red), median wind direction (blue) and median temperature (gray) over the sol together with their standard deviation (filled area). **(b)**: horizontal spectral amplitudes as a function of frequency and hour of the sol (see color bar at the top right). The black lines correspond to the same temperature pattern shown in (a) but amplitude-stretched to fit the amplitude variation of the different lander modes. **(c)**: median horizontal spectral amplitudes (solid lines, filled area is the standard deviation) for different hour ranges of the sol (see color bar at the bottom). The range of different lander modes is denoted by gray box.

Another remarkable feature observed on the HVSR and power spectral curves is the so-called 2.4 Hz resonance. This mode is mainly observed on the vertical component of the ground motion during low wind speed periods when the recorded spectral amplitudes are close to the instrumental self-noise of VBB. It can also be noted on the vertical spectra at high wind speed levels, e.g., during autumn/winter evenings (Fig. 4.14a) or for wind speeds between 3.5 and 6 m/s (Fig. 4.16a). However, as the wind speed increases, the vertical amplitude of the 2.4 Hz resonance increases at a lower rate than the background noise level. This is revealed by the less prominent (but still visible) peak at relatively high wind speeds (3.5-6 m/s), compared to the more noticeable peak at low wind speeds (Fig. 4.16a). Therefore, the dependence on the wind speed is similar to the 1.6 Hz resonance, but it is, in general, less dependent than the other lander modes. Besides, unlike the lander modes, the 2.4 Hz mode has an almost vertical incidence angle during the low wind speed periods ($\Theta_V \sim 0$, Fig. 4.16e) whereas no variation with temperature has been observed. These characteristics suggest a completely different origin or source. Because of these features, the 2.4 Hz might be understood as a resonance related to the subsurface structure.

For the purpose of this work, this characterization of the lander modes is enough to assess the convenience of using the HVSR from ambient noise recordings. Further discussion and investigation about the lander modes can be found in Dahmen et al. (2021b) and Hurst et al. (2021).

4.5 Summary and concluding remarks

In summary, the HVSR curves obtained from the ambient vibrations recorded during different times of the Martian year, of the sol and under different environmental conditions offer little (or no) information to perform a classical HVSR analysis.

On the one hand, the spectral amplitudes recorded during the low-noise period (evenings during the northern summer/spring or low wind speed periods) likely correspond to the instrument self-noise (either SP or VBB). Namely, the amplitudes generated by the excitation of the local subsurface structure lie below the self-noise level of the instruments and thus the obtained HVSR has no structural information. In the best case, the frequency range 0.5-3 Hz could be interpreted to have a natural origin and be related to the underground structure. This includes the 2.4 Hz resonance, as suggested by its nearly vertical incidence, low dependence on the wind speed and apparent no variation with temperature.

On the other hand, during *noisy* periods, e.g., during the local daytime or high wind speed periods, the vertical and horizontal spectra (and consequently the HVSR curves) start to get distorted due to the influence of the wind. Particularly, a broad trough below 1 Hz is the result of the tilt and vertical and horizontal ground motions generated by pressure waves propagating at high wind speeds. Above 1 Hz, the so-called lander modes are excited and contaminate the recordings. These are a set of resonant modes with nearly horizontal incidence, spectral amplitudes strongly driven by the wind speed and a temperature-dependent resonant frequency. They are generated by the interaction between the environmental conditions, the subsurface structure and the InSight lander. As the wind speed increases, these resonances are clearly strongly excited and contaminate the spectra. Besides, larger horizontal than vertical ground motions are recorded at high frequencies (> 5 Hz), likely due to the propagation of shear stress.

In all these cases, the HVSR curves cannot be directly related to the subsurface structure because they do not correspond to its self-resonance. Instead, further parameters must be involved and different theoretical approaches, like compliance theory or precise modeling of the wind-lander interaction, must be used. Another possibility is to investigate the HVSR obtained from the coda of Martian seismic events, as presented in the next chapter.

CHAPTER 5

Shallow subsurface structure from Martian seismic events HVSR

The variability assessment performed in Chapter 4 discourages using Martian ambient vibrations for HVSR analysis and subsequent inversion for the shallow subsurface structure. As presented in Chapter 2, the coda waves of seismic events are expected to be under the diffuse regime and, thus, the characteristic horizontal-to-vertical spectral ratio (HVSR) of the InSight landing site can be derived from them. This chapter presents the HVSR analysis based on the coda of Martian seismic events, together with the non-linear inversion of the resulting HVSR curve. The shallow subsurface structure obtained from the inversion is interpreted in terms of the geological information available and some implications are provided. The results and interpretations of this chapter are part of the following publications:

1. **Carrasco, S.**, Knapmeyer-Endrun, B., Margerin, L., Schmelzbach, C., Onodera, K., Pan, L. *et al.* (2023). *Empirical HVSR spectral ratios at the InSight landing site and implications for the Martian subsurface structure*. Geophysical Journal International, 232(2), 1293–1310. doi:10.1093/gji/ggac391.

2. Menina, S., Margerin, L., Kawamura, T., Lognonné, P., Marti, J., Drilleau, M., ..., **Carrasco, S.** *et al.* (2021). *Energy Envelope and Attenuation Characteristics of High-Frequency (HF) and Very-High-Frequency (VF) Martian Events*. Bulletin of the Seismological Society of America, 111(6), 3016–3034. doi:10.1785/0120210127.

5.1 HVSR from the coda of Martian seismic events (eHV)

5.1.1 The Martian seismic events

After the ambient vibrations have been discouraged from being used for HVSR analysis (Chapter 4), the coda of the Martian seismic events is of main interest for its computation, especially as it is expected to be in the diffuse field regime (e.g., Shapiro et al., 2000; Margerin et al., 2009).

To this end, Martian seismic events with quality A and B detected between March 2019 and 2021 September 30, as reported in the MQS catalog V9 (InSight Marsquake Service, 2022), were used. In order to properly cover the frequency range between 0.4 and 10 Hz, the LF, BB, 2.4HZ, HF and VF events are analyzed. Only SF events were excluded due to the absence of clear phases and their short duration. In total, 139 seismic events were used to compute the HVSR curve, from which the 2.4 Hz events are the most abundant, as shown in Table 5.1. In the same way, the 100 sps channels (SP and VBB) were preferred whenever they were available. Otherwise, the 20 sps channels were used.

The VF events are of special interest for this study as they contain energy well above 5 Hz, which allows shallower depths at the ILS to be mapped. Even though quality A VF events have not been reported by the MQS, there are 21 VF events with quality B (see Table 5.1). As shown in Table 5.1, VBB data at 100 sps are available for ten VF events whereas SP data at 100 sps are available for nine events, with just one of them being recorded simultaneously by both SP and VBB.

	Events			*Recordings*			
	QA	QB	**Total**	VBB@20sps	VBB@100sps	SP@20sps	SP@100sps
LF	4	9	**13**	13	2	3	5
BB	2	6	**8**	8	2	2	2
2.4HZ	0	46	**46**	46	7	27	20
HF	0	51	**51**	49	12	27	22
VF	0	21	**21**	20	10	7	9
Total	6	133	**139**	136	33	66	58

Table 5.1: Summary of Martian seismic events used for HVSR computation as reported by MQS as of September 30th, 2021. The events are differentiated by event type as classified by MQS. The two main columns indicate the number of events identified by the MQS and the number of events recorded either by VBB or SP at different sampling rates.

5.1.2 Diffuse coda waves on Mars

One of the strongest assumptions behind using the full-wavefield diffuse field approach (DFA) with the HVSR from coda waves is the hypothesis of them being in a diffuse regime and that energy equipartition occurs. The latter is difficult to confirm from single-station measurements because of the spatial derivatives involved in the definition for P-wave and S-wave energies, for which array measurements are needed (e.g., Shapiro et al., 2000; Hennino et al., 2001). Nevertheless, some proxies from single-station measurements allow interpretating the coda waves being under a diffuse regime.

Initial analysis of the InSight data showed that, for the event S0128a, there is a stabilization of the V^2/H^2 quotient during the event signal, compared to the same quotient obtained from the pre-event data window (Lognonné et al., 2020). This has been interpreted as characteristic of multiply-scattered short-period wavefield (e.g., Hennino et al., 2001). Besides, the ratio between the East and Horizontal energy (E^2/N^2) is close to 1, the theoretical value for a diffuse wavefield. More recently, a thorough investigation of the diffusive properties of Martian seismic events has been performed by (Menina et al., 2021). They show that the coda wave envelopes of HF and VF events can be well modeled by envelopes using elastic radiative transfer theory, which is suitable for explaining diffuse fields. This supports the idea that the characteristics of Martian events can be explained by multiple scattering of elastic waves generated by internal sources.

Furthermore, the VF and HF events have been shown to be depolarized and so it is their coda waves (van Driel et al., 2021; Menina et al., 2021). In this sense, the low degree of polarization can be considered another characteristic of a diffuse wavefield, where the ground motion occurs in all directions without preference (and therefore, it is *diffuse*). These diffuse-like observations can be revealed, for example, during the event S0794a (Fig. 5.1), where the HVSR (analogous of V^2/H^2 as in Lognonné et al. (2020)) is stabilized in the coda window as well as most of the signals are depolarized, especially below 10 Hz. This is different from what is observed before the event, where polarized signals are observed between 5 and 10 Hz.

All these observations support the idea of using the coda of Martian seismic events to derive the characteristic HVSR of the InSight landing site and invert the measurements under the full-wavefield DFA.

5.1.3 *eHV* determination

The HVSR of the Martian seismic events (eHV) was obtained in a similar way as the ambient vibrations, but based on the phase picks provided by the MQS. For events with quality A and B, the MQS provides the times of the P- and S-wave onsets and also includes the times of the characteristic background seismic noise before the event (Clinton et al., 2021). The HVSR of the S-wave coda, according to this catalog, was computed. The duration of this coda window is variable and is provided by the MQS such that it is a good representation of the S-wave coda and free of non-seismic perturbations (e.g., glitches). The HVSR computation was performed using consecutive 20 s data windows with an overlap of 50%.

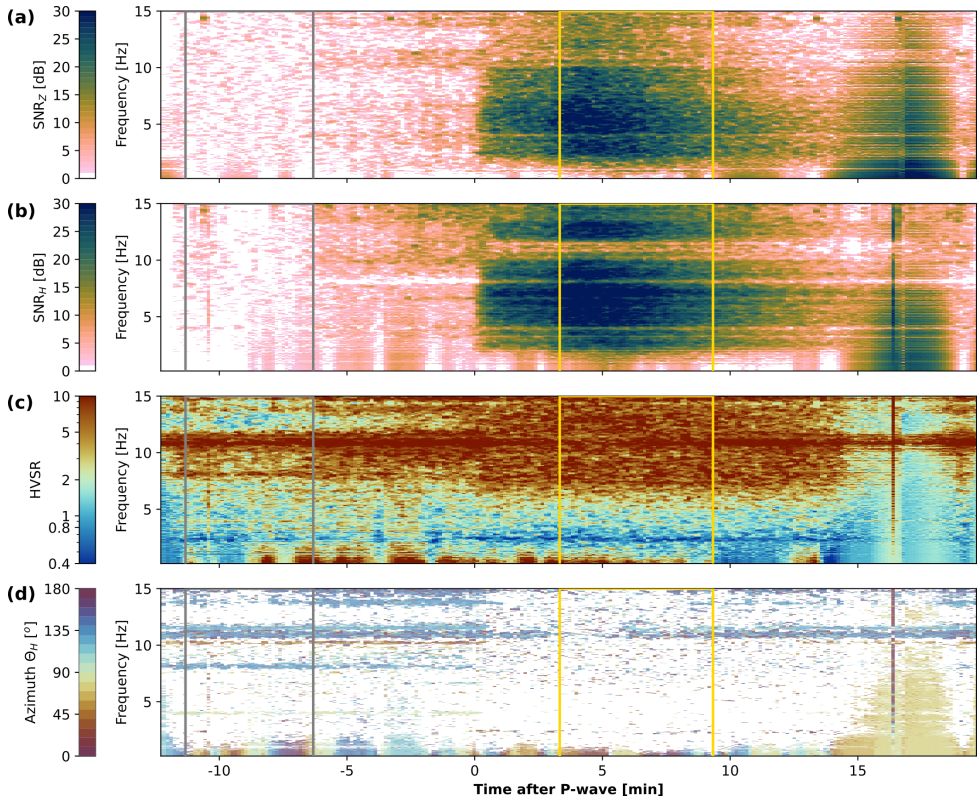


Figure 5.1: Spectral and polarization attributes of the S0794a event. From top to bottom: (a) Temporal variation of vertical spectral signal-to-noise ratio (SNR_Z), (b) Temporal variation of horizontal spectral signal-to-noise ratio (SNR_H), (c) Temporal variation of HVSR before and during the event, (d) Temporal variation of horizontal incidence angle (Azimuth Θ_H) of incoming signals with degree of polarization $dop > 0.7$. The x-axis is the time with respect to the observed P-wave arrival (t_P = 2012-02-19 01:26:23 UTC). The signal-to-noise ratios are computed with respect to the pre-event noise window illustrated as a gray box. A 6-min time window starting at the S-wave arrival and comprising a large part of the coda waves is shown as a yellow box.

For each event and sensor, the vertical spectral signal-to-noise ratio (SNR_Z) was computed using the median power of the vertical component of the coda and the pre-event noise windows. As each type of seismic event excites different frequencies (Fig. 5.2), using a pre-defined frequency range for different event types is meaningless because there might be frequencies that are not excited by some seismic events. Thus, for each sensor, a single event HVSR (eHV) curve is derived as the median of all the segments with SNR_Z larger than 2 dB. The DFA-HV curve is expected to be less smooth than the classical HVSR approach, which typically implements a Konno–Ohmachi smoothing window (Konno and Ohmachi, 1998). Because of this, a visual inspection and manual smoothing following the median of the final eHV is performed in order to also discard any contamination due to lander resonances.

In order to check the SP and VBB differences revealed by the ambient vibrations data, two strong VF events independently recorded by VBB (event S0794a) and SP (event S0756a) are also shown. Both events carry seismic energy above 1 Hz, but especially above 10 Hz (Fig. 5.2). They share HVSR similarities between 1 and 10 Hz, but there are striking differences above 10 Hz. The HVSR obtained from the VBB recordings presents

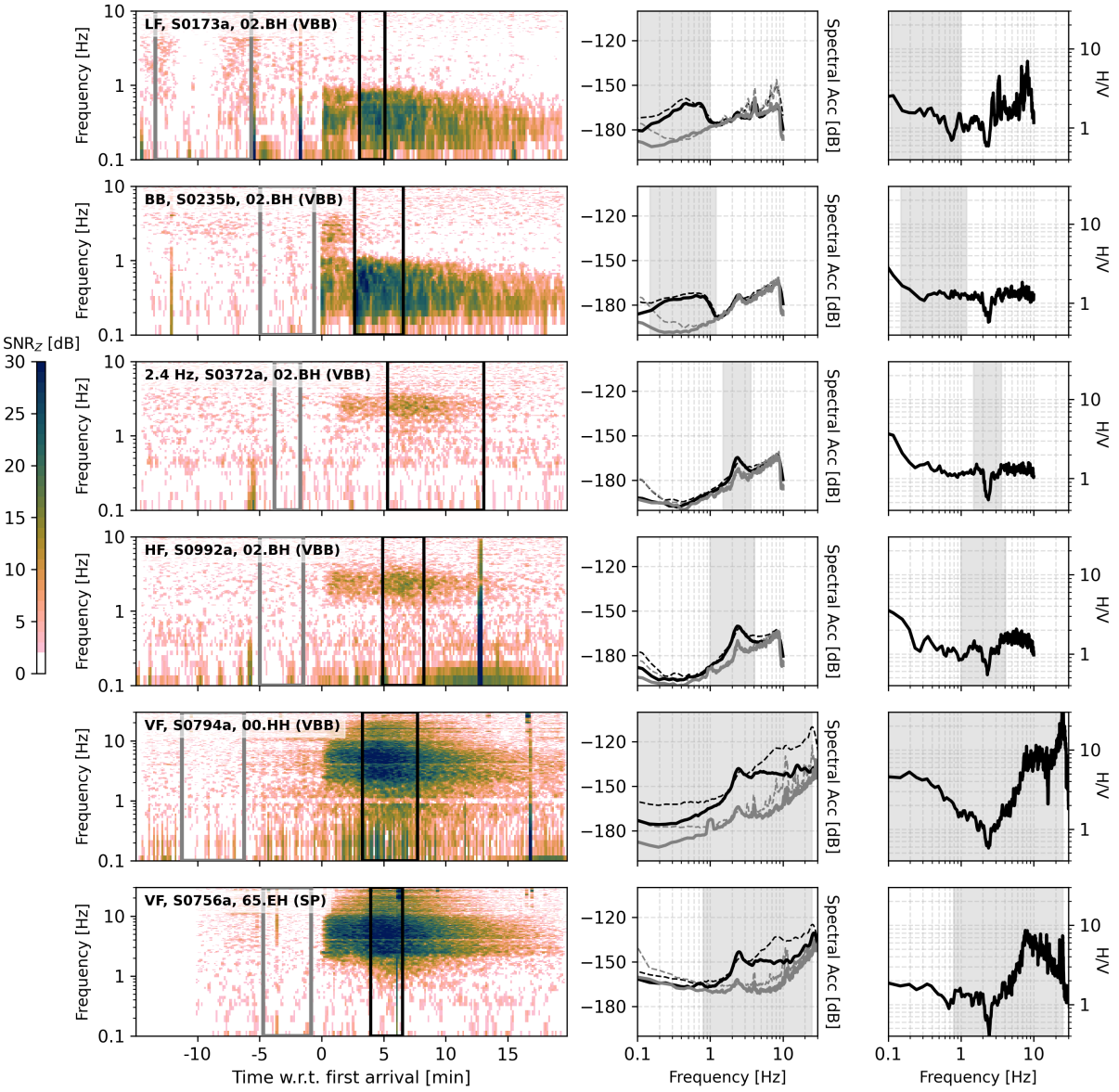


Figure 5.2: Spectral characteristics of different classes of Martian seismic events. From top to bottom: LF (S0173a), BB (S0235b), 2.4 Hz (S0372a), HF (S0992a) and VF (S0794a and S0756a) class. Data from VBB at 20 sps (02.BH) illustrate the characteristics of the LF, BB, 2.4 Hz and HF classes. The VF class is represented by two events independently recorded by VBB (00.HH) and SP (65.EH) at 100 sps. For each event, the SNR_Z is plotted as a function of time, where a characteristic noise and S-wave coda window are indicated as grey and black boxes, respectively. In the second column, the vertical (solid) and horizontal (dashed) spectral power of the S-wave coda signal is compared to the characteristic noise window. The black solid line represents the HVSR computed under the DFA approach. The shaded rectangular areas indicate the frequencies covered by the different types of events. Taken from Carrasco et al. (2022).

a plateau-like shape followed by a strong peak at around 25 Hz, whereas the SP recording reveals a decay towards higher frequencies.

The origin of the VF events, which shape the HVSR curve above 5 Hz, remains unknown, so the observed waveforms and different HVSR curves might be influenced by the environmental conditions. Nevertheless, during the occurrence of both VF events,

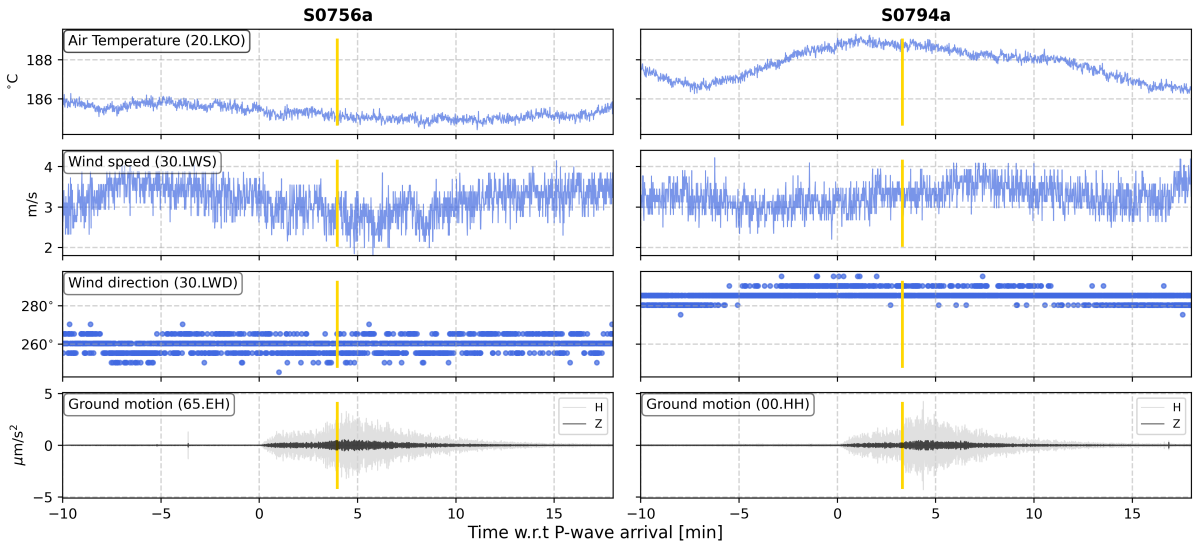


Figure 5.3: Environmental conditions during two large VF events: S0756a (left) and S0794a (right). From top to bottom: air temperature, wind speed, wind direction, vertical acceleration and horizontal acceleration. The vertical (black) and horizontal (grey) ground-motion recordings are bandpass-filtered between 6 and 9 Hz. The vertical yellow line indicates the S-wave arrival time for each event. Taken from Carrasco et al. (2022).

no major environmental changes related to the first arrival of the seismic energy or to the proposed S-wave arrival are observed (Fig. 5.3). This allows the conclusion that the HVSR curves of the VF events are unrelated to the environmental conditions. Also, the seismic events studied here originated at relatively large distances ($> 10°$), so the seismic source can be excluded as a determining feature.

The median HVSR curve for both SP and VBB sensors was computed separately (Fig. 5.4). As the DFA-HV computation leads to unsmoothed curves, a manual smoothing following the resulting median HVSR curve was applied, as shown in Fig. 5.4, which allowed mitigating the effect of lander modes such as the 4.1 Hz resonance. Due to the lack of events with enough energy above the noise, the *eHV* curve for the SP sensor is unreliable for frequencies below ∼2 Hz. Therefore, given the target frequency range between 0.4 and 10 Hz, the preferred *eHV* curve is obtained from the VBB recordings.

Although there are only a few events with energy well above the ambient noise for frequencies above 10 Hz, the HVSR differences between SP and VBB are still notable, similar to what was derived from the ambient vibrations data. Thus, this discrepancy phenomenon is most likely related to the instruments themselves. The reason behind this SP-VBB difference is still unclear but seems to be related to the amplification of the vertical components above 10 Hz. When compared to the horizontals, the VBBZ seems to deamplify the ground motion in the frequency range roughly between 10–35 Hz (see Fig. 4.12), whereas the SP sensor reveals similar amplitudes between SPZ and SPH, especially for frequencies above 5 Hz, where the instrument response is flat (Lognonné et al., 2019). The SP sensor was designed to record ground motion at high frequencies, so it would be preferable here. Nevertheless, as the VBB and SP sensors are placed in different spots on the SEIS Leveling system (LVL, Lognonné et al., 2019), a possible reason for the SP recording larger vertical ground motions is that it could be exposed to larger vertical

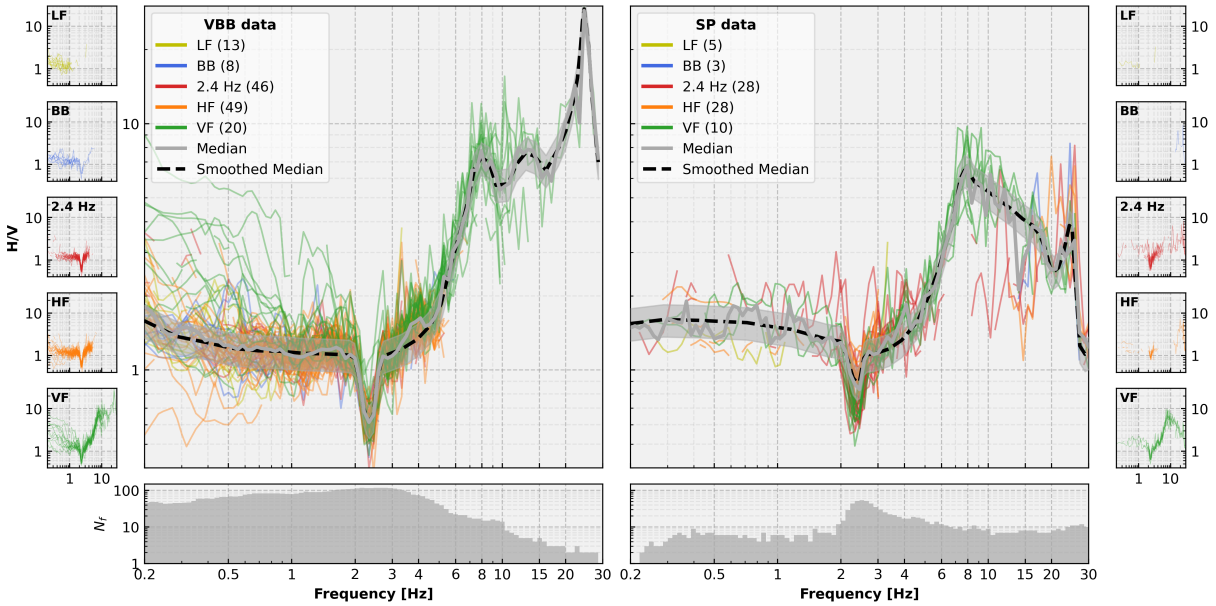


Figure 5.4: Summary of events HVSR (*eHV*). HVSR curves derived from Martian seismic events recorded by VBB (left) and SP (right) with vertical SNR larger than 2 dB. The curves are colored according to different types of marsquakes. The median and smoothed median HVSR are denoted by the continuous grey and dashed black lines. The grey areas illustrate the smoothed median ±15% uncertainty range. The bottom plots indicate the amount of marsquakes with SNRZ > 2 dB per frequency (Nf). Separate HVSR curves for each type of seismic event are also plotted with their corresponding color. Taken from Carrasco et al. (2022).

motions due to rotation of SEIS (Fayon et al., 2018). Due to the persistent incompatibility of VBB and SP recordings at high frequencies (>10 Hz), both from ambient vibrations or seismic events data, using the HVSR curves at high frequencies is dismissed for any further analysis.

Finally, for frequencies below 10 Hz, the VBB HVSR curve is chosen to be the representative *eHV* curve for the InSight landing site, which has a characteristic trough at around 2.4 Hz and a strong peak at around 8 Hz.

5.1.4 Comparison between *nHV* and *eHV*

Once the horizontal-to-vertical spectral ratios have been calculated from the ambient vibrations (*nHV*) and the Martian seismic events data (*eHV*), it is worth comparing and discussing the resulting curves. Clear differences are observed between the VBB *nHV* and *eHV* curves, as shown in Fig. 5.5. On Earth, despite some differences, a generally good agreement between the *nHV* and *eHV* curves is typically observed (e.g., Parolai et al., 2004; Pilz et al., 2009; Rivet et al., 2015). Napolitano et al. (2018) suggested the differences between *nHV* and *eHV* curves can be related to an effect of the local topography. The InSight landing site is however mostly flat, without complex topography in the surroundings. Thus, the difference between the recorded *eHV* and *nHV* curves can be hardly related to a topographical effect. Rather, the reason for the difference between *nHV* and *eHV* is different for the quiet and noisy periods.

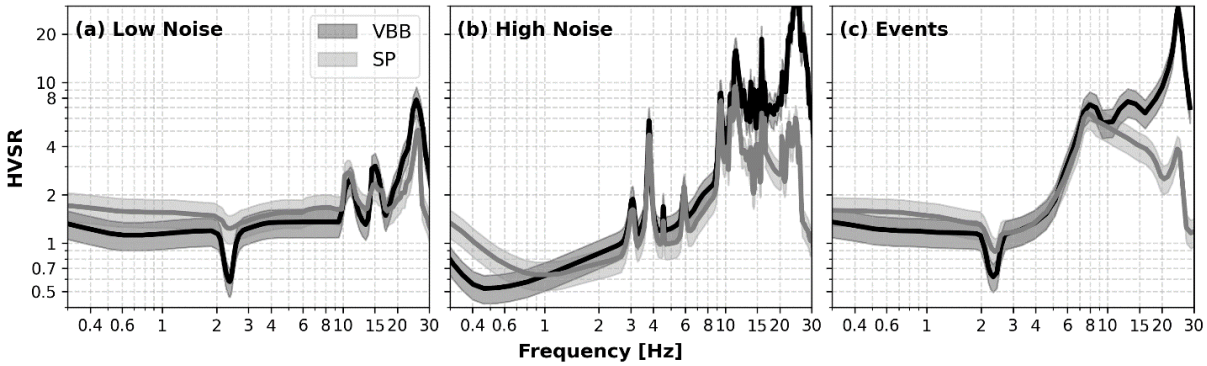


Figure 5.5: HVSR curves for three different contexts at the InSight landing site as recorded by VBB (black) and SP (grey). **(a)** Low noise: mainly recorded during the Martian evening and night, with wind speeds lower than ~ 2.8 m/s. **(b)** High noise: typically recorded during the Martian daytime, when high wind speeds (> 5 m/s) are recorded. **(c)** Events: collection of early S-wave coda of the best recorded Martian seismic events. Taken from Carrasco et al. (2022).

In the low-noise period, the *nHV* is similar to the *eHV* curve at frequencies below ~4 Hz, including the trough around 2.4 Hz. Above 4 Hz, the *eHV* presents a strong peak around 8 Hz that is not visible during the low-noise *nHV* curve. Following the discussion in Section 4.2.1 in Chapter 4, this difference might be caused by VBB most likely recording the instrumental self-noise at frequencies between 5 and 14 Hz. These observations suggest that, at least during the quietest period of a Martian sol, there is either an absence of energy coming from seismic waves propagating through the InSight landing site or the corresponding seismic energy is lower than the instrument self-noise of the SEIS instruments. Due to the proximity and shape similarity of VBBZ to the theoretical self-noise, there is a risk of measuring the corresponding self-noises during this time period and, thus, the obtained HVSR curve might be not representative of the subsurface structure, as has been experienced in some Earth cases (e.g., van Ginkel et al., 2020).

During the quietest period of a Martian sol, the potential sources of noise at the InSight landing site are minimized due to the low wind speeds (Mimoun et al., 2017; Murdoch et al., 2017), so the instrument self-noise is likely recorded either on the horizontal or vertical components. Velocity variations in the frequency range between 6 and 9 Hz have been observed, especially during the quiet periods. These variations are evidenced only on the horizontal (north and east) but not on the vertical component and can be understood as the thermo-elastic perturbation of the Martian regolith sensed by a seismic wavefield (Compaire et al., 2022). Consequently, even if the horizontal ground motion recorded during the quiet period is generated by the propagating seismic wavefield, it is unreliable to retrieve any information related to the subsurface structure from the HVSR curves because the vertical component is likely dominated by the instrument self-noise.

During mid- and high-noise periods, the differences between the *eHV* and the *nHV* curves are caused by different factors. The high-frequency signals recorded during these windy times, especially in the high-noise period, are above the instrumental noise, so they can be interpreted as actual ground-motion signals. The strong winds excite frequencies around 3.3, 4.1 and 6.9 Hz, which coincide with the lander modes investigated by Dahmen

et al. (2021b). Stronger excitation of frequencies around 11, 15, 20 and 25 Hz, which likely have a mechanical origin due to the interaction between the wind and the lander, are also observed. In the high-noise period, many of the narrow peaks are also related to the lander resonances, for example, 3.0, 3.8 and 5.8 Hz. These are the same lander modes observed during the mid-noise period, but their eigenfrequencies are shifted because of the daily variation due to temperature changes (Dahmen et al., 2021b). A similar behavior is observed at higher frequencies, where the frequencies around 11, 15, 20 and 25 Hz are strongly excited and shifted.

In definitive, the influence of the lander is highly visible on the *nHV* curves during mid- and high-noise periods. Between 1 and 10 Hz, even though these *nHV* curves also show an increase towards higher frequencies (Fig. 5.5b), its shape is different (less steep) than the preferred VBB *eHV* curve (Fig. 5.5c). For instance, the HVSR amplitude at 8 Hz is lower on the high-noise *nHV* (~ 2) than the *eHV* (~ 8). Thus, the VBB *eHV* curve is preferred for the inversion of the subsurface structure instead of any of the *nHV* curves. In particular, the VBB *eHV* is suitable for the HVSR inversion under the diffuse field approach because of the high diffusivity and strong multiple-scattering revealed for the Martian crust (Lognonné et al., 2020; Menina et al., 2021; van Driel et al., 2021). These phenomena lead to a diffuse seismic coda, where a combination of scattered body and surface waves is expected and therefore the full-wavefield DFA is a good representation.

5.2 Non-linear inversion of *eHV*

Since the InSight landing, some attempts have been made to reveal the subsurface structure at the InSight landing site. First, the SEIS recordings of the hammering sessions of the HP^3 (Heat Flow and Physical Properties Package) experiment were used to derive the seismic wave velocities in the first tens of centimeters below the ground surface (Brinkman et al., 2019; Lognonné et al., 2020). A re-evaluation of this data has determined the P-wave velocity to be 119 ± 29 m/s and the S-wave velocity to be 61 ± 20 m/s in the first $\sim$40 cm of the shallowest layer (Brinkman et al., 2022). Kenda et al. (2020) derived a subsurface model based on ground-motion compliance (the surface response to atmospheric pressure loading) measurements, which was extended by Onodera (2022), who proposed a model with a single discontinuity at $\sim$1 m depth in the first $\sim$75 m of the subsurface below the lander, corresponding to the Martian regolith over a layer of coarse blocky material. In addition, Hobiger et al. (2021) proposed a subsurface model to explain the surface wave ellipticity features that they observed between 1 and 5 Hz. They propose a buried low-velocity layer (bLVL) sandwiched between older and younger lava flows to explain a trough in the ellipticity curve. The model is proposed to span down to $\sim$200 m depth, but it lacks resolution in the first 20 m below the surface. A model with better resolution at shallow depths can be obtained by evaluating the HVSR curve over a broader range of frequencies, so frequencies between 0.4 and 10 Hz and a different approach (DFA) are used in this study.

The *eHV* curve (hereafter, the final HVSR and renamed as *fHV*) is chosen to be a good representation of the HVSR response of the subsurface structure at the InSight landing site. This *fHV* curve is aimed to be inverted to retrieve a 1-D shear-wave velocity

model (V_s) using the diffuse field approach. The inversion scheme can be divided into two parts: the theoretical HVSR forward modeling and the non-linear inversion procedure.

5.2.1 HVSR forward modeling under DFA

Given a 1-D layered subsurface model (including P- and S-wave velocities, density and thickness of each layer), the theoretical HVSR spectral curve under the DFA can be computed from the corresponding Green's functions (GFs), following Eq. 2.5 in Chapter 2. In this work, the HVSR is calculated using the technique developed by Margerin (2009), which consists of the summation of the generalized eigenfunctions of the layered elastic medium (see Section 3.2.2). This technique is implemented via an open-source code that has been already successfully applied to terrestrial data (e.g., Margerin et al., 2009; Galluzzo et al., 2015).

The code calculates the vertical and horizontal spectral energies for each P, S, Love and Rayleigh waves individually, so the contribution of body and surface waves can be separately derived. The HVSR curve for the full wavefield, including the contribution of all the types of waves, can also be obtained. Given the diffuse nature of the seismic coda used for the *eHV* curve, the full-wavefield HVSR curve is used as the forward theoretical prediction to explain the interpreted signal of the *eHV* curve at the Insight landing site. This differs from Hobiger et al. (2021), as they use the fundamental mode of the Rayleigh wave only to explain the HVSR measured on the Rayleigh-wave part of the ambient vibrations (i.e., the ellipticity).

5.2.2 Inversion algorithm and parametrization

In order to find the best subsurface models explaining the observed *fHV* curve, the Neighbourhood Algorithm (NA) was implemented, which was developed by Sambridge (1999) and adjusted for this particular case by Wathelet (2008). This technique was implemented via the *dinver* toolbox included in the Geopsy package (Wathelet et al., 2020). The NA is suitable for this type of inversion due to the intrinsic non-uniqueness problem of the HVSR curves, i.e., without further information or constraints, the same HVSR curve can be explained by different subsurface models (e.g., Piña-Flores et al., 2016). In this way, the NA provides an efficient exploration of the parameters space in order to retrieve different subsurface models that properly fit the HVSR curve.

The NA makes use of the misfit between observed and theoretical HVSR curves to explore the area of the parameter space where the models with low misfits are expected. The misfit function ϕ_{hv} is defined as follows:

$$\phi_{\mathrm{hv}}(\mathbf{m}) = \sqrt{\frac{1}{N}\sum_{i=1}^{N}\frac{\left(\log\left(\frac{H}{V}_{\mathrm{m}i}\right) - \log\left(\frac{H}{V}_{\mathrm{d}i}\right)\right)^2}{\sigma_{\mathrm{d}i}^2}}, \tag{5.1}$$

where $\mathbf{m}$ is the evaluated model, N is the number of frequency points of the observed ($\frac{H}{V}_{\mathrm{d}}$) and full-wavefield modelled ($\frac{H}{V}_{\mathrm{m}}$) curves. $\sigma_{\mathrm{d}i}$ is the standard deviation of the $\frac{H}{V}_{\mathrm{d}}$ curve at a given frequency. Following Lontsi et al. (2015), a logarithmic misfit

was implemented in order to avoid overweighting strong peaks in the HVSR curve. After the parameters space is explored with the NA, for a given parameters setting, a number of best models with the misfit around the global minimum are selected as the possible models explaining the observed *fHV* curve.

Only the shear-wave velocity structure was inverted, as it has been demonstrated to be the main parameter affecting the HVSR curve (e.g., Malischewsky and Scherbaum, 2004; Bonnefoy-Claudet et al., 2006). For the inversion, the parameters space explored by the NA is bounded by the prior knowledge based on the pre-landing model, as presented in Section 2.1.6 in Chapter 2. This pre-landing model, based on the size range of rocky ejecta craters and exposures in nearby fracture zones, suggests a transition from the shallow regolith to a coarse ejecta layer, followed by a fractured basaltic layer and a deeper pristine basaltic unit (Golombek et al., 2017; Knapmeyer-Endrun et al., 2017; Warner et al., 2017). Based on the size range of the rocky-ejecta craters and ghost craters, previous mapping suggests that the basalt layer has a thickness of $\sim$ 170 m thick near the landing area (Warner et al., 2017; Golombek et al., 2018; Pan et al., 2020) and are underlain by sedimentary rocks likely of Noachian age (Pan et al., 2020).

Thus, based on the pre-landing model for the first 50 m, the parameter space is defined for a model with four layers over a half-space (4LOH). The results of the inversion are affected by this constraint such that a different number of layers will likely lead to different solutions. Table 5.2 presents the value ranges of the parameter spaces explored in the different inversion runs. Further details on these values are explained below.

The inversion of the HVSR curve alone, without further observations, has been demonstrated to be heavily affected by the non-uniqueness phenomenon (e.g., Piña-Flores et al., 2016). Therefore, constraining the parameter space is relevant for obtaining the proper model. So far, the best new constraints of the inversion are the shear wave velocities obtained from the hammering experiment (Lognonné et al., 2020; Brinkman et al., 2022), determined to be lower than 80 m/s at the surface, and the thickness of the shallow regolith layer, expected to be no deeper than 10 m (Golombek et al., 2020b,a). Due to the expected compaction, the S-wave velocity of the first layer is modeled as a power law increase. Because the HVSR inversion is not very sensitive to variations in density, this parameter is fixed for each layer, as well as the V_p/V_s ratio. This way, the P-wave velocity is derived from the inverted S-wave velocity. In particular, for the shallowest layer, V_p/V_s

	Bottom depth [m]	V_S [m/s]	Density [kg/m^3]	V_p/V_s
Layer 1	0-10	Top: 40 - 80 Bottom: 70 - 300	1350	1.87
Layer 2	3-30	100 - 2000 (1000, 1500)	2000	1.73
Layer 3	5-60	100 - 2000 (1000, 1500)	2900	1.73
Layer 4	10-100	100 - 2000 (1000, 1500)	2900	1.73
Half-space	-	200 - 2000 (1000, 1500)	3300	1.73

Table 5.2: Range of values defining the parameter spaces to be explored during the inversion of the *fHV* curve. The values in parenthesis correspond to the maximum shear-wave velocity for the small (S) and medium (M) parameter spaces, respectively. Density and V_p/V_s are fixed for each layer.

= 1.87 was used, as reported by Brinkman et al. (2022), and $\rho = 1350$ kg/m^3, following the pre-landing assessment of this site (Morgan et al., 2018). This V_p/V_s lies in the range 1.68–2.56 for dry unconsolidated material, as shown by investigations on Earth samples and also derived for the Lunar regolith (e.g., Uyanik, 2010; Dal Moro, 2015). The density and V_p/V_s of the deeper layers are set to standard values of volcanic regions on Earth (e.g., Lesage et al., 2018).

Regarding the deeper layers, in volcanic areas on Earth, the shear wave velocities of basaltic layers have been shown to range from 500 to 2000 m/s at shallow depths (Delage et al., 2017). On the other hand, an unexpected low-velocity layer should be placed at larger depths to explain the 2.4 Hz resonance (Hobiger et al., 2021). A large parameter space was explored, with shear wave velocities between 100 and 2000 m/s extending down to 100 m. In particular, different inversion runs were performed with different maximum shear wave velocities of 1000 (small), 1500 (medium) and 2000 m/s (large model).

As shown in Fig. 5.5, the target *fHV* has a strong peak at around 8 Hz and a steep left flank leading to a narrow trough at around 2.4 Hz. No clear peaks or troughs are observed at low frequencies between 0.4 and 2 Hz. For each frequency, a common uncertainty range of 15% of the HVSR amplitude was set. For each 4LOH parameters space presented in Table 5.2 (S1, M1, L1), a total of $\sim$ 45000 models were explored using the NA, for which three different inversion runs were performed in order to have a better search of the models fitting the *fHV* curve. For each parameter space, the best-fitting models with a misfit lower than 0.3 were chosen, from which 200 random models are plotted in Fig. 5.6. This way, three different subsets of models that fit the *fHV* curve well can be identified. The best misfit of these models is obtained from the M1 inversion runs (0.242). However, an overall good fitting of the *fHV* curve is obtained for models with misfit values lower than 0.3, and thus, all these models can be a good representation of the subsurface structure.

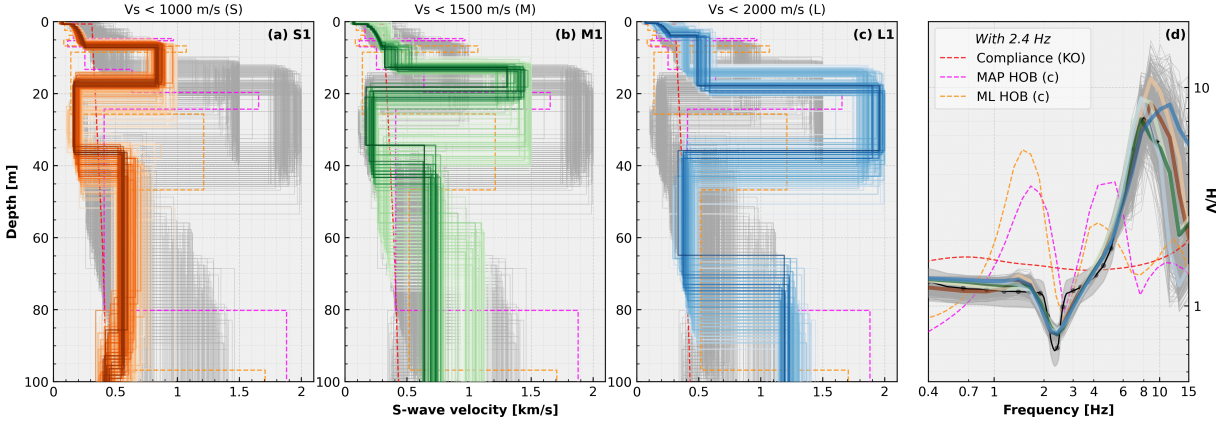


Figure 5.6: Sets of models obtained from the inversion of the *fHV* curve, between 0.4 and 10 Hz, using different parameter spaces. 200 best random models are plotted for each of the three parameters space explored: (a) S1 (small, orange), (b) M1 (medium, green) and (c) L1 (large, blue). For each parameter space, the models with the darkest colors indicate a best (lower) misfit. (d) Synthetic full wavefield HVSR response of the different models drawn in subfigures (a)–(c). Two representative models from each parameter space are plotted following the corresponding color pattern. Besides, the constrained MAP and ML models from Hobiger et al. (2021) and the model derived from ground compliance measurements (Onodera, 2022), together with their corresponding synthetic full-wavefield HVSR response, are plotted as magenta, yellow and red dashed lines, respectively. Taken from Carrasco et al. (2022).

5.3 Implications for the subsurface structure

5.3.1 Models from *fHV* inversion

Some similarities and differences can be highlighted from the comparison of the S1, M1 and L1 models (the SML1 models) in Fig. 5.6a-c. They all present a characteristic shallow high-velocity layer (SHVL) followed by a buried low-velocity layer (bLVL) with a sharp contrast between the SHVL and the bLVL. The latter bLVL has been proposed to cause the 2.4 Hz resonance due to seismic waves trapped in this low-velocity layer (Hobiger et al., 2021). Against the pre-landing subsurface models, the bLVL in the resulting models of this work, as well as Hobiger et al. (2021), is an unexpected feature of the subsurface structure. A similar sharp contrast is expected between the SHVL and the subsurface structure above, which can be understood as the mechanism to generate the 8 Hz peak on the *eHV* curve. The bLVL is followed by a faster half-space, which has lower velocities than the SHVL and, therefore, represents a less sharp discontinuity.

The bLVL of the L1 models is in good agreement with the bLVL proposed by Hobiger et al. (2021) to explain the 2.4 Hz trough. Nevertheless, in the L1 case, the units below the bLVL have relatively lower velocities than the SHVL whereas, in the Hobiger et al. (2021) models, the bLVL is followed by a layer with velocities even higher than the SHVL, which generates an HVSR peak between 1 and 2 Hz that is not observed from the SEIS data, as shown in Fig. 5.6d. The models arrive at different velocities and thicknesses of each layer, which is a demonstration of the non-uniqueness problem of the HVSR inversion. In general, depending on the thickness and velocity of the SHVL, the bLVL will be placed at shallower or larger depths with a thickness between 15 and 25 m and a velocity ranging between 100 and 500 m/s. In any case, a generic subsurface pattern of a bLVL below a SHVL is required to simultaneously generate an HVSR peak around 8 Hz and trough around 2.4 Hz.

These results suggest the features of the *fHV* curve can be explained by the full wavefield rather than by a single type of wave. In particular, the 2.4 Hz resonance is not derived from the fundamental Rayleigh mode (see Fig. 5.7). Instead, this resonance is closely coinciding with a P-wave resonance. Similarly, the HVSR peak around 8 Hz is a product of the full wavefield, closely related to a resonance of the surface waves and particularly the Rayleigh waves (Fig. 5.7).

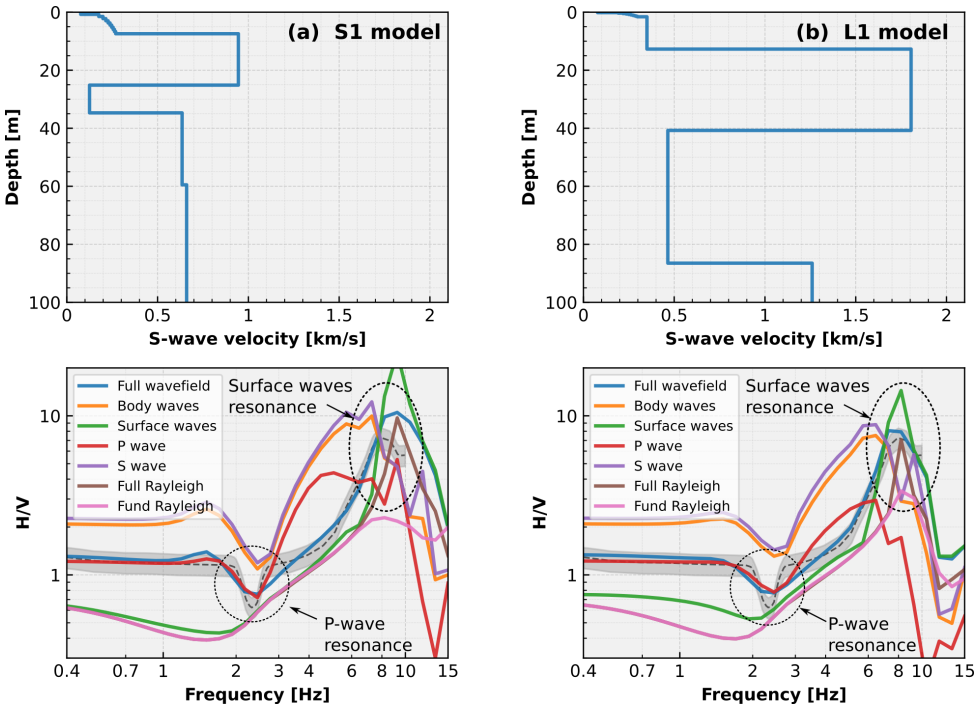


Figure 5.7: Theoretical HVSR curves for two characteristic models obtained from the SML1 inversion results. **Left:** HVSR curves for an exemplary S1 model. **Right:** HVSR curves for an exemplary L1 model. The HVSR curves are plotted for: the full wavefield (blue), body waves (orange), surface waves (green), P waves (red), S waves (magenta) and Rayleigh wave including all available modes (brown) and Fundamental mode only (pink).

Geological interpretation of the SML1 models

For the L1 models, the bLVL coincides with what has been proposed to be a geological unit sandwiched between Early Hesperian to Early Amazonian basalt flows, which may have a sedimentary origin (Hobiger et al., 2021). The SHVL then corresponds to the Early Amazonian basaltic lava flows ($\sim$ 1.7 Ga, Warner et al., 2017; Wilson et al., 2019). Meanwhile, the half-space below the bLVL must be either a layer within the Early Amazonian or the Early Hesperian basalt lava flows (Warner et al., 2017; Hobiger et al., 2021).

Crater statistics suggest significant erosion and landscape degradation between an Early Hesperian volcanic surface (3.6 Ga) and the early Amazonian effusive volcanism (1.7 Ga), which is estimated to be $\sim$140 m thick (Warner et al., 2022). Furthermore, throughout the dichotomy boundary between the southern Noachian highlands and the northern plains, there are Noachian through Hesperian transition units that indicate active erosion and deposition of sedimentary materials (Tanaka et al., 2014; Pan et al., 2017, 2020). To the south of the InSight lander, some of the Amazonian–Hesperian transition units are sedimentary deposits (Pan et al., 2020) as well as the Medusae Fossae Formation (Tanaka et al., 2014). In addition, alluvial activity has occurred further south in Gale crater during this period (Grant et al., 2014; Grant and Wilson, 2019). Given this evidence for aqueous activity in the geological record, it is possible that there was both erosion of the Early Hesperian surface and deposition of sedimentary deposits prior to the deposition of the Early Amazonian basalt flows.

If Early Hesperian lava flows are beneath the bLVL, these rocks would be expected to be more fractured by impact cratering due to the higher cratering rate of the Hesperian (e.g., Hartmann and Neukum, 2001) or longer exposure to the surface; and to be more altered by aqueous activity than the Early Amazonian volcanics. The expected greater physical and chemical weathering of the basalt flows in Early Hesperian presents a reasonable explanation for the relatively lower seismic velocities of the half-space beneath bLVL compared to the SHVL.

In the case of the S1 and M1 models, the bLVL is located at shallower depths ($<$ 40 m) and the corresponding SHVL right above it is a thin and fast layer. Although these models cannot be completely discarded, the thin SHVL and the extremely low velocities of the bLVL, considering the effects of the overburden pressure, seem unlikely and disfavor these models. Nevertheless, if the SHVL had higher velocities, its thickness would also increase and therefore the bLVL would be placed at larger depths. In any case, the thickness of the bLVL would range between 15–25 m, which is less than the $\sim$50 m thickness proposed by Hobiger et al. (2021).

There is a lack of resolution for the structure above the SHVL because the higher frequencies were excluded from the analysis. For instance, by taking a characteristic L1 model and considering the 8 Hz peak is related to the discontinuity between 10 and 20 m depth, then the minimum depth of investigation can be estimated as $z_{min} \simeq 10$ m (with $< v_s >^a \simeq 400$ m/s and $f_{max} = 10$ Hz, in Eq. 2.6). Nevertheless, the inversion of compliance measurements suggests the regolith layer is most likely about 1 m thick and everything below is associated with coarse blocky ejecta material (Onodera, 2022). This shallow interface would generate an HVSR peak between 25 and 30 Hz, which is out of the frequency range here investigated. An HVSR peak at these frequencies is hardly observed from the data due to the strong excitation of a highly polarized resonance at this frequency range (see Figs 4.3 and 4.6 in Chapter 4), which might be related to the LSA (Hurst et al., 2021). This shallow discontinuity between the regolith and the coarse ejecta layer cannot be discarded. Therefore, the top of the SHVL is likely below the coarse ejecta layer and does not correspond to the regolith interface.

5.3.2 Alternative model without 2.4 Hz trough

The inversions above were performed assuming the origin of the 2.4 Hz resonance is related to the subsurface structure. In fact, this has not yet been proven and the mechanism for generating this resonance remains unclear. An interesting observation is that this trough is clearly observed from seismic noise data and also from seismic events data, which is in contradiction to previous observations on Earth, where the effect of a bLVL on the HVSR curve has been observed to be less visible in the noise data than the events (Di Giacomo et al., 2005; Panzera et al., 2015). Because of this, a second round of *fHV* inversions was performed, using the same parametrization but simultaneously fitting the frequency ranges between 0.4–2 and 3–10 Hz, so the 2.4 Hz is ignored. Once again, three parameter spaces are explored and are analogously referred as S2, M2 and L2 models (SML2) and illustrated in Fig. 5.8 in the same way as for the SML1 models in Fig. 5.6.

From these new inversion runs, the non-uniqueness problem is still apparent, so it is difficult to provide one single model for the subsurface structure. The SML2 models are analogous to the SML1 models. However, some interesting features can be highlighted. In both sets of models, the SHVL is required for modeling the strong 8 Hz peak and low velocities below it are needed. Nevertheless, in the SML2 models, the velocity contrast between the SHVL and the underlying bLVL is less sharp than those derived for the SML1 models. Thus, the presence of a bLVL is likely, even when the 2.4 Hz trough is ignored. The difference between generating a 2.4 Hz resonance and not will depend on the sharpness of the contrast between the SHVL and the bLVL.

Consequently, the geological interpretation of the SML2 models is similar to the interpretation of the SML1 models. The main difference lies in the properties of the bLVL such that a weaker bLVL will generate the 2.4 Hz resonance due to the sharp contrast with respect to the SHVL, whereas a more consolidated bLVL will properly model the *fHV* curve without the 2.4 Hz trough.

Lower velocities are required immediately below the SHVL to model the *fHV* curve, with or without the 2.4 Hz trough. Figure 5.9a shows that models without a clear bLVL (lightest colors) will also generate an HVSR peak around 8 Hz, but with a larger amplitude and a poor fitting of the left-flank decay. Besides the SHVL, in order to fit both peak and decay, a bLVL is required, which becomes an essential feature to explain the whole *fHV* curve. As shown in Fig. 5.9b, if the layer below the bLVL has higher relative velocities, then a secondary peak at lower frequencies, not observed from the data, would be generated. Therefore, general low velocities are required below the SHVL.

The lower velocities below the SHVL can be explained by the presence of a sedimentary layer and the differences in the physical weathering process between the Early Hesperian and Early Amazonian lavas. This difference between the shallow Amazonian and deeper Hesperian layers is always required, either for the SML1 or SML2 models, as it allows for the characteristic steep left flank of the *fHV* curve.

Another relevant aspect is the different velocity ranges explored in the parameter spaces of the SML1 and SML2 models. On Earth, Lesage et al. (2018) studied the velocity profiles for different volcanic areas, including andesitic and basaltic deposits, and they found that shear-wave velocities lower than 500 m/s are typically observed in the first 50 m depth. In a similar way, Panzera et al. (2015) compared a stratigraphic

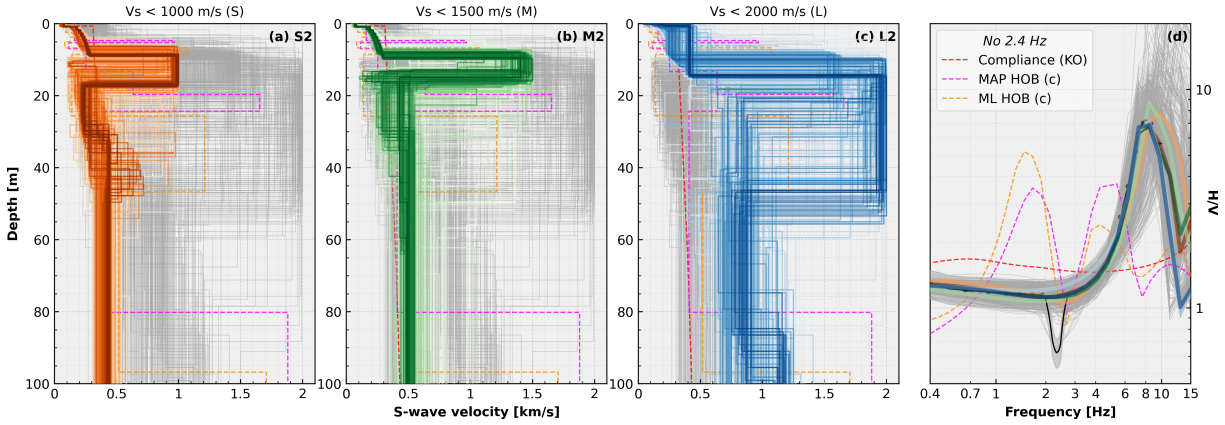


Figure 5.8: Sets of models obtained from the inversion of the *fHV* curve in two different frequency ranges, between 0.4–2 and 3–10 Hz, using different parameter spaces. 200 best random models are plotted for each of the three parameters space explored. The color patterns and other features are analogous to Fig. 5.6. Taken from Carrasco et al. (2022).

sequence from borehole data with the velocity model derived from HVSR inversion for a site near Mt. Etna. They associated shear-wave velocities between 500–1000 m/s with the corresponding basaltic layer underneath. These regions on Earth share some similarities with western Elysium Planitia (Golombek et al., 2017, 2020b). Under this context, the velocities obtained for models S1 and S2 are well within the expected range of shallow velocities in a volcanic region. Assuming these lower velocities, the thickness of the SHVL would be no greater than 15 m, which falls in the reasonable range of basaltic lava flow thicknesses. Nevertheless, shear-wave velocities around 2000 m/s have been obtained from laboratory experiments for basaltic rock samples under the influence of confining pressure (e.g., Vinciguerra et al., 2005). Also, differences between the shear wave velocities derived from indirect seismic and lab samples have been revealed (Lesage et al., 2018). Therefore, an SHVL with higher velocities, likely thicker, is still possible.

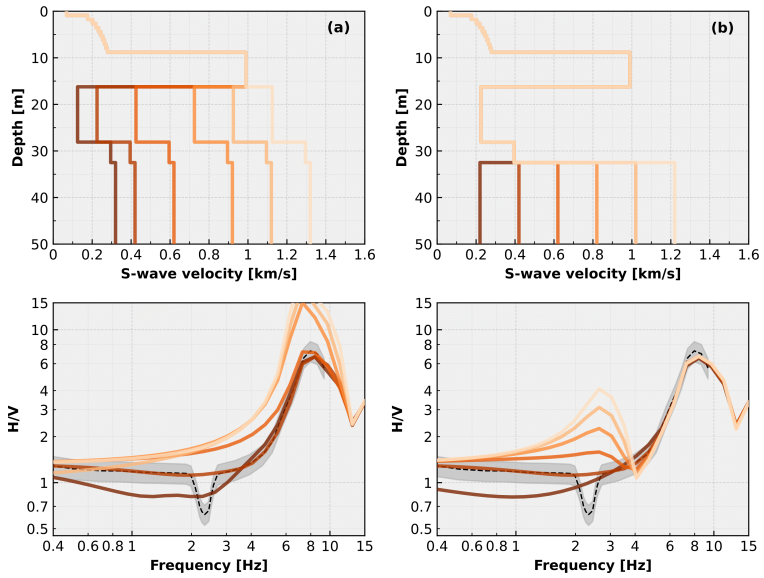


Figure 5.9: Synthetic modeling of HVSR using different velocity profiles below the SHVL. **(a)** Different overall velocities below the SHVL. **(b)** Fixed bLVL velocity and varying velocity of the half-space below. Taken from Carrasco et al. (2022).

5.4 Compatibility with compliance observations

Besides the HVSR analysis, the ground compliance is an independent observation that can help to understand the first tens of meters underneath the InSight landing site. In this regard, Onodera (2022) computed the ground compliance using the SEIS and pressure data for a large set of convective vortices in the nearby region. The inversion under a Bayesian approach of this data set allowed him to provide a most likely model consisting of a thin shallow regolith (∼1 m thick) followed by a coarse ejecta layer without further discontinuities below (see Figs. 5.6, 5.8 and 5.10), at least down to ∼75 m.

The models proposed in this work differ from the compliance inversion models because the first few meters of the subsurface structure at the InSight landing site are unresolved, whereas compliance data is highly sensitive to the shallow depths close to the surface. Nevertheless, the models proposed in this work are constrained by the velocities derived from the hammering experiment, which are in good agreement with those from the compliance inversion.

In order to assess the validity of models proposed in this work in terms of the observed ground compliance, among the best-fitting models, one model representing each S1, M1, L1 and S2, M2, L2 model subsets is chosen, for which their synthetic ground compliance response is calculated, following the same approach as in Onodera (2022). The characteristic models and their synthetic compliance are plotted in Fig. 5.10.

The synthetic compliance shows that the models proposed here generate a compliance response that fits well within the error range of the measurements. Because of this, the rejection of models based on compliance measurements can be hardly carried out.

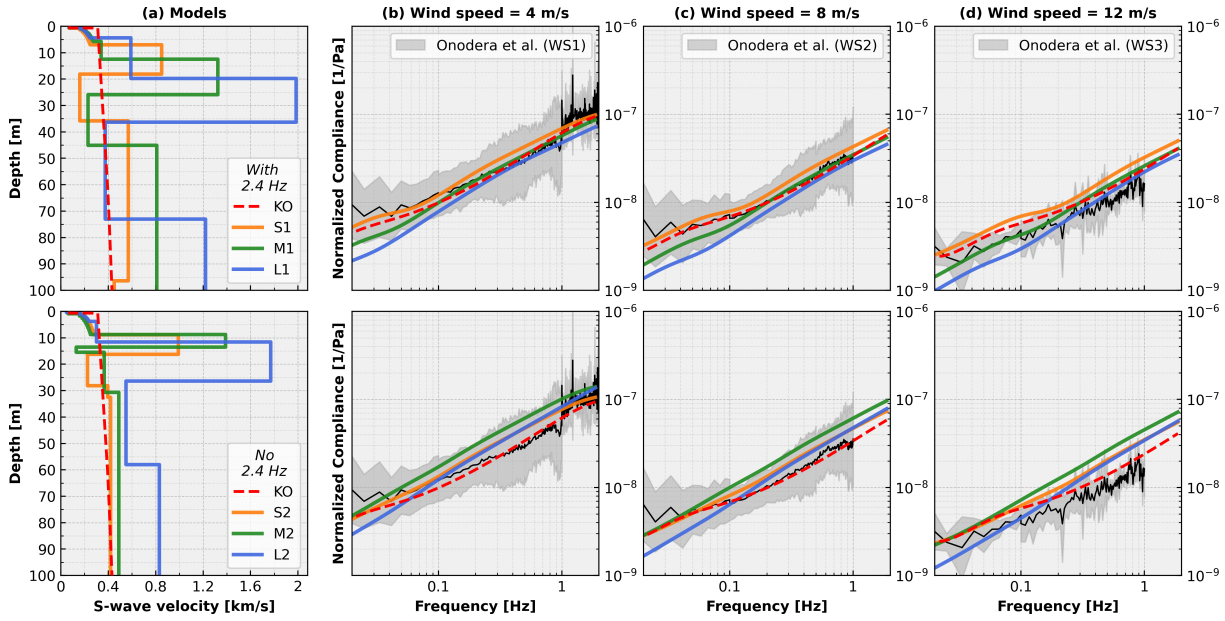


Figure 5.10: Characteristic models from set of models S1, M1 and L1 (top) and S2, M2 and L2 (bottom) and their synthetic ground compliance. **(a)** Shear wave velocity structure for characteristic models from the SML1 (top) and SML2 models (bottom). The model proposed by Onodera (2022) is plotted with a dashed red line. The respective synthetic compliance response and the measured ground compliance (black curve and dark grey area) are plotted for different wind levels: **(b)** 0–6 m/s, **(c)** 6–12 m/s and **(d)** 12–18 m/s.

Particularly, the presence of the SHVL and the bLVL cannot be discarded. It is important to note that, given the Bayesian approach, the models obtained from the inversion of the compliance data are the most likely models given a set of a priori conditions. Nevertheless, models with unexpected rigidity, such as a high- or a low-velocity layer, can also explain the observations, as shown in Fig. 5.10 and Fig. A3.10 in the Appendix.

5.5 Implications for the seismological recordings

One of the advantages of using ambient vibrations data for the HVSR analysis is certainly the abundance of recordings. On the contrary, using seismic events on Mars is less efficient not only due to the low seismic activity (Giardini et al., 2020) but also because the events are required to excite a wide frequency range.

Even though more than 900 events have been reported by the MQS, only the VF events have excited the resonance frequency at 8 Hz, and only a few of them have been properly recorded by SEIS. The scarcity of these events is not a problem because the S-wave coda is used, which is produced by the multiple scattering of seismic waves. The multiple scattering phenomenon is expected to be the same for events occurring at different distances and/or azimuths, as long as they carry enough seismic energy above 5 Hz (Aki and Chouet, 1975). Thus, future events exciting the high-frequency part of the spectrum are expected to generate the same HVSR curve from the S-wave coda. The latter can be interpreted as the interference of multiple reverberations due to local conversions in the subsurface structure underneath, which generates surface-wave-like ground motion rather than recording direct Rayleigh or Love waves. Therefore, the full wavefield approach is an appropriate technique for modeling the corresponding HVSR.

Although the hypocentral distance can be estimated by the Sg—Pg time, determining the back-azimuth of the VF events has been not possible yet due to the depolarization of the first arrival (van Driel et al., 2021). Therefore, the epicenter locations of these events have not been obtained yet and the high-frequency propagation mechanism is still unclear (Clinton et al., 2021; van Driel et al., 2021). At least, according to the meteorological data, these events seem to be unrelated to atmospheric or environmental perturbations. A possible mechanism explaining the propagation of such high frequencies for very long distances (i.e. large Sg—Pg time) might be similar to the propagation of T-phases on Earth through the SOFAR channel (Walker et al., 1992; Okal, 2008), but traveling through a thick waveguide with a really thin scattering layer inside so the energy is not leaked out. Further investigation of this mechanism is out of the scope of this work.

An interesting feature of the VF events is the almost negligible vertical ground motion in the frequency range between 6 and 9 Hz. This observation can be explained by a strong local site effect at the InSight landing site due to the subsurface structure underneath. Given an input ground motion, the horizontal ground motion is largely enhanced, while the vertical one is weakly augmented. In fact, the horizontal ground motion is about 7–8 times larger than the vertical one (see Fig. 5.4) due to the site effect and so the amplitudes may easily surpass the horizontal ambient noise. On the other hand, the apparent absence of vertical ground motion can be understood as having lower vertical amplitudes than the ambient noise. This is also revealed by the analysis of the average

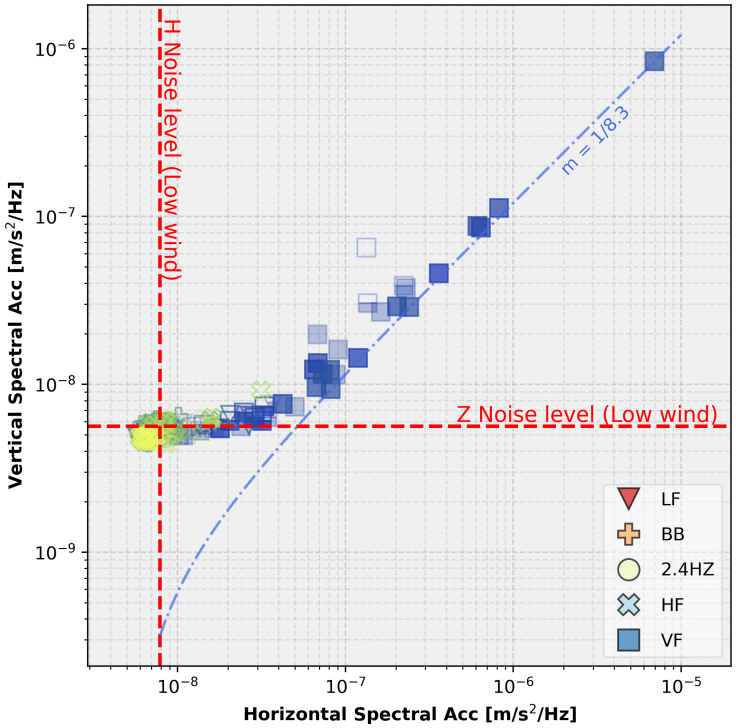


Figure 5.11: Vertical and horizontal ground acceleration around 8 Hz for all the marsquakes with quality A, B and C reported by the MQS. The red dashed lines represent the median ground acceleration recorded during the quietest period of sols 422 and 423 for both vertical and horizontal components. Different markers correspond to different type of marsquakes. The dotted–dashed blue line is a linear regression between the horizontal and the vertical acceleration, using events with SNRZ $>$ 2 dB (related to the HVSR amplitude at 8 Hz). The filling pattern of the marker indicates SNR $>$ 2 dB for the horizontal (lower half), vertical (upper half) or both components (fully filled).

ground acceleration around 8 Hz for all the events with quality A, B and C from the MQS catalog, as shown in Fig. 5.11. In this case, the data shows that, given a horizontal ground motion slightly above the noise level of the quietest period of the sol, the expected vertical ground-motion lies below the median vertical noise level obtained from the same quiet period, when most of the marsquakes are recorded. Hence, as the vertical noise level is higher than the expected vertical ground motion, there is no seismic signal on the vertical component associated with such an event.

5.6 Summary and concluding remarks

The VBB and SP seismic data recorded by SEIS instruments at the InSight landing site were used to investigate the HVSR spectral ratios at frequencies between 0.4 and 10 Hz. The HVSR was computed from both ambient vibrations (nHV) and seismic events data (eHV).

The HVSR curves obtained from VBB and SP data are similar for frequencies below 10 Hz whereas, above this frequency, the VBB HVSR curves (both *nHV* and *eHV*) show higher amplitudes. This difference is related to a different amplification of the vertical component at high frequencies. The origin of this difference is still unclear, so ignoring the frequencies above 10 Hz for any further analysis of the HVSR curve is suggested.

The *eHV* curves were obtained from the S-wave coda of all recorded Martian seismic events with energy well above the background noise. The resulting *eHV* curve shares similarities and differences with the *nHV* curves, particularly during the low-noise period. They both present a trough at 2.4 Hz and a similar shape for frequencies below $\sim$ 4 Hz but a steep left flank leading to a peak at around 8 Hz is observed on the *eHV* curve. The inversion of the *fHV* (i.e., the *eHV* from VBB data) using the full wavefield under the diffuse field approach results in three different subsets of models, all of them suggesting the presence of a shallow high-velocity layer (SHVL) followed by a buried low-velocity layer (bLVL). Because the origin of the 2.4 Hz resonance remains unclear, the *fHV* curve was also inverted in the frequency ranges between 0.4–2 and 3–10 Hz. The resulting models share the presence of a high-velocity layer emplaced over layers with lower velocities and also a bLVL. In any case, the features of the HVSR curve can be properly explained by the effect of the full wavefield and not only one type of wave.

The emplacement of a high-velocity layer at shallow depths (SHVL), likely an effusive Early Amazonian basaltic lava flow, is proposed to explain the strong excitation of the 8 Hz resonance during the VF events. There is a lack of resolution to map the subsurface structure above the SHVL, but the pre-landing models and inversion of compliance data suggest the presence of a thin regolith followed by a coarse ejecta layer, which overlay the SHVL and are compatible with the *fHV*. Lower velocities below the SHVL are required to obtain the observed steep left flank of the 8 Hz peak. The latter is related to a surface, mainly Rayleigh, waves resonance. These deeper low velocities may be related to a more physically and chemically weathered Early Hesperian or Early Amazonian basaltic unit. A bLVL, likely corresponding to a sedimentary layer interrupting these two basaltic units, is needed to explain the *fHV* curve with or without the 2.4 Hz trough. The 2.4 Hz resonance is generated as long as there is a sharp contrast between the bLVL and the SHVL and it would be related to a P-wave resonance.

CHAPTER 6

Constraints for crustal structure from Rayleigh-waves ellipticity

After the shallow subsurface structure at the InSight landing site (ILS) has been investigated, the next step of this research is to go deeper and map the kilometers-scale crustal structure of Mars at this location. How possible is this to be done by utilizing data from one seismological station only? Throughout this chapter, the ground-motion recordings of Rayleigh waves generated by large seismic events on Mars were used to derive a 1-D model for the local crust at the ILS. To do this, the ellipticity of Rayleigh waves recorded by InSight was extracted, investigated and finally used in a joint inversion, together with P-to-s Receiver Functions and P-wave lag times from autocorrelations, to provide a consistent crustal model.

The analyses, interpretations and results presented here have been part of the following publications:

1. Kim, D., Banerdt, W. B., Ceylan, S., Giardini, D., Lekić, V., Lognonné, P., Beghein, C., **Carrasco, S.** *et al.* (2022). *Surface waves and crustal structure on Mars.* Science, 378(6618), 417-421, doi:10.1126/science.abq7157.

2. Panning, M. P., Banerdt, W. B., Beghein, C., **Carrasco, S.**, Ceylan, S. *et al.* (2023). *Locating the largest event observed on Mars with multi-orbit surface waves.* Geophysical Research Letters, 50(1), e2022GL101270, doi:10.1029/2022GL101270.

3. **Carrasco, S.**, Knapmeyer-Endrun, B., Margerin, L., Xu, Z., Joshi, R., Schimmel, M., *et al.* (2023). *Constraints for the Martian crustal structure from Rayleigh waves ellipticity of large seismic events.* Geophysical Research Letters, 50, e2023GL104816. doi:10.1029/2023GL104816

4. **Carrasco, S.** (2023). *Martian crustal models at the InSight landing site from joint inversion of ellipticity, P-to-s RFs and autocorrelations times (0.1) [Data set].* Zenodo. doi:10.5281/zenodo.8051337

6.1 Introduction

The structure and properties of the Martian crust are important for understanding the evolution of Mars and rocky planets. In this context, the InSight mission (Banerdt et al., 2020), which landed on Elysium Planitia in November 2018, aims to study the interior of Mars by means of one seismological station placed on the Martian surface (Lognonné et al., 2019).

After more than three years of data collection, the Martian crust has been studied by a thorough analysis of the InSight seismological data. Locally at the InSight landing site, early analysis of P-to-s receiver functions (RFs) allowed to derive a shallow layer with low seismic velocities in the first 8-11 km of the Martian crust (Lognonné et al., 2020). Further investigation including more marsquakes suggests a layered local Martian crust with two discontinuities at 8 ± 2 km and 20 ± 5 km, and a bimodal estimation of the crust thickness of either 20 ± 5 or 39 ± 8 km (Knapmeyer-Endrun et al., 2021). Subsequently, the analysis of further seismic events and the identification of other secondary phases (PPs, Sp and three new crustal multiples) favor a 3-layer crustal model (Kim et al., 2021b; Joshi et al., 2023), for which the crust-mantle boundary would be located at $\sim$ 40 km depth. The shallow discontinuity around 8 km depth has been confirmed by the detection of SsPp phases (Li et al., 2022b) and SH-wave reflections (Li et al., 2022e). Recently, Shi et al. (2023) proposed a shallow discontinuity at around 2 km depth, based on the analysis of high-frequency RFs. Further properties and characteristics of the Martian crust at regional scales (e.g., Kim et al., 2022a; Beghein et al., 2022; Kim et al., 2022b; Li et al., 2022c), as well as at global scale and away from the lander (e.g. Li et al., 2022d; Wieczorek et al., 2022; Durán et al., 2022), have been derived from the analysis of the InSight seismic data using different approaches.

Table 6.1 presents an overview of the proposed local-scale models, where the main discontinuities and shear-wave velocities are featured. The differences between these models lie in the data and methods used. The models by Knapmeyer-Endrun et al. (2021) were obtained by inverting the P-to-s RFs from three Martian seismic events. Durán et al. (2022) inverted the P-to-s RFs from seven events and included the arrival times of teleseismic phases, developing a more regional crustal model. Joshi et al. (2023) jointly inverted the P-to-s RFs from eight events and their apparent velocity $V_{s,app}$. On the other hand, the model proposed by Shi et al. (2023) is the outcome of a forward modeling study rather than an inversion of the data set.

Besides RFs, the analysis and inversion of the ellipticity of direct Rayleigh waves is a single-station technique that, when measured at intermediate and long periods (>10 s), allows investigating the local underground structure down to crustal depths (Tanimoto and Rivera, 2008; Yano et al., 2009). The ellipticity, understood as the ratio between the radial (R) and the vertical (Z) ground-motion of the Rayleigh wave (Fig. 6.3a), has been shown to be invariant to the seismic source, the wave propagation path or the epicentral distance and rather depend on the local structure directly beneath the receiver (e.g., Ferreira and Woodhouse, 2007a). Even though this methodology was proposed in the 1970s, it has gained popularity only in recent years and with successful applications on Earth (e.g., Lin et al., 2012; Li et al., 2016; Berbellini et al., 2017), but it has not been applied on Mars so far due to the lack of observation of direct Rayleigh waves. Hence,

	Layer 0 (z_0, V_{s0})	Layer 1 (z_1, V_{s1})	Layer 2 (z_2, V_{s2})	Layer 3 (z_3, V_{s3})	Half-space V_{sh}
KE21	-	6-10 km *1.0-2.0 km/s*	15-25 km *1.7-2.7 km/s*	31-48 km *2.5-3.7 km/s*	*3.2-4.0 km/s*
DU22	-	8-12 km *1.6-3 km/s*	22-28 km *2.5-3.3 km/s*	39-50 km *3.5-4.2 km/s*	*4.0-4.5 km/s*
JO23	-	7-9 km *1.6-1.8 km/s*	18-24 km *2.3-2.6 km/s*	37-48 km *3.2-3.6 km/s*	*3.5-4.5 km/s*
SH23	2 km *1 km/s*	8 km *1.85 km/s*	20 km *2.8 km/s*	44 km *3.75 km/s*	*4.33 km/s*

Table 6.1: Summary of available crustal structure models for the InSight landing site. The models correspond to: KE21 (Knapmeyer-Endrun et al., 2021), DU22 (Durán et al., 2022), JO23 (Joshi et al., 2023) and SH23 (Shi et al., 2023). For each model, the bottom depth (z_i) and shear-wave velocity (V_{si}) of each layer are given. Models KE21, DU22 and JO23 have three layers over a half-space (Layers 1, 2 and 3), whereas model SH23 has an extra shallow layer (Layer 0). V_{sh} corresponds to the shear-wave velocity of the half-space, which is understood as the upper mantle for all these cases.

the ellipticity analysis of direct Rayleigh waves is still a pending task that could provide further constraints on the structure of the Martian crust at the InSight landing site, as proposed by Panning et al. (2017).

The analysis of ε data can be used as an independent observation to characterize the Martian crust at the InSight landing site. The inversion of RFs is affected by the non-uniqueness phenomenon and, although these data are highly sensitive to discontinuities, the addition of ε data can provide constraints on long-wavelength velocity features (Chong et al., 2016). As both data sets map the local structure at similar local scales, a joint inversion of ε and P-to-s RFs can be performed. Similarly, the autocorrelation times (hereafter T_a) obtained from the analysis of seismic ambient noise, such as those by Schimmel et al. (2021), are sensitive to the local crustal structure and therefore can be used as an independent data set to constrain the inversion. In fact, the predicted T_a for the crustal models in Table 6.1 differs from the measurements (Table 6.2) whereas, as shown in Fig. 6.4a, the corresponding predicted ellipticity curves fail to match the measured ε. These mismatches further encourage a joint inversion of the three data sets.

In this chapter, the ellipticity and phase shift of the Rayleigh waves related to three large seismic events: S1000a, S1094b and S1222a, the largest event ever recorded on Mars, are analyzed in order to obtain further constraints on the structure of the Martian crust. In particular, a joint inversion of Rayleigh wave ellipticity, P-to-s RFs and T_a is performed to obtain a consolidated local crustal model.

	KE21	DU22	JO23	SH23
t_{1a} $(6.15 \pm 0.2\,s)$	5.24 s	6.22 s	5.45 s	5.15 s
t_{2a} $(10.6 \pm 0.2\,s)$	11.49 s	11.2 s	11.84 s	10.48 s

Table 6.2: Predicted P-wave reflections times at the first (t_{1a}) and second (t_{2a}) discontinuity for representative crustal models shown in Fig. 6.4c and from autocorrelations analysis (Schimmel et al., 2021).

6.2 Large seismic events on Mars

The detection of seismic events on Mars has been a complex task since the beginning of the InSight mission, partly because of the high noise levels generated due to the interaction between the lander and the wind (Giardini et al., 2020; Clinton et al., 2021). The largest events recorded during almost the first 1000 sols of the mission had a magnitude $M_W \sim 3.7$ and were located $\sim 30°$ away from the lander (events S0173a, S0235b and S0325a). These were high-quality events with multiple clear phases and a high signal-to-noise ratio, but no surface waves were reported (Giardini et al., 2020; Clinton et al., 2021).

The first observation of surface waves on Mars came with the event S1000a on 18 September 2021, whereas a second observation of surface waves was related to event S1094b, on 24 December 2021. These are quality A events with recordings that allow estimating their epicentral locations and source origin time. By analyzing orbital images taken by MRO Context Camera (CTX, Malin et al., 2007), and considering the estimated origin times, Posiolova et al. (2022) found that these events can be related to two fresh impact craters on the Martian surface > 130 m in diameter. This is specifically supported by evident geomorphological changes before and after the recordings of events S1000a and S1094b, suggesting that these events correspond to the impact of meteorites on the Martian surface. The hypocentral location of these events can thus be well-constrained and their magnitudes were estimated as M_W 4.1 and 4.0, respectively for S1000a and S1094b (Posiolova et al., 2022). Given the shallow source, (Kim et al., 2022a) showed that seismic waves with increased amplitudes and elliptical motion can be identified at low frequencies (< 0.5 Hz) for these events, which were interpreted as the first recordings of Rayleigh waves on Mars.

Besides, on May 4, 2022, the InSight lander recorded the S1222a event, which had a moment magnitude estimated as M_W 4.7 and thus corresponds to the largest seismic event ever recorded on Mars (Kawamura et al., 2022). The source has been estimated

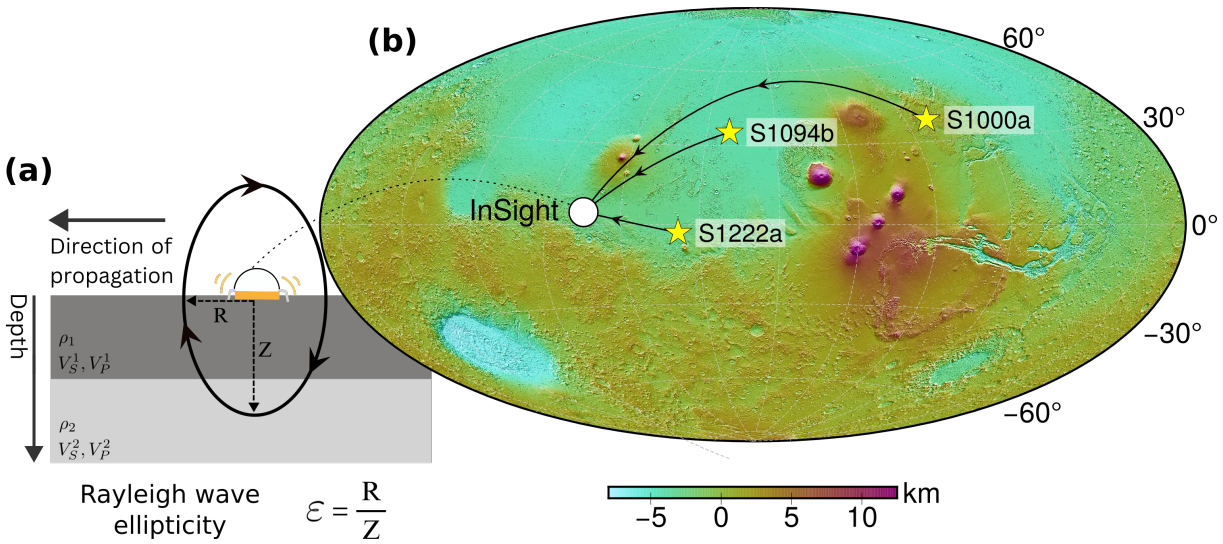


Figure 6.1: Epicentral locations of large seismic events on Mars. **(a)** Schematic representation of Rayleigh wave ellipticity using the radial (R) and vertical (Z) ground motion. **(b)** Topographic map of Mars, from the Mars Orbiter Laser Altimeter (Smith et al., 2001), showing the epicenter of events S1000a, S1094b, S1222a and the InSight lander. Taken from Carrasco et al. (2023).

to be located 37° distance from the SEIS seismometer and, using different approaches including the one presented in the next section, it has a back-azimuth between 100° and 140° (Panning et al., 2022). Unlike S1000a and S1094b, no new impact craters have been associated with this event, so its origin is likely tectonic (Fernando et al., 2023). Indeed, based on waveform modeling to constrain its focal mechanism, Maguire et al. (2023) suggested that this event can be related to active compressional tectonics near the Martian dichotomy boundary at shallow depths (< 25 km) due to thermal contraction from planetary cooling. This event exhibits clear surface waves (both Love and Rayleigh) that have been used for studying lithospheric properties along the source-receiver path (e.g., Beghein et al., 2022; Li et al., 2022c; Kim et al., 2022b; Xu et al., 2023), and also at global scale (Kim et al., 2023), but is also a unique opportunity to investigate the local crustal structure through ellipticity analysis of Rayleigh waves.

These three large seismic events, whose source locations are shown in Fig. 6.1b, are the only events for which surface waves have been identified so far and, thus, they are excellent candidates to perform a Rayleigh wave ellipticity analysis that allows constraining the mechanical properties of the local crust at the ILS.

6.2.1 Back-azimuth determination for S1222a

Due to its definition, the Rayleigh-wave ellipticity analysis must be performed on the ZRT (Vertical, Radial, Transverse) coordinate system, where the Radial component is along the direction of propagation of the seismic ray and the Vertical is orthogonal to the planet's surface. For this conversion, the back-azimuth (BAZ, the angle between the geographical North and the source location) of the event must be used to rotate from the ZNE into ZRT coordinate system. As S1000a and S1094b have been identified as impacts with source locations confirmed by orbital images (Posiolova et al., 2022), their BAZs are well constrained at around 36° and 51°, respectively. For S1222a, even though there are estimates for the location of the source (e.g., Kawamura et al., 2022), there is no ground-truth location as for S1000a and S1094b.

An independent methodology to estimate the BAZ of S1222a is applied, based on the fact that the Rayleigh waves propagate in the ZR plane. Basically, the ground-motion amplitudes on the Z and R components are maximized while minimizing the ground motion on the T component. To do this, the BAZ that maximizes the $\frac{Z_e R_e}{T_e}$ coefficient, where e denotes the time-domain envelope of the corresponding component, is grid-searched in the range between 0 and 360° for different period ranges. For each period range, the Z, R and T components are bandpass-filtered accordingly and their envelopes are obtained. As shown in Fig. 6.2, this methodology has a 180° ambiguity because two BAZs maximize this coefficient. These two solutions result in propagating Rayleigh waves with retrograde (phase shift>0°) and prograde motion (phase shift < 0°). As Rayleigh waves typically exhibit a retrograde ground-motion at the surface, the preferred BAZ is the one providing a positive phase shift between the R and Z components.

For S1222a, the estimated BAZs from this work are in the range 114°-137°, with a median value of 129°, which is used in this work. This BAZ is in the range obtained from the analysis of multi-orbit Rayleigh waves (Panning et al., 2022) and differs by $\sim$ 30° from the BAZ derived from body waves by the MQS (Kawamura et al., 2022).

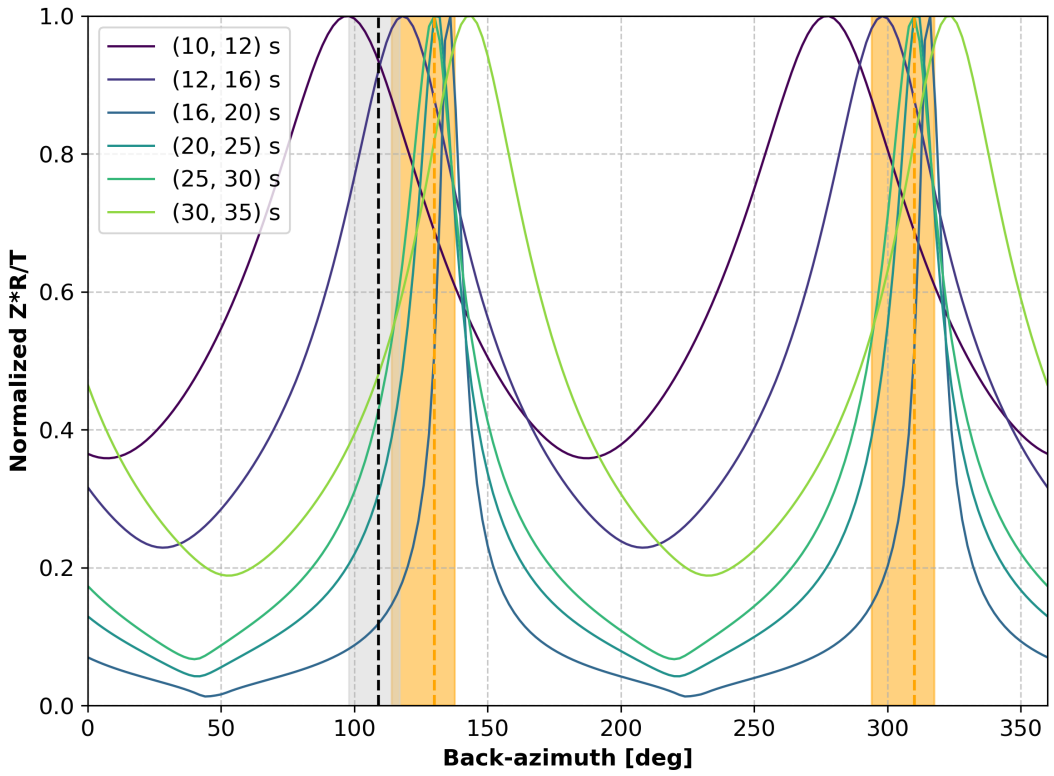


Figure 6.2: Determination of back-azimuth (BAZ) of S1222a. Different curves represent the $\frac{Z_e R_e}{T_e}$ coefficients for a range of BAZs when filtering in different period bands. Two BAZ estimates are obtained for each period band, due to a 180° ambiguity. The orange dashed vertical bars are the BAZs estimated in this work with their uncertainty range (orange area). The black dashed vertical is the BAZ estimated by the MQS from body wave data and its uncertainty (light gray area). Taken from Carrasco et al. (2023).

6.3 *Rellipy*: a python tool for extracting Rayleigh-wave ellipticity

In order to systematically retrieve the Rayleigh-waves ellipticity from seismic events, *Rellipy* was developed in the context of this work. *Rellipy* is an open-source package implemented in Python, which makes extensive use of scientific libraries like ObsPy (Beyreuther et al., 2010), Numpy (Harris et al., 2020), Scipy (Virtanen et al., 2020) and Matplotlib (Hunter, 2007). The main output of this set of codes is to determine the characteristic Rayleigh-wave ellipticity curve of a specific site using three-component ground-motion recordings of a given seismological station and a set of events with their hypocentral information (catalog). It was initially developed for working on Martian seismic events only, but it has been adapted to be utilized with waveforms from custom stations, either stored locally or publicly available online (via FDSN services), and a custom catalog of events. The reader is invited to test it at his/her convenience. An overview of the processing steps is provided here, using the three large Martian seismic events as example, and further details can be found in the Github repository.

To retrieve the characteristic ellipticity at the ILS, a time-domain processing was performed in a similar way as has been done on Earth (e.g., Ferreira and Woodhouse,

2007a; Berbellini et al., 2016; Ferreira et al., 2020), following the steps shown in Fig. 6.3. First, the time windows where the Rayleigh waves arrive are roughly estimated, in this case, given the low amplitude of the signals, by manual inspection, following the identification by Kim et al. (2022a) for S1000a and S1094b and the time estimates by the Marsquake Service (MQS) for S1222a (Kawamura et al., 2022), and assuming they correspond to the fundamental mode ($_0R_1$). These arrival time windows are shown in Fig. 6.3a. In Earth cases, large-magnitude events (M_W>6.0) should be preferred as they generate Rayleigh waves with large amplitudes. In this case, the time window where the Rayleigh wave is expected is determined automatically by taking the epicentral distance of the event and minimum/maximum average Rayleigh-wave group velocities of 2.5 and 4.5 km/s. Unlike Earth, there were no well-known group velocities on Mars before deriving them from the same events, so a more specific time window identification was needed

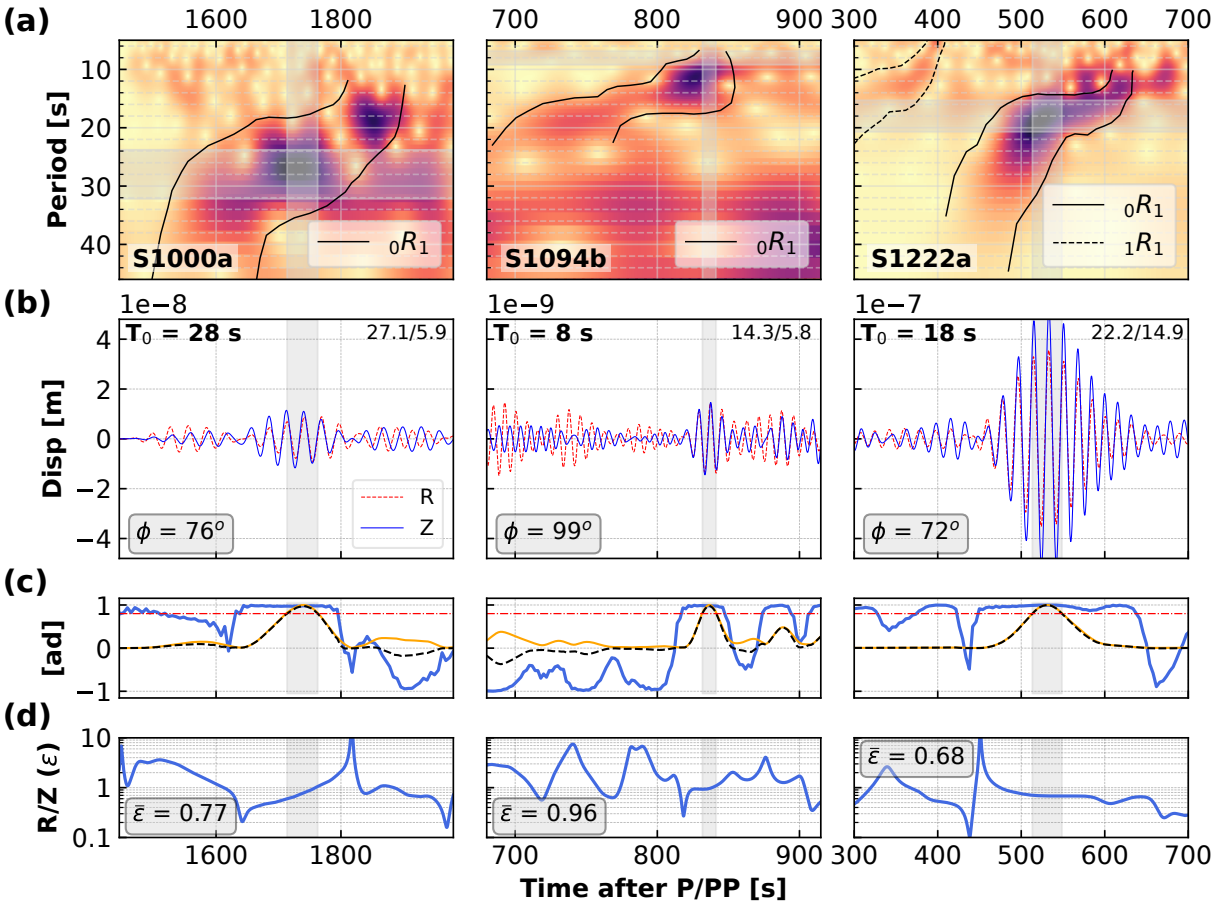


Figure 6.3: *Rellipy* processing steps. From left to right, columns correspond to the *Rellipy* processing steps of events S1000a, S1094b and S1222a. From top to bottom: **(a)** S-transform spectrogram of the Z component, where the observed fundamental mode ($_0R_1$) and first overtone of the Rayleigh waves ($_1R_1$) are highlighted. **(b)** Shifted Z and R waveforms using the optimal phase shift ϕ. The Z and R components are bandpass-filtered with a 30% bandwidth around the central period T_0, as indicated at the top left of each subplot. The SNR_Z and SNR_R are given at the top right corner of each plot. **(c)** Cross-correlation factor $\nu(t)$ between shifted Z and R components (blue), normalized envelope $\eta(t)$ (yellow) and characteristic function $\chi(t) = \nu(t)\eta(t)$ (dashed black). The red dot-dashed horizontal line denotes a threshold for at 0.8. **(d)** Ellipticity $\varepsilon(t)$. For each event and each central period, the average ellipticity ($\bar{\varepsilon}$) is computed over the time window where $\chi \geq 0.8$ (gray box). Taken from Carrasco et al. (2023).

for the Martian events in order to avoid the effect of noise signals on the phase shift calculation.

The raw data (InSight Mars SEIS Data Service, 2019) have been deglitched using the UCLA method (Scholz et al., 2020), restituted to ground motion (displacement) and transferred into the ZNE coordinates system. The data are then rotated into a ZRT coordinates system using each event's back-azimuth. After rotating into the ZRT coordinates system, the Z and R components are bandpass-filtered, with a 30% bandwidth, around different central periods T_0 (Fig. 6.3b). In this way, every T_0 will be associated with one ellipticity value.

Subsequently, the *optimal phase shift* (ϕ) was retrieved by maximizing the cross-correlation between the Z and R components. Examples of resulting ϕ and optimally shifted waveforms are shown in Fig. 6.3c. Once optimally shifted, the cross-correlation factor $\nu(t)$ was calculated between the shifted Z and R components (Fig. 6.3c, blue curve). The normalized envelope $\eta(t)$, also shown in Fig. 6.3c (yellow curve) and given by the multiplication of the Z and R envelopes, is calculated and used to find the specific time window where the energy is maximized. In order to discard low-amplitude signals with high cross-correlation (or vice versa), a characteristic function $\chi(t) = \nu(t)\eta(t)$ is calculated (Fig. 6.3c, dashed black curve). The final ellipticity for the central period T_0, computed as the R/Z quotient, is the average of the ellipticities in the time window where the characteristic function χ is larger than 0.8, as shown in Fig. 6.3d.

These processing steps are performed on the ${}_0R_1$ of events S1000a, S1094b and S1222a. In order to combine these measurements, even though radial and azimuthal anisotropy may be present, it is assumed that these would affect ellipticity to a lesser extent than the underlying crustal structure. To get a single characteristic ellipticity curve at the InSight landing site, only pairs of event-T_0 with actual Rayleigh wave signal are considered, i.e., when the signal-to-noise ratio (SNR) is larger than a given threshold in both Z and R components. The thresholds $\mathrm{SNR}_Z \geq 10$ and $\mathrm{SNR}_R \geq 5$ (given the higher noise levels on the horizontals) are used. The final Rayleigh ellipticity curve for the InSight site is then calculated as the smoothed median of the valid ε values, obtained by means of a Savitzky-Golay filter (Savitzky and Golay, 1964).

6.4 Ellipticity and phase-shift measurements

6.4.1 Ellipticity analysis on Martian seismic events

The resulting ε and ϕ values are shown in Fig. 6.4a and b, respectively. Besides the limited number of events analyzed, there is a lack of valid ellipticity measurements due to the low-amplitude energy on the radial component. The valid ε values define an ellipticity curve between 15 and 35 s and two points at 8 and 9 s (Fig. 6.4a). The period range between 15 and 35 s is the main focus of this work, where the horizontal contribution of the tilt induced by Rayleigh waves can be neglected. Due to the lack of further observations, a common 15% uncertainty is utilized, which properly covers the observations. The ellipticity measurements shape a relatively flat curve without noticeable peaks or troughs, unlike the HVSR curve from the coda of seismic events studied in Chapter 4 and Chapter 5. Because of this, the ellipticity curve cannot provide information on the discontinuities but rather on the range of accepted average shear-wave velocities only. Further discussion on this topic is provided in the next section.

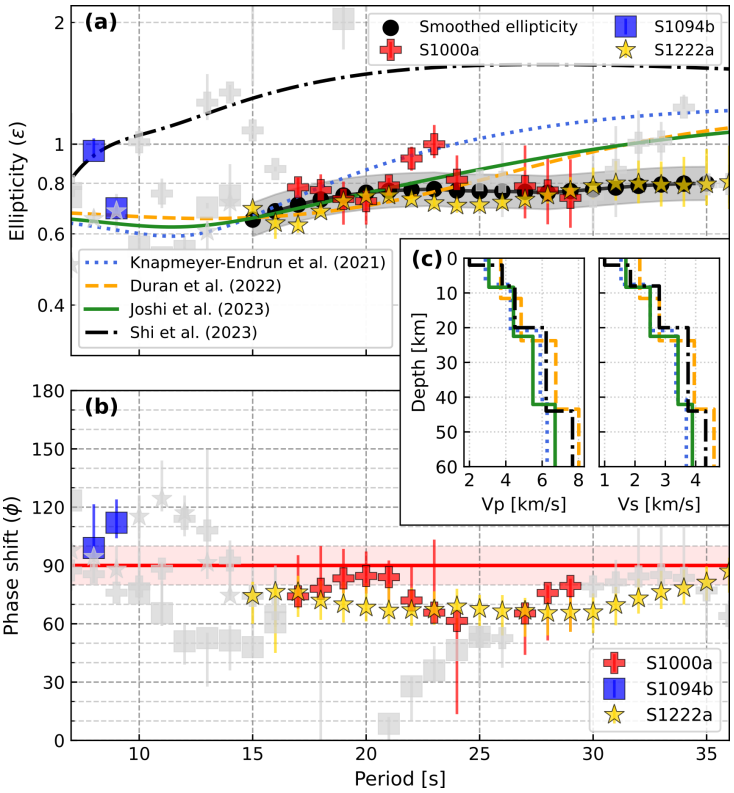


Figure 6.4: Rayleigh wave ellipticity and phase shift results. **(a)** Rayleigh wave ellipticity (ε) curve for events S1000a (red cross), S1094b (blue square) and S1222a (yellow star). Colored markers correspond to periods where the SNR criteria are fulfilled. Background light gray markers did not meet the minimum SNR threshold. The final ellipticity curve for the InSight site is denoted by the black circles, and a 15% uncertainty range has been imposed (gray area). Synthetic ellipticity curves are illustrated for characteristic crustal models from Knapmeyer-Endrun et al. (2021), Durán et al. (2022), Joshi et al. (2023) and Shi et al. (2023). **(b)** Phase shift ϕ between Z and R components of ${}_0R_1$ for the same events and with the same color code as in (a). The light red area corresponds to ϕ in the range 90±10°. **(c)** Vp and Vs models for the InSight crust used for synthetic calculation of ε in (a). Taken from Carrasco et al. (2023).

On Earth, the ellipticity curve of one specific site is obtained from the recordings of a large number of earthquakes. In this work, even though three events were initially investigated, the ellipticity curve is mainly ruled by S1222a and, therefore, the lack of observations can be disadvantageous for further analysis and interpretation. Ellipticity data can have a large spread (e.g. Berbellini et al., 2016; Attanayake et al., 2017), which might be associated with complex Rayleigh wave propagation effects (Sexton et al., 1977; Pedersen et al., 2015) or due to local-scale heterogeneities near the receiver, as suggested by Ferreira and Woodhouse (2007a) after analyzing two close sta-

tions in California. Considering the lower tectonic activity and smooth topography in the local surrounding of InSight, as compared to the terrestrial case, it is assumed that the ellipticity measurements from this event can be a good representation. Besides, the ${}_0R_1$ of S1222a has a high SNR in both Z and R components, so the final smoothed ε is expected to be a good representation of the local structure.

The resulting Z-R phase shifts, mainly ruled by S1222a, suggest ϕ values between 60° and 70° (Fig. 6.4b), which are persistently lower than the theoretical phase shift for Rayleigh waves under isotropic and homogeneous conditions (90°). These low ϕ are obtained even when using different BAZ angles (Fig. 6.5).

On Earth, large deviations up to ±30° have been found and have been related to small-scale heterogeneities (e.g., Ferreira and Woodhouse, 2007a). From the analysis of ellipticity in one station on Earth (see following subsection 6.4.2), low ϕ $(60 - 75°)$ were measured for some events at specific period ranges, but not as a characteristic feature of the site. These observations suggest that anomalous ϕ might be related to the Rayleigh-wave path, or even the source, rather than the characteristics of the receiver site. Tanuma and Man (2008) also proposed that variations of ϕ with respect to the isotropic theoretical value depend on the perturbation of the initial stress conditions of the medium. Although crustal anisotropy was reported along the path of S1222a (Beghein et al., 2022; Kim et al., 2022b), its influence on the phase shift is unclear and should not be discarded. Thus, the low ϕ measured at the InSight landing site might be due to a combination of path, source effects, the mechanical properties of the crust and even the temporal stress conditions at the InSight landing site. In any case, low ϕ values have previously been observed on Earth to occur in some cases. Further analysis of this phenomenon is beyond the scope of this work.

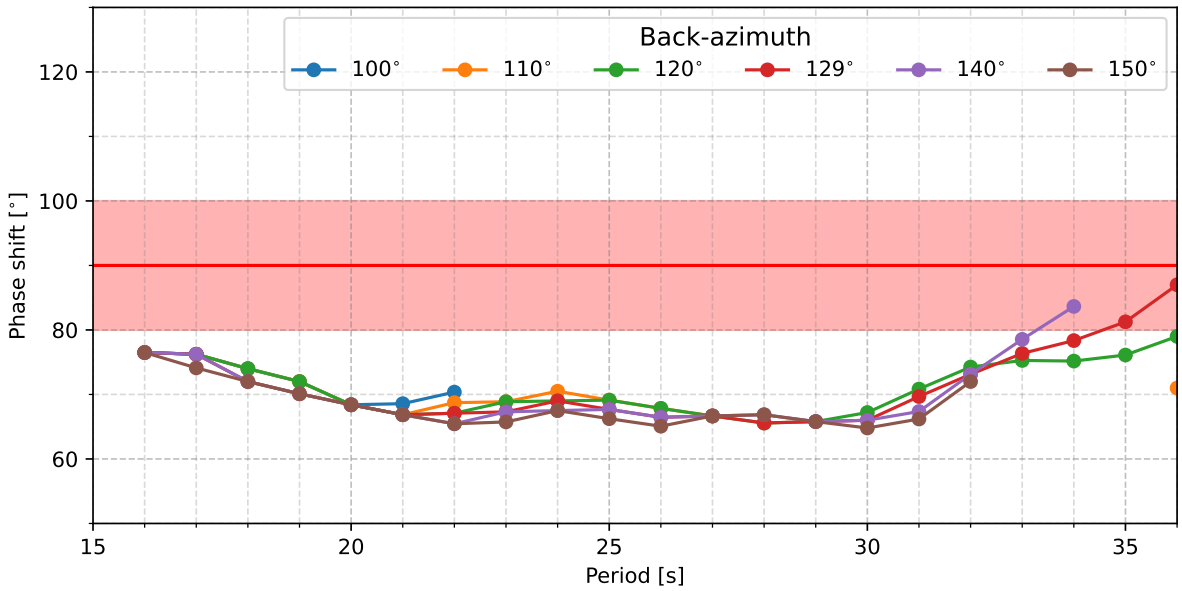


Figure 6.5: Phase shift between Z and R components of the Rayleigh-wave fundamental mode of event S1222a using different back-azimuths (see legend). The solid red line denotes the theoretical phase shift 90° whereas the light red area demarks the 80° and 100° range. Taken from Carrasco et al. (2023).

6.4.2 Comparative analysis of ellipticity data on Earth

In order to assess the results from the Martian events, the same ellipticity analysis was performed for the station DREG on Earth, in Germany, which belongs to the Bensberg Earthquake Observatory of the University of Cologne (BQ network, 2016). Using the event catalog of the Global Centroid Moment Tensor project (gCMT, Dziewonski et al., 1981; Ekström et al., 2012), the earthquakes selection consisted of events occurring between February 2016 and December 2022, with magnitudes between M_w 6.5 and 8.2, at epicentral distances between 10°and 120°, focal depths shallower than 100 km and no restrictions on the back-azimuth. Considering the data availability and these criteria, 140 earthquake recordings were available for this analysis.

The characteristic ellipticity and phase shifts for the Earth site are obtained from the collection of all the available recordings (Fig. 6.6), unlike the Martian case, where the characteristic ellipticity curve is ruled by one single event. The characteristic ellipticity is a roughly flat curve with a slight curvature between 25 and 70 s. Although data points out of the characteristic curve can be recorded, it is assumed that, for the Martian case, the results lie in the expected range of the median. Single-event ellipticity curves close to the smoothed ellipticity curve show some deviation with respect to it (Fig. 6.7). In particular, some events show different slopes and trends at specific period ranges, with respect to what is observed for the median ellipticity, but the general trend remains similar. Thus, short oscillations on the ellipticity curve should not be over-interpreted when obtained from single-event recordings, like in the Mars case.

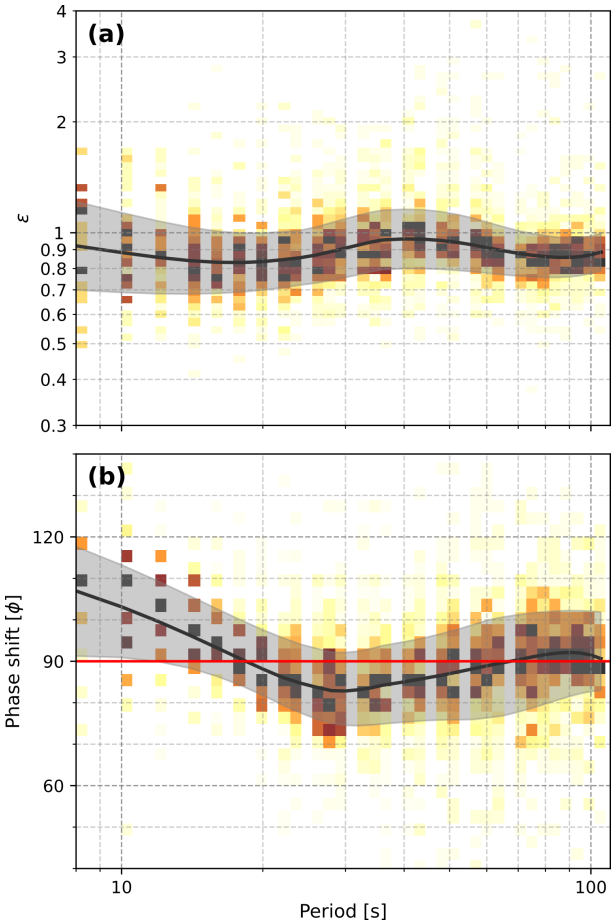


Figure 6.6: Density plot of resulting Rayleigh-waves **(a)** ellipticity and **(b)** phase shifts for station DREG in Germany (BQ network). Darker colors correspond to higher relative occurrence. The characteristic ellipticity and phase shift of this site are derived as the median of all the measurements with $SNR_Z > 10$ and $SNR_R > 5$ (black line and gray dashed area for the uncertainty).

On the other hand, the phase shifts obtained from this Earth case can help to assess the reliability of the anomalously low phase shifts ($\phi < 70°$) over a specific range of periods obtained from the Martian S1222a event (Fig. 6.4b and 6.5). As shown in Fig. 6.6b, a relatively large phase shift, with respect to the theoretical 90°, is observed for periods below 20 s for the DREG case. In the contrary, a trend towards low ϕ (70°-90°) is observed for pe-

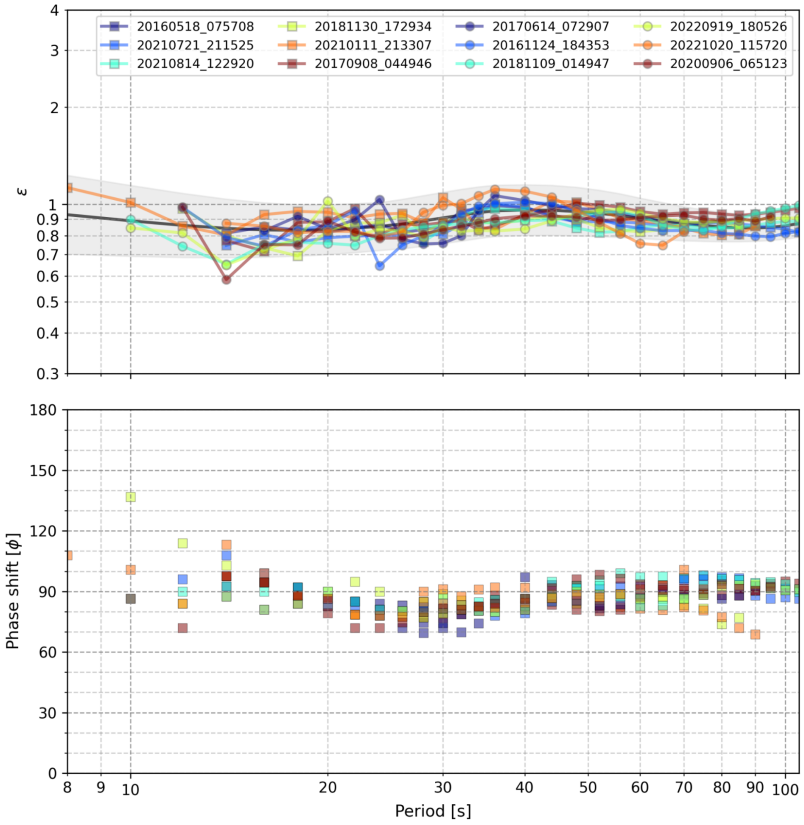


Figure 6.7: Ellipticity and phase shift results for station DREG in Germany (BQ network). The Rayleigh-wave ellipticity curves and the phase shifts of 12 events with best misfits with respect to the smoothed median ellipticity are plotted (event ID according to origin time given in the legend on top panel). Short-wavelength deviations are observed even for the best-fitting events, but long-wavelength features share similarities with the smoothed median ellipticity curve. Taken from Carrasco et al. (2023).

riods between 20 and 40 s, whereas phase shifts in the expected range 80° to 100° are measured for longer periods.

Given the diversity of events here analyzed, the general deviation from the theoretical $\phi_t = 90°$ observed from the resulting phase shifts can be associated with properties or phenomena occurring at the local scale. By definition, the theoretical phase shift is obtained for an isotropic medium, so these variations are likely related to anisotropy at the station site. As earthquakes occurring at different locations are utilized, and thus the Rayleigh waves traveled along different source-receiver paths, the latter can be preliminary discarded as a primary cause of this anomalous phase shift. Further investigation using different approaches is needed to fully understand the mechanical properties of the crust at this site or where the anisotropy source is particularly located.

Differences in the determined phase shift have also been recorded for earthquakes with similar source locations and faulting mechanisms, as shown in Fig. 6.8. In this case, the phase shifts of two off-shore Mexico earthquakes, both located ∼9500 km away from DREG and about 200 km from each other, differ by $\sim 15°$ at periods around 34 s. These events have similar sources, both related to compressional faulting along the contact between the Cocos and the North American plate, and given the proximity between them, the traveled path is also similar for the corresponding wavelength.

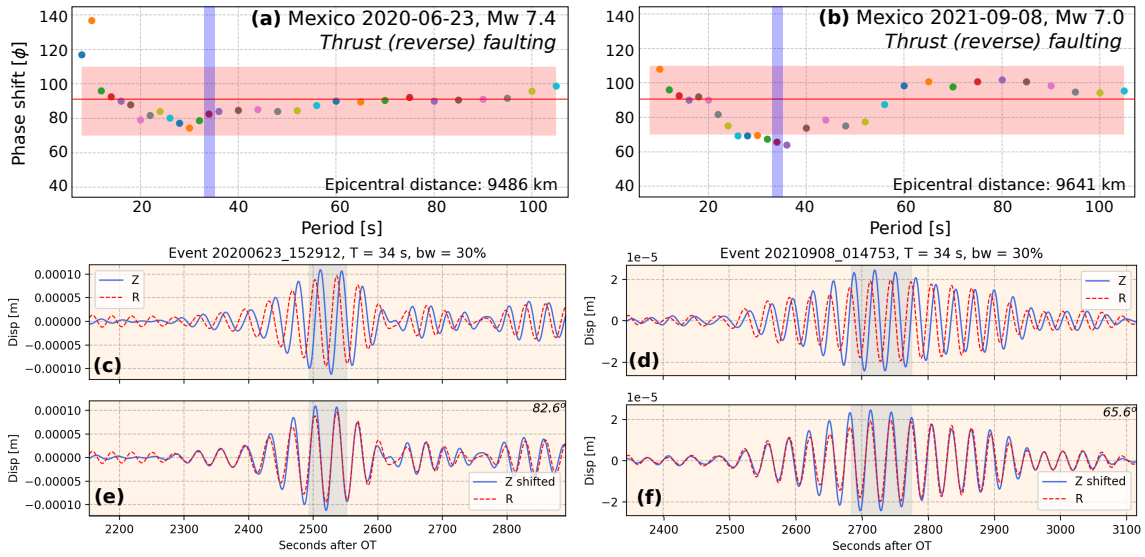


Figure 6.8: Low phase shifts at station BQ.DREG. The phase shifts as a function of the period are shown for the following events: **(a)** Event 1, 2020-06-23 15:29:12, M_w 7.4, **(b)** Event 2, 2021-09-08 01:47:53, M_w 7.0. The unshifted Z and R waveforms of Events 1 and 2 are showing in **(c)** and **(d)**, respectively. The synced Z and R waveforms of Events 1 and 2 are shown in **(e)** and **(f)**, respectively. The phase-shift angle is indicated at the top right corner of (e) and (f). The light orange box is a time window where the Rayleigh wave was searched, whereas the light gray box is the window where the ellipticity is measured.

Thus, different phase shifts can be obtained even under extremely similar earthquake conditions (similar source, path and same site). In fact, the source of the event might play a minor role in explaining this difference, as shown in Fig. 6.9, where another Mexico event, with a similar path as those in Fig. 6.8, but a completely different normal faulting mechanism, shows similar values as the Event 1 in Fig. 6.9. Following these observations, a possible explanation might be the changes in the mechanical properties and anisotropy of the local underground structure or even the particular mechanical state of the crust when the Rayleigh waves pass through this site. Further investigation on the phase shift variation is out of the scope of this PhD thesis but will be pursued in future works.

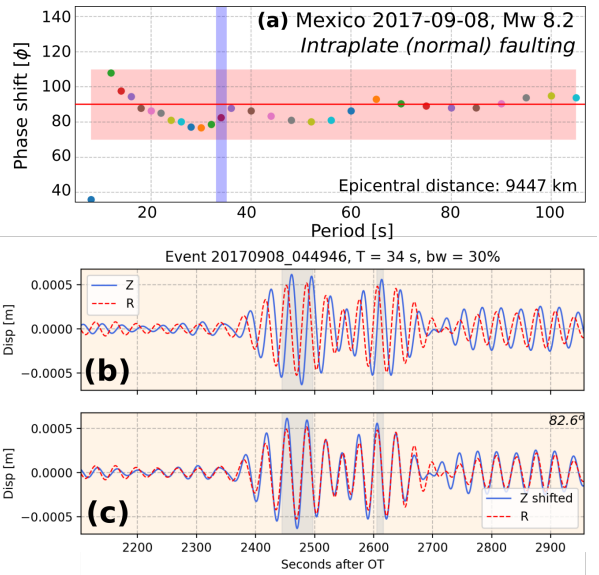


Figure 6.9: Phase shift for normal-faulting Mexico earthquake at station BQ.DREG. **(a)** Phase shifts as a function of the period for an event on 2017-09-08 04:49:46 UTC, M_w 8.2, **(b)** Unshifted Z and R waveforms, **(c)** Synced Z and R waveforms after determining optimal phase shift.

6.5 Joint inversion of ellipticity, P-to-s RFs and T_a

6.5.1 Local-scale measurements

Before recording Rayleigh waves at the ILS, other local-scale measurements were available. Local-scale measurements refer to those data sets that map the crustal structure right beneath and in the immediate vicinity of the InSight station (namely, <50 km). Other structure-related data sets, like group velocity measurements or travel times, are not considered as they map the underground structure along the path of the corresponding waves, which may differ greatly from the local structure, and characterize more regional or global features. A special case of such measurements is when using events in the nearby region, as investigated by Drilleau et al. (2023) and which are not part of this work.

Here, the so-called P-to-s Receiver Functions and lag times from autocorrelations measurements (T_a), two local-scale measurements calculated for the ILS, were used. These methods are briefly explained below to validate them as local-scale measurements and support their incorporation into the inversion scheme. References are given in each case for further details.

P-to-s Receiver Functions

The Receiver Functions (RF) method is one of the available single-station techniques that uses three-component recordings for mapping the crustal structure. It is based on the phenomenon of wave conversion occurring in the local underground structure (either transmitted or reflected waves), which can be observed on the ground-motion recordings.

Particularly, the P-to-s RF uses the P-wave coda of event recordings to study the conversion of incoming-upgoing P waves into SV waves due to the interaction with discontinuities within the local structure, as shown in Fig. 6.10. This requires a set of teleseismic recordings with a good signal-to-noise ratio. The RF method usually works on the LQT coordinate system, for which the incidence angle of the P wave is needed, but good results can also be obtained using a ZRT coordinate system (Vertical, Radial and Transverse components). In this case, the ZRT coordinate system is used.

The recorded ground motion ($U(t)$) corresponds to a convolution of the seismic source ($S(t)$), the near-source structure ($P(t)$), the near-receiver structure ($E(t)$) and the instrument response ($I(t)$). In order to determine the near-receiver structure effect ($E(t)$), the source and path effects must be removed from the recordings. This procedure can be performed in the frequency domain, first removing the instrument response $I(\omega)$ of each component. The direct P wave, mainly observed on the vertical component, is assumed to contain information about all the terms besides $E(t)$. Then, the RF is obtained through a *source-equalization* operation, which roughly consists of deconvolving the vertical component from the radial and transverse components (e.g., Phinney, 1964; Langston, 1979). Due to the inherent instability, different methods have been proposed for the deconvolution operation. Here, the time-domain deconvolution technique based on Wiener filtering has been utilized (Kind et al., 1995) whereas RF amplitudes are not normalized, following Ammon (1991), to keep information on the near-surface velocities. Depending on the frequency band, different structural information can arise. The waveforms are band-pass filtered roughly between 0.1 and 0.8 Hz, thus leading to low-frequency P-to-s RFs. More

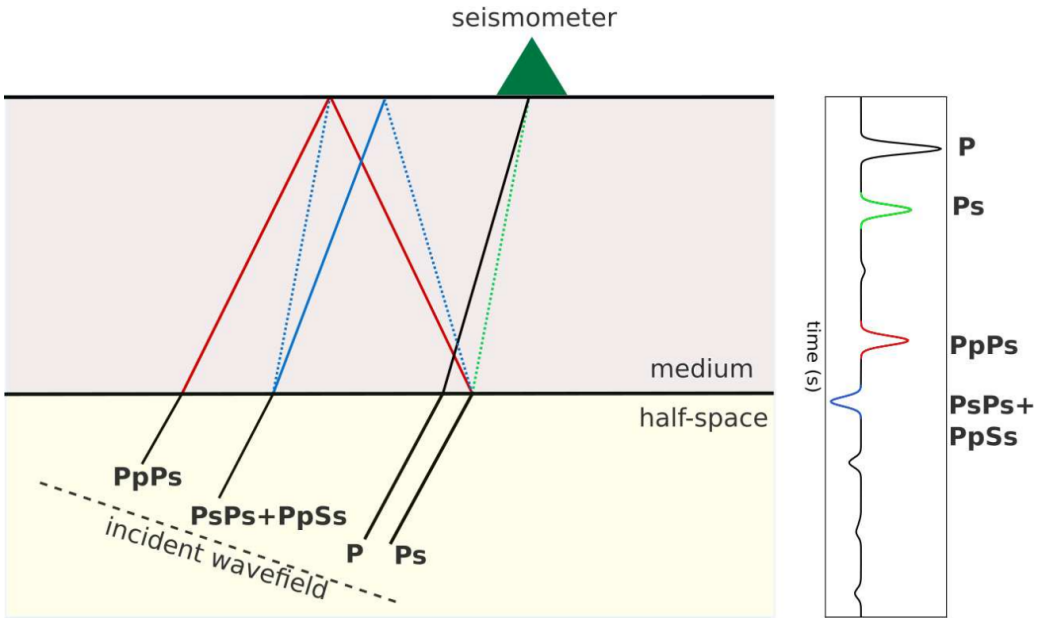


Figure 6.10: Left: P-to-s Receiver Functions sketch showing theoretical ray paths of possible P-wave conversions in a one-layer over a half-space case: direct P wave (P), direct conversion of the incoming P wave into an SV wave at the discontinuity (Ps) and multiple reflections within the layer (PsPs, PpSs and PsPs). **Right**: resulting RF time series. Taken from Joshi (2022).

details on the data processing can be found in Joshi et al. (2023). Assuming a structure with subhorizontal layers, only the deconvolved radial component (RRF) will contain the energy of the converted SV waves, so this is understood as the observed P-to-s RF.

The forward modeling employs the code developed by Shibutani et al. (1996), which uses a reflectivity matrix approach to provide the P-to-s response of a given isotropic layered model to an incident planar P wave. The key for mapping the local structure is using teleseismic events, so the seismic rays are incident from beneath the discontinuity of interest (typically, the Moho). Due to the lower velocity than the incident P wave, the converted SV waves will be steeper than the transmitted P wave, thus mapping an even narrower area. Thus, as schematically shown in Fig. 6.10, using P-to-s conversions allows mapping the most local near-receiver structure, compared to using other multiple reflections, which map a wider area around the seismic station.

Ammon et al. (1990) showed that there is an inherent trade-off between the depth to a discontinuity and the velocity above, because the RF inversion is sensitive to velocity contrasts and relative travel times rather than the absolute velocity, so the inversion with other local-scale observations is recommended.

Ambient noise autocorrelations

The ambient noise autocorrelations is a seismic interferometry technique that has been shown to be useful to map crustal discontinuities on Earth (e.g., Kennett et al., 2015; Becker and Knapmeyer-Endrun, 2018). For this, the recorded ambient seismic wavefield's time series is cross-correlated with itself to detect impulsive signals related to body-wave reflections within the underground local structure.

The principle behind the seismic interferometry, particularly the autocorrelation method, is shown in Fig. 6.11, taken from Becker (2018) and modified after Schuster (2009), where a more comprehensive explanation is provided. Considering a source at depth generating a seismic wave crossing an underground discontinuity, its travel time is recorded at time t_a (Fig. 6.11a). This incoming seismic wave is reflected downward at the surface and then reflected upward at the layer interface, being recorded at the seismic station at a time t_b (Fig. 6.11b). The first travel path in 6.11a can be removed by cross-correlating the signals recorded at the seismic station (*autocorrelation*) at different times (a and b). The resulting signal mimics the phenomenon of having a virtual source at the same location as the station, which generates a seismic wave that travels from the surface down to the layer discontinuity and is reflected upward again in a time $T^* = t_b - t_a$ (Fig. 6.11c). The resulting time T^* (known as the lag or reflection time) and is one of the main outcomes of this method, as it is proportional to the thickness of the layer above the discontinuity.

Retrieving the lag time(s) roughly consists of using the ambient wavefield recorded over a certain time window in one of the components. The data is cut into shorter time windows, which are all then cross-correlated to each other, and the resulting cross-correlation time series are stacked. The lag times where large amplitudes are observed are interpreted as the reflection times from different discontinuities. The lag times used here were obtained by Schimmel et al. (2021) using the vertical component of SEIS recordings, as it contains the traveling P wave), between sol 172 and sol 567. The reader is referred to this work for further details on the data processing.

Because of the nature of this phenomenon (Fig. 6.11), the autocorrelations technique maps the underground structure right beneath the seismic station, so it can be understood as a local-scale measurement.

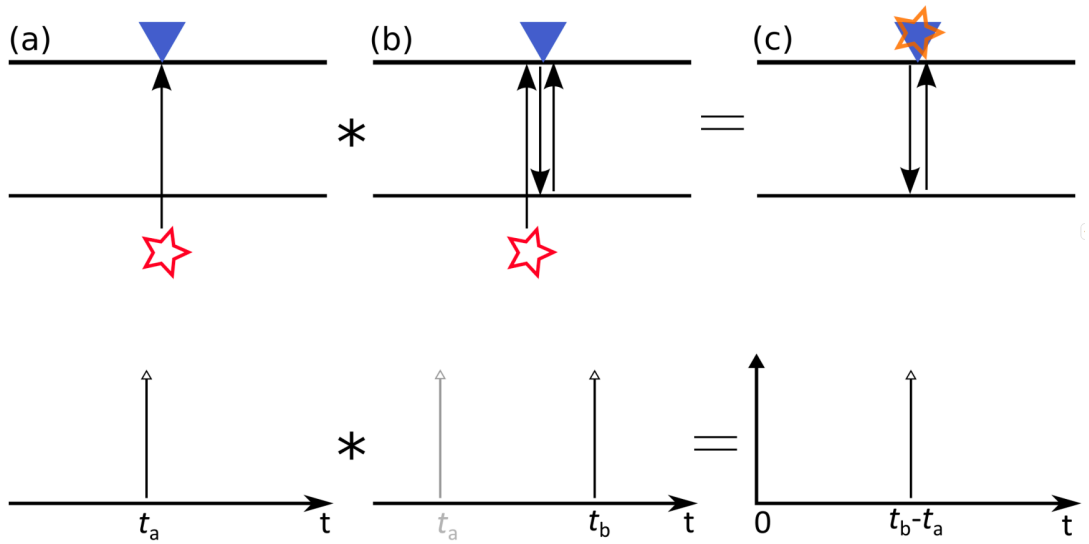


Figure 6.11: Seismic interferometry sketch. **(a)** A seismic wave travels from a source at depth (red star) to a seismic station (blue inverted triangle) on the surface and is recorded at time t_a. (b) The seismic waves reflected downward at the surface and upward at the interface and recorded at time t_b. **(c)** The autocorrelation of the signal results in the seismic station and a virtual source (orange star) being collocated and seismic wave traveling down and being reflected upward again, reaching the statin at time $T^* = t_b - t_a$. Taken from Becker (2018), which is modified after Schuster (2009).

6.5.2 Joint inversion settings and parameterization

As the trade-off between the layer velocities and the depth of the discontinuities is a well-known feature of the ellipticity inversion, the incorporation of independent measurements such as P-to-s RFs and T_a can help to further constrain the possible models (Chong et al., 2016). The 1D crustal structure underneath the InSight landing site was retrieved by jointly inverting the ε measurements (this work) with the mean P-to-s RFs by Joshi et al. (2023), obtained by stacking radial-component low-frequency RFs for eight high-quality marsquakes mainly originating in the Cerberus Fossae region (see Joshi et al. (2023) for further details). Additionally, the T_a obtained by Schimmel et al. (2021) were included, which are understood as the two-way travel times of P waves bouncing back from the first ($\sim 6.15\,s$) and second ($\sim 10.6\,s$) strong discontinuity within the crust.

For every model, the RF forward calculation is performed via a Python implementation of the code by Shibutani et al. (1996), using a fixed ray parameter $p^* = 6.9$ s/deg, suitable for events in the Cerberus Fossae region (Joshi et al., 2023). In the RF, four peaks at around 0, 2.4, 4.8 and 7.2 s are observed, which are related to the direct P phase and three converted phases P_1s, P_2s, P_3s, where the subscript indicates the interface where each phase is generated. The predicted ellipticity curves are obtained via the *gpell* toolbox included in the Geopsy package (Wathelet, 2005). Lastly, the T_a are computed assuming two-way vertical travel paths of the P waves.

The inversion scheme utilized is the Neighbourhood Algorithm (NA), first introduced by Sambridge (1999) and widely used for multiple geophysical applications, including subsurface characterization (e.g., Hobiger et al., 2013; Ferreira et al., 2020; Carrasco et al., 2022). A modified version of the NA was aplied, where the parameters space can be constrained by physical conditions and prior information (Wathelet, 2008). The parameter space is configured as 3-uniform-layers over a half-space (3LOH), where the depths of the discontinuities are constrained by the depth ranges found by Joshi et al. (2023). The shear-wave velocity V_s, P-wave velocity V_p and bottom depth z of each layer were inverted. Density was linked to V_p by using the empirical relationship by Brocher (2005), as suggested by Lin et al. (2012) for handling the trade-off with V_p/V_s, which was allowed to vary between 1.45 and 2.2. The upper mantle is modeled as a half-space with V_s between 4 and 5 km/s, following the results for the surrounding region using surface waves (Kim et al., 2022b) and teleseismic phases (e.g., Drilleau et al., 2022; Durán et al., 2022). These values are assumed to be also valid at the ILS as the composition and characteristics of the upper mantle are expected to be more homogeneous at larger scales than the crust, which is more exposed to local phenomena. See Table 6.3 for further parameterization details. The empirical relationship by Brocher (2005) is:

$$\rho = 1.6612V_p - 0.4721V_p^2 + 0.0671V_p^3 - 0.0043V_p^4 + 0.000106V_p^5 \tag{6.1}$$

The NA is based on a fully non-linear, self-adaptive Monte Carlo approach, which efficiently explores the parameters space in order to find the model $\mathbf{m}$ that minimizes the global misfit function Ψ between the observed and theoretical data. For each explored model $\mathbf{m}$, Ψ is defined as:

	V_s [km/s]	V_p [km/s]	Bottom depth [km]	V_p/V_s
Layer 1	1.0 - 3.0	2.0 - 5.0	5 - 12	1.45 -2.2
Layer 2	1.5 - 4.0	2.5 - 6.0	18 - 28	1.45 -2.2
Layer 3	2.5 - 5.0	3.5 - 7.0	32 - 45	1.45 -2.2
Half-space	4.0 - 4.8	7.5 - 8.5	-	1.45 -2.2

Table 6.3: Constraints of the parameter space utilized during the joint inversion of ellipticity, Receiver Functions and autocorrelations data set, using the Neighbourhood Algorithm and three layers over a half-space configuration (3LOH).

$$\Psi(\mathbf{m}) = W_e\psi_e(\mathbf{m}) + W_{rf}\psi_{rf}(\mathbf{m}) + W_a\psi_a(\mathbf{m}), \tag{6.2}$$

where W_e, W_{rf} and W_a correspond to the weights of the ellipticity, P-to-s Receiver Functions and autocorrelation times, respectively. The individual misfits for each data set are calculated according to the following equations:

$$\psi_e(\mathbf{m}) = \sqrt{\frac{1}{N}\sum_{i=1}^{N}\frac{(\log_{10}(\varepsilon_{\mathrm{m}i}) - \log_{10}(\varepsilon_{\mathrm{d}i}))^2}{\sigma_{\mathrm{d}i}^2}}, \tag{6.3}$$

$$\psi_{rf}(\mathbf{m}) = \sqrt{\frac{1}{M}\sum_{j=1}^{M}\frac{(RF_{\mathrm{m}i} - RF_{\mathrm{d}i})^2}{\sigma_{\mathrm{d}i}^2}}, \tag{6.4}$$

$$\psi_a(\mathbf{m}) = \sqrt{w_{\tau1}\frac{(\tau_1^t - \tau_1^o)^2}{\sigma_t^2} + w_{\tau2}\frac{(\tau_2^t - \tau_2^o)^2}{\sigma_t^2}}, \tag{6.5}$$

where $\psi_e(\mathbf{m})$, $\psi_{rf}(\mathbf{m})$ and $\psi_a(\mathbf{m})$ correspond to the misfit of the ellipticity, P-to-S Receiver Functions and autocorrelation times data sets, respectively. The misfit of the ellipticity curve is calculated in the period range between 15 an 35 s, where N is the total number of discrete periods where the misfit is calculated. ε_{mi}, ε_{di} and ε_{mi}, correspond to the synthetic ellipticity calculation, the measured ellipticity and the standard deviation at the i-th period, respectively. The misfit of P-to-S RFs ψ_{rf} is calculated in the time domain between -1 and 10 s with respect to the direct P-wave arrival, where M is the total number of time samples where the misfit is computed. $RF_{\mathrm{m}j}$, $RF_{\mathrm{d}j}$ and $\sigma_{\mathrm{d}j}$ are the synthetic P-to-s RF calculation, the measured P-to-s RF and the standard deviation at the j-th sample, respectively. Finally, τ_k^t and τ_k^o are the calculated and measured values for the first ($k = 1$) and second ($k = 2$) arrival times of P-wave reflections from autocorrelations analysis (Schimmel et al., 2021). From the observations, a common uncertainty of $\sigma_t = 0.2$ s is used. As the travel time through the first layer is contained in the travel time from the second discontinuity, different weights are used, where $w_{\tau1} = 0.35$ and $w_{\tau1} = 0.65$, respectively. The synthetic P-to-S Receiver Functions are calculated assuming a ray parameter of 6.9 s/deg.

6.5.3 Initial inversions for local crustal structure

Before performing the joint inversion detailed above, it is worth noting that the inversion of ellipticity-data-only cannot constrain the number of layers of the subsurface structure. This is revealed by inverting the characteristic ellipticity curve for the ILS using model parameterizations with one, two, three and four layers over a half-space, as shown in Fig. 6.12. In all these cases, the target ellipticity curve can be adequately inverted but the resulting subsurface models are different from each other. Instead, in the absence of distinctive features like peaks or troughs, the Rayleigh-wave ellipticity curve provides constraints on the average absolute shear-wave velocity over a specific depth range rather than on the number of discontinuities. For this case, it can be inferred that the absolute average velocities fitting the observed ellipticity curve are between 2.5 and 3 km/s roughly in the first 40 km.

On the other hand, the inversion of P-to-s Receiver Functions can map the discontinuities in a subsurface model but there is a strong trade-off between absolute shear-wave velocities and the depth of the discontinuities. Thus, using these different data sets offers a proper way to constrain the crustal structure at the ILS.

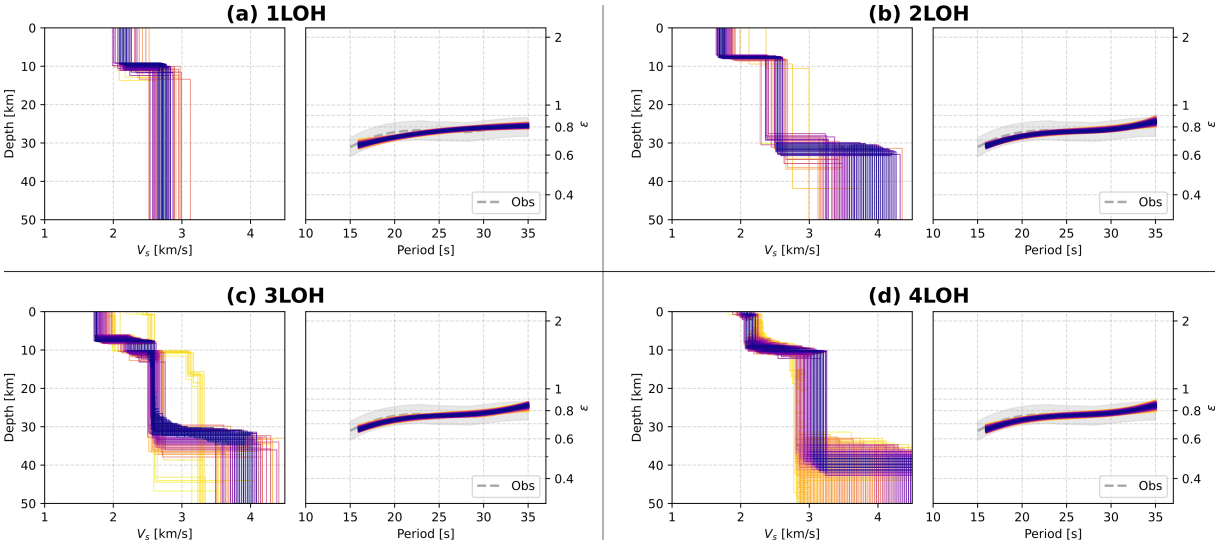


Figure 6.12: Inversion of ellipticity data only using different parameter settings with **(a)** one, **(b)** two, **(c)** three and **(d)** four layers over a half-space. For each case, a collection of models best-fitting the observed ellipticity (gray dashed curve) curve are plotted (darker colors indicate better misfit).

The joint inversion detailed above was performed using the $W_e = W_{rf} = 0.45$ and $W_a = 0.10$. Other combinations of weights were also tested but they provided a worse simultaneous fitting of the three independent data sets (see Appendix A4). The joint inversion results suggest that these local measurements can be well explained by a three-layer model, with an overall good fitting of the three data sets (see Fig. 6.13). However, the amplitude of the P phase (first peak on the RFs), which is not normalized as it provides information on the near-surface velocities (e.g., Ammon, 1991), is clearly overestimated (Fig. 6.13b). As shown by synthetic forward modeling (Fig. 6.14), lower amplitudes for this arrival can be achieved by having lower velocities in the first layer.

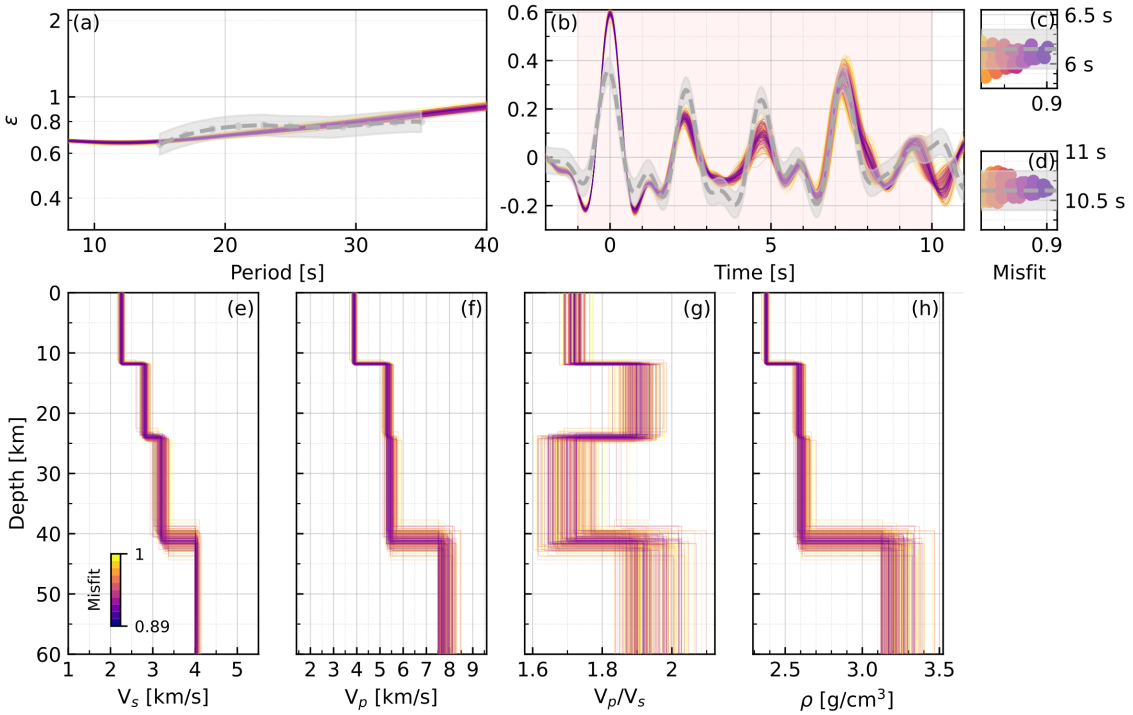


Figure 6.13: Results of joint inversion using 3LOH parameterization. The measurements and the synthetic modeling of 200 random best-fitting crustal models are shown for the **(a)** Rayleigh wave ellipticity, **(b)** P-to-s RFs from Joshi et al. (2023), and the **(c)** first and **(d)** second P-wave reflection times from autocorrelations by Schimmel et al. (2021). In these plots, the light gray dashed line and area correspond to the measured data and their uncertainty, respectively, whereas the synthetic data are colored by their misfit. The corresponding crustal models are shown in terms of (e) Vs, (f) Vp, (g) Vp/Vs and (h) density ρ as a function of depth. Taken from Carrasco et al. (2023).

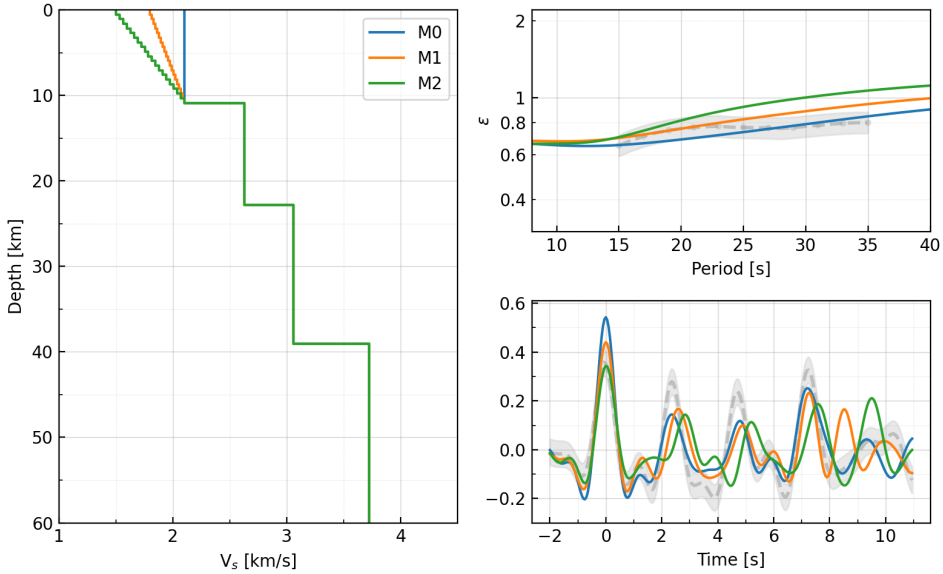


Figure 6.14: Synthetic forward modeling of ellipticity (top right) and P-to-s RFs (bottom right) for three different models. The measured ellipticity and P-to-s RFs are plotted with gray dashed lines. Only the velocities in the first layer are modified for these synthetic calculations. Taken from Carrasco et al. (2023).

6.5.4 Local crustal structure at the InSight landing site

Considering the fact that lower velocities are needed at shallow depths, a second inversion was performed where a shallow low-velocity layer was allowed (4LOH, see Table 6.4 for details on the parameter space). As for the 3LOH case, the same weights of the data sets ($W_e = W_{rf} = 0.45$ and $W_a = 0.1$) were used as they provide the best fit of the observations (see Appendix for results of other inversion runs with different weights). These new models resulting from the 4LOH joint inversion are preferred as they explain the three independent data sets reasonably well (Fig. 6.15a-d), and especially the amplitude of the direct P-phase arrival is well retrieved.

	V_s [km/s]	V_p [km/s]	Bottom depth [km]	V_p/V_s
Layer 0	0.7 - 1.8	1.8 - 4.5	0.5 - 4	1.45 -2.2
Layer 1	1.0 - 3.0	2.0 - 5.0	5 - 12	1.45 -2.2
Layer 2	1.5 - 4.0	2.5 - 6.0	18 - 28	1.45 -2.2
Layer 3	2.5 - 5.0	3.5 - 7.0	32 - 45	1.45 -2.2
Half-space	4.0 - 4.8	7.5 - 8.5	-	1.45 -2.2

Table 6.4: Constraints of the parameter space utilized during the joint inversion of ellipticity, Receiver Functions and autocorrelations data set, using the Neighbourhood Algorithm and three layers over a half-space configuration (4LOH).

A shallow low-velocity layer at the ILS

The joint-inversion results show that a 4-layer crust structure (Fig. 6.15e-g), including a shallow low-velocity layer (sLVL) close to the surface, can explain the local-scale measurements well. The sLVL presents velocities between 1.6 and 1.8 km/s and extends down to 2-3 km depth. Its origin is unclear, but previous works on the shallowest structure of Mars have proposed the presence of sedimentary and heavily fractured basalt layers in the first hundreds of meters (Hobiger et al., 2021; Carrasco et al., 2022), where $V_s < 1$ km/s were derived. Furthermore, Pan et al. (2020) suggested the presence of a sedimentary layer extending from 200-300 m up to kilometers in depth, whereas Warner et al. (2022) showed evidence for heavily fractured basalt units in the surrounding area. Thus, this shallow discontinuity is interpreted as the bottom of this large-scale unit.

The sLVL results from combining the different data sets through the joint inversion, rather than from a specific feature of the RF. Indeed, Shi et al. (2023) showed that the signal at ~ 1 s in the high-frequency RFs, proposed to be related to the sLVL, is absent in the synthetic low-frequency RFs. Despite observing a similar 1 s signal in the low-frequency RF used in this work, the RF-only inversion with 3LOH shows that it is not necessarily related to an sLVL (Fig. A4.1). Instead, given the constraints on the shear-wave velocity of the upper mantle, the ellipticity data allows a range of absolute average crustal V_S to fit the data, which leads to too high velocities near the surface for the RF, so a top layer with lower velocities is required. This shallow layer had not been reported from previous inversion works as ellipticity data was unavailable and a three-layer crustal model was enough to explain the P-to-s RFs, which were the main data set used for the inversion.

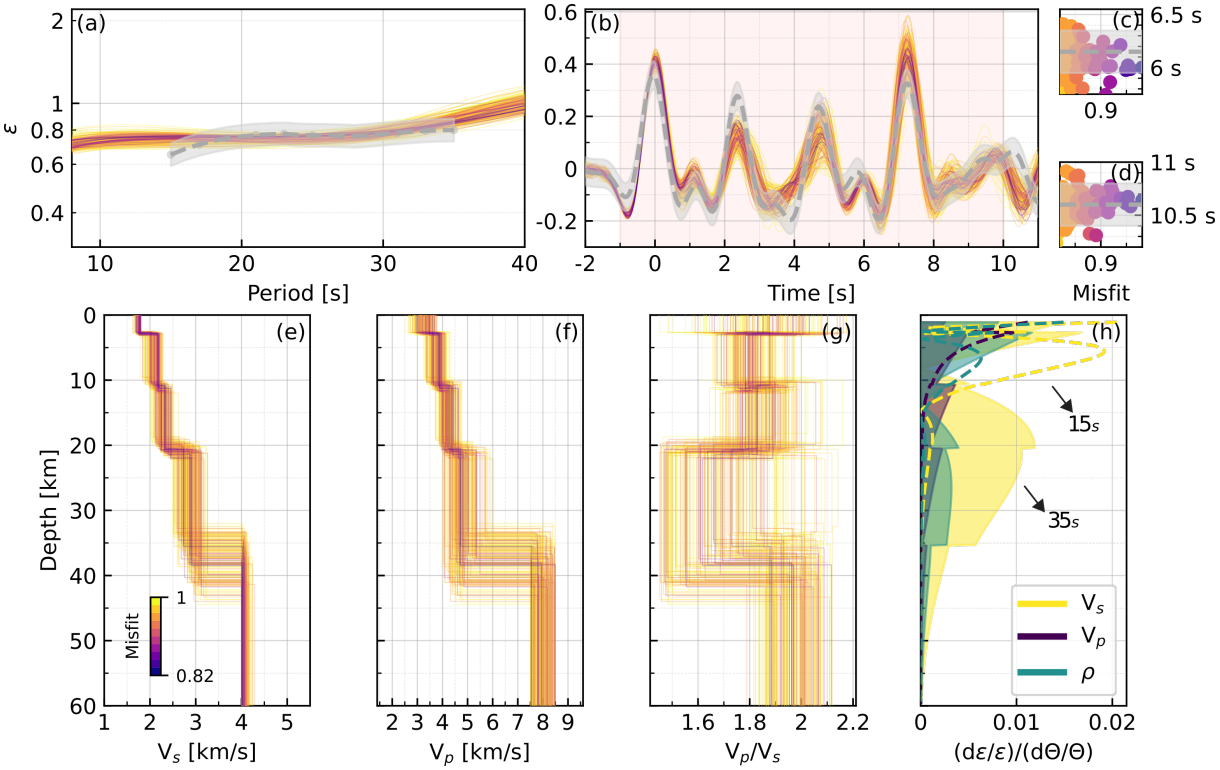


Figure 6.15: Joint-inversion results and resulting Martian crustal models using a 4LOH parameter space. The measurements and the synthetic modeling of 200 best-fitting crustal models are shown for **(a)** Rayleigh wave ellipticity, **(b)** P-to-s RFs from Joshi et al. (2023), and **(c)** first and **(d)** second P-wave reflection times from Schimmel et al. (2021). The light gray dashed line and area correspond to the measured data and their uncertainty, respectively, whereas the synthetic data are colored by their misfit. The corresponding crustal models are shown in terms of **(e)** V_s, **(f)** V_p and **(g)** V_p/V_s, as a function of depth. **(h)** Depth absolute sensitivity kernels of ellipticity data for the best-fitting model, calculated at 15 s (dashed line) and 35 s (filled area) for V_s, V_p and ρ. Light red box in (b) shows the time window where the data was fitted. Taken from Carrasco et al. (2023).

Other independent methodologies and data sets have recently provided further confirmation of this shallow layer. On the one-hand side, Drilleau et al. (2023) used the body wave arrival times and group velocity dispersion curves generated by nearby meteorite impacts ($<$ 100 km distance) to jointly invert for the upper crust structure in the vicinity of the ILS. In this inversion, a similar sLVL 1-2 km thick is required to explain the observations. On the other hand, from the waveform analysis of the S1222a P-wave time window, the anomalous ground motion recorded on the transverse component can be explained by an isotropic sLVL layer over an anisotropic layer (J. Li, pers. comm.). This latter is compatible with the anisotropic nature of the layer with a bottom depth of around 10 km depth (Li et al., 2022e).

Local crustal velocities and Moho depth

In general, below the sLVL, the resulting models have a similar structure and the discontinuities at ∼10 and ∼20 km depth are in good agreement with previously reported models for the local crust (e.g., Knapmeyer-Endrun et al., 2021; Joshi et al., 2023). The discontinuity around 37 km depth is interpreted as the crust-mantle boundary (Moho),

where the sharpest velocity contrast is observed. Even though the ellipticity data has low sensitivity at this depth, it can properly constrain the shallow V_S structure (Fig. 6.15h), which directly affects the deeper structure as they are strongly tied through the RFs. Nevertheless, the ellipticity data can properly constrain the velocities at shallow depths and, given the identification of the P_3s phase on the RFs, the joint-inversion can provide reliable depths for this discontinuity. In this case, the Moho depth is shallower than in other published models due to the trade-off between velocity and discontinuity depth. As comparably lower velocities are required for the crust, the Moho has to be located at a shallower depth to obtain the same travel time for the P-to-s conversion.

Overall, crustal V_p and V_s are lower than 5 and 3 km/s, respectively (Fig. 6.15e,f). Vp/Vs is around 1.8 in the first 20 km of the crust and, even though a large variation is observed, it seems to decrease in the bottom layer of the crust (Fig. 6.15g). In particular, V_s are lower than in other regions on Mars, such as along the path between Amazonis Planitia and the InSight site in the lowlands (Kim et al., 2022a), or between S1222a and the lander, along the dichotomy region (Li et al., 2022c). Although an increase in density is derived from the inversion, the inverted data sets are poorly sensitive to this parameter, as shown for the ellipticity (Fig. 6.15h), so further interpretation is avoided. At a local scale, the proposed V_s are also slightly lower than those previously reported for the InSight site (Knapmeyer-Endrun et al., 2021; Joshi et al., 2023). Therefore, considering that porosity plays an important role in decreasing the velocity of the seismic waves (e.g., Heap, 2019), these lower velocities might be related to an even larger porosity or stronger alteration of the whole crust at the InSight site than previously thought.

6.6 Summary and concluding remarks

For the first time, the ellipticity of the fundamental mode of direct Rayleigh waves was measured on Mars for periods between 15 and 35 s, mainly thanks to S1222a, the largest Martian seismic event ever recorded. Data from events S1000a and S1094b, two large seismic events related to meteorites impacting the Martian surface, were also utilized for certain periods. No further Rayleigh waves directly related to seismic events have been detected on Mars or they have not enough amplitude on the radial components (e.g., R_2 and R_3 from S1222a), so this data set is the best that can be obtained for the Red Planet.

The obtained ellipticity curve is interpreted as a good representation of the characteristic ellipticity at the InSight landing site. It is a relatively flat curve (no clear peaks or troughs), and thus, it does not provide on the number of discontinuities but rather on the absolute average shear-wave velocities over a specific range of depths. Anomalously low phase shifts ($\phi < 70°$) were measured particularly for S1222a, which seem to be unrelated to the long-term mechanical properties of the local crust structure. Similar low phase shift values have also been measured on Earth, but only for specific earthquakes and not as a long-term feature of a subsurface structure or propagation path. This phenomenon is out of the scope of this work and further investigation on this topic is encouraged.

In order to consolidate the local crustal model, a joint inversion of local-scale observations (Rayleigh-wave ellipticity, P-to-s RFs and P-wave reflection times) was performed, which map the crust at a similar scale. The parameterization of the model plays a key role in determining the proper subsurface structure. A three layers over a half-space (3LOH) model cannot fit all the observations simultaneously because it particularly overestimates the amplitude of the direct P phase on the P-to-s RFs. Therefore, a parameterization allowing lower velocities close to the surface is needed.

A parameterization with four layers over a half-space (4LOH) is preferred for the joint inversion. The inversion results suggest that a four-layer crustal model, with a shallow low-velocity layer (sLVL) of about 2-3 km thickness at the ILS explains the observations well. Other discontinuities around 10, 20 and 37 km depth, the latter interpreted as the Moho depth, correlate well with previously reported models. One of the most distinctive features of the crustal model proposed derived from the joint inversion is the confirmation of the thin sLVL at the ILS. This layer has been previously proposed by Shi et al. (2023) as a possible way to explain the high-frequency P-to-s RFs from S1222a and has also been derived from the inversion and analysis of other independent measurements (e.g., local-scale dispersion of surface waves, waveform modeling). The origin of this first discontinuity is understood as the bottom of a shallow sedimentary or highly-fractured layer proposed from geological analyses. These crustal models are publicly available in a Zenodo repository (Carrasco, 2023).

The resulting P- and S-wave velocities for the crustal layers are lower than previous estimates for the local crust. This is due to the constraint on the shear-wave velocity of the upper mantle and the Rayleigh-wave ellipticity measurements, which combined allow a specific range of average absolute shear-wave velocities. Simultaneously, these local-crust velocities are lower than the crustal wave velocities determined for other regions on Mars, suggesting a higher porosity or alteration of the Martian crust at the InSight landing site due to local-scale phenomena.

CHAPTER 7

Towards a consolidated model of the subsurface structure at the InSight landing site

Throughout this work, two different approaches have been taken in order to investigate the subsurface structure at the InSight landing site (ILS) at different scales: in the order of meters, with the horizontal-to-vertical spectral ratios (HVSR), and at a kilometers-crustal scale, using the Rayleigh-wave ellipticity measurements, P-to-s Receiver Functions and reflection times from autocorrelations. Here, the models proposed in Chapter 5, for the shallow subsurface, and Chapter 6, for the crust, are studied together, aiming at having an integral model that explains the different observations simultaneously. In addition, after other works with similar objectives have been published, the subsurface structure models found in this work are compared with others proposed for the ILS as well as for more regional and global scales.

7.1 The ILS subsurface structure at intermediate depths

The models proposed throughout this work cover different scales of the subsurface structure: while models in Chapter 5 reach depths of tens of meters, due to the frequency range 0.4-10 Hz, the models in Chapter 6 cover the kilometers-scale characteristics of the ILS underground structure by using the frequency range roughly between 0.03-0.07 Hz. A harmonization of these models, i.e., a single consolidated subsurface structure including all these features, is necessary to get a more complete picture of the processes occurring at the InSight landing site.

The lack of observations in the frequency range 0.07-0.4 Hz generates a gap in the mapping at intermediate depths, from tens of meters to a couple of kilometers. This frequency range was not covered due to (i) the lack of HVSR observations with enough

seismic energy in this frequency range, from the coda of the seismic events at that time, and (ii) the low signal-to-noise ratio of the recorded Rayleigh waves at higher frequencies (periods lower than ∼15 s). As the high-frequency measurements map the tens of meters and the low-frequency ones cover the kilometers-scale structure, this intermediate frequency range is related to the subsurface structure at intermediate depths, namely between tens to hundreds or couple thousand of meters. Some brief initial discussion on this is given in Chapter 6, where the shallow low-velocity layer is related to a heavily fractured first layer or a sedimentary layer of several hundred meters (Warner et al., 2022; Pan et al., 2020), but further assessment is needed.

7.1.1 HVSR from S1222a coda

The seismic event S1222a, used in Chapter 6, presented a several-minute-long S-wave coda with significant vertical and horizontal ground motion at frequencies even lower than 0.1 Hz (Fig. 7.1a and b), which offers the opportunity to study the H/V response at the missing intermediate frequencies. In fact, the HVSR is relatively stable (Fig. 7.1c) and the coda is depolarized (Fig. 7.1d) between 20 and 90 minutes after the P-wave

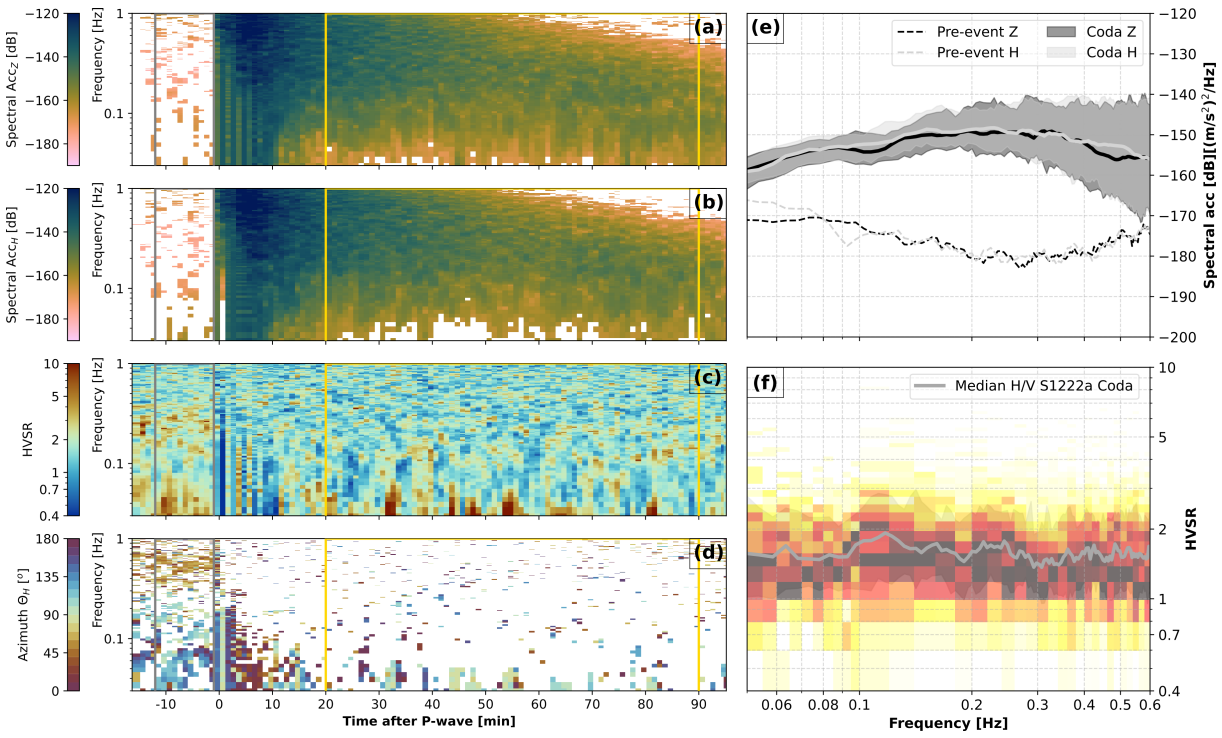


Figure 7.1: Spectral features and HVSR of S1222a. **(a)** Vertical and **(b)** horizontal spectral power between 0.03 and 1 Hz. Only frequency-time windows above the pre-event noise level are colored. The pre-event noise level is computed using an 11-minute time window before the arrival of the P-wave, as given by the gray box in the spectrograms. The yellow box delimitates the window of interest for the coda analysis. **(c)** Evolution of HVSR for event S1222a. **(d)** Horizontal incidence angle (azimuth Θ_H) of incoming signal. Only highly polarized signals ($dop > 0.7$) are colored. **(e)** Spectral power of the vertical and horizontal components in the coda of S1222a event. **(f)** Histogram of Horizontal-to-vertical spectral ratio of S1222a coda using 120 s time windows with 50% overlap over the 70-min coda window shown in (a)-(d). Darker colors represent a higher number of occurrences. The median H/V between 0.05 and 0.6 Hz is plotted as a gray curve.

arrival. This 70-minute long time window is enough to obtain a reliable HVSR curve in the frequency range 0.05-0.5 Hz, where vertical and horizontal ground-motion amplitudes larger than the pre-event noise level are recorded (Fig. 7.1a, b and e). The H/V is calculated on 120-seconds long time windows with 50% overlapping (69 time windows in total). The resulting histogram and median HVSR are shown in Fig. 7.1f, from which no strong peaks or troughs are observed in the frequency range 0.06-0.6 Hz, preliminarily suggesting the absence of strong discontinuities at intermediate depths. Interestingly, the HVSR amplitudes in the range 0.1-0.2 Hz shape a slight peak potentially related to the subsurface structure. As for the case of the events, this HVSR curve in this frequency range is expected to be characteristic of this site.

7.1.2 Forward modeling of possible models

The intermediate frequencies 0.06-0.6 Hz, covered by the S1222a coda HVSR, can help to gain information about the subsurface structure at intermediate depths (tens to hundreds or a few thousands of meters). In order to evaluate possible structural features in this depth range, forward modeling using possible transitions from shallow to crustal depths is performed. For this, one characteristic model from the joint inversion in Chapter 6 is used as a representative crustal structure at the ILS. At shallow depths, as different models were proposed depending on the maximum allowed shear-wave velocity, two models representing the M2 and L2 families were evaluated. The S2 models are disregarded as they present unrealistic bLVL (extremely narrow or low speeds). The SML1 models are also not considered to avoid further complexities and because they can be understood as extreme cases of the SML2 models, with even lower velocities for the bLVL.

Theoretical predictions were computed for a new model built from the combination of the shallow and crustal models (M2-crust, L2-crust), for which a transition layer was inserted. This transition layer is a homogeneous layer with the same velocity as the half-space of the representative shallow structure, followed by a layer with the properties of the shallowest layer of the representative crustal model. Different thicknesses of the transition layer were tested by placing its bottom at 500 m, 1000 m and 1500 m depth (Fig. 7.3a and 7.2a). For each of these models, the predicted Rayleigh-wave ellipticity and full-wavefield HVSR are compared against the observations (Fig. 7.2b and 7.3b), as well as the theoretical P-to-s RFs (Fig. 7.2c and 7.3c).

The synthetic curves in Fig. 7.2 and 7.3 allow some preliminary conclusions about this type of transition layer. For the M2 model, a clear full-wavefield resonance peak is generated at low frequencies. The resonance peak is shifted towards lower frequencies and has a larger amplitude as the thickness of the transition layer increases (Fig. 7.2b). Although a slight peak is observed between 0.1 and 0.2 Hz from the S1222a coda HVSR measurements, this is not comparable to the synthetic peak. The predicted Rayleigh-wave ellipticity is also inconsistent with the observations. Besides, there is a clear mismatch between the predicted and observed P-to-s RFs (Fig. 7.2c). Similarly, although more subtle, the subsurface structures using the L2 models also show some inconsistencies, mainly related to the mismatch between the predicted and observed P-to-s RFs (Fig. 7.3c). The predicted ellipticity and HVSR are more in line with the observations (Fig. 7.3b).

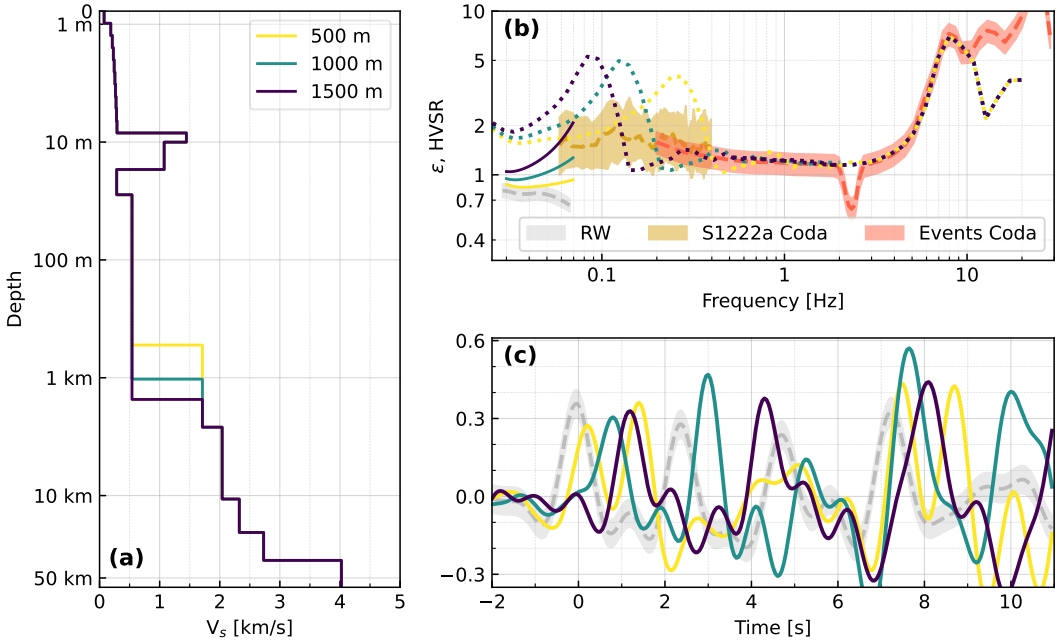


Figure 7.2: Consolidated ILS subsurface model using a homogeneous intermediate layer and a representative M2 model for the shallow subsurface. **(a)** Shear-wave velocity vs depth profile combining a representative shallow subsurface model M2, as derived in Chapter 5, and a representative model for the crust, as derived in Chapter 6. The shallow subsurface and crustal models are linked using a homogeneous layer, whose bottom depth is at 500 m (yellow), 1000 m (green) and 1500 m (dark blue) depth. **(b)** Fitting of synthetic Rayleigh-wave ellipticity (solid lines) and full-wavefield HVSR (dotted) to corresponding measurements of direct Rayleigh waves (gray), S1222a coda (orange) and coda of seismic events (red). **(c)** Fitting of synthetic P-to-s Receiver Functions to measurements from Joshi et al. (2023).

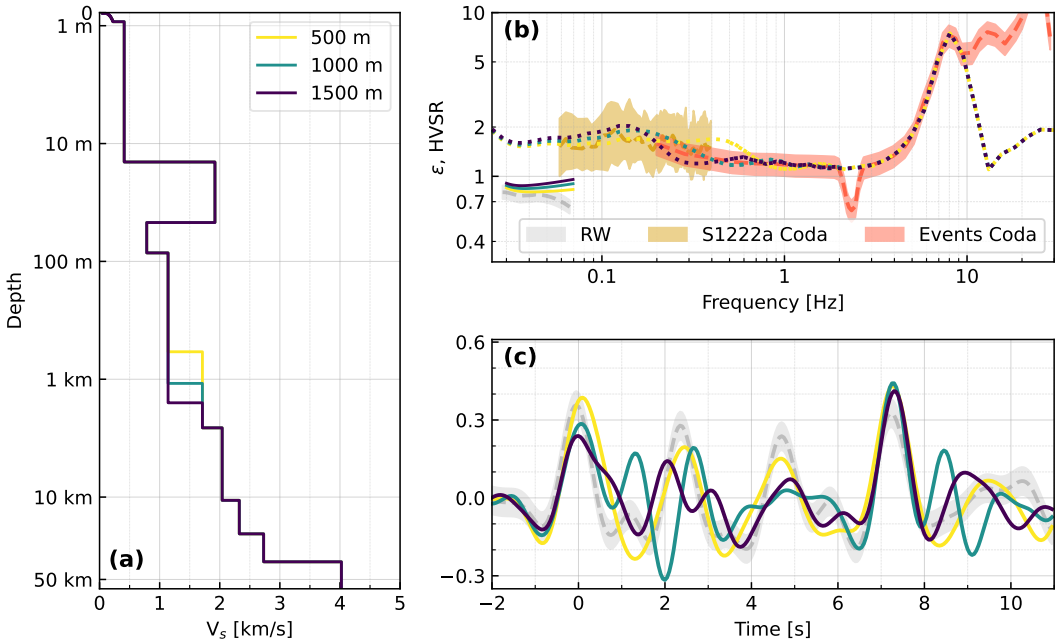


Figure 7.3: Consolidated ILS subsurface model using a homogeneous intermediate layer and a representative L2 model for the shallow subsurface. **(a)**, **(b)** and **(c)** show the same as in Fig. 7.2, but using the representative L2 model at shallow depths.

Due to these differences between predictions and observations, and given the presence of resonant peaks, a second set of models was tested using a smoother transition layer. This transition layer was modeled as a layer with a power-law velocity increase. For this, the top and bottom velocities of the transition layer are given by the half-space of the shallow structure and the first layer of the crustal structure, respectively. The velocity then increases as a power of four. The bottom of the transition layer is again evaluated at 500 m, 1000 m and 1500 m (Fig. 7.4a and 7.5a). The predictions are shown in Fig. 7.4b,c and 7.5b,c.

Despite the smoother transition, the computed synthetics using the M2 model show some clear resonant HVSR peaks, now at frequencies between 0.5 and 2 Hz, unobserved in the data (Fig. 7.4b). A mismatch is also observed towards higher frequencies in the Rayleigh-wave ellipticity curve. Nevertheless, there is a better fit of the P-to-s RFs for all the evaluated models (Fig. 7.4c), compared to the homogeneous transition layer case. The L2-crust model, including the smooth transition layer, seems to present an even better fit to all the observations assessed here (Fig. 7.4) than the M2-crust case. In particular, the predicted full-wavefield HVSR fits well with the observations in the frequency range of 0.06-0.4 Hz. Some deviations are observed between 0.4 and 1 Hz, but these are not as large as in the M2-crust case. In both cases, there is a mismatch at high frequencies in the Rayleigh-wave ellipticity curve, which can be related to the lack of observations, as well as a better fit to the P-to-s RFs.

Although this is a first-order analysis, some interesting conclusions can be drawn. First, a transition layer with increasing velocity at intermediate depths seems more likely than a homogeneous layer, as this latter would generate strong resonant HVSR peaks and incompatible P-to-s RFs. This smooth transition layer can be understood as a thick sedimentary layer, as proposed by Pan et al. (2020), for which such increasing velocity profiles have been proposed due to sediment compaction with depth (e.g., Faust, 1951). Secondly, the L2 shallow subsurface models seem to be more compatible with the proposed crustal structure than the M2 models, which, due to the lower velocities, generate stronger resonant HVSR peaks that are not observed in the data. Instead, the L2-crust model with a smooth transition layer can satisfactorily predict the different data sets. However, some differences are observed, such as the mismatch of the Rayleigh-wave ellipticity towards high frequencies, which may be due to other complexities of the model. For these purposes, a joint inversion using all these observations and allowing the different parameters to vary in suitable ranges is strongly encouraged.

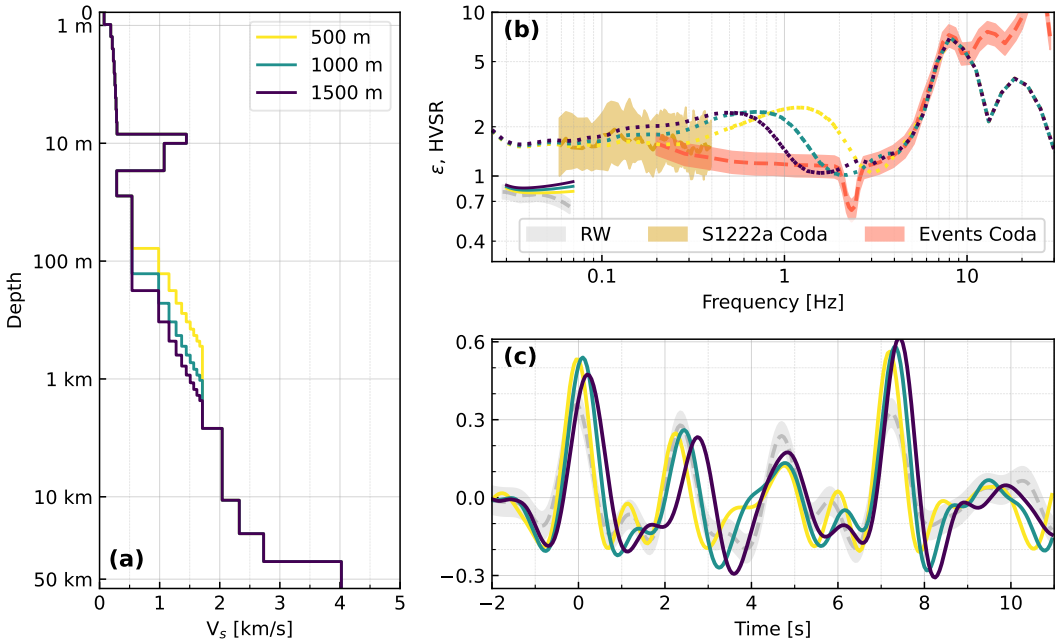


Figure 7.4: Consolidated ILS subsurface model using an intermediate layer with power-law velocity increase and a representative M2 model for the shallow subsurface. **(a)**, **(b)** and **(c)** show the same as in Fig. 7.2, but using a power-law transition layer from shallow to crustal depths. In this case, the indicated depth corresponds to the bottom depth of the power-law transition layer.

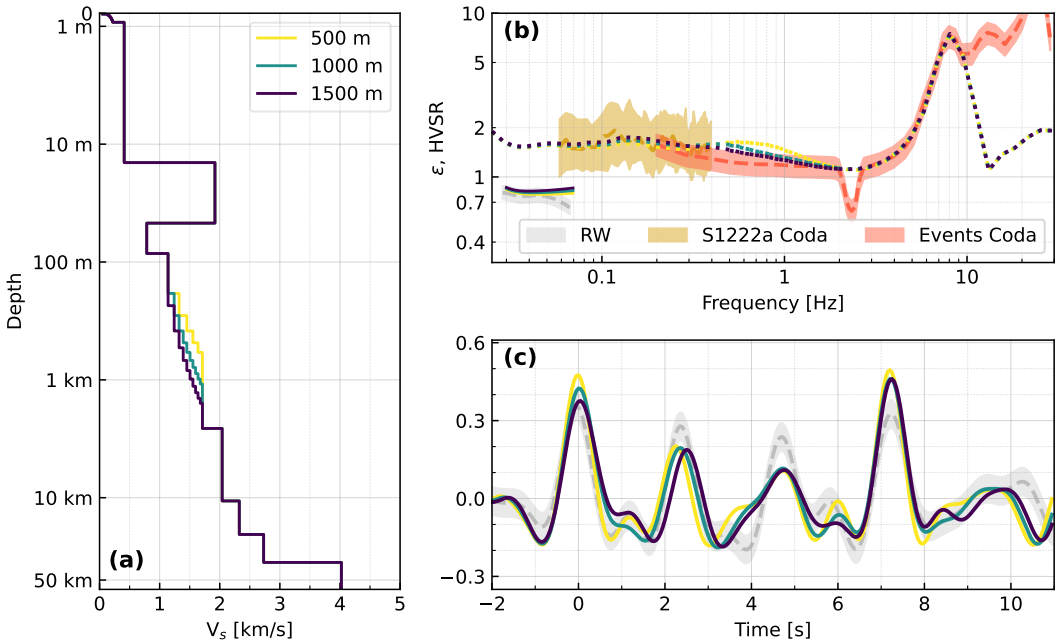


Figure 7.5: Consolidated ILS subsurface model using an intermediate layer with power-law velocity increase and a representative L2 model for the shallow subsurface. **(a)**, **(b)** and **(c)** show the same as in Fig. 7.4, but using the representative L2 model at shallow depths.

7.2 A consolidated subsurface structure at the ILS

The above forward modeling analysis provides valuable insights for a more comprehensive understanding of the subsurface structure at the ILS, both at shallow (in the range of meters) and crustal (kilometers) scales. In this section, a consolidated model involving both parts, shallow and crustal, is presented in terms of the geological history of Mars and discussed against recent independent observations through different approaches. Rather than deciding which model is closest to the real one, which is unknown, this section is limited to assessing the proposed model's validity.

7.2.1 The shallow subsurface

The shallow subsurface structure models (in the order of meters) were obtained using the horizontal-to-vertical spectral ratios (HVSR) from the coda of Martian seismic events. Because of the non-uniqueness problem intrinsic to this technique and the difficulties in defining the number of layers without further observations, a set of inversions using different velocity constraints and layering defined by pre-landing orbital imagery was performed. These different constraints provided three families of solutions to explain the HVSR features, including the 2.4 Hz resonance as a natural phenomenon or not. The different families mainly differ in the range of velocities, but the overall structure and pattern were roughly the same. Therefore, the most reliable outcome of the HVSR inversion was the pattern of velocity changes through the structure, rather than the absolute velocities or depths. Nevertheless, combining the HVSR features of the S1222a event coda and the crustal-scale observations, the forward modeling results in Section 7.1 suggest that the L2 models are more compatible with the deeper crustal structure than M2 models, so a shallow subsurface structure as such models is preferred. The following interpretations are thus based on the L2 model utilized in Section 7.1.

The first resolvable feature of the shallow subsurface structure is the discontinuity around 14 m depth. This discontinuity is directly related to the HVSR peak observed around 8 Hz and is the interface between the shallow units and a layer with high shear-wave velocity. As the maximum frequency utilized during the inversion is 10 Hz, the subsurface of the first ∼10 m (roughly above the resonant discontinuity) could not be resolved. The units above this discontinuity likely correspond to the impact-generated regolith, a sandy, unconsolidated layer close to the surface (Golombek et al., 2017), and an ejecta layer possibly mixed with some heavily fractured basalt. The physical weathering due to meteorite impacts and eolian erosion can lead to a high porosity and fracturing degree, drastically reducing the shear-wave velocity of these units (Saroglou and Kallimogiannis, 2017; Heap, 2019). Even using the constraints from hammering experiments (Brinkman et al., 2022) and a power-law increase for the velocity, as expected for the regolith (Morgan et al., 2018), this layer is unresolved, but such low velocities are compatible with the proposed models.

Due to the poor resolution at shallower depths, the possible discontinuities between these layers are also not resolved by the HVSR technique. In this regard, based on the inversion of ground compliance measurements, a change from a low-rigidity unit to a more consolidated material has been proposed to occur between 5 and 20 m, which has been interpreted as the transition from the ejecta layer to a more fractured basalt (Onodera

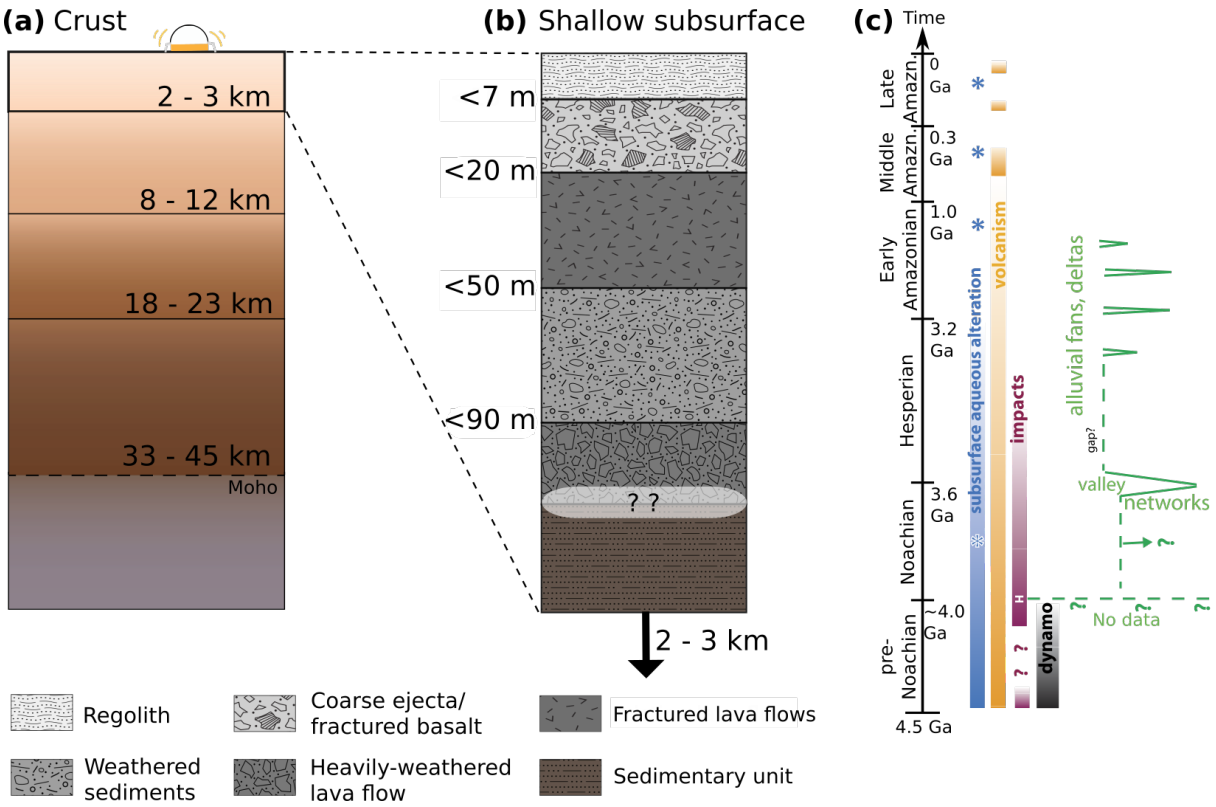


Figure 7.6: Schematic profile of subsurface structure at the ILS. **(a)** Crustal structure at the ILS, as derived in chapter 6, showing the depth ranges of the intracrustal discontinuities and the Moho. **(b)** Shallow subsurface structure, as inferred from L2 models in Chapter 5, presenting five layers including a regolith, coarse ejecta/fractured basalt, a pristine lava flow, a weathered sedimentary layer and a heavily-weathered lava flow, over a thick sedimentary layer that continuing down to the 2-3 km deep crustal discontinuity. The depth range of the discontinuities is indicated correspondingly. **(c)** Timeline of global processes on Mars, taken from Kite (2019). The geological ages roughly match the depths of the shallow subsurface units and discontinuities. H = Hellas impact event. * = subsurface aqueous alteration as recorded by Mars meteorites (). Dynamo timing is from Lillis et al. (2013). The horizontal span of fluvial processes (green) are scaled by the map-view scale of the landforms shown. Neither the thicknesses of the layers in (a) and (b), nor the duration of geologic eras in (c), are to scale.

et al., 2023). Similarly, the regolith layer has been estimated to be no thicker than ∼7 m (Kenda et al., 2020). Thus, the proposed shallow subsurface model at the ILS is expected to have a regolith layer with a thickness of less than ∼7 m, overlying an ejecta layer with a bottom discontinuity in the first 20 m depth, leading to a fractured basalt unit (Fig. 7.6b).

Beneath the ILS, the study of the age of the lava flows, based on the size-frequency distribution of craters and cratering production, suggests the presence of Early Hesperian and Amazonian lava flows (Warner et al., 2017; Wilson et al., 2019). Amazonian lava flows (∼1.7 Ga) are observed for craters with a diameter of 200-700 m, which reach shallower depths, whereas Early Hesperian lava flows (∼3.6 Ga) are revealed by analyzing craters with a diameter above 2 km, which excavate greater depths. Thus, the shallow high-velocity layer (sHVL), underlying the proposed ejecta layer and starting at ∼14 m, can be interpreted as Amazonian lava flows exposed to physical weathering. This sHVL was initially thought to be a pristine lava flow due to the high velocity (and contrast), but recent work shows that it coincides with a high stiffness layer, whose Young's modulus

is in the range of fractured basalts (Onodera et al., 2023). The relatively low velocities for a lava flow also support this idea (e.g., Fortin et al., 2011). Depending on this unit's degree of fracturing and porosity, and how these are removed with depth, the transition to a more pristine unit might be undetected. There is considerable uncertainty on the thickness of this layer (Fig. 5.8 in Chapter 5), but a model with a 20-40 m thick lava flow, as sketched in Fig. 7.6b, fits the HVSR observations. Beneath this high-velocity layer, there is a sharp transition to low velocities, leading to a buried low-velocity layer (bLVL), discussed in more detail below.

The buried low-velocity layer (bLVL) as a sedimentary unit

Although a more comprehensive study is needed to determine its exact origin, the bLVL can be interpreted as a sedimentary layer, due to the low shear-wave velocities, with a thickness of about 30-40 m. This sedimentary unit is followed by a deeper layer with slightly higher velocities, not higher than the sHVL, which is interpreted as another volcanic lava flow exposed to heavy and aqueous weathering processes before and during the formation process of the bLVL (Fig. 7.6b).

This bLVL was first proposed by Hobiger et al. (2021) and was interpreted as a sedimentary deposit *sandwiched* by an Amazonian layer, on top, and an Amazonian/Hesperian unit underneath. The observation of other sedimentary deposits cataloged as Amazonian-Hesperian transition units in nearby regions supports the possibility of having a sedimentary layer beneath the ILS (Tanaka et al., 2014). In fact, sedimentary deposits have been observed in the closest ∼400 km around the ILS, to the south with a 10-30 m thickness and beneath the Kalpin crater (Pan et al., 2020). Therefore, the bLVL can be understood as a sedimentary Amazonian-Hesperian transition layer.

Alluvial activity during the Hesperian has been documented ∼550 km to the south in the Gale crater (Grant et al., 2014; Grant and Wilson, 2019). Besides, the Late Hesperian to Amazonian transition has been cataloged as a global period with elevated precipitation that led to the formation of alluvial fans and deltas in different regions of the planet (e.g., Kite, 2019, and references therein). A similar trapped layer has been mapped near Utopia Planitia, using ground-penetrating radar (GPR) onboard the Zhurong rover (Li et al., 2022a), identified as a sedimentary layer ∼50 m thick related to a massive flood event during the Late Hesperian to Early Amazonian period. Although in another region of Mars and not necessarily representing the processes at the ILS, this finding is further evidence of enhanced global fluvial activity during the Late Hesperian-Amazonian transition period.

Recent works using different geophysical measurements and approaches provide subsurface models where the bLVL might be a possible structural feature. As shown by Onodera et al. (2023), the inversion of ground compliance measurements in the high-frequency band (>0.1 Hz) does not support the presence of a deep low-rigidity layer, interpretable as the bLVL proposed in this work. However, such a layer is needed when using the low-frequency band (0.01-0.05 Hz), but it is not preferred due to the unclear validity of Sorrell's theory at such low frequencies. Similarly, Xu et al. (2022) mapped the shallow subsurface using high-frequency dispersive seismic signals recorded by InSight, interpreted as the acoustic-to-seismic coupling of infrasound generated by the entry and

impact of meteorites. Their proposed model has a thin regolith layer (<5 m) and a 40-m thick layer that is interpreted as the coarse ejecta layer, over a half-space of $V_S \sim 1.5$ km/s. However, they show that a model including a bLVL, like Hobiger et al. (2021), provides reasonable results, although not as satisfactory as the inverted model. Due to the different depth sensitivities, spatial extent and the parameters involved, none of the models can be chosen as the closest to the actual subsurface. The potential joint inversion of these different meters-scale observations is under evaluation.

The heavily weathered lava flow

Below the bLVL, a layer with slightly larger velocities is present. These velocities differ from the models proposed by Hobiger et al. (2021), which have a corresponding layer with velocities even larger than the sHVL. These higher velocities in the deeper layer would generate a secondary prominent peak around 1-2 Hz that is not observed in the data. Unlike that work, the bottom depth of this layer is not resolved from the inversion process presented here, either due to a smooth transition to the underlying layer, because it is below the maximum resolvable depth (∼600 m), or a combination of both. In any case, the bottom depth of this lava flow layer might be around 200-300 m depth, as suggested by the cutoff diameter of rocky ejecta craters (Golombek et al., 2018).

Considering the geological pre-landing assessment of the ILS, this deep layer is interpreted as an Early Hesperian lava flow. The low velocities can be explained by highly fractured and altered lava flows that have undergone heavy weathering and likely aqueous alteration processes in the past. The range of shear-wave velocities of this layer (∼1 km/s) are low for theoretical or experimental weathered basaltic material (e.g., Vinciguerra et al., 2005; Heap, 2019), but similar values have been observed for lavas or volcanic breccia in Earth volcanic regions at depths around 100 m (Mora et al., 2006; Nardone and Maresca, 2011; Lesage et al., 2018).

This layer is proposed to have a volcanic origin, like the sHVL, but the different velocities are explained by a different degree of weathering due to different deposition times. On the one hand, this deeper volcanic layer was deposited during the Early Hesperian, when subsurface alteration was likely due to abundant aqueous processes and physical weathering was intense due to a high impact rate (Hartmann and Neukum, 2001). On the contrary, the sHVL was probably emplaced during the Late Hesperian or Early Amazonian (see Fig. 7.6b and c), when the impact rate decreased significantly compared to the Early Hesperian or Noachian periods, so physical weathering was less intense, and the aqueous processes were diminishing as well (e.g., Kite, 2019; Carr and Head, 2010).

The intermediate-depth sedimentary unit

As explained above, the HVSR inversion could not map changes in the subsurface structure deeper than ∼600 m depth for the L2 models. Thus, the intermediate-depth structure was inferred by evaluating the forward modeling results of a set of models obtained by connecting the crustal and shallow subsurface structures. The preferred models are those with a gradual velocity increase with depth rather than those with a sharp discontinuity.

This gradual increase in velocity is consistent with a large (2-3 km thick) sedimentary unit beneath the lava flows at the ILS, as proposed by Pan et al. (2020), based on regional geological evolution. Other similar sedimentary deposits (>2 km thick) have been proposed to have occurred during the Late Noachian in nearby regions like Aeolis Mensae (Irwin et al., 2004), about 500 km southeast of ILS. This idea is also supported by the general observation of regionally-integrated valley networks formed due to intense pluvial and fluvial activity during the Late Noachian to Early Hesperian periods (Fig. 7.6c), as proposed by various authors (e.g., Carr and Head, 2010; Hynek et al., 2010; Kite, 2019). Therefore, this sedimentary unit at the ILS likely corresponds to a sedimentary basin formed during the Late Noachian.

The transition from the heavily weathered Early Hesperian lava flow to the deep Late Noachian sedimentary unit would be rather smooth as no prominent peak is observed in the HVSR curve at low frequencies. It might be the case that the velocity difference between the lava flow and the top of the underlying sedimentary unit is imperceptible to the methods involved here. Based on the geological preliminary information, the deep sedimentary unit would start at around 200-300 m (similar to the dark blue model in Fig. 7.5) and will extend down to the first discontinuity of the crustal model proposed in this work, around 2-3 km depth. Analogous cases of similar sedimentary deposits can be found on Earth, like in the Los Angeles basin (LAB), a well-studied sedimentary structure that presents shear-wave velocities increasing from ∼0.5 km/s, close the surface, to ∼1.8 km/s at around 2 km depth (e.g., Jia and Clayton, 2021; Perton et al., 2020). Although the maximum thickness of the LAB is 8 km, local sub-basins can easily reach the basement at 2-3 km depth (Villa et al., 2023; Li et al., 2023), just like at the ILS.

7.2.2 The crustal scale

The Martian crustal structure at the ILS is divided into four layers overlying a half-space, interpreted as the upper mantle. The Moho is located at ∼38 km, where the most significant shear-wave velocity contrast is revealed (∼1 km/s). The intra-crustal discontinuities are located around 2-3 km, 8-12 km and 18-23 km depth. The corresponding shear-wave velocities are 1.6-1.8 km/s, 2.0-2.3 km/s, 2.2-2.5 km/s and 2.5-3.2 km/s for all the crustal layers, and ∼4.1 km/s for the upper mantle. This model concept and range of values are presented in Fig. 7.7.

Before this work, three sets of ILS crustal models based on the inversion of seismological data were proposed: KE21 (Knapmeyer-Endrun et al., 2021), DU22 (Durán et al., 2022) and JO23 (Joshi et al., 2023). The set of models by Durán et al. (2022) uses P-to-s RFs combined with regional and teleseismic body waves, resulting in a more regional-scale model. Thus, the crustal structure proposed here (hereafter, SC23) is more comparable to KE21 and JO23. The analysis of PP RFs by Kim et al. (2021b) narrowed down the possible KE21 models explaining the data, which are identified as KE21K in the following. Given the constraints used for the SC23 inversion, the depth ranges of the intracrustal discontinuities are similar to the previous local models (Fig. 7.7a). The major difference is the shallow 2-3 km thick layer in SC23, unreported by these works due to the lack of evidence at that time and the intrinsic non-uniqueness problem of the RFs inversion. This layer has also been proposed by Shi et al. (2023), based on forward

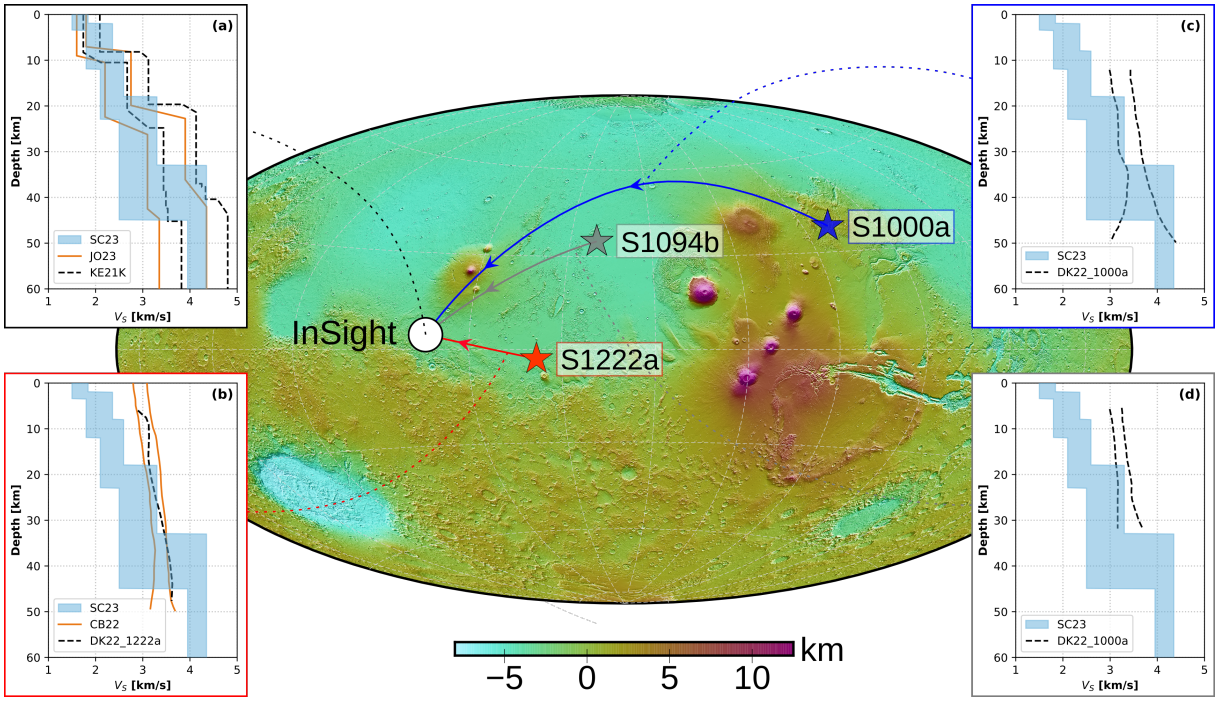


Figure 7.7: Comparison of available crustal structures on Mars for: **(a)** The ILS, as proposed by SC23 (this work), JO23 (Joshi et al., 2023) and KE21K (Knapmeyer-Endrun et al. (2021) after constraints from Kim et al. (2021b)). **(b)**The S1222a path, proposed by CB22 (Beghein et al., 2022) and DK22_1222a (Kim et al., 2022b). Given the evidence of anisotropy along this path, V_S corresponds to the Voigt velocity $V_S = \sqrt{\frac{2V_{SV}^2+V_{SH}^2}{3}}$. **(c)** The S1000a path, proposed by DK22_1000a (Kim et al., 2022a). **(d)** The S1094b path, proposed by DK22_1094b (Kim et al., 2022a). The range of values of the SC23 models are plotted as a blue area in all the cases. The topographic map shows the location of the InSight lander, the epicenter of events S1000a, S1094b and S1222a and their corresponding surface-waves paths.

modeling of high-frequency RFs of S1222a event, and recently by Drilleau et al. (2023), through the inversion of surface waves group velocities and body-wave travel times from seismic events occurring at a close distance ($<$ 100 km).

Available crustal models for the InSight landing site

Compared to the previously published ILS models, some differences are observed in the layer's absolute shear-wave velocities and the velocity changes at the crustal discontinuities (Fig. 7.7a). The shear-wave velocity (hereafter, also velocity alone) of the shallow layer in KE21K and JO23 corresponds to a rough average of the velocities of the two layers proposed by SC23 in this depth range. The ∼10 km discontinuity is less sharp in the SC23 than in KE21K and JO23 models. The velocities of the mid-crust layer (roughly between 10-20 km depth) are similar between SC23 and JO23 but they are slightly lower than those of the KE21K models. Due to the use of observations particularly sensitive to shallow structure, i.e., ellipticity data in SC23 and apparent S-wave velocity in JO23, these models offer suitable and possibly better constraints for these depths than KE21K, primarily based on RF measurements. The lower crust (between ∼20 km depth and the Moho) is slower in SC23 than in KE21K and JO23, which is related to the sharper velocity change at the Moho in SC23. A possible explanation for this difference is the assumption of the fourth peak of the observed P-to-s RFs being a P wave converted into a crustal

S wave at the Moho, in the SC23 inversion, instead of a combination with a reflected phase, as done by JO23, where further reflected phases were included. Due to their low amplitude and unambiguous observation, these internally reflected crustal phases were not included in the SC23 inversion. A longer window of the synthetic P-to-s RFs (Fig. A6.9) shows that similar oscillations can be obtained with some of the SC23 models, although there is low fitting of the apparent S-wave velocity curve (also used by Joshi et al. (2023)). Because of this, an extended joint inversion, including all these available local-scale measurements, is encouraged.

Different phenomena can explain the velocity changes and layering of the Martian crust, as explained by Wieczorek et al. (2022), involving factors like chemical composition, porosity or fluid content. In particular, higher porosity (content of porous in the material) and cracks can reduce the seismic velocities and the Poisson's ratio (e.g., Heap, 2019; Lutz and Zimmerman, 2021). The latter is directly related to V_p/V_s. The interpretation of previous available ILS crustal models by Wieczorek et al. (2022) suggested a first shallow layer (∼8 km thick) as a mixture of sediments and/or volcanic material deposited in the early Hesperian, Noachian and pre-Noachian periods, which might have undergone substantial fracturing process and aqueous alteration at a later date. The intermediate layer between 8-20 km depth was interpreted as an ancient ejecta unit from the large-scale impact shaping the Utopia basin. The bottom layer would correspond to the initial crust formed during the differentiation of the Borealis impact melt sheet.

The ILS crustal model proposed in this work offers a slightly different interpretation: the first shallow layer (2-3 km thick) would correspond to a mixture of Amazonian and Hesperian lava flows, close to the surface (<100 m), and a late Noachian sedimentary unit down to the first interface. The second and third layers have similar shear-wave velocities (∼ 10% variation), which can be interpreted as having a similar origin but a different alteration and porosity. Similarly, the V_p/V_s of these two layers are ∼ 1.8, well constrained by the P-wave lag times from autocorrelations, with the third layer being also ∼ 10% slightly larger. A possible interpretation is that both layers correspond to a ∼ 18 km thick ejecta unit from the Utopia impact basin, proposed to have occurred during the Noachian period (McGill, 1989). The second layer would have undergone aqueous alteration and physical weathering processes, leading to a reduction of the V_s and V_p/V_s, while the third layer retained the porosity and fracturing of the ejecta material. An alternative explanation would involve lava flows due to intense volcanic activity after or before the Utopia impact. There would be different implications for the volcanic activity of the region, depending on the origin and timing of these layers, but the second layer was likely exposed to heavy weathering. In any case, the general low upper-crustal velocities might also be influenced by porosity, which would be completely closed only at depths greater than ∼20 km (Gyalay et al., 2020). Similar to Wieczorek et al. (2022), the fourth layer can be understood as the initial crust formed during the Borealis impact melt sheet, although the shear-wave velocity is slightly lower than expected for a basaltic layer without porosity (∼3.6 km/s, Heap, 2019). Larger velocities might be derived from a joint inversion considering the fourth peak of the RFs as a superposition with reflected waves.

The InSight landing site compared to regional crustal models

Compared to regional models, the large seismic events S1222a, S1000a and S1094b allowed the mapping of the Martian crustal structure along the path of the generated surface waves. Various studies have mapped the crustal structure along the path between S1222a and the ILS using Love and Rayleigh waves (e.g., Beghein et al., 2022; Li et al., 2022c; Kim et al., 2022b; Xu et al., 2023), whereas Kim et al. (2022a) studied the crustal characteristics along the Rayleigh-waves path of events S1000a and S1094b. Along the S1222a path, close to the dichotomy boundary, the velocities are similar below 20 km, and higher above this depth, than the corresponding velocities at the ILS (Fig. 7.7b). Here, the Moho has been proposed to be located at ∼60 km depth (Kim et al., 2022b), deeper than at the ILS, suggesting an average thicker crust along the path. Likewise, a similar velocity pattern is observed for the S1000a and S1094b Rayleigh-wave paths (Fig. 7.7c and d, respectively), although the Moho depth is not revealed.

The similar velocities in the 20-40 km depth range for the different regions suggest that the lower-crust layer at the ILS would be a common feature all over the northern plains and around the dichotomy boundary. This would be in line with the assumption that the bottom layer would be formed during the differentiation of the Borealis impact melt sheet. Conversely, the upper crust layers (<20 km) at the ILS are not comparable to the other regions and might have a different origin and/or be affected by different processes. The velocities along the S1000a and S1094b paths have been proposed to be higher due to different compositions or reduced porosity of the upper crust layers (Kim et al., 2022a). This is supported by their surface waves traveling through Elysium Rise or Amazonis Planitia, two volcanic areas where thick lava flows of Hesperian to Amazonian ages are observed on the surface (Platz and Michael, 2011; Tanaka et al., 2014). At the InSight landing site, due to its far distance, the lava flows from Elysium Mons have been identified to have limited thickness (Golombek et al., 2018, 2020b), so they likely have little influence on the subsurface structure at crustal scale.

Some implications for understanding Mars interior

The upper crust (<20 km depth) of the S1222a path differs from the ILS, despite the relative proximity (∼2100 km) and similar geological units in the surroundings, as shown in Fig. 2.4. A possible explanation is that the ILS crust has a different origin from the surroundings of the epicenter of S1222a, like massive lava flows from Cerberus Fossae (Plescia, 2003), or that it has been more affected by local-scale processes during its formation. The presence of a Utopia ejecta unit in the surroundings of S1222a is not secured due to the greater distance to the basin center and because Olympus Mons is in the way, which could have blocked part of the ejecta's path.

Interestingly, the proposed Moho depth along the S1222a path is ∼ 20 km deeper than at the ILS, which is suspicious for such topographically similar regions. Depending on the estimated back-azimuth (BAZ), the S1222a epicenter could be located more towards the northern lowlands, using the MQS solution, or to the south of the dichotomy boundary, using the BAZs from surface waves, defining a 40° area for possible S1222a paths (Fig. 7.8a). With the crustal thickness at the ILS as a constraint (∼39 km from Knapmeyer-Endrun et al. (2021), supported by this work), topography and gravity measurements,

Wieczorek et al. (2022) modeled the global crustal thickness considering different density contrasts (Fig. 7.8b). The largest Moho depths in the possible S1222a paths area are obtained in the highlands (∼60 km depth), when the densities in the northern lowlands (ρ_n) and southern highlands (ρ_s) are the same (Fig. 7.8b). As the crustal densities differ, the crustal thicknesses get more homogeneous, with a smaller deviation from ∼40 km depth (e.g., $\rho_n > \rho_s$ in Fig. 7.8b). If the proposed discontinuity along the S1222a path is the actual Moho, then the S1222a event would have occurred south of the dichotomy boundary, so these large crustal thicknesses along the path could have been mapped. If so, the differences in the upper crust between the S1222a path and the ILS would be explained by the larger upper-crust velocities in the highlands, as derived from the R_2 path of S1222a (Li et al., 2022c), which covers a large part of it. A different approach, based on the modeling of high-frequency seismogram envelopes of S1222a and four near impacts, proposed the whole crust to be the origin of the scattering observed, varying from average ∼20 km around the ILS to 60 km on the path to S1222a (Menina et al., 2023). Otherwise, i.e., if the S1222a epicenter is well constrained by MQS and in the northern lowlands, then the proposed discontinuity might correspond to an anomalous structural feature in the upper mantle or an artifact of the inversion. Further investigation in this regard is encouraged.

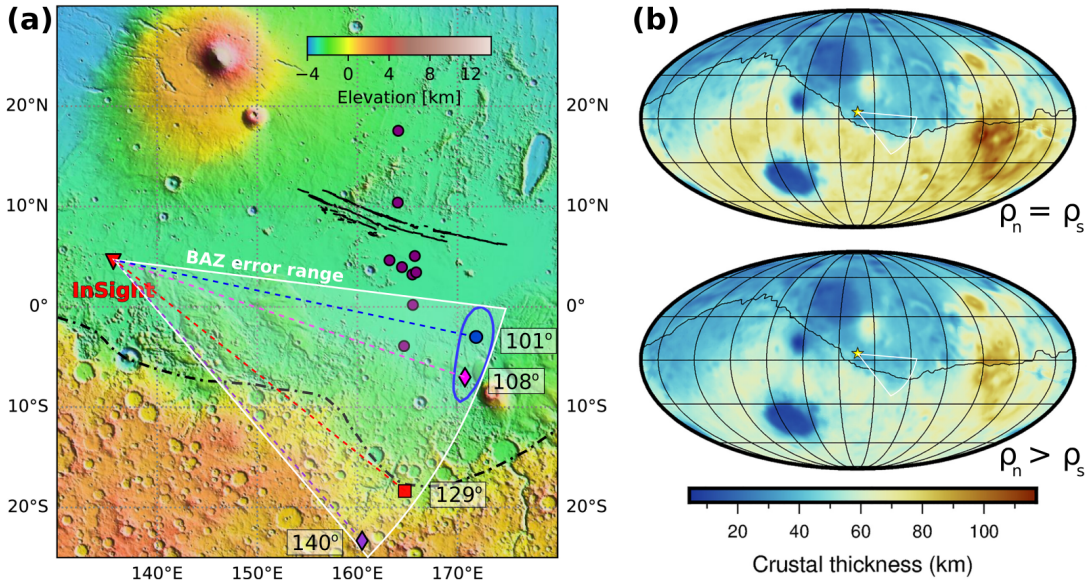


Figure 7.8: S1222a path and Martian crustal structure. **(a)** Topographic map showing the possible solutions for the epicenter of S1222a. Purple dots are events located by MQS around the Cerberus Fossae (black lines). The other symbols are estimated locations of S1222a from the MQS solution (Kawamura et al. (2022), blue circle and ellipse is the uncertainty), based on the multi-orbit distance estimation and the back-azimuth (BAZ) estimated from the broadband polarization of R_1 by Panning et al. (2022) (magenta diamond), this work as shown in Chapter 6 (red square) and the BAZ estimated from the average of the correlation functions across the high-quality narrow band frequency estimates by Panning et al. (2022) (purple diamond). **(b)** Global crustal thickness models using different densities in the northern lowlands (ρ_n) and southern highlands (ρ_s). The crustal thickness is constrained to be 39 km beneath the InSight lander (anchor point), and the mantle and core density are from the Khan2022 model specified in Wieczorek et al. (2022). The white area in (a) is plotted in the global maps for reference. The yellow star is the ILS. The dichotomy boundary is based on Andrews-Hanna et al. (2008) (black dot-dashed line in a, black solid line in b). Figure (a) is modified from Panning et al. (2022) and Figure (b) is modified from Wieczorek et al. (2022).

As a summary of the crustal scale, the lower crust at the InSight landing site is proposed to be a regional feature in the northern lowlands and surroundings. The first shallow crustal layer at the ILS is expected to be a local feature. Although regional models show higher velocities close to the surface, there is a lack of resolution at such depths, so this sedimentary unit should not be completely discarded to be present in other regions. The second and third layers have lower velocities than other regions in the northern lowlands and their origins are unclear, but they might also be related to some more local-scale processes affecting the ILS.

7.3 Summary and concluding remarks

Since the beginning of the mission, there have been diverse attempts to map the subsurface structure of Mars, from meters to kilometers in depth. For this, different methodologies have been implemented using different data sets and approaches. Throughout this chapter, an attempt has been made to harmonize the results obtained from the mapping of the shallow subsurface structure, using the HVSR technique, with the crustal models from the joint inversion of local-kilometers-scale observations. Through this harmonization, achieving a consolidated model of the subsurface structure at the InSight landing site was possible.

To achieve this consolidated model, determining the HVSR curve at intermediate frequencies (0.06-0.5 Hz) was key to assessing the acceptable layering for the transition from shallow to crustal structures. For this, the coda of the S1222a event, the largest seismic event ever recorded on Mars, was used as it had seismic energy in this frequency range well above the pre-event noise level for over one hour.

Through forward modeling, a set of possible models with different intermediate depth (100 m-2 km) transitions were evaluated by comparing the local-scale observations (HVSR at high and intermediate frequencies, Rayleigh-wave ellipticity and P-to-s Receiver Functions) against the predicted values. The assessment suggested that L2-like models are more compatible with crustal models than M2 models and that a layer with power-law velocity increase is more suitable than a sharp discontinuity in depth. This transition layer is interpreted as a large-scale sedimentary unit ranging from hundreds of meters in depth ($\sim$200-300 m) to the first intracrustal discontinuity proposed in this work ($\sim 2-3$ km).

With this, a consolidated model of the subsurface structure at the ILS has been proposed on the scale of meters and kilometers. The proposed model could explain the local-scale observations well and might be consistent with the geological history of Mars and/or the geological observations in the surroundings of the ILS. Differences with respect to other available models, either at shallow or crustal depths, can be explained by possible differences in sensitivity to certain parameters, the spatial coverage of the phenomena studied or the exclusion of certain data sets, among other factors. In this sense, independent joint inversions for the shallow and the crustal part of the subsurface structure are encouraged.

CHAPTER 8

Conclusions and Outlook

In November 2018, the InSight spacecraft landed on Elysium Planitia, Mars, where geophysical instruments were deployed, including the first seismological experiment on the Martian surface (SEIS). Throughout this thesis, the ground-motion data recorded by SEIS have been investigated in order to obtain information about the subsurface structure beneath the InSight landing site (ILS), from shallow, in the range of tens of meters, to crustal depths, in the order of kilometers. To this end, the Martian ambient vibrations and seismic events recorded during the first Martian year (roughly two terrestrial years) have been used for mapping the shallow subsurface using the horizontal-to-vertical spectral ratios (HVSR) technique under the diffuse field approach (DFA). After large seismic events and direct Rayleigh waves were detected, these were used to characterize the structure of the Martian crust at the ILS, particularly constrained by Rayleigh-wave ellipticity measurements.

In the first part of this thesis, due to the novelty of the data set, the ambient vibrations recordings were assessed in the frequency range 0.2-30 Hz, in order to confirm their usability for HVSR analysis and inversion under the DFA. It has been shown that non-seismic signals observed in the InSight data (e.g., donks, glitches) distort the HVSR calculation, so they must be treated appropriately. Clear spectral differences were observed between the Very Broadband (VBB) and Short-Period (SP) seismometers at frequencies higher than 10 Hz. These differences are poorly understood but might be related to possible rotational motions recorded by SP and the underperformance of VBB at such high frequencies. Thus, the frequencies above 10 Hz are discarded for HVSR analysis. The variations of the ambient vibrations over a sol (i.e., the Martian day), over a Martian year and with respect to environmental conditions were investigated. The recorded spectral amplitudes strongly depend on the wind speed level at the ILS. Using ambient vibrations for HVSR analysis in the 0.2-10 Hz frequency range is discouraged due to two main reasons:

(i) During the low wind speed periods, and above 5 Hz, the recorded ground-motion amplitudes are low and close to the corresponding theoretical instrument self-noise of VBB and SP. This makes the resulting HVSR curve to be unrelated to the subsurface structure. Although less clear, a similar phenomenon might occur between 3 and 5 Hz. Only the frequency range ∼0.5-3 Hz may correspond to the ambient wavefield and can be potentially used for HVSR analysis.

(ii) During the high wind speed periods, the ground-motion recordings are affected by the interaction between the wind and the InSight lander, as revealed by clear HVSR peaks related to the so-called lander modes. The ambient wavefield is polarized and the resulting HVSR curve does not represent the natural response of the subsurface structure and, therefore, it cannot be used for HVSR analysis.

In the second part, the HVSR curve obtained from the coda of 139 Martian seismic events (named *eHV*) was analyzed. The coda of the Martian events shows properties of a diffuse field so that the full-wavefield DFA can be assumed. The *eHV* can be understood as the characteristic HVSR of the ILS, which presents a strong peak around 8 Hz, a steep decay towards lower frequencies and a narrow trough around 2.4 Hz. The *eHV* was inverted for the subsurface structure in the frequency range 0.4-10 Hz, using the non-linear Neighbourhood Algorithm (NA) and assuming a 1D layered model space. The parameter space explored by the NA was constrained using a pre-landing model and surface velocities from a hammering experiment. Due to the non-uniqueness problem inherent to HVSR inversion and lack of clarity about the possible shallow shear-wave velocities on Mars, the *eHV* curve can be explained by three sets of models with four layers over a half-space. Without further constraints, the most reliable feature derived from the HVSR inversion is the pattern in velocity changes with depth.

The inverted models show the emplacement of a high-velocity layer at shallow depths (SHVL), between 5 and 20 m depth depending on the set of models, which generates the strong HVSR peak around 8 Hz. The minimum depth of investigation is limited by the maximum frequency of investigation (10 Hz), so the properties slightly above this layer are difficult to constrain. A buried low-velocity layer (bLVL) is needed below the SHVL to explain the steep decay towards low frequencies. The HVSR trough around 2.4 Hz is proposed to be related to a P-wave resonance generated when there is a large impedance (sharp shear-wave contrast) between the SHVL and bLVL. For lower shear-wave contrasts, the 2.4 Hz resonance is not generated. Instead, the 8 Hz HVSR peak is related to a Rayleigh-waves resonance. The bLVL is underlain by a layer with slightly larger velocities but lower than the SHVL. A consolidated geological interpretation of this subsurface model is provided after the investigation of the crust and the intermediate depths.

In the third part, the ellipticity of Rayleigh waves generated by large Martian seismic events was investigated, in order to determine constraints for the crustal structure. To this end, an open-source Python-based package was developed (*Rellipy*), which allows extracting the ellipticity and phase shift from direct Rayleigh waves generated by seismic events and was released for public use custom data. Due to the signal-to-noise ratio, the Rayleigh-wave ellipticity measurements are ruled by the largest event ever recorded on Mars (S1222a) and roughly cover the frequency range of 0.03-0.07 Hz (periods 15-35 s). It is a relatively flat ellipticity curve to which previously reported ILS models

show a significant misfit. Anomalously low phase shifts (<70°) were obtained. In order to assess the results obtained with few events at a single station, the same procedure was performed for an Earth station (BQ.DREG, belonging to the Bensberg Earthquake Station), suggesting that short variations should not be considered.

A joint inversion of the resulting ellipticity curve with P-to-s Receiver Functions (from Joshi et al., 2023) and P-wave lag times from autocorrelations (from Schimmel et al., 2021) was performed using the NA and constraints from previous works. A new crustal layer close to the surface, about 2-3 km thick, was revealed by the joint inversion and explained by the combination of the data sets together with the constrained shear-wave velocity of the upper mantle. This is one of the first times this layer has been reported from the inversion of seismological data.

In the last part of this work, the subsurface models at shallow and crustal scales were combined into a single harmonized ILS underground structure. To this end, the 70-minute coda window of the S1222a event was investigated. This is the only coda window containing large enough ground-motion data in the low-frequency range of 0.06-0.5 Hz, not covered by the other approaches used in this work, so it offered a unique opportunity to explore intermediate-transition depths (from the order of hundreds of meters to a couple of kilometers). The resulting HVSR curve presents a slight peak between 0.1 and 0.2 Hz. Representative models from two different sets obtained from the shallow characterization (M2 and L2) were combined with a characteristic model from the crustal-scale inversion by using different transition layers. Through forward modeling, this evaluation suggested that (i) shallow models with larger velocities (L2) are more compatible with crustal models and (ii) the transition from shallow to crustal depths is gradual rather than with a sharp discontinuity. Based on this and geological information, a comprehensive model was proposed for the ILS.

The subsurface at the ILS is characterized by a first shallow regolith layer, whose transition to coarse ejecta was not resolved by this work, but likely occurs in the first 7 m below the surface. These are two low-velocity units overlying a high-velocity Amazonian fractured lava flow, emplaced at ∼15 m depth and about 20-40 m thick. This sharp transition from low to high velocities generates the HVSR peak at 8 Hz. The bLVL is interpreted as a sedimentary unit (∼30-40 m thick) deposited in the Late Hesperian-Amazonian transition period, when episodes of fluvial activity still occurred on Mars. The unit below corresponds to a heavily weathered lava flow that was physically eroded and exposed to aqueous activity during the Early Hesperian period, where the impact rate and global fluvial activity were still high. The bottom depth of this volcanic unit is proposed to be around 200-300 m depth, where a rather smooth transition to a massive sedimentary unit occurs. This sedimentary unit would have been deposited during the Late Noachian, when intense pluvial and fluvial activity occurred and valley networks were formed. Due to compaction with depth, the velocity profile within sedimentary units explains the gradual velocity increase towards the first crustal discontinuity around 2-3 km depth. All these units form the first shallow layer of the crust unveiled by the joint inversion of this work.

The crustal structure at the ILS presents intracrustal discontinuities at 2-3 km, 8-12 km and 18-23 km depth. The Moho is in the range 33-45 km depth, slightly shallower but still in the range reported in previous models. The bottom layer of the ILS crust

has similar velocities as other regions of Mars, suggesting a common lower crust in the northern lowlands and likely related to the large-scale Borealis impact melt sheet. The shear-wave velocities above 20 km depth are lower than 2.5 km/s. These upper-crust layers (between the Late Noachian sedimentary unit and the ∼20 km discontinuity) might be a thick ejecta unit from the Utopia impact basin, whose shallower part has been highly weathered and the porosity of the deeper part has been reduced. These velocities are lower than in other regions of Mars, supporting the idea of being formed due to more local processes and/or of having been affected by more local-scale processes.

In conclusion, three-component single-station seismological techniques allowed a multi-scale mapping of the Martian subsurface beneath InSight, from shallow to crustal depths, that is compatible with the geological history of Mars and other independent observations. Combining the different approaches was the key to moving towards a consolidated model. Although having many stations is easier nowadays, single-station seismological techniques and the new developments offer a robust way to complement multi-station approaches. This research, and the works of the InSight mission, prove that these powerful techniques will allow exploring other planets and celestial bodies at different scales in the future but, without going any further, they can also be used now for exploring remote underinvestigated regions of the Earth.

Outlook

Even though a consolidated subsurface model has been proposed here, this explains mainly the measurements involved in the inversions of this work. Other observations are available, like ground compliance and seismo-acoustic coupling signals for the shallow scale or surface-waves dispersion curves and travel times related to nearby events, for the crustal scale. It is encouraged to explore the possibility of jointly inverting same-scale observations (shallow or crust) for better constraining the proposed models. A joint inversion of all the available observations at both scales is ambitious but would deliver a much more consolidated model of the InSight landing site. How much can these models be improved? How to explain the differences among the available models? Is it possible to find a single model explaining all the observations?

Besides, the phase shift of Rayleigh waves is a feature that has been little explored in the literature. The anomalously small values obtained for the S1222a event on Mars and the observation of some cases on Earth left the door open for further research on this topic. A more systematic analysis and also a theoretical investigation on this topic could provide some insights about the dependence of the phase shift, which could be potentially useful as a future single-station technique.

This research was limited to 10 Hz because unclear discrepancies above this frequency were observed. Understanding the differences may help to use higher frequencies to map the shallower part of the ILS, including the suspected regolith-coarse ejecta transition.

Bibliography

Aki, K. 1969. Analysis of the seismic coda of local earthquakes as scattered waves. *Journal of geophysical research*, **74**(2): 615–631.

Aki, K. and Chouet, B. 1975. Origin of coda waves: source, attenuation, and scattering effects. *Journal of geophysical research*, **80**(23): 3322–3342.

Ammon, C. J. 1991. The isolation of receiver effects from teleseismic P waveforms. *Bull. Seismol. Soc. Am*, **81**(6): 2504–2510.

Ammon, C. J., Randall, G. E., and Zandt, G. 1990. On the nonuniqueness of receiver function inversions. *Journal of Geophysical Research: Solid Earth*, **95**(B10): 15303–15318.

Anderson, D. L., Miller, W., Latham, G., Nakamura, Y., Toksöz, M., Dainty, A., Duennebier, F., Lazarewicz, A. R., Kovach, R., and Knight, T. 1977. Seismology on mars. *Journal of Geophysical Research*, **82**(28): 4524–4546.

Andrews-Hanna, J. C., Zuber, M. T., and Banerdt, W. B. 2008. The Borealis basin and the origin of the martian crustal dichotomy. *Nature*, **453**: 1212–1215. ISSN 1476-4687. doi: 10.1038/nature07011.

Arai, H. and Tokimatsu, K. 2000. Effects of Rayleigh and Love waves on microtremor H/V spectra. In *Proceedings of the 12th world conference on earthquake engineering*, volume 2232, p. 1–8. New Zealand Society for Earthquake Engineering Inc, Auckland, New Zealand.

Arai, H. and Tokimatsu, K. 2004. S-wave velocity profiling by inversion of microtremor H/V spectrum. *Bulletin of the Seismological Society of America*, **94**(1): 53–63.

Attanayake, J., Ferreira, A. M., Berbellini, A., and Morelli, A. 2017. Crustal structure beneath Portugal from teleseismic Rayleigh Wave Ellipticity. *Tectonophysics*, **712-713**: 344–361. ISSN 0040-1951. doi: https://doi.org/10.1016/j.tecto.2017.06.001.

Bagheri, A., Khan, A., Al-Attar, D., Crawford, O., and Giardini, D. 2019. Tidal response of Mars constrained from laboratory-based viscoelastic dissipation models and geophysical data. *Journal of Geophysical Research: Planets*, **124**(11): 2703–2727.

Banerdt, W., Smrekar, S., Alkalai, L., Hoffman, T., Warwick, R., Hurst, K., Folkner, W., Lognonné, P., Spohn, T., Asmar, S., et al. 2012. InSight: An integrated exploration of the interior of Mars.

Banerdt, W., Smrekar, S., Lognonné, P., Spohn, T., Asmar, S., Banfield, D., Boschi, L., Christensen, U., Dehant, V., Folkner, W., et al. 2013. InSight: a discovery mission to explore the interior of Mars. In *44th Annual Lunar and Planetary Science Conference*, number 1719, p. 1915.

Banerdt, W., Smrekar, S., Banfield, D., Giardini, D., and et al. 2020. Initial results from the InSight mission on Mars. *Nature Geoscience*, **13**: 183–189. doi: 10.1038/s41561-020-0544-y.

Banfield, D., Rodriguez-Manfredi, J., Russell, C., Rowe, K., Leneman, D., Lai, H., Cruce, P., Means, J., Johnson, C., Mittelholz, A., et al. 2019. InSight auxiliary payload sensor suite (APSS). *Space Science Reviews*, **215**(1): 1–33. https://doi.org/10.1007/s11214-018-0570-x.

Banfield, D., Spiga, A., Newman, C., Forget, F., Lemmon, M., Lorenz, R., Murdoch, N., Viudez-Moreiras, D., Pla-Garcia, J., Garcia, R., Lognonné, P., and et al. 2020. The atmosphere of Mars as observed by InSight. *Nature Geoscience*, **13**: 190–198. doi: 10.1038/s41561-020-0534-0.

Baratoux, D., Samuel, H., Michaut, C., Toplis, M. J., Monnereau, M., Wieczorek, M., Garcia, R., and Kurita, K. 2014. Petrological constraints on the density of the Martian crust. *Journal of Geophysical Research: Planets*, **119**(7): 1707–1727.

Bard, P.-Y. et al. 1999. Microtremor measurements: a tool for site effect estimation. *The effects of surface geology on seismic motion*, **3**: 1251–1279.

Barlow, N. 2008. *Mars: An Introduction to its Interior, Surface and Atmosphere*. Cambridge Planetary Science. Cambridge University Press. doi: 10.1017/CBO9780511536069.

Becker, G. and Knapmeyer-Endrun, B. 2018. Crustal thickness across the Trans-European Suture Zone from ambient noise autocorrelations. *Geophysical Journal International*, **212**(2): 1237–1254.

Becker, G. K. 2018. Crustal thickness from seismic noise correlations in preparation for the InSight mission to Mars. *Ph.D. Thesis*.

Beghein, C., Li, J., Weidner, E., Maguire, R., Wookey, J., Lekić, V., Lognonné, P., and Banerdt, W. 2022. Crustal Anisotropy in the Martian lowlands from surface waves. *Geophysical Research Letters*, **49**(24): e2022GL101508.

Berbellini, A., Morelli, A., and Ferreira, A. M. 2016. Ellipticity of Rayleigh waves in basin and hard-rock sites in Northern Italy. *Geophysical Journal International*, **206**(1): 395–407.

Berbellini, A., Morelli, A., and G. Ferreira, A. M. 2017. Crustal structure of northern Italy from the ellipticity of Rayleigh waves. *Physics of the Earth and Planetary Interiors*, **265**: 1–14. ISSN 0031-9201. doi: https://doi.org/10.1016/j.pepi.2016.12.005. URL https://www.sciencedirect.com/science/article/pii/S0031920116302412.

Bertka, C. M. and Fei, Y. 1997. Mineralogy of the Martian interior up to core-mantle boundary pressures. *Journal of Geophysical Research: Solid Earth*, **102**(B3): 5251–5264.

Beyreuther, M., Barsch, R., Krischer, L., Megies, T., Behr, Y., and Wassermann, J. 2010. ObsPy: A Python toolbox for seismology. *Seismological Research Letters*, **81**(3): 530–533.

Bonnefoy-Claudet, S., Cécile, C., Pierre-Yves, B., Fabrice, C., Peter, M., Jozef, K., and Fäh, D. 2006. H/V ratio: a tool for site effects evaluation. Results from 1-D noise simulations. *Geophysical Journal International*, **167**(2): 827–837.

Bonnefoy-Claudet, S., Köhler, A., Cornou, C., Wathelet, M., and Bard, P.-Y. 2008. Effects of Love waves on microtremor H/V ratio. *Bulletin of the Seismological Society of America*, **98**(1): 288–300.

Bora, N., Biswas, R., and Malischewsky, P. 2020. Imaging subsurface structure of an urban area based on diffuse-field theory concept using seismic ambient noise. *Pure and Applied Geophysics*, **177**(10): 4733–4753.

Böse, M., Clinton, J. F., Ceylan, S., Euchner, F., van Driel, M., Khan, A., Giardini, D., Lognonne, P., and Banerdt, W. B. 2017. A probabilistic framework for single-station location of seismicity on Earth and Mars. *Physics of the Earth and Planetary Interiors*, **262**: 48–65.

Böse, M., Stähler, S. C., Deichmann, N., Giardini, D., Clinton, J., Lognonné, P., Ceylan, S., van Driel, M., Charalambous, C., Dahmen, N., et al. 2021. Magnitude scales for Marsquakes calibrated from InSight data. *Bulletin of the Seismological Society of America*, **111**(6): 3003–3015.

BQ network. Bensberg Earthquake Network, 2016. URL https://www.fdsn.org/networks/detail/BQ/.

Brinkman, N., Schmelzbach, C., Sollberger, D., ten Pierick, J., Edme, P., Haag, T., Kedar, S., and et al. 2022. In-situ regolith seismic velocity measurement at the 1 InSight landing site on Mars (submitted). *Journal of Geophysical Research: Planets*.

Brinkman, N., Schmelzbach, C., Sollberger, D., van Driel, M., ten Pierick, J., Robertsson, J. O., Andersson, F., Stähler, S., Giardini, D., Kedar, S., et al. 2019. The first active seismic experiment on Mars to characterize the shallow subsurface structure at the InSight landing site. In *SEG Technical Program Expanded Abstracts 2019*, p. 4756–4760. Society of Exploration Geophysicists.

Brocher, T. M. 2005. Empirical relations between elastic wavespeeds and density in the Earth's crust. *Bulletin of the seismological Society of America*, **95**(6): 2081–2092.

Campillo, M. 2006. Phase and correlation inrandom'seismic fields and the reconstruction of the green function. *Pure and applied geophysics*, **163**: 475–502.

Campillo, M. and Paul, A. 2003. Long-range correlations in the diffuse seismic coda. *Science*, **299**(5606): 547–549.

Carr, M. H. 2007. *The surface of Mars*, volume 6. Cambridge University Press.

Carr, M. H. and Head, J. W. 2010. Geologic history of Mars. *Earth Planet. Sci. Lett.*, **294**(3): 185–203. ISSN 0012-821X. doi: 10.1016/j.epsl.2009.06.042.

Carrasco, S., Knapmeyer-Endrun, B., Margerin, L., Schmelzbach, C., Onodera, K., Pan, L., Lognonné, P., Menina, S., Giardini, D., Stutzmann, E., Clinton, J., Staehler, S., Schimmel, M., Golombek, M., Hobiger, M., Hallo, M., Kedar, S., and Banerdt, W. 2022. Empirical H/V spectral ratios at the InSight landing site and implications for the martian subsurface structure. *Geophysical Journal International*, **232**(2): 1293–1310. doi: 10.1093/gji/ggac391. URL https://doi.org/10.1093/gji/ggac391.

Carrasco, S. Martian crustal models at the InSight landing site from joint inversion of ellipticity, P-to-s RFs and autocorrelations times, 2023. URL https://doi.org/10.5281/zenodo.8051337.

Carrasco, S., Knapmeyer-Endrun, B., Margerin, L., Xu, Z., Joshi, R., Schimmel, M., Stutzmann, E., Charalambous, C., Lognonné, P., and Banerdt, W. B. 2023. Constraints for the Martian crustal structure from Rayleigh waves ellipticity of large seismic events. *Geophysical Research Letters*, **50**(16): e2023GL104816.

Ceylan, S., Clinton, J. F., Giardini, D., Böse, M., Charalambous, C., van Driel, M., Horleston, A., Kawamura, T., Khan, A., Orhand-Mainsant, G., et al. 2021. Companion guide to the marsquake catalog from InSight, Sols 0–478: Data content and non-seismic events. *Physics of the Earth and Planetary Interiors*, **310**: 106597.

Ceylan, S., Clinton, J. F., Giardini, D., Stähler, S. C., Horleston, A., Kawamura, T., Böse, M., Charalambous, C., Dahmen, N. L., van Driel, M., Durán, C., Euchner, F., Khan, A., Kim, D., Plasman, M., Scholz, J.-R., Zenhäusern, G., Beucler, E., Garcia, R. F., Kedar, S., Knapmeyer, M., Lognonné, P., Panning, M. P., Perrin, C., Pike, W. T., Stott, A. E., and Banerdt, W. B. 2022. The marsquake catalogue from InSight, sols 0–1011. *Phys. Earth Planet. Inter.*, **333**: 106943. ISSN 0031-9201. doi: 10.1016/j.pepi.2022.106943.

Chicarro, A., Scoon, G., and Coradini, M. 1994. INTERMARSNET-an international network of stations on Mars for global martian characterisation. *ESA Journal*, **18**(3): 207–218.

Chong, J., Ni, S., Chu, R., and Somerville, P. 2016. Joint Inversion of Body-Wave Receiver Function and Rayleigh-Wave Ellipticity. *Bulletin of the Seismological Society of America*, **106**(2): 537–551.

Clinton, J., Giardini, D., Böse, M., Ceylan, S., van Driel, M., Euchner, F., Garcia, R. F., Kedar, S., Khan, A., Stähler, S. C., et al. 2018. The Marsquake service: Securing daily analysis of SEIS data and building the Martian seismicity catalogue for InSight. *Space Science Reviews*, **214**(8): 1–33.

Clinton, J. F., Ceylan, S., van Driel, M., Giardini, D., Stähler, S. C., Böse, M., Charalambous, C., Dahmen, N. L., Horleston, A., Kawamura, T., Khan, A., Orhand-Mainsant, G., Scholz, J.-R., Euchner, F., Banerdt, W. B., Lognonné, P., Banfield, D., Beucler, E., Garcia, R. F., Kedar, S., Panning, M. P., Perrin, C., Pike, W. T., Smrekar, S. E., Spiga, A., and Stott, A. E. 2021. The Marsquake catalogue from InSight, sols 0–478. *Physics of the Earth and Planetary Interiors*, **310**: 106595. URL https://doi.org/10.1016/j.pepi.2020.106595.

Compaire, N., Margerin, L., Garcia, R. F., Pinot, B., Calvet, M., Orhand-Mainsant, G., Kim, D., Lekic, V., Tauzin, B., Schimmel, M., Stutzmann, E., Knapmeyer-Endrun, B., Lognonné, P., Pike, W. T., Schmerr, N., Gizon, L., and Banerdt, W. B. 2021. Autocorrelation of the Ground Vibrations Recorded by the SEIS-InSight Seismometer on Mars. *Journal of Geophysical Research: Planets*, **126**(4): e2020JE006498. URL https://agupubs.onlinelibrary.wiley.com/doi/abs/10.1029/2020JE006498. https://doi.org/10.1029/2020JE006498.

Compaire, N., Margerin, L., Monnereau, M., Garcia, R. F., Lange, L., Calvet, M., Dahmen, N., Stähler, S., Mueller, N., Grott, M., et al. 2022. Seasonal variations of subsurface seismic velocities monitored by the SEIS-InSight seismometer on Mars. *Geophysical Journal International*, **229**(2): 776–799.

Dahmen, N. L., Clinton, J. F., Ceylan, S., van Driel, M., Giardini, D., Khan, A., Stähler, S. C., Böse, M., Charalambous, C., Horleston, A., Kawamura, T., Orhand-Mainsant, G., Scholz, J.-R., Euchner, F., Pike, W. T., Weber, R. C., Lognonné, P., and Banerdt, W. B. 2021a. Super High Frequency Events: A New Class of Events Recorded by the InSight Seismometers on Mars. *Journal of Geophysical Research: Planets*, **126**(2): e2020–006599. URL https://doi.org/10.1029/2020JE006599.

Dahmen, N. L., Zenhäusern, G., Clinton, J. F., Giardini, D., Stähler, S. C., Ceylan, S., Charalambous, C., van Driel, M., Hurst, K. J., Kedar, S., et al. 2021b. Resonances and lander modes observed by insight on Mars (1–9 Hz). *Bulletin of the Seismological Society of America*, **111**(6): 2924–2950.

Dal Moro, G. 2015. Joint analysis of Rayleigh-wave dispersion and HVSR of lunar seismic data from the Apollo 14 and 16 sites. *Icarus*, **254**: 338–349. doi: 10.1016/j.icarus.2015.03.017.

Dal Moro, G. 2020. On the Identification of Industrial Components in the Horizontal-to-Vertical Spectral Ratio (HVSR) from Microtremors. *Pure Appl. Geophys.*, **177**(8): 3831–3849. ISSN 1420-9136. doi: 10.1007/s00024-020-02424-0.

Dehant, V., Lognonné, P., and Sotin, C. 2004. Network science, NetLander: a European mission to study the planet Mars. *Planetary and Space Science*, **52**(11): 977–985.

Delage, P., Karakostas, F., Dhemaied, A., Belmokhtar, M., Lognonné, P., Golombek, M., De Laure, E., Hurst, K., Dupla, J.-C., Kedar, S., et al. 2017. An investigation of the mechanical properties of some Martian regolith simulants with respect to the surface properties at the InSight mission landing site. *Space Science Reviews*, **211**(1): 191–213.

Di Giacomo, D., Gallipoli, M. R., Mucciarelli, M., Parolai, S., and Richwalski, S. M. 2005. Analysis and modeling of HVSR in the presence of a velocity inversion: the case of Venosa, Italy. *Bulletin of the Seismological Society of America*, **95**(6): 2364–2372.

Dreibus, G. and Wanke, H. 1985. Mars, a volatile-rich planet. *Meteoritics*, **20**: 367–381.

Drilleau, M., Beucler, , Shi, J., Knapmeyer-Endrun, B., Garcia, R., Kim, D., Ansan, V., Lognonné, P., and Banerdt, B. 2023. Structure of the Martian crust below InSight from surface waves and body waves generated by nearby meteoroid impacts. *Submitted to GRL*.

Drilleau, M., Samuel, H., Garcia, R. F., Rivoldini, A., Perrin, C., Michaut, C., Wieczorek, M., Tauzin, B., Connolly, J. A., Meyer, P., et al. 2022. Marsquake locations and 1-D seismic models for Mars from InSight data. *Journal of Geophysical Research: Planets*, **127**(9): e2021JE007067.

Durán, C., Khan, A., Ceylan, S., Zenhäusern, G., Stähler, S., Clinton, J., and Giardini, D. 2022. Seismology on Mars: An analysis of direct, reflected, and converted seismic body waves with implications for interior structure. *Physics of the Earth and Planetary Interiors*, **325**: 106851. ISSN 0031-9201. doi: https://doi.org/10.1016/j.pepi.2022.106851. URL https://www.sciencedirect.com/science/article/pii/S0031920122000127.

Dziewonski, A. M., Chou, T.-A., and Woodhouse, J. H. 1981. Determination of earthquake source parameters from waveform data for studies of global and regional seismicity. *Journal of Geophysical Research: Solid Earth*, **86**(B4): 2825–2852.

Ekström, G., Nettles, M., and Dziewoński, A. 2012. The global CMT project 2004–2010: Centroid-moment tensors for 13,017 earthquakes. *Physics of the Earth and Planetary Interiors*, **200**: 1–9.

Elkins-Tanton, L. T. 2011. Formation of early water oceans on rocky planets. *Astrophysics and Space Science*, **332**: 359–364.

Endrun, B. 2011. Love wave contribution to the ambient vibration H/V amplitude peak observed with array measurements. *Journal of seismology*, **15**(3): 443–472.

Fäh, D., Kind, F., and Giardini, D. 2001. A theoretical investigation of average H/V ratios. *Geophysical Journal International*, **145**(2): 535–549.

Faust, L. Y. 1951. Seismic velocity as a function of depth and geologic time. *Geophysics*, **16**(2): 192–206.

Fayon, L., Knapmeyer-Endrun, B., Lognonné, P., Bierwirth, M., Kramer, A., Delage, P., Karakostas, F., Kedar, S., Murdoch, N., Garcia, R. F., et al. 2018. A numerical model of the SEIS leveling system transfer matrix and resonances: Application to SEIS rotational seismology and dynamic ground interaction. *Space Science Reviews*, **214**(8): 1–39.

Fergason, R. L., Kirk, R. L., Cushing, G., Galuszka, D. M., Golombek, M. P., Hare, T. M., Howington-Kraus, E., Kipp, D. M., and Redding, B. L. 2017. Analysis of local slopes at the InSight landing site on Mars. *Space Science Reviews*, **211**: 109–133.

Fernando, B., Daubar, I. J., Charalambous, C., Grindrod, P. M., Stott, A., Al Ateqi, A., Atri, D., Ceylan, S., Clinton, J., Hauber, E., et al. 2023. A tectonic origin for the largest marsquake observed by InSight. *Authorea Preprints*.

Ferreira, A. M. and Woodhouse, J. H. 2007a. Observations of long period Rayleigh wave ellipticity. *Geophysical Journal International*, **169**(1): 161–169.

Ferreira, A. M. and Woodhouse, J. H. 2007b. Source, path and receiver effects on seismic surface waves. *Geophysical Journal International*, **168**(1): 109–132.

Ferreira, A. M., Marignier, A., Attanayake, J., Frietsch, M., and Berbellini, A. 2020. Crustal structure of the Azores Archipelago from Rayleigh wave ellipticity data. *Geophysical Journal International*, **221**(2): 1232–1247.

Field, E. and Jacob, K. 1993. The theoretical response of sedimentary layers to ambient seismic noise. *Geophysical research letters*, **20**(24): 2925–2928.

Folkner, W. M., Dehant, V., Le Maistre, S., Yseboodt, M., Rivoldini, A., Van Hoolst, T., Asmar, S. W., and Golombek, M. P. 2018. The rotation and interior structure experiment on the InSight mission to Mars. *Space Science Reviews*, **214**: 1–16.

Folkner, W., Yoder, C., Yuan, D., Standish, E., and Preston, R. 1997. Interior structure and seasonal mass redistribution of Mars from radio tracking of Mars Pathfinder. *Science*, **278**(5344): 1749–1752.

Fortin, J., Stanchits, S., Vinciguerra, S., and Guéguen, Y. 2011. Influence of thermal and mechanical cracks on permeability and elastic wave velocities in a basalt from Mt. Etna volcano subjected to elevated pressure. *Tectonophysics*, **503**(1): 60–74. ISSN 0040-1951. doi: 10.1016/j.tecto.2010.09.028.

Galluzzo, D., La Rocca, M., Margerin, L., Del Pezzo, E., and Scarpa, R. 2015. Attenuation and velocity structure from diffuse coda waves: Constraints from underground array data. *Physics of the Earth and Planetary Interiors*, **240**: 34–42.

García-Jerez, A., Piña-Flores, J., Sánchez-Sesma, F. J., Luzón, F., and Perton, M. 2016. A computer code for forward calculation and inversion of the H/V spectral ratio under the diffuse field assumption. *Comput. Geosci.*, **97**: 67–78. ISSN 0098-3004. doi: 10.1016/j.cageo.2016.06.016.

Genova, A., Goossens, S., Lemoine, F. G., Mazarico, E., Neumann, G. A., Smith, D. E., and Zuber, M. T. 2016. Seasonal and static gravity field of Mars from MGS, Mars Odyssey and MRO radio science. *Icarus*, **272**: 228–245.

Giardini, D., Lognonné, P., Banerdt, W. B., Pike, W. T., Christensen, U., Ceylan, S., Clinton, J. F., van Driel, M., Stähler, S. C., Böse, M., et al. 2020. The seismicity of Mars. *Nature Geoscience*, **13**(3): 205–212.

Goins, N. R. and Lazarewicz, A. R. 1979. Martian seismicity. *Geophysical Research Letters*, **6**(5): 368–370.

Golombek, M., Kass, D., Williams, N., Warner, N., Daubar, I., Piqueux, S., Charalambous, C., and Pike, W. 2020a. Assessment of InSight landing site predictions. *Journal of Geophysical Research: Planets*, **125**(8): e2020JE006502.

Golombek, M., Warner, N., Grant, J., Hauber, E., Ansan, V., Weitz, C., Williams, N., Charalambous, C., Wilson, S., DeMott, A., et al. 2020b. Geology of the InSight landing site on Mars. *Nature communications*, **11**(1): 1–11.

Golombek, M., Kipp, D., Warner, N., Daubar, I. J., Fergason, R., Kirk, R. L., Beyer, R., Huertas, A., Piqueux, S., Putzig, N., et al. 2017. Selection of the InSight landing site. *Space Science Reviews*, **211**(1): 5–95.

Golombek, M., Grott, M., Kargl, G., Andrade, J., Marshall, J., Warner, N., Teanby, N., Ansan, V., Hauber, E., Voigt, J., et al. 2018. Geology and physical properties investigations by the InSight lander. *Space Science Reviews*, **214**(5): 1–52.

Golombek, M., Williams, N., Warner, N., Parker, T., Williams, M., Daubar, I., Calef, F., Grant, J., Bailey, P., Abarca, H., et al. 2020c. Location and setting of the Mars InSight lander, instruments, and landing site. *Earth and Space Science*, **7**(10): e2020EA001248.

Golombek, M. P., Banerdt, W. B., Tanaka, K. L., and Tralli, D. M. 1992. A prediction of Mars seismicity from surface faulting. *Science*, **258**(5084): 979–981.

Golombek, M. 2002. A revision of Mars seismicity from surface faulting. In *Lunar and Planetary Science Conference*, p. 1244.

Goossens, S., Sabaka, T. J., Genova, A., Mazarico, E., Nicholas, J. B., and Neumann, G. A. 2017. Evidence for a low bulk crustal density for Mars from gravity and topography. *Geophysical research letters*, **44**(15): 7686–7694.

Gosselin, J. M., Dosso, S. E., Askan, A., Wathelet, M., Savvaidis, A., and Cassidy, J. F. 2022. A review of inverse methods in seismic site characterization. *J. Seismolog.*, **26**(4): 781–821. ISSN 1573-157X. doi: 10.1007/s10950-021-10047-8.

Grant, J. A. and Wilson, S. A. 2019. Evidence for late alluvial activity in Gale crater, Mars. *Geophysical Research Letters*, **46**(13): 7287–7294.

Grant, J. A., Wilson, S. A., Mangold, N., Calef III, F., and Grotzinger, J. P. 2014. The timing of alluvial activity in Gale crater, Mars. *Geophysical Research Letters*, **41**(4): 1142–1149.

Grant, J. A., Warner, N. H., Weitz, C. M., Golombek, M. P., Wilson, S. A., Baker, M., Hauber, E., Ansan, V., Charalambous, C., Williams, N., et al. 2020. Degradation of Homestead hollow at the InSight landing site based on the distribution and properties of local deposits. *Journal of Geophysical Research: Planets*, **125**(4): e2019JE006350.

Gutenberg, B. 1914. Über Erdbebenwellen VIIA. *Nachr. Ges. Wiss. Göttingen, math.-physik. Kl.*, p. 166–218.

Gyalay, S., Nimmo, F., Plesa, A.-C., and Wieczorek, M. 2020. Constraints on thermal history of Mars from depth of pore closure below InSight. *Geophysical Research Letters*, **47**(16): e2020GL088653.

Harris, C. R., Millman, K. J., van der Walt, S. J., Gommers, R., Virtanen, P., Cournapeau, D., Wieser, E., Taylor, J., Berg, S., Smith, N. J., Kern, R., Picus, M., Hoyer, S., van Kerkwijk, M. H., Brett, M., Haldane, A., del Río, J. F., Wiebe, M., Peterson, P., Gérard-Marchant, P., Sheppard, K., Reddy, T., Weckesser, W., Abbasi, H., Gohlke, C., and Oliphant, T. E. 2020. Array programming with NumPy. *Nature*, **585**(7825): 357–362. URL https://doi.org/10.1038/s41586-020-2649-2. 10.1038/s41586-020-2649-2.

Hartmann, W. K. and Neukum, G. 2001. Cratering chronology and the evolution of Mars. In *Chronology and evolution of Mars*, p. 165–194. Springer.

Hartmann, W. K., Anguita, J., de la Casa, M. A., Berman, D. C., and Ryan, E. V. 2001. Martian Cratering 7: The Role of Impact Gardening. *Icarus*, **149**(1): 37–53. ISSN 0019-1035. doi: 10.1006/icar.2000.6532.

Heap, M. J. 2019. P-and S-wave velocity of dry, water-saturated, and frozen basalt: Implications for the interpretation of Martian seismic data. *Icarus*, **330**: 11–15.

Hennino, R., Trégourès, N., Shapiro, N., Margerin, L., Campillo, M., Van Tiggelen, B., and Weaver, R. 2001. Observation of equipartition of seismic waves. *Physical review letters*, **86**(15): 3447.

Hillers, G., Ben-Zion, Y., Campillo, M., and Zigone, D. 2015. Seasonal variations of seismic velocities in the San Jacinto fault area observed with ambient seismic noise. *Geophys. J. Int.*, **202**(2): 920–932. ISSN 0956-540X. doi: 10.1093/gji/ggv151.

Hobiger, M., Hallo, M., Schmelzbach, C., Stähler, S., Fäh, D., Giardini, D., Golombek, M., Clinton, J., Dahmen, N., Zenhäusern, G., Knapmeyer-Endrun, B., Carrasco, S., Charalambous, C., Hurst, K., Kedar, S., and Banerdt, W. 2021. The shallow structure of Mars at the InSight landing site from inversion of ambient vibrations. *Nature Communications*, **12**(1): 1–13.

Hobiger, M., Cornou, C., Wathelet, M., Giulio, G. D., Knapmeyer-Endrun, B., Renalier, F., Bard, P.-Y., Savvaidis, A., Hailemikael, S., Le, B. N., et al. 2013. Ground structure imaging by inversions of Rayleigh wave ellipticity: sensitivity analysis and application to European strong-motion sites. *Geophysical Journal International*, **192**(1): 207–229.

Hong, T.-K. and Menke, W. 2008. Imaging laterally varying regional heterogeneities from seismic coda using a source-array analysis. *Physics of the Earth and Planetary Interiors*, **166**(3-4): 188–202.

Horleston, A. C., Clinton, J. F., Ceylan, S., Giardini, D., Charalambous, C., Irving, J. C., Lognonné, P., Stähler, S. C., Zenhäusern, G., Dahmen, N. L., et al. 2022. The far side of Mars: Two distant marsquakes detected by InSight. *The Seismic Record*, **2**(2): 88–99.

Hoshiba, M. 1991. Simulation of multiple-scattered coda wave excitation based on the energy conservation law. *Physics of the Earth and Planetary Interiors*, **67**(1-2): 123–136.

Hunter, J. D. 2007. Matplotlib: A 2D graphics environment. *Computing in Science & Engineering*, **9**(3): 90–95. 10.1109/MCSE.2007.55.

Hurst, K., Fayon, L., Knapmeyer-Endrun, B., Schmelzbach, C., van Driel, M., Ervin, J., Kedar, S., Pike, W. T., Calcutt, S., Warren, T., Charalambous, C., Stott, A., Bierwirth, M., Lognonne, P., de Raucourt, S., Gabsi, T., Nebut, T., Robert, O., Tillier, S., Ceylan, S., Böse, M., Clinton, J., Giardini, D., Horleston, A., Kawamura, T., Khan, A., Orhand-Mainsant, G., Scholz, J., Stähler, S., Stevanovic, J., and Banerdt, W. B. 2021. Resonances of the InSight Seismometer on Mars. *Bulletin of the Seismological Society of America*, **111**(6): 2951–2963. ISSN 0037-1106. URL https://doi.org/10.1785/0120210137. 10.1785/0120210137.

Hynek, B. M., Beach, M., and Hoke, M. R. T. 2010. Updated global map of Martian valley networks and implications for climate and hydrologic processes. *J. Geophys. Res. Planets*, **115**(E9). ISSN 0148-0227. doi: 10.1029/2009JE003548.

InSight Mars SEIS Data Service. SEIS raw data, Insight Mission. IPGP, JPL, CNES, ETHZ, ICL, MPS, ISAE-Supaero, LPG, MFSC, 2019. URL https://doi.org/10.18715/SEIS.INSIGHT.XB_2016. 10.18715/SEIS.INSIGHT.XB_2016.

InSight Marsquake Service. 2022. Mars Seismic Catalogue, InSight Mission; V9 2022-01-01. *ETHZ, IPGP, JPL, ICL, ISAE-Supaero, MPS, Univ. Bristol.*

IRIS. 2012. Standard for the Exchange of Earthquake Data (SEED) Manual. *URL*. URL http://www.fdsn.org/pdf/SEEDManual.V2.4.pdf.

Irwin, R. P., Watters, T. R., Howard, A. D., and Zimbelman, J. R. 2004. Sedimentary resurfacing and fretted terrain development along the crustal dichotomy boundary, Aeolis Mensae, Mars. *J. Geophys. Res. Planets*, **109**(E9). ISSN 0148-0227. doi: 10.1029/2004JE002248.

Jia, Z. and Clayton, R. W. 2021. Determination of near surface shear-wave velocities in the central Los Angeles basin with dense arrays. *Journal of Geophysical Research: Solid Earth*, **126**(5): e2020JB021369.

Joshi, R., 2022. *Single-station inversion of seismic data for the InSight mission to Mars*. PhD thesis, LMU.

Joshi, R., Knapmeyer-Endrun, B., Mosegaard, K., Wieczorek, M. A., Igel, H., Christensen, U., and Lognonné, P. H. 2023. Joint Inversion of receiver functions and apparent incidence angles to determine the crustal structure of Mars. *Geophysical Research Letters*, p. e2022GL100469. doi: 10.1029/2022GL100469. URL https://doi.org/10.1029/2022GL100469.

Jurkevics, A. 1988. Polarization analysis of three-component array data. *Bulletin of the seismological society of America*, **78**(5): 1725–1743.

Kaula, W. M. 1979. The moment of inertia of Mars. *Geophysical Research Letters*, **6**(3): 194–196.

Kawamura, T., Clinton, J. F., Zenhäusern, G., Ceylan, S., Horleston, A. C., Dahmen, N. L., Duran, C., Kim, D., Plasman, M., Stähler, S. C., Euchner, F., Charalambous, C., Giardini, D., Davis, P., Sainton, G., Lognonné, P., Panning, M., and Banerdt, W. B. 2022. S1222a - the largest Marsquake detected by InSight. *Geophysical Research*

Letters, **n/a**(n/a): e2022GL101543. doi: https://doi.org/10.1029/2022GL101543. e2022GL101543 2022GL101543.

Kenda, B., Drilleau, M., Garcia, R., Kawamura, T., Murdoch, N., and et al., N. C. 2020. Subsurface structure at the InSight landing site from compliance measurements by seismic and meteorological experiments. *Journal of Geophysical Research: Planets*, **125**. doi: 10.1029/2020JE006387.

Kenda, B., Lognonné, P., Spiga, A., Kawamura, T., Kedar, S., Banerdt, W. B., Lorenz, R., Banfield, D., and Golombek, M. 2017. Modeling of Ground Deformation and Shallow Surface Waves Generated by Martian Dust Devils and Perspectives for Near-Surface Structure Inversion. *Space Sci. Rev.*, **211**(1): 501–524. ISSN 1572-9672. doi: 10.1007/s11214-017-0378-0.

Kennett, B., Saygin, E., and Salmon, M. 2015. Stacking autocorrelograms to map Moho depth with high spatial resolution in southeastern Australia. *Geophysical Research Letters*, **42**(18): 7490–7497.

Khan, A., van Driel, M., Böse, M., Giardini, D., Ceylan, S., Yan, J., Clinton, J., Euchner, F., Lognonné, P., Murdoch, N., et al. 2016. Single-station and single-event marsquake location and inversion for structure using synthetic Martian waveforms. *Physics of the Earth and Planetary Interiors*, **258**: 28–42.

Khan, A., Liebske, C., Rozel, A., Rivoldini, A., Nimmo, F., Connolly, J., Plesa, A.-C., and Giardini, D. 2018. A geophysical perspective on the bulk composition of Mars. *Journal of Geophysical Research: Planets*, **123**(2): 575–611.

Kim, D., Banerdt, W., Ceylan, S., Giardini, D., Lekić, V., Lognonné, P., Beghein, C., Beucler, E., Carrasco, S., Charalambous, C., et al. 2022a. Surface waves and crustal structure on Mars. *Science*, **378**(6618): 417–421.

Kim, D., Stähler, S. C., Ceylan, S., Lekic, V., Maguire, R., Zenhäusern, G., Clinton, J., Giardini, D., Khan, A., Panning, M. P., Davis, P., Wieczorek, M., Schmerr, N., Lognonné, P., and Banerdt, W. B. 2022b. Structure Along the Martian Dichotomy Constrained by Rayleigh and Love Waves and their Overtones. *Geophysical Research Letters*, **n/a**(n/a): e2022GL101666. doi: https://doi.org/10.1029/2022GL101666. e2022GL101666 2022GL101666.

Kim, D., Duran, C., Giardini, D., Plesa, A.-C., Stähler, S. C., Boehm, C., Lekić, V., McLennan, S. M., Ceylan, S., Clinton, J. F., Davis, P., Khan, A., Knapmeyer-Endrun, B., Panning, M. P., Wieczorek, M., Lognonné, P., and Banerdt, W. B. 2023. Global Crustal Thickness Revealed by Surface Waves Orbiting Mars. *Geophys. Res. Lett.*, **50**(12): e2023GL103482. ISSN 0094-8276. doi: 10.1029/2023GL103482.

Kim, D., Davis, P., Lekić, V., Maguire, R., Compaire, N., Schimmel, M., Stutzmann, E., C. E. Irving, J., Lognonné, P., Scholz, J., Clinton, J., Zenhäusern, G., Dahmen, N., Deng, S., Levander, A., Panning, M. P., Garcia, R. F., Giardini, D., Hurst, K., Knapmeyer-Endrun, B., Nimmo, F., Pike, W. T., Pou, L., Schmerr, N., Stähler, S. C., Tauzin, B., Widmer-Schnidrig, R., and Banerdt, W. B. 2021a. Potential Pitfalls in the Analysis and Structural Interpretation of Seismic Data from the Mars InSight Mission.

Bulletin of the Seismological Society of America, **111**(6): 2982–3002. ISSN 0037-1106. URL https://doi.org/10.1785/0120210123. 10.1785/0120210123.

Kim, D., Lekić, V., Irving, J. C., Schmerr, N., Knapmeyer-Endrun, B., Joshi, R., Panning, M., Tauzin, B., Karakostas, F., Maguire, R., et al. 2021b. Improving constraints on planetary interiors with PPS receiver functions. *Journal of Geophysical Research: Planets*, **126**(11): e2021JE006983.

Kind, R., Kosarev, G., and Petersen, N. 1995. Receiver functions at the stations of the German Regional Seismic Network (GRSN). *Geophysical Journal International*, **121**(1): 191–202.

Kite, E. S. 2019. Geologic constraints on early Mars climate. *Space Science Reviews*, **215**: 1–47.

Knapmeyer, M., Oberst, J., Hauber, E., Wählisch, M., Deuchler, C., and Wagner, R. 2006. Working models for spatial distribution and level of Mars' seismicity. *Journal of Geophysical Research: Planets*, **111**(E11). doi: https://doi.org/10.1029/2006JE002708.

Knapmeyer, M., Schneider, S., Misun, M., Wählisch, M., and Hauber, E. 2008. An extended global Inventory of Mars Surface Faults. In *European Geosciences Union - General Assembly*, volume 10 of *Geophysical Research Abstracts*. URL https://elib.dlr.de/53941/.

Knapmeyer-Endrun, B., Panning, M., Bissig, F., Joshi, R., Khan, A., D, D. K., Lekić, V., Tauzin, B., Tharimena, S., Plasman, M., Compaire, N., Garcia, R., and et al. 2021. Thickness and structure of the martian crust from InSight seismic data. *Science*, **373**(6553): 438–443. doi: 10.1126/science.abf8966.

Knapmeyer-Endrun, B., Golombek, M. P., and Ohrnberger, M. 2017. Rayleigh wave ellipticity modeling and inversion for shallow structure at the proposed InSight landing site in Elysium Planitia, Mars. *Space Science Reviews*, **211**(1): 339–382.

Knapmeyer-Endrun, B., Murdoch, N., Kenda, B., Golombek, M. P., Knapmeyer, M., Witte, L., Verdier, N., Kedar, S., Lognonné, P., and Banerdt, W. B. 2018. Influence of Body Waves, Instrumentation Resonances, and Prior Assumptions on Rayleigh Wave Ellipticity Inversion for Shallow Structure at the InSight Landing Site. *Space Sci. Rev.*, **214**(5): 1–42. ISSN 1572-9672. doi: 10.1007/s11214-018-0529-y.

Köhler, A., Ohrnberger, M., Scherbaum, F., Wathelet, M., and Cornou, C. 2007. Assessing the reliability of the modified three-component spatial autocorrelation technique. *Geophysical Journal International*, **168**(2): 779–796.

Konno, K. and Ohmachi, T. 1998. Ground-motion characteristics estimated from spectral ratio between horizontal and vertical components of microtremor. *Bulletin of the Seismological Society of America*, **88**(1): 228–241.

Konopliv, A. S., Asmar, S. W., Folkner, W. M., Karatekin, Ö., Nunes, D. C., Smrekar, S. E., Yoder, C. F., and Zuber, M. T. 2011. Mars high resolution gravity fields from MRO, Mars seasonal gravity, and other dynamical parameters. *Icarus*, **211**(1): 401–428.

Konopliv, A. S., Park, R. S., and Folkner, W. M. 2016. An improved JPL Mars gravity field and orientation from Mars orbiter and lander tracking data. *Icarus*, **274**: 253–260.

Ksanfomaliti, L. V., Zubkova, V. M., Morozov, N. A., and Petrova, E. V. 1982. Microseisms at the VENERA-13 and VENERA-14 Landing Sites. *Soviet Astronomy Letters*, **8**: 241–242.

Lachet, C. and Bard, P.-Y. 1994. Numerical and theoretical investigations on the possibilities and limitations of Nakamura's technique. *Journal of Physics of the Earth*, **42**(5): 377–397.

Lam, G. Q., Billets, S., Norick, T., and Warwick, R. 2016. Solar array design for the Mars InSight lander mission. In *14th International Energy Conversion Engineering Conference*, p. 4520.

Langston, C. A. 1979. Structure under Mount Rainier, Washington, inferred from teleseismic body waves. *Journal of Geophysical Research: Solid Earth*, **84**(B9): 4749–4762.

Lecocq, T., Hicks, S. P., Van Noten, K., Van Wijk, K., Koelemeijer, P., De Plaen, R. S., Massin, F., Hillers, G., Anthony, R. E., Apoloner, M.-T., et al. 2020. Global quieting of high-frequency seismic noise due to COVID-19 pandemic lockdown measures. *Science*, **369**(6509): 1338–1343.

Lehman, I. 1936. P'. *Publ. Bur. Cent. Seism. Int.*, **14**: 81–115.

Lemoine, F. G., Smith, D. E., Rowlands, D. D., Zuber, M., Neumann, G., Chinn, D., and Pavlis, D. 2001. An improved solution of the gravity field of Mars (GMM-2B) from Mars Global Surveyor. *Journal of Geophysical Research: Planets*, **106**(E10): 23359–23376.

Lermo, J. and Chávez-García, F. J. 1994. Are microtremors useful in site response evaluation? *Bulletin of the seismological society of America*, **84**(5): 1350–1364.

Lesage, P., Heap, M. J., and Kushnir, A. 2018. A generic model for the shallow velocity structure of volcanoes. *Journal of Volcanology and Geothermal Research*, **356**: 114–126.

Li, C., Zheng, Y., Wang, X., Zhang, J., Wang, Y., Chen, L., Zhang, L., Zhao, P., Liu, Y., Lv, W., et al. 2022a. Layered subsurface in Utopia Basin of Mars revealed by Zhurong rover radar. *Nature*, **610**(7931): 308–312.

Li, G., Chen, H., Niu, F., Guo, Z., Yang, Y., and Xie, J. 2016. Measurement of Rayleigh wave ellipticity and its application to the joint inversion of high-resolution S wave velocity structure beneath northeast China. *Journal of Geophysical Research: Solid Earth*, **121**(2): 864–880.

Li, J., Beghein, C., Davis, P., Wieczorek, M. A., Mclennan, S. M., Kim, D., Lekić, V., Golombek, M., Schimmel, M., Stutzmann, E., et al. 2022b. Crustal Structure Constraints from the Detection of the SsPp Phase on Mars. *Earth and Space Science*, p. e2022EA002416.

Li, J., Beghein, C., Lognonné, P., McLennan, S. M., Wieczorek, M., Panning, M., Knapmeyer-Endrun, B., Davis, P., and Banerdt, W. B. 2022c. Different Martian Crustal Seismic Velocities across the Dichotomy Boundary from Multi-Orbiting Surface Waves. *Geophysical Research Letters*, p. e2022GL101243.

Li, J., Beghein, C., McLennan, S. M., Horleston, A. C., Charalambous, C., Huang, Q., Zenhäusern, G., Bozdağ, E., Pike, W. T., Golombek, M., et al. 2022d. Constraints on the martian crust away from the InSight landing site. *Nature Communications*, **13**(1): 7950.

Li, J., Beghein, C., Wookey, J., Davis, P., Lognonné, P., Schimmel, M., Stutzmann, E., Golombek, M., Montagner, J.-P., and Banerdt, W. B. 2022e. Evidence for crustal seismic anisotropy at the InSight lander site. *Earth and Planetary Science Letters*, **593**: 117654.

Li, Y., Villa, V., Clayton, R. W., and Persaud, P. 2023. Shear Wave Velocities in the San Gabriel and San Bernardino Basins, California. *J. Geophys. Res. Solid Earth*, **128**(7): e2023JB026488. ISSN 2169-9313. doi: 10.1029/2023JB026488.

Lillis, R. J., Robbins, S., Manga, M., Halekas, J. S., and Frey, H. V. 2013. Time history of the Martian dynamo from crater magnetic field analysis. *Journal of Geophysical Research: Planets*, **118**(7): 1488–1511.

Lin, F.-C., Schmandt, B., and Tsai, V. C. 2012. Joint inversion of Rayleigh wave phase velocity and ellipticity using USArray: Constraining velocity and density structure in the upper crust. *Geophysical Research Letters*, **39**(12).

Lobkis, O. I. and Weaver, R. L. 2001. On the emergence of the Green's function in the correlations of a diffuse field. *The Journal of the Acoustical Society of America*, **110**(6): 3011–3017.

Lognonné, P., Zharkov, V., Karczewski, J., Romanowicz, B., Menvielle, M., Poupinet, G., Brient, B., Cavoit, C., Desautez, A., Dole, B., et al. 1998. The seismic OPTIMISM experiment. *Planetary and Space Science*, **46**(6-7): 739–747.

Lognonné, P., Giardini, D., Banerdt, B., Gagnepain-Beyneix, J., Mocquet, A., Spohn, T., Karczewski, J., Schibler, P., Cacho, S., Pike, W., et al. 2000. The NetLander very broad band seismometer. *Planetary and Space Science*, **48**(12-14): 1289–1302.

Lognonné, P. 2005. Planetary seismology. *Annu. Rev. Earth Planet. Sci.*, **33**: 571–604.

Lognonné, P. and Pike, W. Planetary seismometry, 2015.

Lognonné, P., Beyneix, J. G., Banerdt, W. B., Cacho, S., Karczewski, J. F., and Morand, M. 1996. Ultra broad band seismology on InterMarsNet. *Planetary and Space Science*, **44**(11): 1237–1249.

Lognonné, P., Banerdt, W. B., Giardini, D., Pike, W. T., Christensen, U., Laudet, P., De Raucourt, S., Zweifel, P., Calcutt, S., Bierwirth, M., et al. 2019. SEIS: Insight's seismic experiment for internal structure of Mars. *Space Science Reviews*, **215**(1): 1–170.

Lognonné, P., Banerdt, W. B., Pike, W. T., Giardini, D., Christensen, U., Garcia, R. F., Kawamura, T., Kedar, S., Knapmeyer-Endrun, B., Margerin, L., et al. 2020. Constraints on the shallow elastic and anelastic structure of Mars from InSight seismic data. *Nature Geoscience*, **13**(3): 213–220. doi: 10.1038/s41561-020-0536-y.

Lontsi, A. M., Sánchez-Sesma, F. J., Molina-Villegas, J. C., Ohrnberger, M., and Krüger, F. 2015. Full microtremor H/V (z, f) inversion for shallow subsurface characterization. *Geophysical Journal International*, **202**(1): 298–312.

Lorell, J., Born, G., Christensen, E., Jordan, J., Laing, P., Martin, W., Sjogren, W., Shapiro, I., Reasenberg, R., and Slater, G. 1972. Mariner 9 celestial mechanics experiment: Gravity field and pole direction of Mars. *Science*, p. 317–320.

Lorenz, R. D., Nakamura, Y., and Murphy, J. R. 2017. Viking-2 seismometer measurements on Mars: PDS data archive and meteorological applications. *Earth and Space Science*, **4**(11): 681–688.

Lott, F. F., Ritter, J. R., Al-Qaryouti, M., and Corsmeier, U. 2017. On the analysis of wind-induced noise in seismological recordings. *Pure and Applied Geophysics*, **174**(3): 1453–1470.

Lunedei, E. and Albarello, D. 2010. Theoretical HVSR curves from full wavefield modelling of ambient vibrations in a weakly dissipative layered Earth. *Geophysical Journal International*, **181**(2): 1093–1108.

Lunedei, E. and Malischewsky, P. 2015. A Review and Some New Issues on the Theory of the H/V Technique for Ambient Vibrations. In *Perspectives on European Earthquake Engineering and Seismology*, p. 371–394. Springer, Cham, Switzerland. ISBN 978-3-319-16964-4. doi: 10.1007/978-3-319-16964-4_15.

Lutz, M. P. and Zimmerman, R. W. 2021. The effect of pore shape on the Poisson ratio of porous materials. *Math. Mech. Solids*, **26**(8): 1191–1203. ISSN 1081-2865. doi: 10.1177/10812865211023535.

MacDonald, G. J. 1962. On the internal constitution of the inner planets. *Journal of Geophysical Research*, **67**(7): 2945–2974.

Maguire, R., Lekić, V., Kim, D., Schmerr, N., Li, J., Beghein, C., Huang, Q., Irving, J. C., Karakostas, F., Lognonné, P., et al. 2023. Focal Mechanism Determination of Event S1222a and Implications for Tectonics Near the Dichotomy Boundary in Southern Elysium Planitia, Mars. *Journal of Geophysical Research: Planets*, p. e2023JE007793.

Maki, J., Golombek, M., Deen, R., Abarca, H., Sorice, C., Goodsall, T., Schwochert, M., Lemmon, M., Trebi-Ollennu, A., and Banerdt, W. 2018. The color cameras on the InSight lander. *Space Science Reviews*, **214**: 1–34.

Malin, M. C., Bell, J. F., Cantor, B. A., Caplinger, M. A., Calvin, W. M., Clancy, R. T., Edgett, K. S., Edwards, L., Haberle, R. M., James, P. B., Lee, S. W., Ravine, M. A., Thomas, P. C., and Wolff, M. J. 2007. Context Camera Investigation on board the Mars Reconnaissance Orbiter. *J. Geophys. Res. Planets*, **112**(E5). ISSN 0148-0227. doi: 10.1029/2006JE002808.

Malischewsky, P. G. and Scherbaum, F. 2004. Love's formula and H/V-ratio (ellipticity) of Rayleigh waves. *Wave motion*, **40**(1): 57–67.

Margerin, L., Campillo, M., Shapiro, N., and van Tiggelen, B. 1999. Residence time of diffuse waves in the crust as a physical interpretation of coda Q: application to seismograms recorded in Mexico. *Geophysical Journal International*, **138**(2): 343–352.

Margerin, L. 2009. Generalized eigenfunctions of layered elastic media and application to diffuse fields. *The Journal of the Acoustical Society of America*, **125**(1): 164–174.

Margerin, L. 2017. Breakdown of equipartition in diffuse fields caused by energy leakage. *The European Physical Journal Special Topics*, **226**(7): 1353–1370.

Margerin, L., Campillo, M., Van Tiggelen, B., and Hennino, R. 2009. Energy partition of seismic coda waves in layered media: theory and application to Pinyon Flats Observatory. *Geophysical Journal International*, **177**(2): 571–585.

McEwen, A. S., Eliason, E. M., Bergstrom, J. W., Bridges, N. T., Hansen, C. J., Delamere, W. A., Grant, J. A., Gulick, V. C., Herkenhoff, K. E., Keszthelyi, L., Kirk, R. L., Mellon, M. T., Squyres, S. W., Thomas, N., and Weitz, C. M. 2007. Mars Reconnaissance Orbiter's High Resolution Imaging Science Experiment (HiRISE). *J. Geophys. Res. Planets*, **112**(E5). ISSN 0148-0227. doi: 10.1029/2005JE002605.

McGill, G. E. 1989. Buried topography of Utopia, Mars: Persistence of a giant impact depression. *Journal of Geophysical Research: Solid Earth*, **94**(B3): 2753–2759.

McSween Jr, H. Y. and Keil, K. 2000. Mixing relationships in the Martian regolith and the composition of globally homogeneous dust. *Geochimica et Cosmochimica Acta*, **64**(12): 2155–2166.

Menina, S., Margerin, L., Kawamura, T., Heller, G., Drilleau, M., Xu, Z., Calvet, M., Garcia, R. F., Knapmeyer-Endrun, B., Carrasco, S., Onodera, K., Lognonné, P., Stott, A., and Banerdt, W. B. 2023. Stratification of Heterogeneity in the Lithosphere of Mars From Envelope Modeling of Event S1222a and Near Impacts: Interpretation and Implications for Very-High-Frequency Events. *Geophys. Res. Lett.*, **50**(7): e2023GL103202. ISSN 0094-8276. doi: 10.1029/2023GL103202.

Menina, S., Margerin, L., Kawamura, T., Lognonné, P., Marti, J., Drilleau, M., Calvet, M., Compaire, N., Garcia, R., Karakostas, F., Schmerr, N., van Driel, M., Stähler, S. C., Plasman, M., Giardini, D., Carrasco, S., Knapmeyer-Endrun, B., Sainton, G., and Banerdt, W. B. 2021. Energy Envelope and Attenuation Characteristics of High-Frequency (HF) and Very-High-Frequency (VF) Martian Events. *Bulletin of the Seismological Society of America*, **111**(6): 3016–3034. ISSN 0037-1106. URL https://doi.org/10.1785/0120210127. 10.1785/0120210127.

Mimoun, D., Murdoch, N., Lognonné, P., Hurst, K., Pike, W. T., Hurley, J., Nébut, T., and Banerdt, W. B. 2017. The noise model of the SEIS seismometer of the InSight mission to Mars. *Space Science Reviews*, **211**(1): 383–428.

Mohorovicic, A. 1910. Das Beben vom 8. x. 1909. *Jahrbuch Meterologie Observatorie Zagrab*, **9**: 1–63.

Mora, M. M., Lesage, P., Valette, B., Alvarado, G. E., Leandro, C., Métaxian, J.-P., and Dorel, J. 2006. Shallow velocity structure and seismic site effects at Arenal volcano, Costa Rica. *J. Volcanol. Geotherm. Res.*, **152**(1): 121–139. ISSN 0377-0273. doi: 10.1016/j.jvolgeores.2005.09.013.

Morgan, P., Grott, M., Knapmeyer-Endrun, B., Golombek, M., Delage, P., Lognonné, P., Piqueux, S., Daubar, I., Murdoch, N., Charalambous, C., et al. 2018. A pre-landing assessment of regolith properties at the InSight landing site. *Space Science Reviews*, **214**(6): 1–47.

Mucciarelli, M., Gallipoli, M. R., Di Giacomo, D., Di Nota, F., and Nino, E. 2005. The influence of wind on measurements of seismic noise. *Geophysical Journal International*, **161**(2): 303–308.

Mulargia, F. 2012. The seismic noise wavefield is not diffuse. *The Journal of the Acoustical Society of America*, **131**(4): 2853–2858.

Mulargia, F. and Castellaro, S. 2016. HVSR deep mapping tested down to ∼1.8km in Po Plane Valley, Italy. *Phys. Earth Planet. Inter.*, **261**: 17–23. ISSN 0031-9201. doi: 10.1016/j.pepi.2016.08.002.

Munirova, L. and Yanovskaya, T. 2001. Spectral ratio of the horizontal and vertical Rayleigh wave components and its application to some problems of seismology. *Izvestiya. Physics of the Solid Earth*, **37**(9): 709–716.

Murchie, S., Arvidson, R., Bedini, P., Beisser, K., Bibring, J.-P., Bishop, J., Boldt, J., Cavender, P., Choo, T., Clancy, R. T., Darlington, E. H., Marais, D. D., Espiritu, R., Fort, D., Green, R., Guinness, E., Hayes, J., Hash, C., Heffernan, K., Hemmler, J., Heyler, G., Humm, D., Hutcheson, J., Izenberg, N., Lee, R., Lees, J., Lohr, D., Malaret, E., Martin, T., McGovern, J. A., McGuire, P., Morris, R., Mustard, J., Pelkey, S., Rhodes, E., Robinson, M., Roush, T., Schaefer, E., Seagrave, G., Seelos, F., Silverglate, P., Slavney, S., Smith, M., Shyong, W.-J., Strohbehn, K., Taylor, H., Thompson, P., Tossman, B., Wirzburger, M., and Wolff, M. 2007. Compact Reconnaissance Imaging Spectrometer for Mars (CRISM) on Mars Reconnaissance Orbiter (MRO). *J. Geophys. Res. Planets*, **112**(E5). ISSN 0148-0227. doi: 10.1029/2006JE002682.

Murdoch, N., Mimoun, D., Garcia, R. F., Rapin, W., Kawamura, T., Lognonné, P., Banfield, D., and Banerdt, W. B. 2017. Evaluating the wind-induced mechanical noise on the InSight seismometers. *Space Science Reviews*, **211**(1): 429–455.

Naderyan, V., Hickey, C. J., and Raspet, R. 2016. Wind-induced ground motion. *Journal of Geophysical Research: Solid Earth*, **121**(2): 917–930.

Nakamura, Y. 1989. A method for dynamic characteristics estimation of subsurface using microtremor on the ground surface. *Railway Technical Research Institute, Quarterly Reports*, **30**(1).

Nakamura, Y. 2005. Farside deep moonquakes and deep interior of the Moon. *Journal of Geophysical Research: Planets*, **110**(E1).

Nakamura, Y. 2008. On the H/V spectrum. In *The 14th World Conf. on Earthquake Engineering*, p. 12–17 October 2008. Beijing, China.

Nakamura, Y. et al. 2000. Clear identification of fundamental idea of Nakamura's technique and its applications. In *Proceedings of the 12th world conference on earthquake engineering*, volume 2656, p. 1–8. Auckland/New Zealand.

Napolitano, F., Gervasi, A., La Rocca, M., Guerra, I., and Scarpa, R. 2018. Site effects in the Pollino region from the HVSR and polarization of seismic noise and earthquakes. *Bulletin of the Seismological Society of America*, **108**(1): 309–321.

Nardone, L. and Maresca, R. 2011. Shallow Velocity Structure and Site Effects at Mt. Vesuvius, Italy, from HVSR and Array Measurements of Ambient Vibrations. *Bull. Seismol. Soc. Am.*, **101**(4): 1465–1477. ISSN 0037-1106. doi: 10.1785/0120100165.

Neumann, G., Zuber, M., Wieczorek, M. A., McGovern, P., Lemoine, F. G., and Smith, D. 2004. Crustal structure of Mars from gravity and topography. *Journal of Geophysical Research: Planets*, **109**(E8).

Nimmo, F. 2002. Admittance estimates of mean crustal thickness and density at the Martian hemispheric dichotomy. *Journal of Geophysical Research: Planets*, **107**(E11): 27–1.

Nogoshi, M. and Igarashi, T. 1971. On the amplitude characteristics of microtremor (Part 2). *Zisin (Journal of the Seismological Society of Japan)*, **24**: 26–40. doi: 10.4294/zisin1948.24.1_26.

Oberst, J. and Nakamura, Y. 1987. Distinct meteoroid families identified on the lunar seismograms. *Journal of Geophysical Research: Solid Earth*, **92**(B4): E769–E773.

Ojha, L. and Lewis, K. 2018. The density of the Medusae Fossae Formation: Implications for its composition, origin, and importance in Martian history. *Journal of Geophysical Research: Planets*, **123**(6): 1368–1379.

Okal, E. A. 2008. The generation of T waves by earthquakes. *Advances in Geophysics*, **49**: 1–65.

Oldham, R. D. 1906. The constitution of the interior of the Earth, as revealed by earthquakes. *Quarterly Journal of the Geological Society*, **62**(1-4): 456–475.

Onodera, K. 2022. Subsurface structure of the Moon and Mars from 3D seismic wave propagation simulation and analysis of Apollo and InSight seismic data. *Doctoral Dissertation of The Graduate University for Advanced Studies, SOKENDAI and Université Paris Cité.*

Onodera, K., Nishida, K., Kawamura, T., Murdoch, N., Drilleau, M., Otsuka, R., Lorenz, R., Horleston, A., Widmer-Schnidrig, R., Schimmel, M., et al. 2023. Description of Martian convective vortices observed by InSight and implications for vertical vortex structure and subsurface physical properties. *Journal of Geophysical Research: Planets*, **128**(8): e2023JE007896.

Pan, L., Ehlmann, B. L., Carter, J., and Ernst, C. M. 2017. The stratigraphy and history of Mars' northern lowlands through mineralogy of impact craters: A comprehensive survey. *Journal of Geophysical Research: Planets*, **122**(9): 1824–1854.

Pan, L., Quantin-Nataf, C., Tauzin, B., Michaut, C., Golombek, M., Lognonné, P., Grindrod, P., Langlais, B., Gudkova, T., Stepanova, I., et al. 2020. Crust stratigraphy and heterogeneities of the first kilometers at the dichotomy boundary in western Elysium Planitia and implications for InSight lander. *Icarus*, **338**: 113511. doi: 10.1016/j.icarus.2019.113511.

Panning, M. P., Banerdt, W. B., Beghein, C., Carrasco, S., Ceylan, S., Clinton, J. F., Davis, P., Drilleau, M., Giardini, D., Khan, A., Kim, D., Knapmeyer-Endrun, B., Li, J., Lognonné, P., Stähler, S. C., and Zenhäusern, G. 2022. Locating the largest event observed on Mars with multi-orbit surface waves. *Geophysical Research Letters*, **n/a**(n/a): e2022GL101270. doi: https://doi.org/10.1029/2022GL101270. e2022GL101270 2022GL101270.

Panning, M. P., Beucler, É., Drilleau, M., Mocquet, A., Lognonné, P., and Banerdt, W. B. 2015. Verifying single-station seismic approaches using Earth-based data: Preparation for data return from the InSight mission to Mars. *Icarus*, **248**: 230–242.

Panning, M. P., Lognonné, P., Bruce Banerdt, W., Garcia, R., Golombek, M., Kedar, S., Knapmeyer-Endrun, B., Mocquet, A., Teanby, N. A., Tromp, J., et al. 2017. Planned products of the Mars structure service for the InSight mission to Mars. *Space Science Reviews*, **211**(1): 611–650.

Panning, M. P., Pike, W. T., Lognonné, P., Banerdt, W. B., Murdoch, N., Banfield, D., Charalambous, C., Kedar, S., Lorenz, R. D., Marusiak, A. G., et al. 2020. On-deck seismology: Lessons from InSight for future planetary seismology. *Journal of Geophysical Research: Planets*, **125**(4): e2019JE006353.

Panzera, F., Lombardo, G., Monaco, C., and Di Stefano, A. 2015. Seismic site effects observed on sediments and basaltic lavas outcropping in a test site of Catania, Italy. *Natural Hazards*, **79**(1): 1–27.

Park, J., Vernon III, F. L., and Lindberg, C. R. 1987. Frequency dependent polarization analysis of high-frequency seismograms. *Journal of Geophysical Research: Solid Earth*, **92**(B12): 12664–12674.

Parolai, S., Richwalski, S. M., Milkereit, C., and Bormann, P. 2004. Assessment of the stability of H/V spectral ratios from ambient noise and comparison with earthquake data in the Cologne area (Germany). *Tectonophysics*, **390**(1-4): 57–73.

Parolai, S., Picozzi, M., Richwalski, S., and Milkereit, C. 2005. Joint inversion of phase velocity dispersion and H/V ratio curves from seismic noise recordings using a genetic algorithm, considering higher modes. *Geophysical research letters*, **32**(1).

Pedersen, H., Boué, P., Poli, P., and Colombi, A. 2015. Arrival angle anomalies of Rayleigh waves observed at a broadband array: a systematic study based on earthquake data, full waveform simulations and noise correlations. *Geophysical Supplements to the Monthly Notices of the Royal Astronomical Society*, **203**(3): 1626–1641.

Perrin, C., Jacob, A., Lucas, A., Myhill, R., Hauber, E., Batov, A., Gudkova, T., Rodriguez, S., Lognonné, P., Stevanović, J., et al. 2022. Geometry and segmentation of Cerberus Fossae, Mars: Implications for marsquake properties. *Journal of Geophysical Research: Planets*, **127**(1): e2021JE007118.

Perton, M., Sánchez-Sesma, F., Rodríguez-Castellanos, A., Campillo, M., and Weaver, R. L. 2009. Two perspectives on equipartition in diffuse elastic fields in three dimensions. *The Journal of the Acoustical Society of America*, **126**(3): 1125–1130.

Perton, M., Spica, Z. J., Clayton, R. W., and Beroza, G. C. 2020. Shear wave structure of a transect of the Los Angeles basin from multimode surface waves and H/V spectral ratio analysis. *Geophys. J. Int.*, **220**(1): 415–427. ISSN 0956-540X. doi: 10.1093/gji/ggz458.

Phillips, R. J. 1991. Expected rate of marsquakes. In *Scientific Rationale and Requirements for a Global Seismic Network on Mars. LPI Tech. Rept., 91-02, Lunar and Planetary Inst., Houston*, p. 35–38.

Phinney, R. A. 1964. Structure of the Earth's crust from spectral behavior of long-period body waves. *Journal of Geophysical Research*, **69**(14): 2997–3017.

Pilz, M., Parolai, S., Leyton, F., Campos, J., and Zschau, J. 2009. A comparison of site response techniques using earthquake data and ambient seismic noise analysis in the large urban areas of Santiago de Chile. *Geophysical Journal International*, **178**(2): 713–728.

Piña-Flores, J., Perton, M., García-Jerez, A., Carmona, E., Luzón, F., Molina-Villegas, J. C., and Sánchez-Sesma, F. J. 2016. The inversion of spectral ratio H/V in a layered system using the diffuse field assumption (DFA). *Geophysical Journal International*, **208**: 577–588. 10.1093/gji/ggw416.

Piña-Flores, J., Cárdenas-Soto, M., García-Jerez, A., Campillo, M., and Sánchez-Sesma, F. J. 2021. The search of diffusive properties in ambient seismic noise. *Bulletin of the Seismological Society of America*, **111**(3): 1650–1660.

Platz, T. and Michael, G. 2011. Eruption history of the Elysium volcanic province, Mars. *Earth and Planetary Science Letters*, **312**(1-2): 140–151.

Plesa, A.-C., Knapmeyer, M., Golombek, M., Breuer, D., Grott, M., Kawamura, T., Lognonné, P., Tosi, N., and Weber, R. 2018a. Present-day Mars' seismicity predicted from 3-D thermal evolution models of interior dynamics. *Geophysical Research Letters*, **45**(6): 2580–2589.

Plesa, A.-C., Padovan, S., Tosi, N., Breuer, D., Grott, M., Wieczorek, M., Spohn, T., Smrekar, S., and Banerdt, W. 2018b. The thermal state and interior structure of Mars. *Geophysical Research Letters*, **45**(22): 12–198.

Plescia, J. B. 2003. Cerberus Fossae, Elysium, Mars: a source for lava and water. *Icarus*, **164**(1): 79–95. ISSN 0019-1035. doi: 10.1016/S0019-1035(03)00139-8.

Poli, P., Boaga, J., Molinari, I., Cascone, V., and Boschi, L. 2020. The 2020 coronavirus lockdown and seismic monitoring of anthropic activities in Northern Italy. *Scientific Reports*, **10**(1): 9404.

Posiolova, L. V., Lognonné, P., Banerdt, W. B., Clinton, J., Collins, G. S., Kawamura, T., Ceylan, S., Daubar, I. J., Fernando, B., Froment, M., et al. 2022. Largest recent impact craters on Mars: Orbital imaging and surface seismic co-investigation. *Science*, **378**(6618): 412–417.

Reasenberg, R., Shapiro, I., and White, R. 1975. The gravity field of Mars. *Geophysical Research Letters*, **2**(3): 89–92.

Rigo, A., Sokos, E., Lefils, V., and Briole, P. 2021. Seasonal variations in amplitudes and resonance frequencies of the HVSR amplification peaks linked to groundwater. *Geophys. J. Int.*, **226**(1): 1–13. ISSN 0956-540X. doi: 10.1093/gji/ggab086.

Rivet, D., Campillo, M., Sanchez-Sesma, F., Shapiro, N. M., and Singh, S. K. 2015. Identification of surface wave higher modes using a methodology based on seismic noise and coda waves. *Geophysical Journal International*, **203**(2): 856–868.

Rivoldini, A., Van Hoolst, T., Verhoeven, O., Mocquet, A., and Dehant, V. 2011. Geodesy constraints on the interior structure and composition of Mars. *Icarus*, **213**(2): 451–472.

Roberts, G. P., Matthews, B., Bristow, C., Guerrieri, L., and Vetterlein, J. 2012. Possible evidence of paleomarsquakes from fallen boulder populations, Cerberus Fossae, Mars. *Journal of Geophysical Research: Planets*, **117**(E2).

Saito, T., Sato, H., and Ohtake, M. 2002. Envelope broadening of spherically outgoing waves in three-dimensional random media having power law spectra. *Journal of Geophysical Research: Solid Earth*, **107**(B5): ESE–3.

Sambridge, M. 1999. Geophysical inversion with a neighbourhood algorithm—I. Searching a parameter space. *Geophysical journal international*, **138**(2): 479–494.

Samson, J. 1983. Pure states, polarized waves, and principal components in the spectra of multiple, geophysical time-series. *Geophysical Journal International*, **72**(3): 647–664.

Samson, J. and Olson, J. 1980. Some comments on the descriptions of the polarization states of waves. *Geophysical Journal International*, **61**(1): 115–129.

Sánchez-Sesma, F. J. 2017. Modeling and inversion of the microtremor H/V spectral ratio: physical basis behind the diffuse field approach. *Earth, Planets and Space*, **69**(1): 1–9.

Sánchez-Sesma, F. J. and Campillo, M. 2006. Retrieval of the Green's function from cross correlation: the canonical elastic problem. *Bulletin of the Seismological Society of America*, **96**(3): 1182–1191.

Sánchez-Sesma, F. J., Pérez-Ruiz, J. A., Luzon, F., Campillo, M., and Rodríguez-Castellanos, A. 2008. Diffuse fields in dynamic elasticity. *Wave motion*, **45**(5): 641–654.

Sánchez-Sesma, F. J., Rodríguez, M., Iturrarán-Viveros, U., Luzón, F., Campillo, M., Margerin, L., García-Jerez, A., Suarez, M., Santoyo, M. A., and Rodriguez-Castellanos, A. 2011. A theory for microtremor H/V spectral ratio: application for a layered medium. *Geophysical Journal International*, **186**(1): 221–225.

Santoli, F., Fiorenza, E., Lefevre, C., Lucchesi, D. M., Lucente, M., Magnafico, C., Morbidini, A., Peron, R., and Iafolla, V. 2020. ISA, a High Sensitivity Accelerometer in the Interplanetary Space. *Space Sci. Rev.*, **216**(8): 1–30. ISSN 1572-9672. doi: 10.1007/s11214-020-00768-6.

Saroglou, C. and Kallimogiannis, V. 2017. Fracturing process and effect of fracturing degree on wave velocity of a crystalline rock. *J. Rock Mech. Geotech. Eng.*, **9**(5): 797–806. ISSN 1674-7755. doi: 10.1016/j.jrmge.2017.03.012.

Sato, H. 1982. Amplitude attenuation of impulsive waves in random media based on travel time corrected mean wave formalism. *The Journal of the Acoustical Society of America*, **71**(3): 559–564.

Sato, H. and Fehler, M. C. 1998. *Seismic Wave Propagation and Scattering in the Heterogeneous Earth*. Springer, New York, NY, USA. ISBN 978-1-4612-7457-5. URL https://link.springer.com/book/9781461274575.

Savitzky, A. and Golay, M. J. 1964. Smoothing and differentiation of data by simplified least squares procedures. *Analytical chemistry*, **36**(8): 1627–1639.

Scherbaum, F., Hinzen, K.-G., and Ohrnberger, M. 2003. Determination of shallow shear wave velocity profiles in the Cologne, Germany area using ambient vibrations. *Geophysical Journal International*, **152**(3): 597–612.

Schimmel, M., Stutzmann, E., Lognonné, P., Compaire, N., Davis, P., Drilleau, M., Garcia, R., Kim, D., Knapmeyer-Endrun, B., Lekic, V., Margerin, L., Panning, M., Schmerr, N., Scholz, J. R., Spiga, A., Tauzin, B., and Banerdt, B. 2021. Seismic Noise Autocorrelations on Mars. *Earth and Space Science*, **8**(6): e2021EA001755. doi: https://doi.org/10.1029/2021EA001755. URL https://agupubs.onlinelibrary.wiley.com/doi/abs/10.1029/2021EA001755.

Scholz, J.-R., Widmer-Schnidrig, R., Davis, P., Lognonné, P., Pinot, B., Garcia, R. F., Hurst, K., Pou, L., Nimmo, F., Barkaoui, S., de Raucourt, S., Knapmeyer-Endrun, B., Knapmeyer, M., Orhand-Mainsant, G., Compaire, N., Cuvier, A., Beucler, , Bonnin, M., Joshi, R., Sainton, G., Stutzmann, E., Schimmel, M., Horleston, A., Böse, M., Ceylan, S., Clinton, J., van Driel, M., Kawamura, T., Khan, A., Stähler, S. C., Giardini, D., Charalambous, C., Stott, A. E., Pike, W. T., Christensen, U. R., and Banerdt, W. B. 2020. Detection, Analysis, and Removal of Glitches From InSight's Seismic Data From Mars. *Earth and Space Science*, **7**(11): e2020EA001317. doi: https://doi.org/10.1029/2020EA001317. URL https://agupubs.onlinelibrary.wiley.com/doi/abs/10.1029/2020EA001317.

Schuster, G. T. 2009. *Seismic Interferometry*. Cambridge University Press. doi: 10.1017/CBO9780511581557.

SESAME. 2004. Guidelines for the implementation of the H/V spectral ratio technique on ambient vibrations: Measurements, processing, and interpretations.

Sexton, J. L., Rudman, A., and Mead, J. 1977. Ellipticity of Rayleigh waves recorded in the Midwest. *Bulletin of the Seismological Society of America*, **67**(2): 369–382.

Shapiro, N. M., Campillo, M., Margerin, L., Singh, S. K., Kostoglodov, V., and Pacheco, J. 2000. The Energy Partitioning and the Diffusive Character of the Seismic Coda. *Bull. Seismol. Soc. Am.*, **90**(3): 655–665. ISSN 0037-1106. doi: 10.1785/0119990021.

Shapiro, N. M. and Campillo, M. 2004. Emergence of broadband Rayleigh waves from correlations of the ambient seismic noise. *Geophysical Research Letters*, **31**(7).

Shearer, P. M. 2019. *Introduction to Seismology*. Cambridge University Press, 3 edition. doi: 10.1017/9781316877111.

Shi, J., Plasman, M., Knapmeyer-Endrun, B., Xu, Z., Kawamura, T., Lognonné, P., McLennan, S., Sainton, G., Banerdt, W., Panning, M., and Wang, T. 2023. High-frequency receiver functions with event S1222a reveal a discontinuity in the Martian shallow crust. *Geophysical Research Letters*, **50**(5): e2022GL101627. doi: https://doi.org/10.1029/2022GL101627.

Shibutani, T., Sambridge, M., and Kennett, B. 1996. Genetic algorithm inversion for receiver functions with application to crust and uppermost mantle structure beneath eastern Australia. *Geophysical Research Letters*, **23**(14): 1829–1832.

Slepian, D. 1978. Prolate spheroidal wave functions, Fourier analysis, and uncertainty—V: The discrete case. *Bell System Technical Journal*, **57**(5): 1371–1430.

Smith, D. E., Sjogren, W. L., Tyler, G. L., Balmino, G., Lemoine, F. G., and Konopliv, A. S. 1999a. The gravity field of Mars: results from Mars Global Surveyor. *Science*, **286**(5437): 94–97.

Smith, D. E., Zuber, M. T., Solomon, S. C., Phillips, R. J., Head, J. W., Garvin, J. B., Banerdt, W. B., Muhleman, D. O., Pettengill, G. H., Neumann, G. A., et al. 1999b. The global topography of Mars and implications for surface evolution. *science*, **284**(5419): 1495–1503.

Smith, D. E., Zuber, M. T., Frey, H. V., Garvin, J. B., Head, J. W., Muhleman, D. O., Pettengill, G. H., Phillips, R. J., Solomon, S. C., Zwally, H. J., et al. 2001. Mars Orbiter Laser Altimeter: Experiment summary after the first year of global mapping of Mars. *Journal of Geophysical Research: Planets*, **106**(E10): 23689–23722.

Smrekar, S. E., Lognonné, P., Spohn, T., Banerdt, W. B., Breuer, D., Christensen, U., Dehant, V., Drilleau, M., Folkner, W., Fuji, N., et al. 2019. Pre-mission InSights on the interior of Mars. *Space Science Reviews*, **215**: 1–72.

Sorrells, G. 1971. A preliminary investigation into the relationship between long-period seismic noise and local fluctuations in the atmospheric pressure field. *Geophysical Journal International*, **26**: 71–82. doi: 10.1111j.1365-246X.1971.tb03383.x.

Spica, Z., Caudron, C., Perton, M., Lecocq, T., Camelbeeck, T., Legrand, D., Piña-Flores, J., Iglesias, A., and Syahbana, D. K. 2015. Velocity models and site effects at Kawah Ijen volcano and Ijen caldera (Indonesia) determined from ambient noise cross-correlations and directional energy density spectral ratios. *J. Volcanol. Geotherm. Res.*, **302**: 173–189. ISSN 0377-0273. doi: 10.1016/j.jvolgeores.2015.06.016.

Spica, Z. J., Perton, M., Nakata, N., Liu, X., and Beroza, G. C. 2018. Site characterization at Groningen gas field area through joint surface-borehole H/V analysis. *Geophysical Journal International*, **212**(1): 412–421.

Spohn, T., Grott, M., Smrekar, S., Knollenberg, J., Hudson, T., Krause, C., Müller, N., Jänchen, J., Börner, A., Wippermann, T., et al. 2018. The heat flow and physical properties package (HP 3) for the InSight mission. *Space Science Reviews*, **214**: 1–33.

Stevenson, D. J., Cutts, J. A., Mimoun, D., Arrowsmith, S., Banerdt, W. B., Blom, P., Brageot, E., Brissaud, Q., Chin, G., Gao, P., et al. 2015. Probing the interior structure of Venus.

Stutzmann, E., Schimmel, M., Lognonné, P., Horleston, A., Ceylan, S., van Driel, M., Stahler, S., Banerdt, B., Calvet, M., Charalambous, C., Clinton, J., Drilleau, M., Fayon, L., Garcia, R. F., Giardini, D., Hurst, K., Jacob, A., Kawamura, T., Kenda, B., Margerin, L., Murdoch, N., Panning, M., Pike, T., Scholz, J. R., and Spiga, A. 2021. The Polarization of Ambient Noise on Mars. *Journal of Geophysical Research: Planets*, **126**(1): e2020JE006545. URL https://doi.org/10.1029/2020JE006545. https://doi.org/10.1029/2020JE006545.

Tanaka, K., Skinner, J., Dohm, J., Irwin III, R., Kolb, E., Fortezzo, C., Platz, T., Michael, G., and Hare, T. 2014. Geologic map of Mars. *U.S. Geological Survey Scientific Investigations Map 3292*. doi: 10.3133/sim3292.

Tanimoto, T. and Rivera, L. 2008. The ZH ratio method for long-period seismic data: sensitivity kernels and observational techniques. *Geophysical Journal International*, **172**(1): 187–198.

Tanuma, K. and Man, C.-S. 2008. Perturbation formulas for polarization ratio and phase shift of Rayleigh waves in prestressed anisotropic media. *Journal of Elasticity*, **92**(1): 1–33.

Taylor, F. W., Svedhem, H., and Head, J. W. 2018. Venus: the atmosphere, climate, surface, interior and near-space environment of an Earth-like planet. *Space Science Reviews*, **214**: 1–36.

Toksőz, M., Press, F., Anderson, K., Dainty, A., Latham, G., Ewing, M., Dorman, J., Lammlein, D., Nakamura, Y., Sutton, G., et al. 1972. Velocity structure and properties of the lunar crust. *The moon*, **4**: 490–504.

Trebi-Ollennu, A., Kim, W., Ali, K., Khan, O., Sorice, C., Bailey, P., Umland, J., Bonitz, R., Ciarleglio, C., Knight, J., et al. 2018. InSight Mars lander robotics instrument deployment system. *Space Science Reviews*, **214**: 1–18.

Uyanik, O. 2010. Compressional and shear-wave velocity measurements in unconsolidated top-soil and comparison of the results. *International Journal of the Physical Sciences*, **5**(7): 1034–1039.

van Driel, M., Ceylan, S., Clinton, J. F., Giardini, D., Horleston, A., Margerin, L., Stähler, S. C., Böse, M., Charalambous, C., Kawamura, T., et al. 2021. High-frequency

seismic events on Mars observed by InSight. *Journal of Geophysical Research: Planets*, **126**(2): e2020JE006670.

van Ginkel, J., Ruigrok, E., and Herber, R. 2020. Using horizontal-to-vertical spectral ratios to construct shear-wave velocity profiles. *Solid Earth*, **11**(6): 2015–2030.

Vaucher, J., Baratoux, D., Mangold, N., Pinet, P., Kurita, K., and Grégoire, M. 2009. The volcanic history of central Elysium Planitia: Implications for martian magmatism. *Icarus*, **204**(2): 418–442.

Vidale, J. E. 1986. Complex polarization analysis of particle motion. *Bulletin of the Seismological society of America*, **76**(5): 1393–1405.

Villa, V., Li, Y., Clayton, R. W., and Persaud, P. 2023. Three-Dimensional Basin Depth Map of the Northern Los Angeles Basins From Gravity and Seismic Measurements. *J. Geophys. Res. Solid Earth*, **128**(7): e2022JB025425. ISSN 2169-9313. doi: 10.1029/2022JB025425.

Vinciguerra, S., Trovato, C., Meredith, P., and Benson, P. 2005. Relating seismic velocities, thermal cracking and permeability in Mt. Etna and Iceland basalts. *International Journal of Rock Mechanics and Mining Sciences*, **42**(7): 900–910. ISSN 1365-1609. URL https://www.sciencedirect.com/science/article/pii/S1365160905000717. Rock Physics and Geomechanics.

Vinnik, L., Chenet, H., Gagnepain-Beyneix, J., and Lognonne, P. 2001. First seismic receiver functions on the Moon. *Geophysical research letters*, **28**(15): 3031–3034.

Virtanen, P., Gommers, R., Oliphant, T. E., Haberland, M., Reddy, T., Cournapeau, D., Burovski, E., Peterson, P., Weckesser, W., Bright, J., et al. 2020. SciPy 1.0: fundamental algorithms for scientific computing in Python. *Nature methods*, **17**(3): 261–272.

Walker, D. A., McCreery, C. S., and Hiyoshi, Y. 1992. T-phase spectra, seismic moments, and tsunamigenesis. *Bulletin of the Seismological Society of America*, **82**(3): 1275–1305.

Wänke, H. and Dreibus, G. 1994. Chemistry and accretion history of Mars. *Philosophical Transactions of the Royal Society of London. Series A: Physical and Engineering Sciences*, **349**(1690): 285–293.

Wapenaar, K. 2004. Retrieving the elastodynamic Green's function of an arbitrary inhomogeneous medium by cross correlation. *Physical review letters*, **93**(25): 254301.

Warner, N., Golombek, M., Sweeney, J., Fergason, R., Kirk, R., and Schwartz, C. 2017. Near surface stratigraphy and regolith production in southwestern Elysium Planitia, Mars: implications for Hesperian-Amazonian terrains and the InSight lander mission. *Space Science Reviews*, **211**(1): 147–190.

Warner, N., Grant, J., Wilson, S., Golombek, M., DeMott, A., Charalambous, C., Hauber, E., Ansan, V., Weitz, C., Pike, T., et al. 2020. An impact crater origin for the InSight landing site at Homestead hollow, Mars: Implications for near surface stratigraphy, surface processes, and erosion rates. *Journal of Geophysical Research: Planets*, **125**(4): e2019JE006333. doi: 10.1029/2019JE006333.

Warner, N., Golombek, M., Ansan, V., Marteau, E., Williams, N., Grant, J., and et al. 2022. In situ and orbital stratigraphic characterization of the InSight landing site—A type example of a regolith-covered lava plain on Mars. *Journal of Geophysical Research: Planets*, **127**. doi: 10.1029/2022JE007232.

Wathelet, M. 2008. An improved neighborhood algorithm: parameter conditions and dynamic scaling. *Geophysical Research Letters*, **35**(L09301). doi: 10.1029/2008GL033256.

Wathelet, M., J.-L. Chatelain, J.-L., Cornou, C., Di Giulio, G., Guillier, B., Ohrnberger, M., and Savvaidis, A. 2020. Geopsy: A User-Friendly Open-Source Tool Set for Ambient Vibration Processing. *Seismological Research Letters*, **91**(3): 1878–1889. doi: 10.1785/0220190360.

Wathelet, M. 2005. Array recordings of ambient vibrations: surface-wave inversion. *PhD Diss., Liége University*, **161**.

Wathelet, M., Jongmans, D., and Ohrnberger, M. 2004. Surface-wave inversion using a direct search algorithm and its application to ambient vibration measurements. *Near surface geophysics*, **2**(4): 211–221.

Weaver, R., Froment, B., and Campillo, M. 2009. On the correlation of non-isotropically distributed ballistic scalar diffuse waves. *The Journal of the Acoustical Society of America*, **126**(4): 1817–1826.

Weaver, R. L. 1982. On diffuse waves in solid media. *The Journal of the Acoustical Society of America*, **71**(6): 1608–1609.

Weber, R. C., Lin, P.-Y., Garnero, E. J., Williams, Q., and Lognonné, P. 2011. Seismic detection of the lunar core. *science*, **331**(6015): 309–312.

Wieczorek, M. A. and Zuber, M. T. 2004. Thickness of the Martian crust: Improved constraints from geoid-to-topography ratios. *J. Geophys. Res. Planets*, **109**(E1). ISSN 0148-0227. doi: 10.1029/2003JE002153.

Wieczorek, M. A., Broquet, A., McLennan, S. M., Rivoldini, A., Golombek, M., Antonangeli, D., Beghein, C., Giardini, D., Gudkova, T., Gyalay, S., Johnson, C. L., Joshi, R., Kim, D., King, S. D., Knapmeyer-Endrun, B., Lognonné, P., Michaut, C., Mittelholz, A., Nimmo, F., Ojha, L., Panning, M. P., Plesa, A.-C., Siegler, M. A., Smrekar, S. E., Spohn, T., and Banerdt, W. B. 2022. InSight Constraints on the Global Character of the Martian Crust. *Journal of Geophysical Research: Planets*, **127**(5): e2022JE007298. doi: https://doi.org/10.1029/2022JE007298. URL https://agupubs.onlinelibrary.wiley.com/doi/abs/10.1029/2022JE007298. e2022JE007298 2022JE007298.

Wilcox, B., Robinson, M., Thomas, P., and Hawke, B. 2005. Constraints on the depth and variability of the lunar regolith. *Meteoritics & Planetary Science*, **40**(5): 695–710.

Williams, D. R. 2004. Mars fact sheet. *http://nssdc. gsfc. nasa. gov/planetary/factsheet/marsfact. html*.

Wilson, S., Warner, N., Grant, J., Golombek, M., DeMott, A., Kopp, M., Berger, L., Weitz, C., Hauber, E., Ansan, V., et al. 2019. Crater retention ages at the InSight Landing Site: implications for the degradation history of the Homestead Hollow. In *50th Lunar and Planetary Science Conference*, volume 2132, p. 2161.

Woodhouse, J. 1974. Surface waves in a laterally varying layered structure. *Geophysical Journal International*, **37**(3): 461–490.

Xu, Z., Froment, M., Garcia, R. F., Beucler, É., Onodera, K., Kawamura, T., Lognonné, P., and Banerdt, W. B. 2022. Modeling Seismic Recordings of High-Frequency Guided Infrasound on Mars. *Journal of Geophysical Research: Planets*, **127**(11): e2022JE007483.

Xu, Z., Broquet, A., Fuji, N., Kawamura, T., Lognonné, P., Montagner, J.-P., Pan, L., Schimmel, M., Stutzmann, E., and Banerdt, W. B. 2023. Investigation of Martian Regional Crustal Structure Near the Dichotomy Using S1222a Surface-Wave Group Velocities. *Geophysical Research Letters*, **50**(8): e2023GL103136.

Yamanaka, H., Takemura, M., Ishida, H., and Niwa, M. 1994. Characteristics of long-period microtremors and their applicability in exploration of deep sedimentary layers. *Bulletin of the Seismological Society of America*, **84**(6): 1831–1841.

Yano, T., Tanimoto, T., and Rivera, L. 2009. The ZH ratio method for long-period seismic data: inversion for S-wave velocity structure. *Geophysical Journal International*, **179**(1): 413–424.

Yoder, C. and Standish, E. 1997. Martian precession and rotation from Viking lander range data. *Journal of Geophysical Research: Planets*, **102**(E2): 4065–4080.

Yoder, C., Konopliv, A., Yuan, D., Standish, E., and Folkner, W. 2003. Fluid core size of Mars from detection of the solar tide. *Science*, **300**(5617): 299–303.

Zuber, M. T., Solomon, S. C., Phillips, R. J., Smith, D. E., Tyler, G. L., Aharonson, O., Balmino, G., Banerdt, W. B., Head, J. W., Johnson, C. L., et al. 2000. Internal structure and early thermal evolution of Mars from Mars Global Surveyor topography and gravity. *science*, **287**(5459): 1788–1793.

Zuber, M. T., Lemoine, F. G., Smith, D. E., Konopliv, A. S., Smrekar, S. E., and Asmar, S. W. 2007. Mars Reconnaissance Orbiter radio science gravity investigation. *Journal of Geophysical Research: Planets*, **112**(E5).

Zweifel, P., Mance, D., ten Pierick, J., Giardini, D., Schmelzbach, C., Haag, T., Nicollier, T., Ceylan, S., Stähler, S., van Driel, M., Sollberger, D., Euchner, F., Clinton, J. F., Bierwirth, M., Eberhardt, M., Lognonné, P., Pike, W. T., and Banerdt, W. B. 2021. Seismic High-Resolution Acquisition Electronics for the NASA InSight Mission on Mars. *Bulletin of the Seismological Society of America*, **111**(6): 2909–2923. ISSN 0037-1106. URL https://doi.org/10.1785/0120210071. 10.1785/0120210071.

Appendix

A1 SEIS instrument responses

In the following pages, the instrument responses of the SEIS instruments (both VBB and SP sensors) are shown.

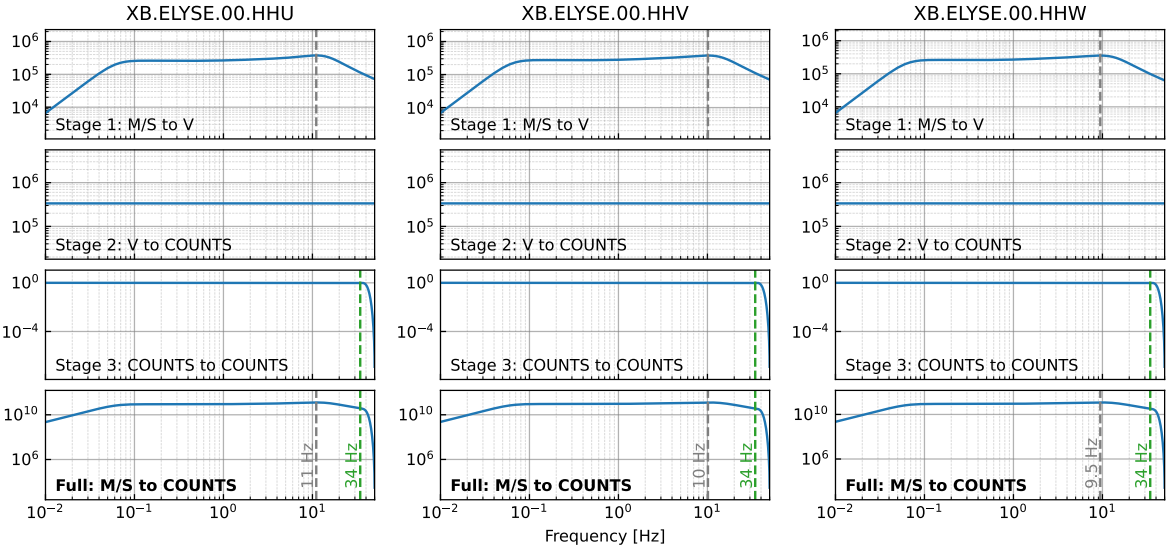


Figure A1.1: Instrument response of VBB@100sps (Channels XB.ELYSE.00.HH). From left to right: the three raw components U, V, W of the seismometer. The different stages of the instrument response are shown from top to bottom. Stage 1 is the response of the instrument of the sensor (from ground-motion to Volts), Stage 2 represents the response of the digitizer (from Volts to Counts) and Stage 3 corresponds to the FIR filter for data decimation. The full response of the instrument is shown at the bottom panels. For each channel, the dashed gray line marks the frequency where the damping of high frequencies begins at the sensor level. The green dashed line indicates the corner frequency of the anti-aliasing FIR filter.

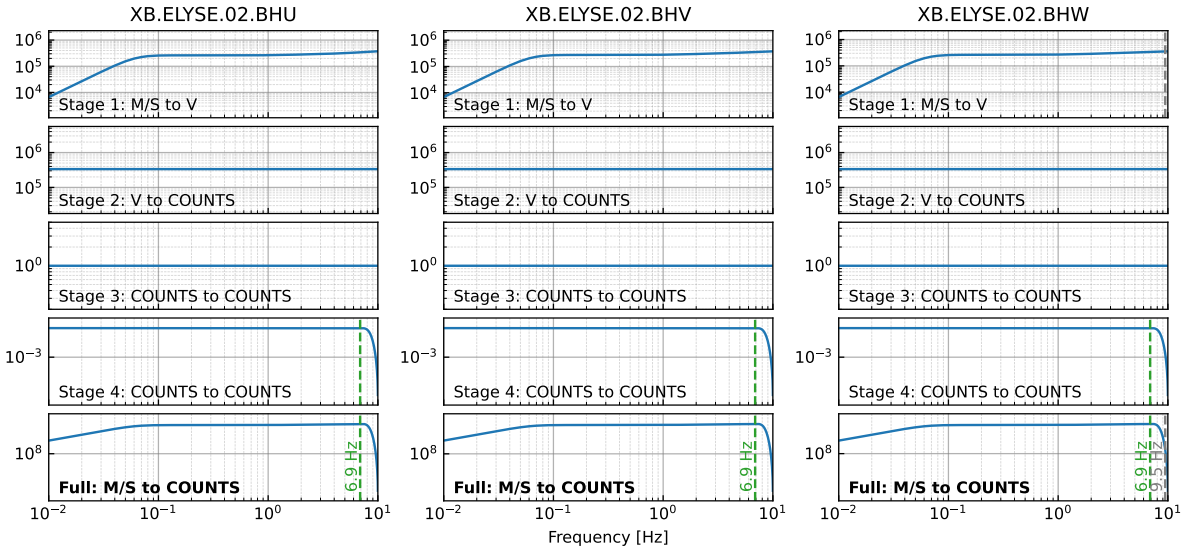


Figure A1.2: Instrument response of VBB@20sps (Channels XB.ELYSE.02.BH). From left to right: the three raw components U, V, W of the seismometer. The different stages of the instrument response are shown from top to bottom. Stage 1 is the response of the instrument of the sensor (from ground-motion to Volts), Stage 2 represents the response of the digitizer (from Volts to Counts), Stage 3 corresponds to the amplification response and Stage 4 shows the FIR filter for data decimation. The full response of the instrument is shown at the bottom panels. For each channel, the green dashed line indicates the corner frequency of the anti-aliasing FIR filter.

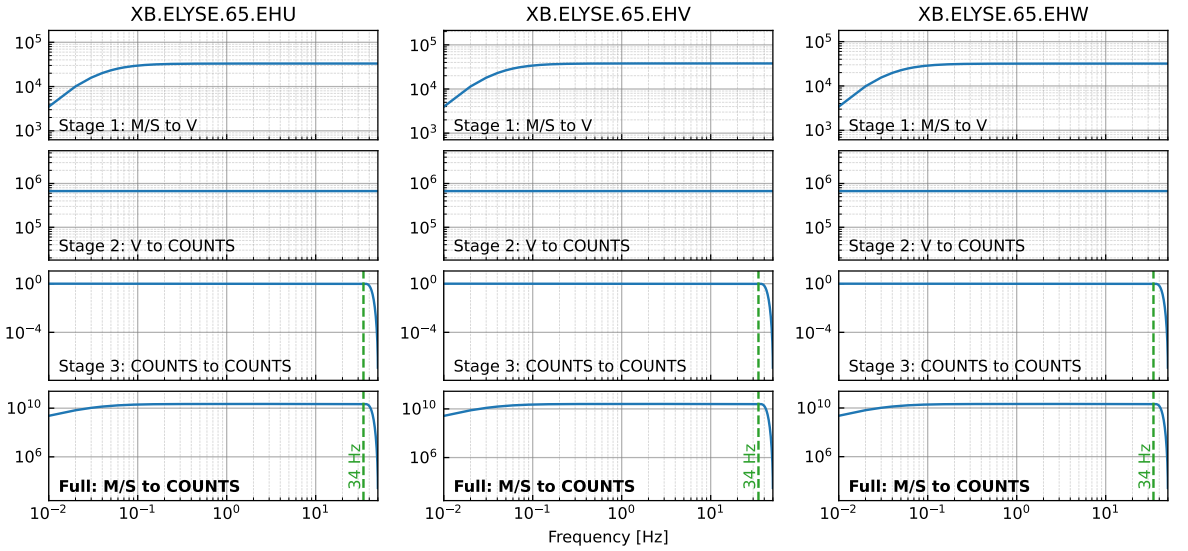


Figure A1.3: Instrument response of SP@100sps (Channels XB.ELYSE.65.EH). From left to right: the three raw components U, V, W of the seismometer. The different stages of the instrument response are shown from top to bottom. Stage 1 is the response of the instrument of the sensor (from ground-motion to Volts), Stage 2 represents the response of the digitizer (from Volts to Counts), Stage 3 shows the response of the FIR filter used for data decimation. The full response of the instrument is shown at the bottom panels. For each channel, the green dashed line indicates the corner frequency of the anti-aliasing FIR filter.

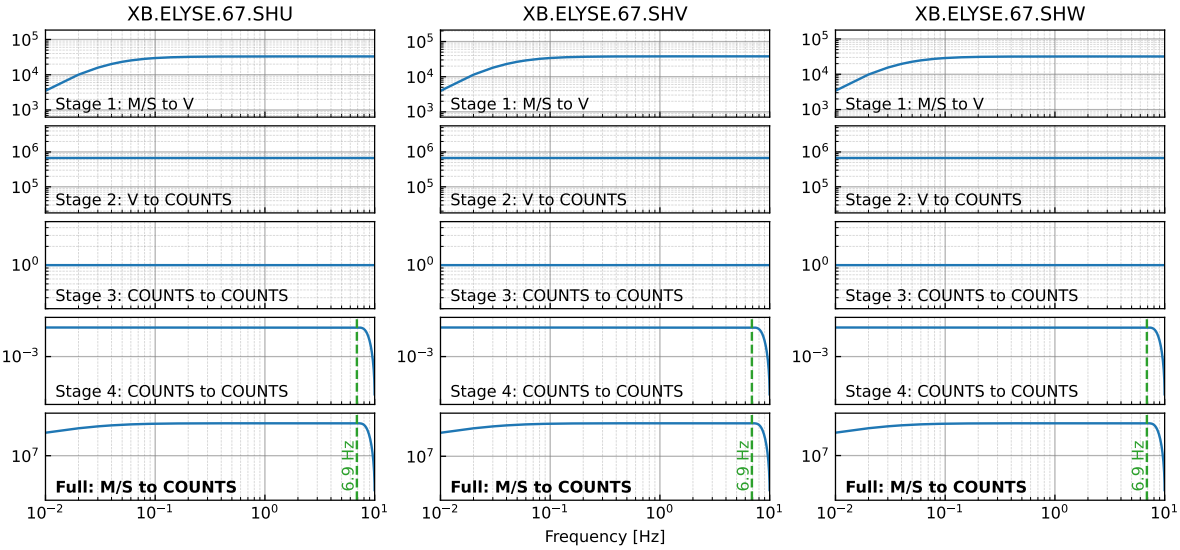


Figure A1.4: Instrument response of SP@20sps (Channels XB.ELYSE.67.SH). From left to right: the three raw components U, V, W of the seismometer. The different stages of the instrument response are shown from top to bottom. Stage 1 is the response of the instrument of the sensor channel (from ground-motion to Volts), Stage 2 represents the response of the digitizer (from Volts to Counts), Stage 3 corresponds to the amplification response and Stage 4 shows the FIR filter for data decimation. The full response of the instrument is shown at the bottom panels. For each channel, the green dashed line indicates the corner frequency of the anti-aliasing FIR filter.

A1.1 Comparison of VBB raw and deglitched data

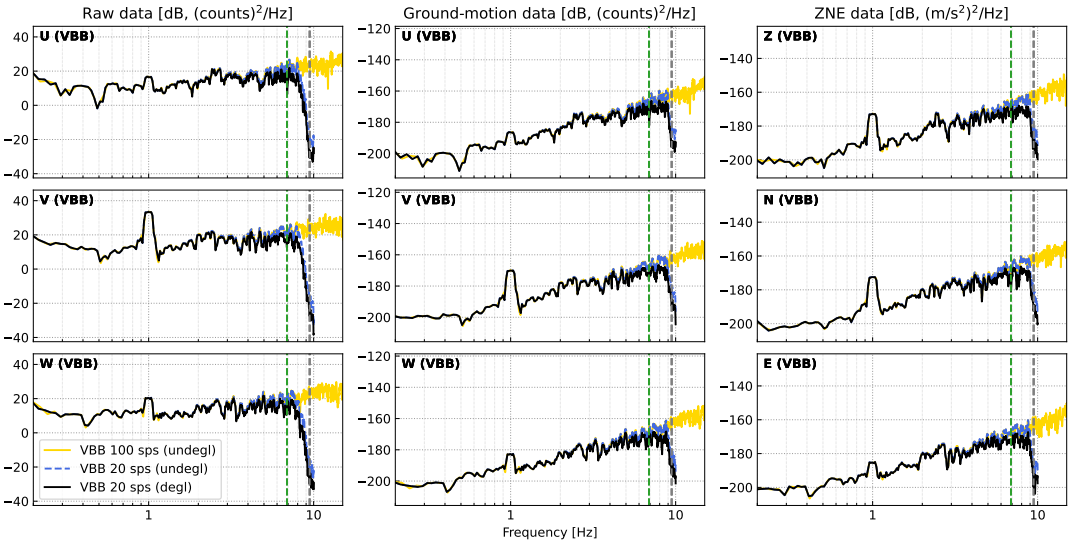


Figure A1.5: Spectral responses of VBB channels using raw 100 sps (solid yellow) or 20 sps (dashed blue) data, as well as deglitched 20 sps data (solid black). From left to right: three components of the raw UVW data (left), ground-motion UVW data (center) and rotated ground-motion ZNE data (right). The corresponding U (or Z for rotated data), V (N) and W (E) are shown from top to bottom. The corner frequencies of the FIR filter and the VBB sensor response are plotted as vertical dashed green and gray lines, respectively.

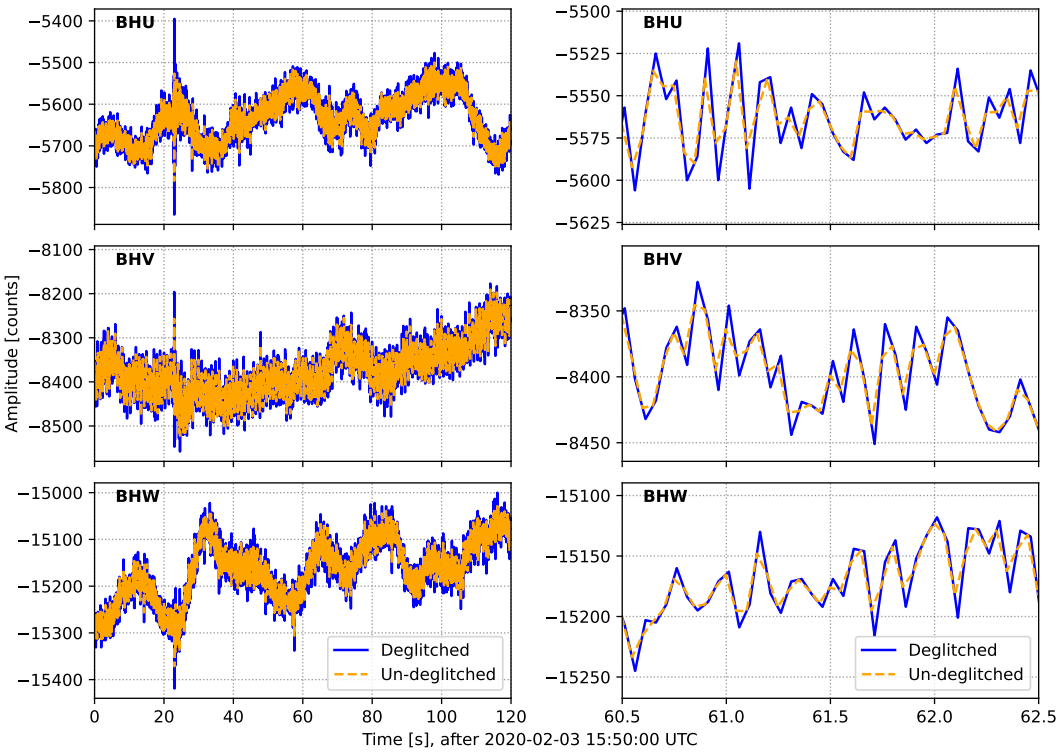


Figure A1.6: Comparison between raw and deglitched VBB@20 sps (channels XB.ELYSE.02.BH). From top to bottom: the three raw components U, V and W. Left panel presents a time span of 120 s. Right panel shows a time window of 2 s.

A1.2 Comparison between SP and VBB

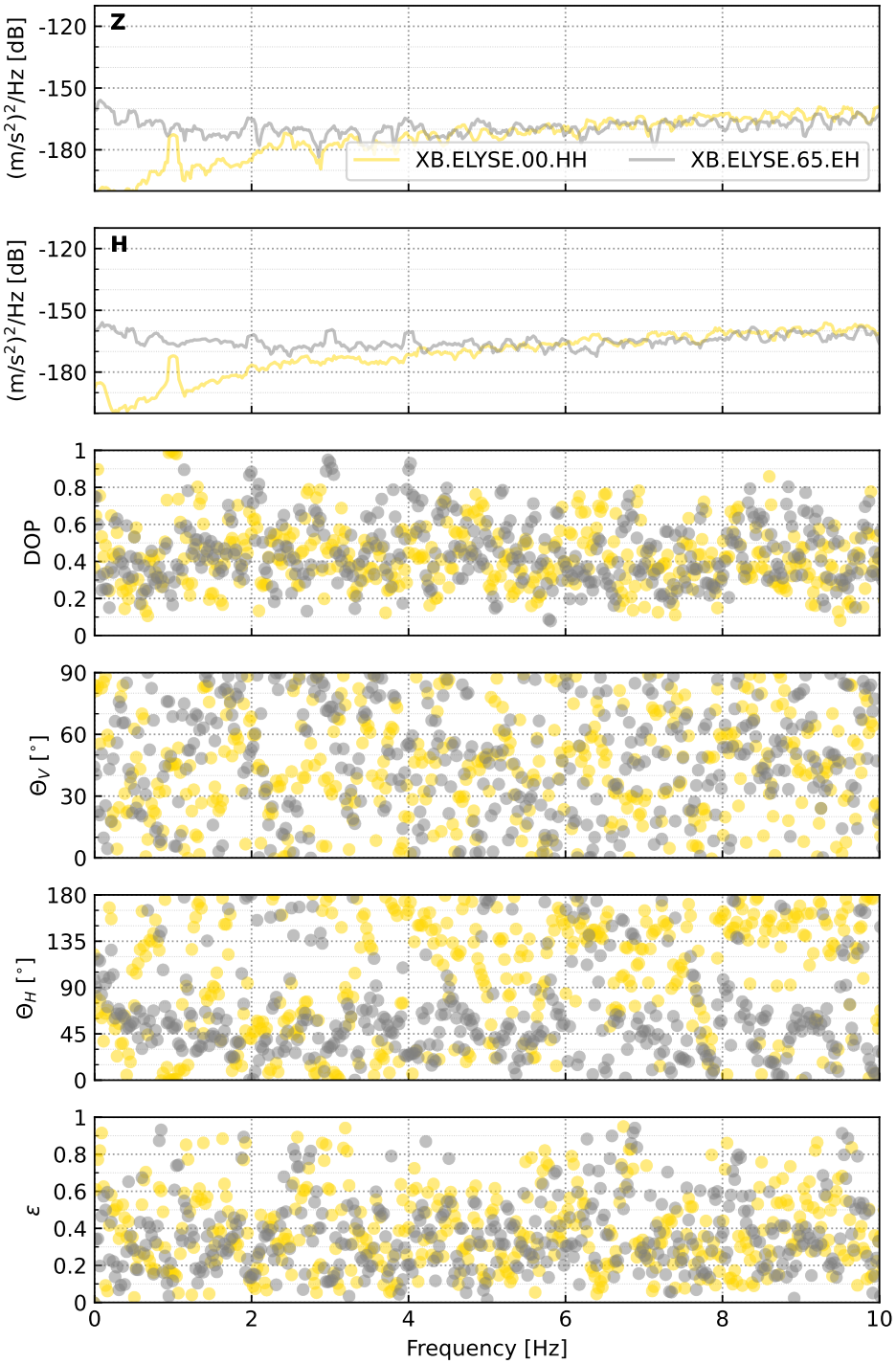


Figure A1.7: Comparison of spectral features from VBB and SP data during a low-wind period. From top to bottom: (a) Vertical spectral amplitude, (b) Horizontal spectral amplitude, (c) Degree of polarization, (d) Vertical incidence angle (Θ_V), (e) Horizontal incidence angle (Θ_H) and (f) Ellipticity.

A1.3 Instruments self-noise

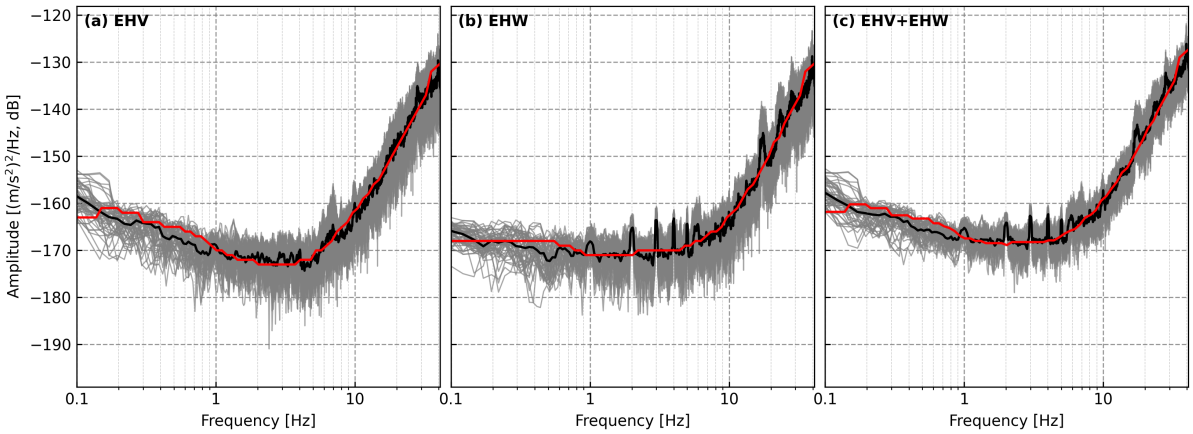


Figure A1.8: Determination of SP self-noise from Cruise data. **(a)** V component of the ground-motion recorded by SP, **(b)** W component of the ground-motion recorded by SP, **(c)** Horizontal component of the ground-motion, defined as the sum of V and W components. Black curve is the median of all the measurements. Red curve is the self-noise calculated by Panning et al. (2020).

A2 Evolution of spectral and polarization features

A2.1 Variation throughout a martian year

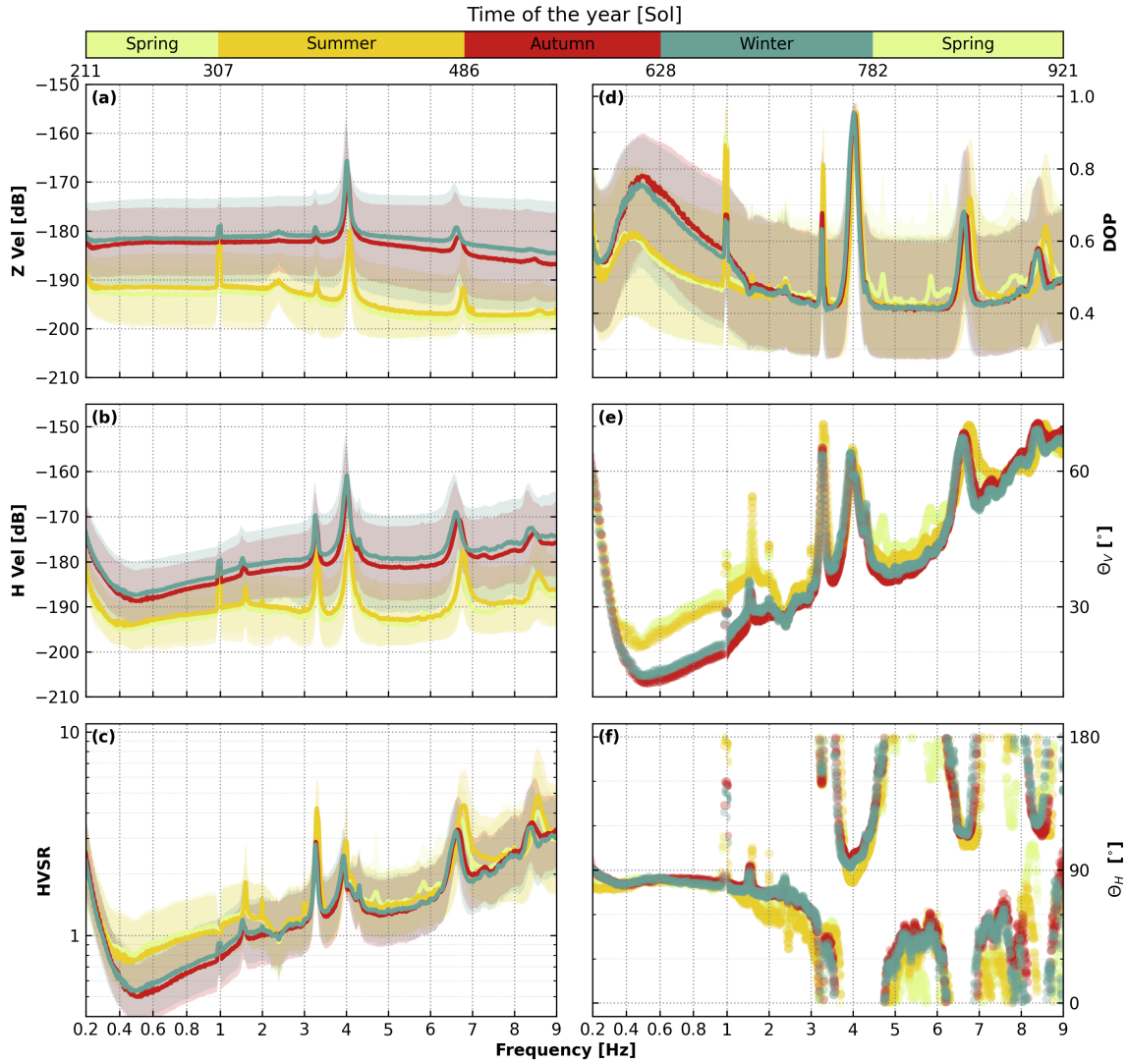


Figure A2.1: Variation of spectral features over a martian year during local night (mid-noise period, 00:00 - 04:00 LMST). **(a)** Vertical spectra, **(b)** Horizontal spectra, **(c)** HVSR, **(d)** degree of polarization (DOP), **(e)** vertical incidence angle Θ_V (with respect to the vertical) and **(f)** horizontal incidence angle Θ_H (clockwise from the North direction). The median values are shown in each case. The color is given by the season of the year.

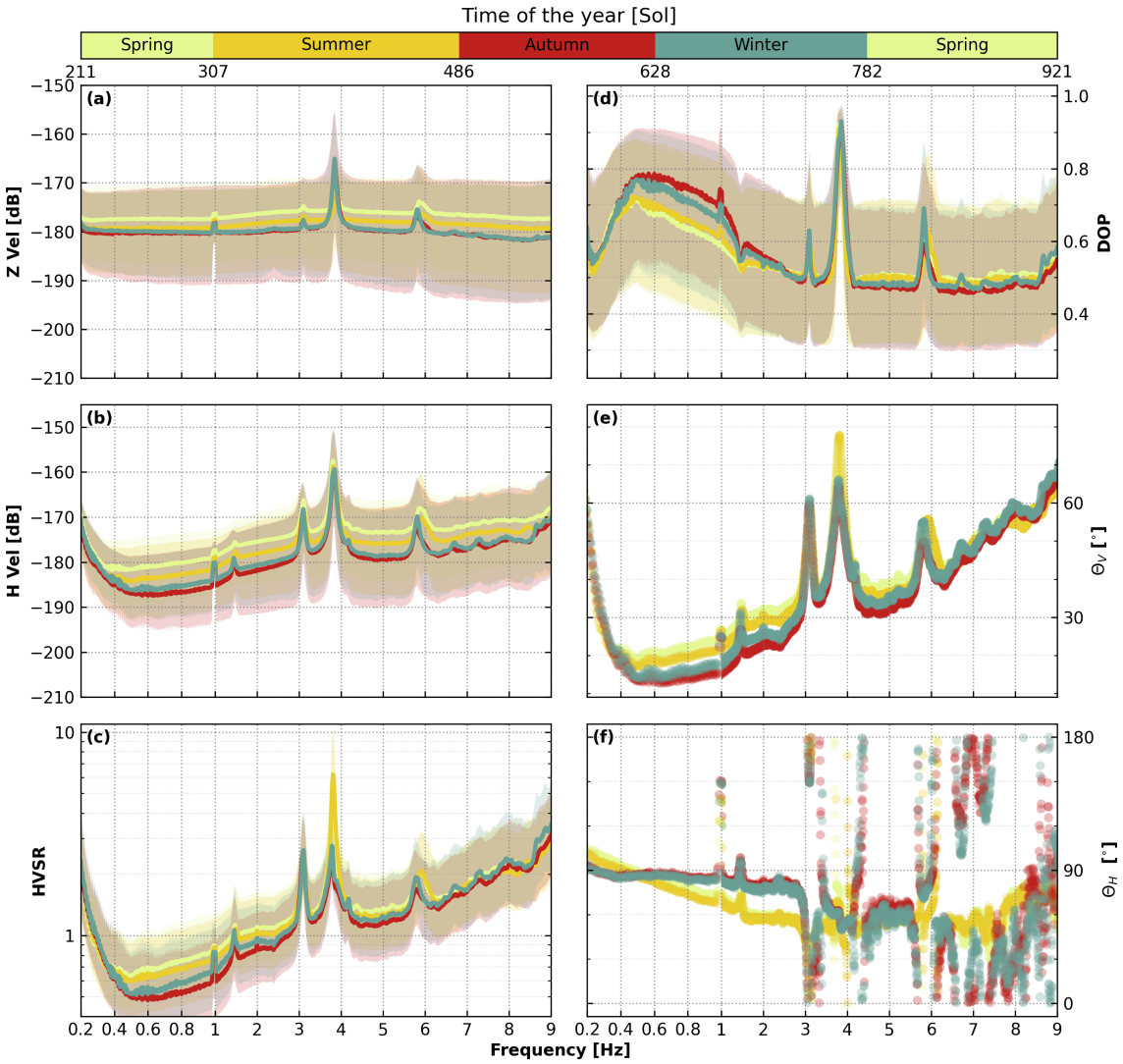


Figure A2.2: Variation of spectral features over a martian year during local day (high-noise period, 12:00 - 16:00 LMST). **(a)** Vertical spectra, **(b)** Horizontal spectra, **(c)** HVSR, **(d)** degree of polarization (DOP), **(e)** vertical incidence angle Θ_V (with respect to the vertical) and **(f)** horizontal incidence angle Θ_H (clockwise from the North direction). The median values are shown in each case. The color is given by the season of the year.

A2.2 Influence of temperature

Figure A2.3 shows the horizontal spectral amplitudes as a function of temperature.

A2.3 Influence of the wind speed

As wind speed is the main driver of the observed spectral amplitudes, Figures A2.4 to A2.9 show the effect of the wind speed on the variation of different polarization features.

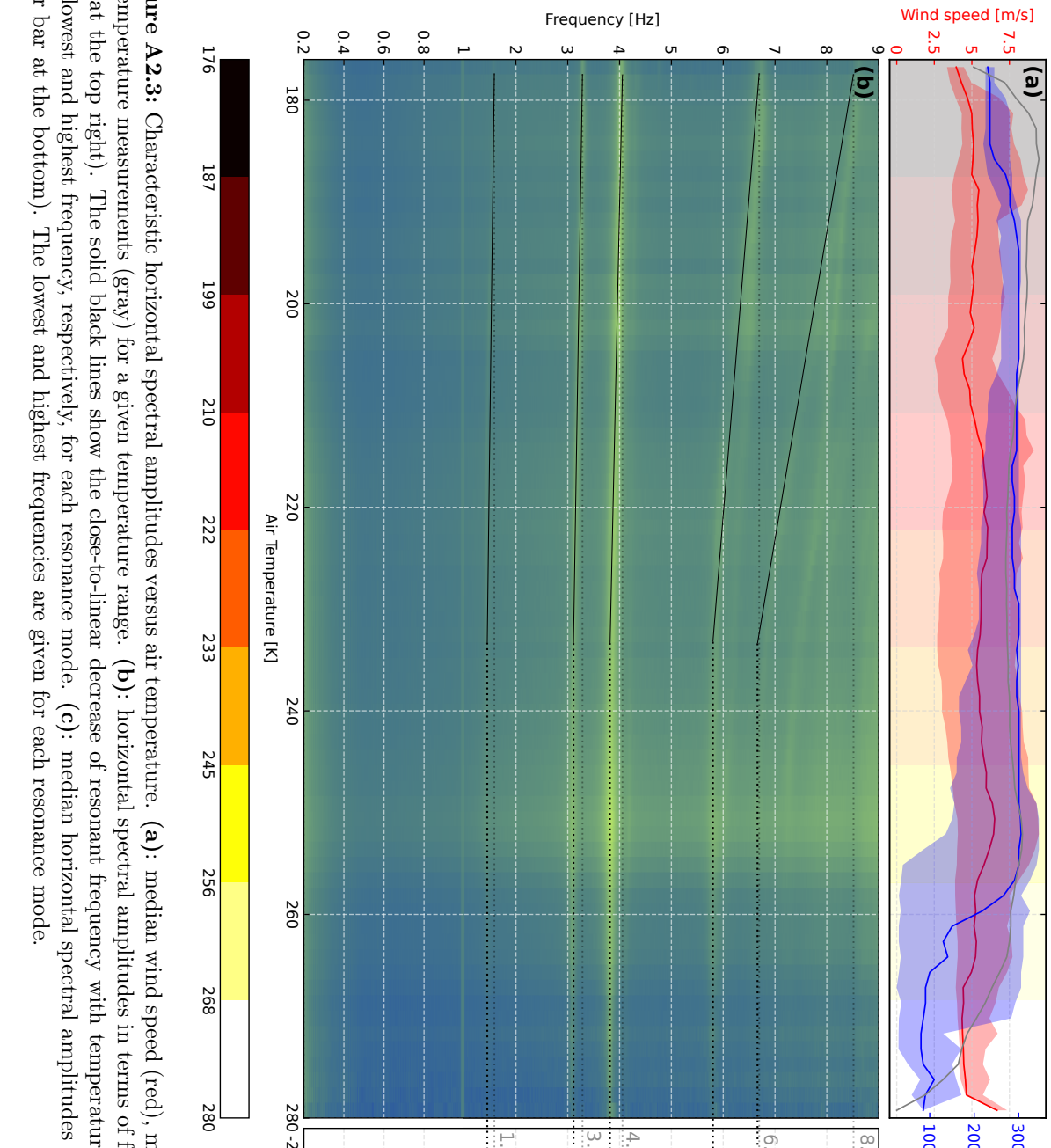


Figure A2.3: Characteristic horizontal spectral amplitudes versus air temperature. **(a)**: median wind speed (red), median wind direction (blue) and number of temperature measurements (gray) for a given temperature range. **(b)**: horizontal spectral amplitudes in terms of frequency and air temperature (see color bar at the top right). The solid black lines show the close-to-linear decrease of resonant frequency with temperature. Dashed black and gray lines connect the lowest and highest frequency, respectively, for each resonance mode. **(c)**: median horizontal spectral amplitudes for different air temperature ranges (see color bar at the bottom). The lowest and highest frequencies are given for each resonance mode.

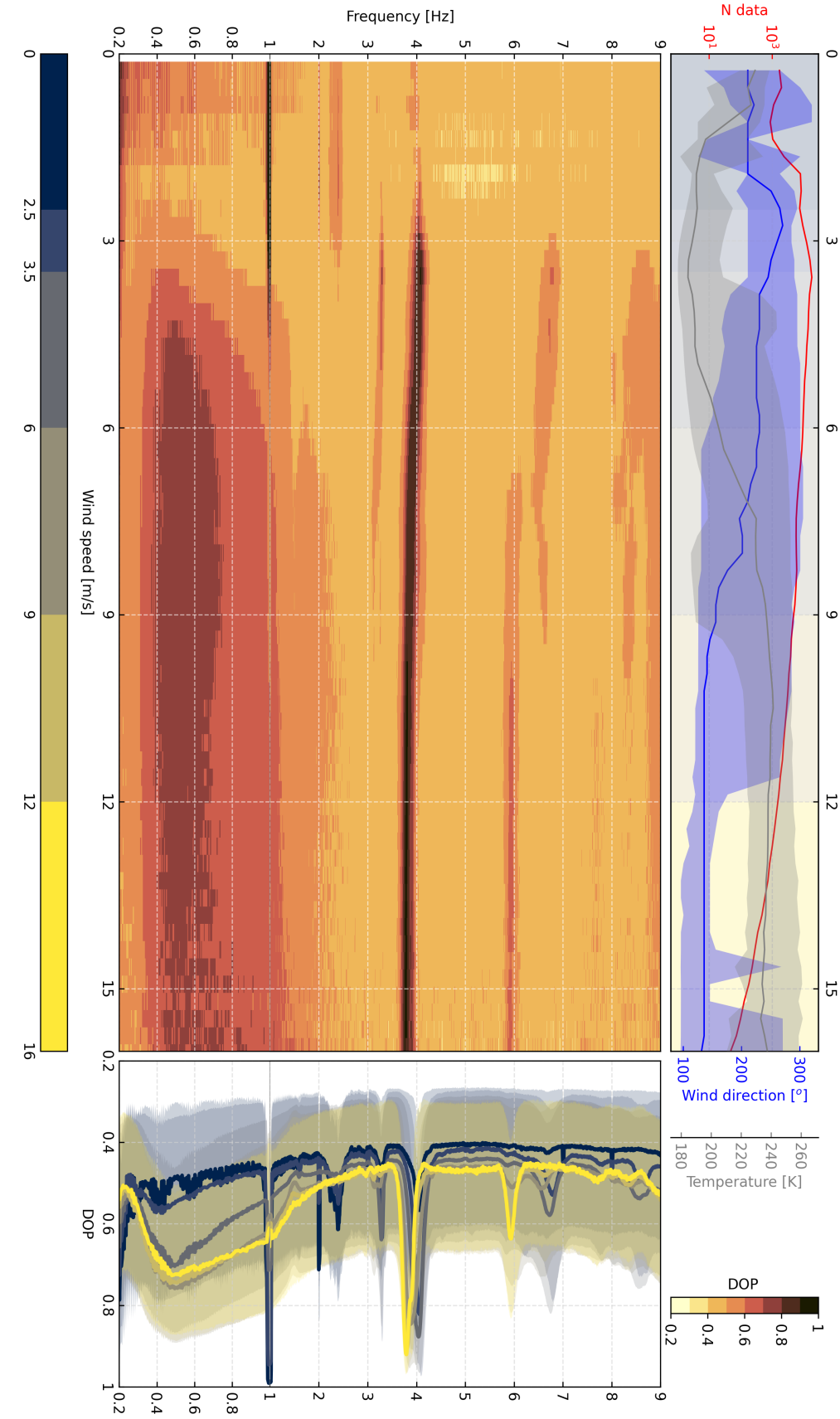


Figure A2.4: Wind speed and DOP. Evolution of DOP of martian ambient vibrations recorded by VBB at 20 sps as a function of wind speed. **Top**: number of wind speed measurements (red), average wind direction (blue) and average temperature (gray) for given wind speed. **Middle left**: variation of DOP with wind speed. **Middle right**: median DOP curves for different wind speed levels (see color bar at the bottom).

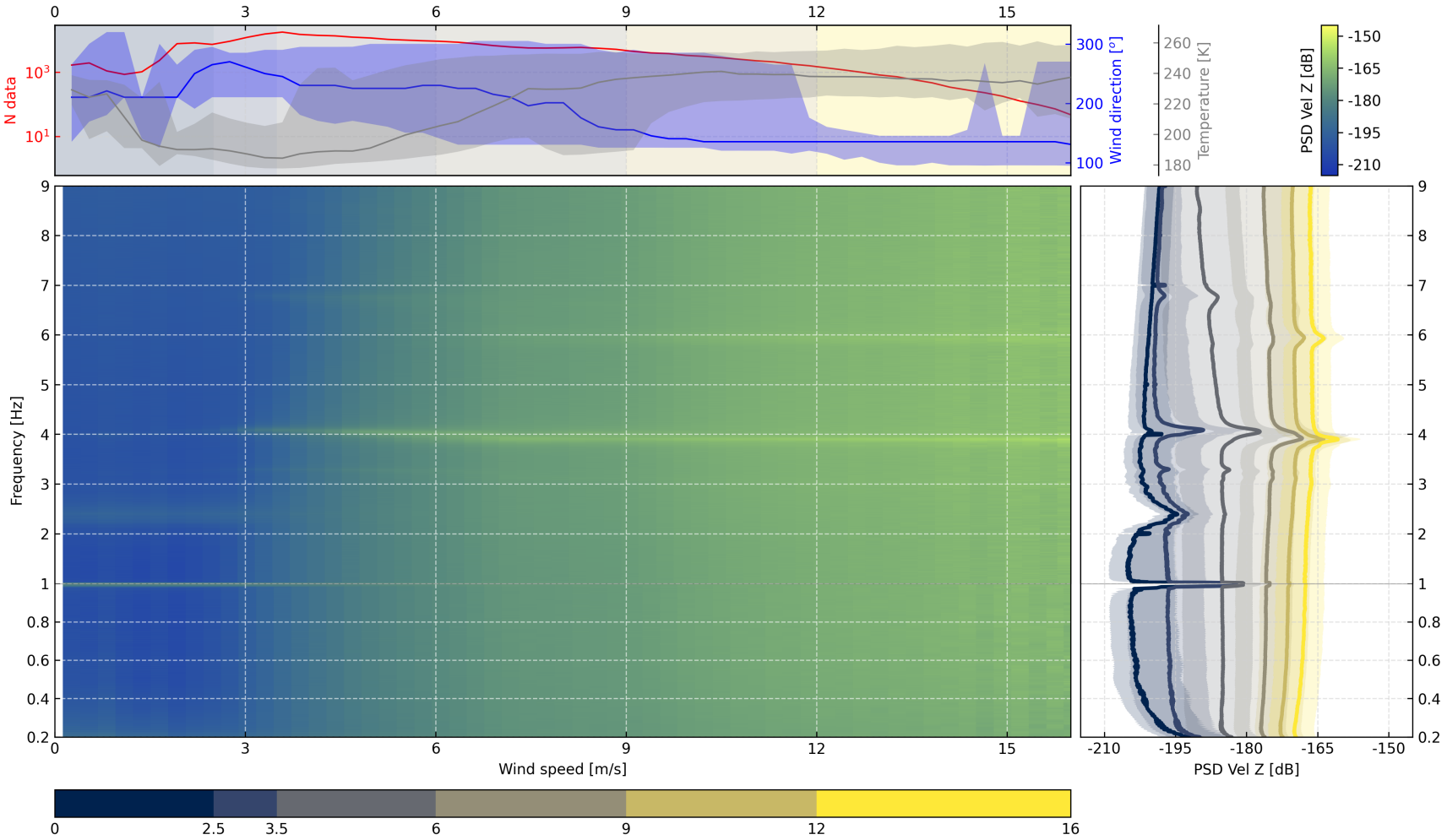


Figure A2.5: Wind speed and Vertical spectral amplitude. Evolution of Vertical spectral amplitude of martian ambient vibrations recorded by VBB at 20 sps as a function of wind speed. **Top**: number of wind speed measurements (red), average wind direction (blue) and average temperature (gray) for given wind speed. **Middle left**: variation of vertical amplitude with wind speed. **Middle right**: median vertical amplitude curves for different wind speed levels (see color bar at the bottom).

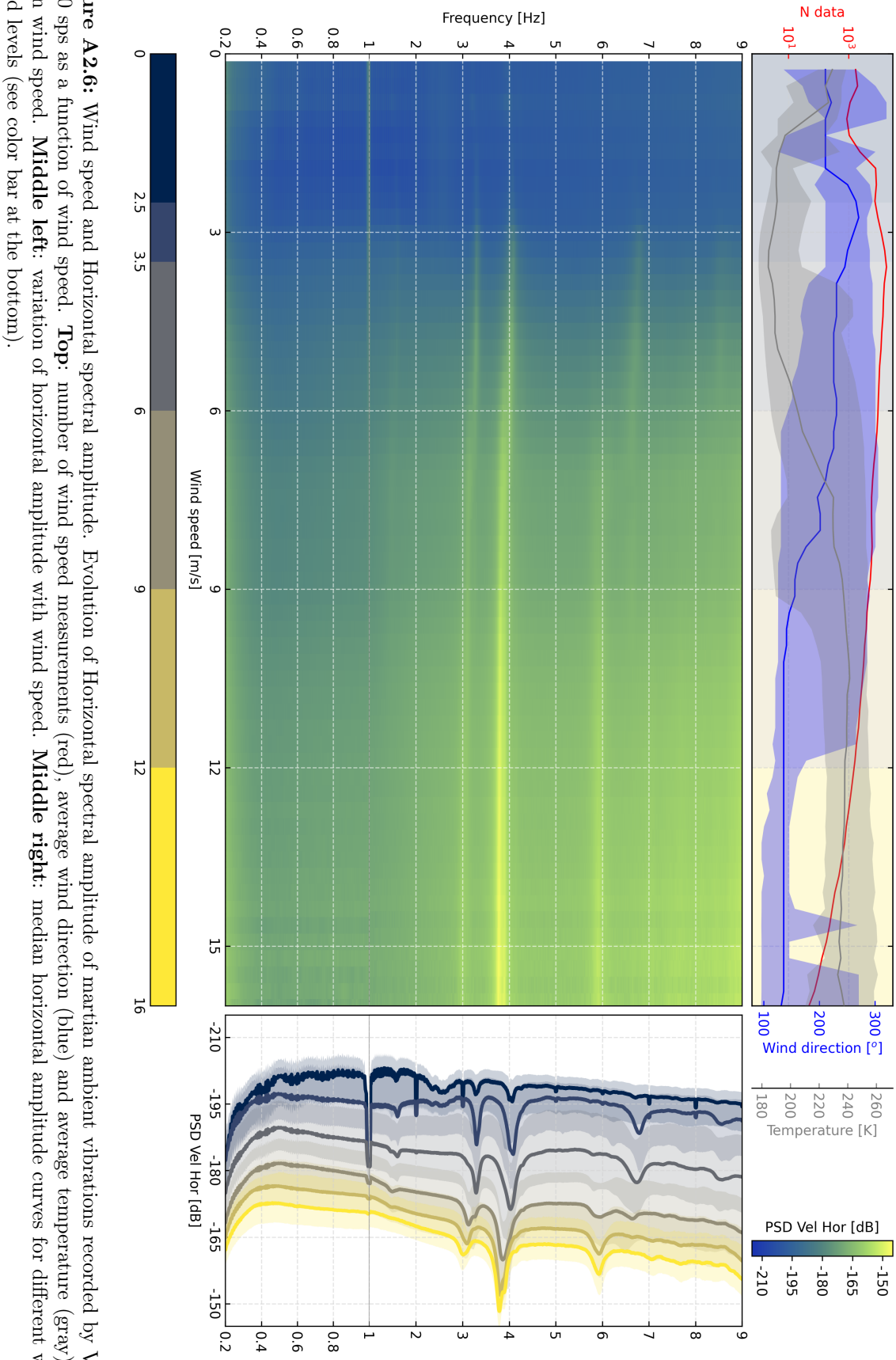


Figure A2.6: Wind speed and Horizontal spectral amplitude. Evolution of Horizontal spectral amplitude of martian ambient vibrations recorded by VBB at 20 sps as a function of wind speed. **Top**: number of wind speed measurements (red), average wind direction (blue) and average temperature (gray) for given wind speed. **Middle left**: variation of horizontal amplitude with wind speed. **Middle right**: median horizontal amplitude curves for different wind speed levels (see color bar at the bottom).

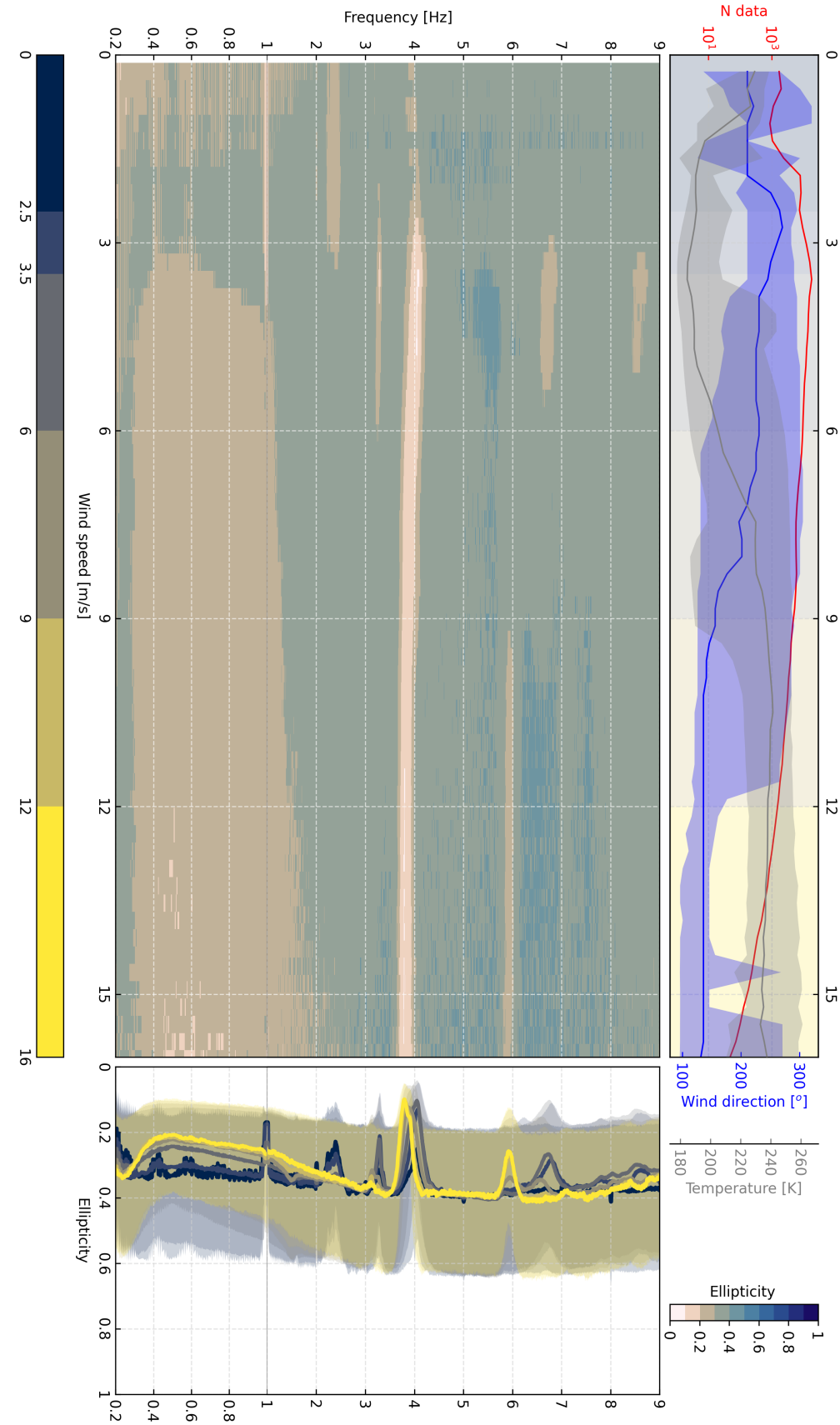


Figure A2.7: Wind speed and Ellipticity. Variation of Ellipticity of martian ambient vibrations recorded by VBB at 20 sps as a function of wind speed. **Top**: number of wind speed measurements (red), average wind direction (blue) and average temperature (gray) for given wind speed. **Middle left**: variation of ellipticity with wind speed. **Middle right**: median ellipticity for different wind speed levels (see color bar at the bottom).

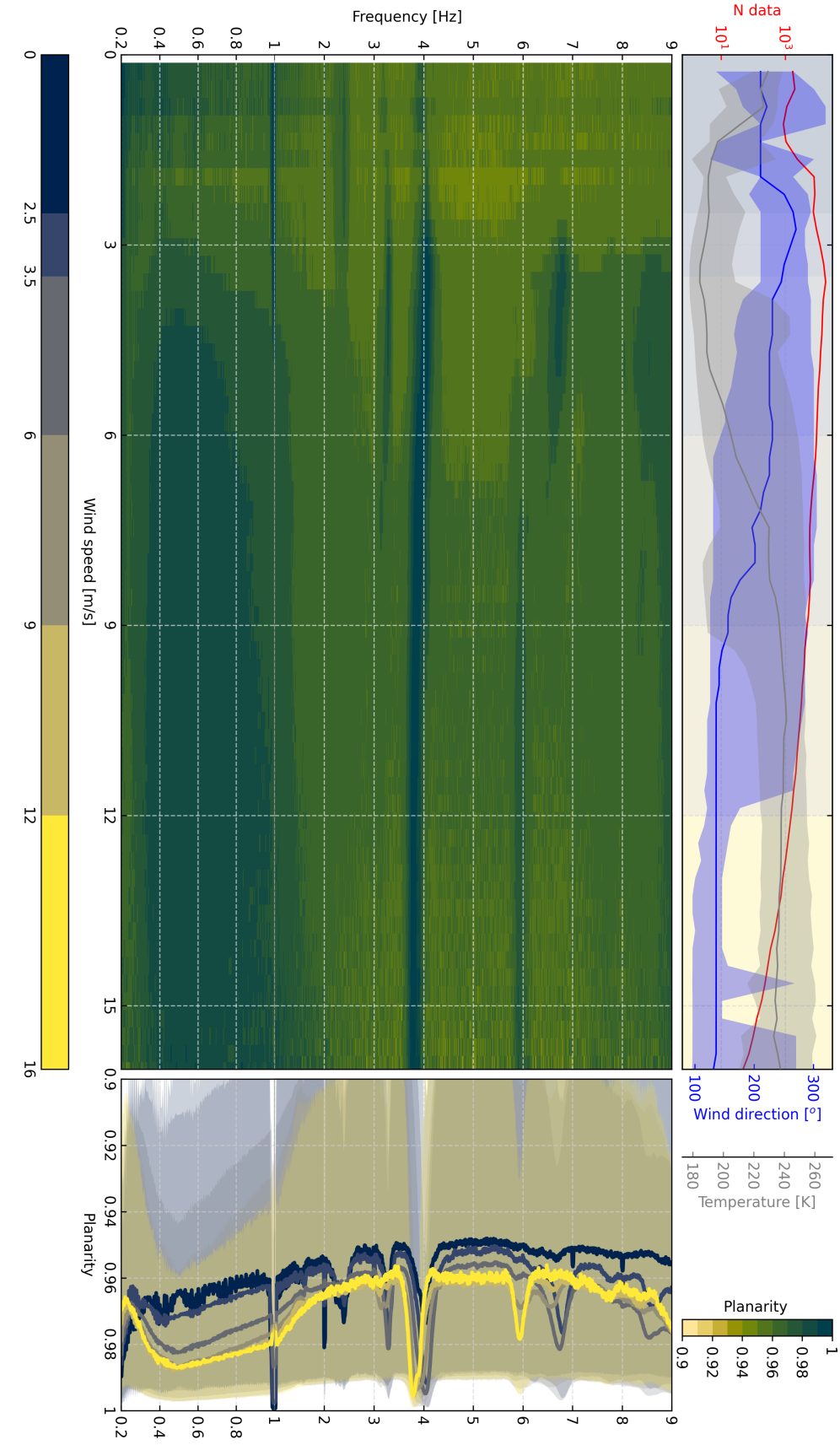


Figure A2.8: Wind speed and Planarity. Variation of Planarity of martian ambient vibrations recorded by VBB at 20 sps as a function of wind speed. **Top**: number of wind speed measurements (red), average wind direction (blue) and average temperature (gray) for given wind speed. **Middle left**: variation of planarity with wind speed. **Middle right**: median planarity for different wind speed levels (see color bar at the bottom).

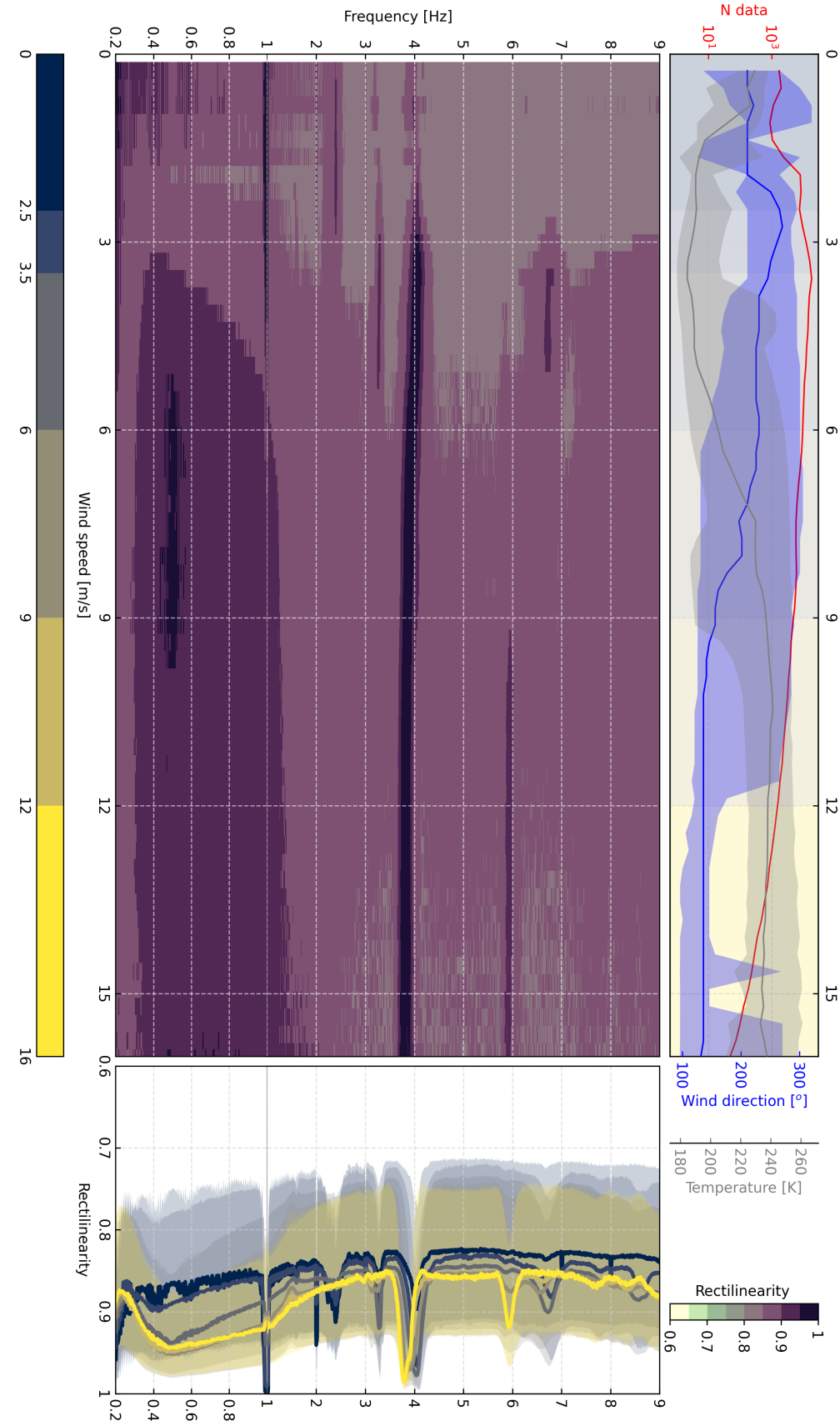


Figure A2.9: Wind speed and Rectilinearity. Variation of Rectilinearity of martian ambient vibrations recorded by VBB at 20 sps as a function of wind speed. **Top**: number of wind speed measurements (red), average wind direction (blue) and average temperature (gray) for given wind speed. **Middle left**: variation of rectilinearity with wind speed. **Middle right**: median rectilinearity for different wind speed levels (see colorbar at the bottom).

A3 Ground compliance inversion

In parallel to this doctoral work, Onodera (2022) studied the response of the ground to pressure changes, also known as the ground compliance, which also allows mapping the subsurface structure. Using a Bayesian inversion approach, the most likely models present a discontinuity around 1 m and another discontinuity at around 5 m, but a shallow layer with high rigidity is not derived from that inversion. Such high-rigidity layer would correspond with the high-velocity layer proposed in this work. Nevertheless, some of the models best fitting the ground compliance observations also allow the presence of such high-rigidity layer, as shown in Fig. A3.10, so it cannot be completely discarded.

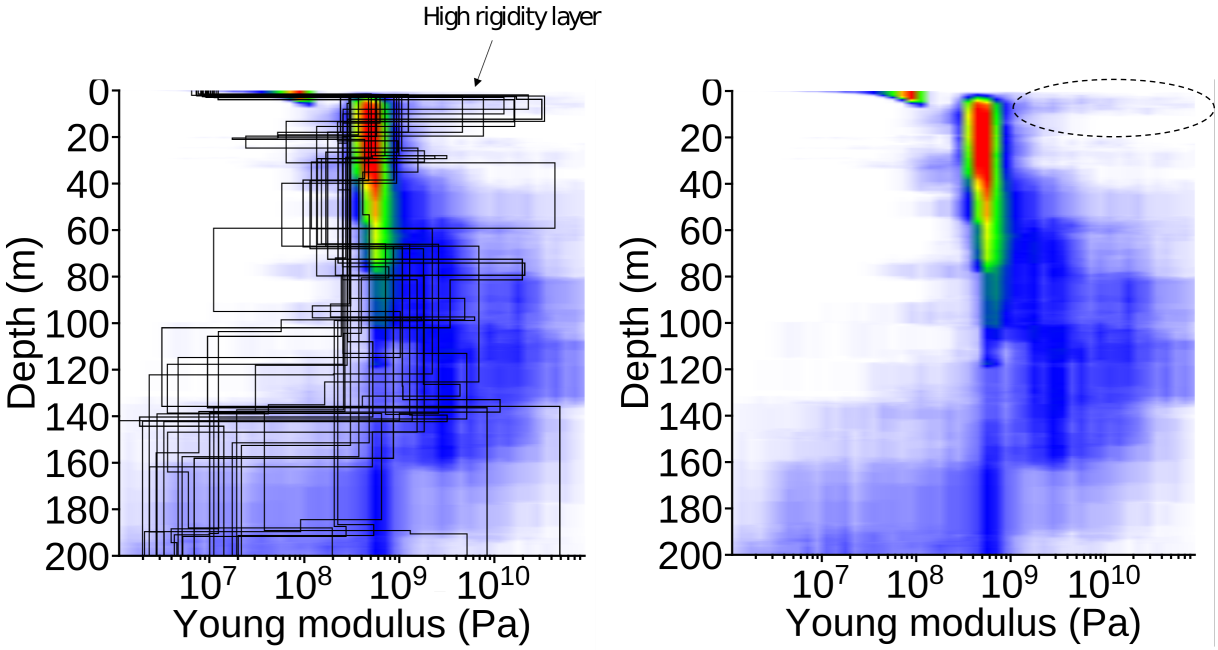


Figure A3.10: Discrete subsurface structure models including a shallow high-velocity layer (black lines) picked from the Bayesian inversion performed by Onodera (2022). The density maps correspond to the output probability density distributions of the Young modulus from surface to 200 m depth, where red and blue colors show high and low probabilities, respectively. Taken from Carrasco et al. (2022).

A4 Additional joint-inversion runs

A4.1 3LOH cases

As mentioned in the main text, a first set of inversion runs was performed by assuming a parameter space configuration of 3 layers over a half-space (3LOH). We run inversions for three different cases with different weighting of the data sets, as shown in Table A1.

Inversion Run	W_e	W_{rf}	W_a
RI1	0.0	1.0	0.0
RI2	0.50	0.50	0.0
RI3	0.45	0.45	0.10

Table A1: The weighting of the different data sets for three inversion runs using 3LOH parameters space.

Figure A4.1 shows the inversion of the P-to-s RF only, without any constraint from the ellipticity or T_a. In this case, the resulting models can properly model the amplitudes and arrival times of the main peaks in the P-to-s RF. Nevertheless, the models overestimate the Rayleigh-wave ellipticity between 25 and 35 s. The predicted times for the P-wave lag times from autocorrelations are too large, so they lie out of the y-axis range in Fig. A4.1c and d. Interestingly, the signal around 1 s can be well modeled without the need for a shallow low-velocity layer.

As seen in Fig. A4.2, the addition of ellipticity data to the inversion generates some misadjustment as average larger velocities are needed close to the surface, which produces an overestimation of the amplitude of the direct P-wave (first peak in the RF). Finally, when the autocorrelation times are included, the amplitude of the direct P-wave is strongly overestimated, suggesting the presence of a shallower layer with lower velocities.

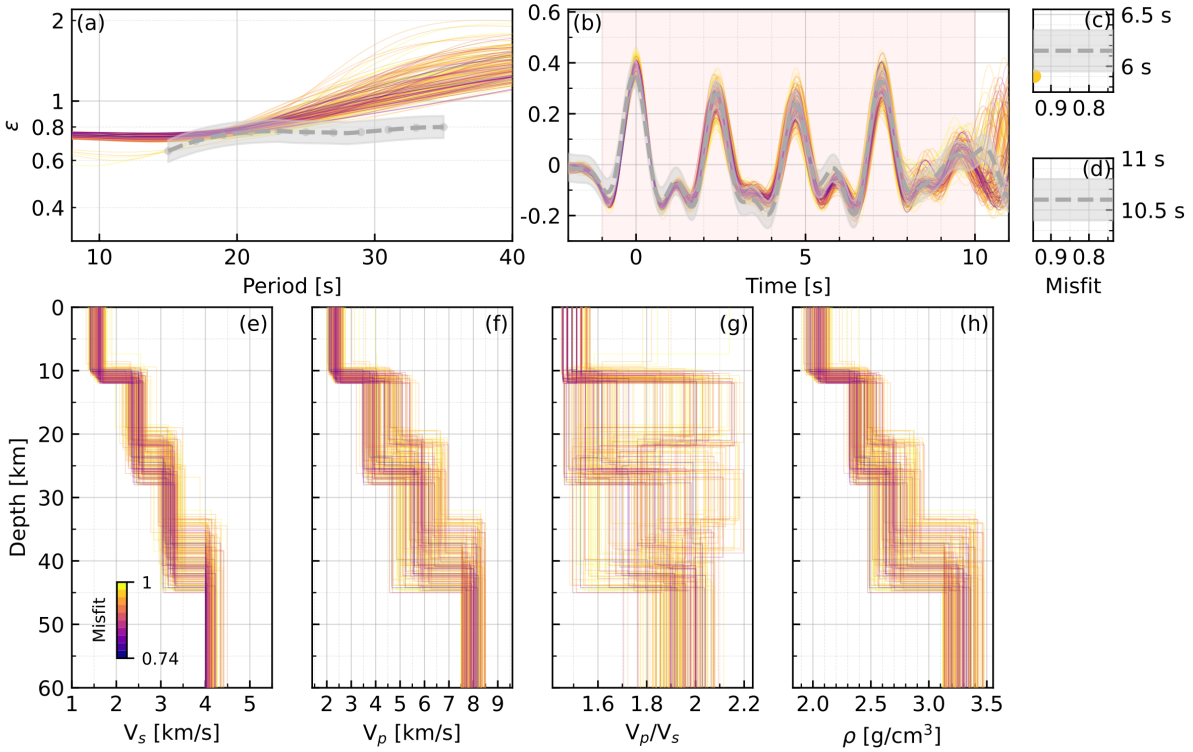


Figure A4.1: Inversion results and resulting local Martian crustal models for inversion run RI1 ($W_e = 0.0$, $W_{rf} = 1.0$, $W_a = 0.0$), using 3LOH parameterization. The measurements and the synthetic modeling of 200 random best-fitting crustal models are shown for the **(a)** Rayleigh wave ellipticity, **(b)** P-to-s RFs from Joshi et al. (2023), and the **(c)** first and **(d)** second P-wave reflection times from autocorrelations by Schimmel et al. (2021). In these plots, the light gray dashed line and area correspond to the measured data and their uncertainty, respectively, whereas the synthetic data are colored by their misfit. The corresponding crustal models are shown in terms of (e) Vs, (f) Vp, (g) Vp/Vs and (h) density ρ, as a function of depth.

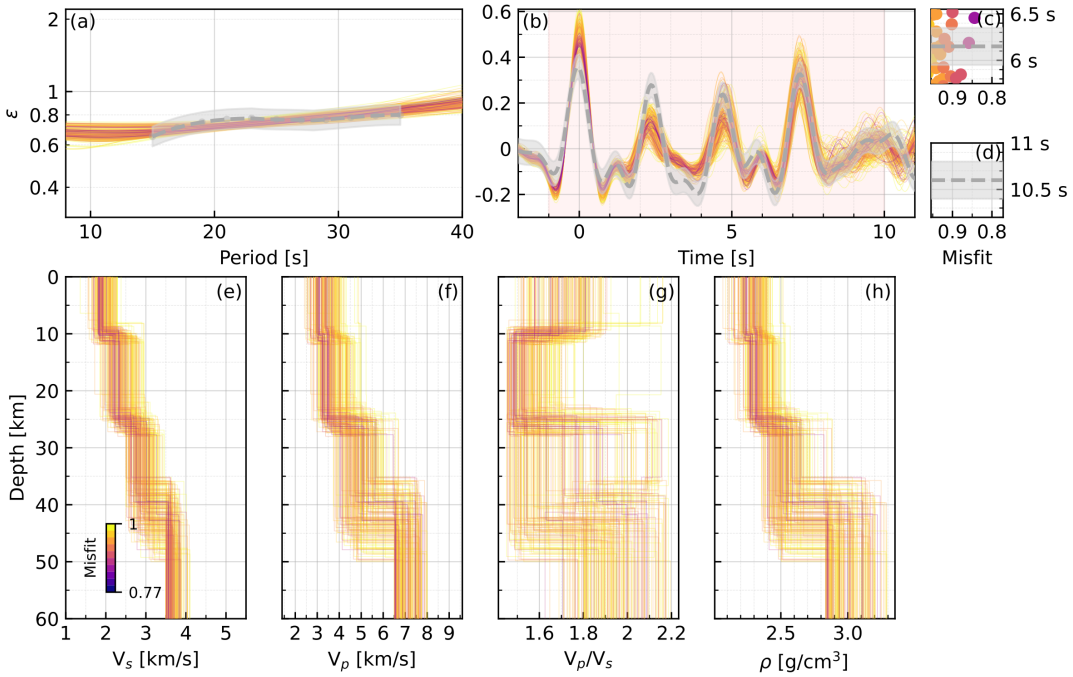


Figure A4.2: Same as Fig. A4.1, but for inversion run RI2 ($W_e = 0.5$, $W_{rf} = 0.5$, $W_a = 0.0$), using 3LOH.

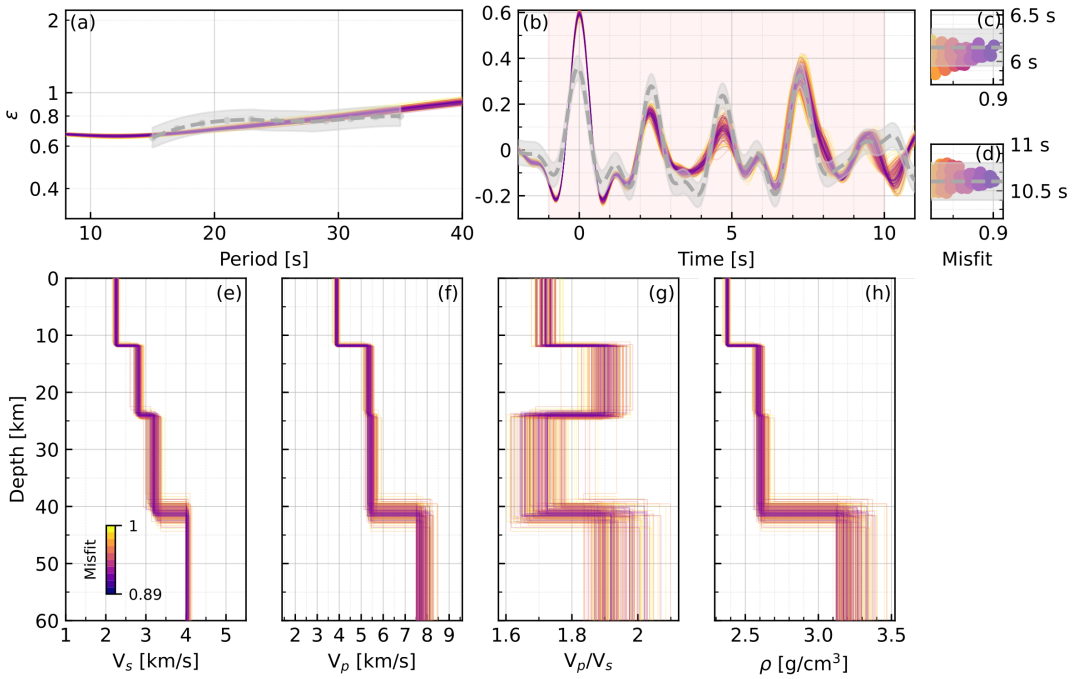


Figure A4.3: Same as Fig. A4.1, but for inversion run RI3 ($W_e = 0.45$, $W_{rf} = 0.45$, $W_a = 0.10$), using 3LOH.

A4.2 4LOH cases

In order to show the effect of different data sets in the inversion, mainly the ellipticity and P-to-s Receiver Functions, we include here the inversion results using different weightings of the data sets. Table A2 presents the weighting of three different data sets for each inversion run. IR1 is an inversion mainly using the P-to-s RF data (Fig. A4.4), IR2 is using the three data sets, with a larger weight of the P-to-s RF data (Fig. A4.6), whereas IR3 uses the three data sets with a larger weight of the ellipticity data (Fig. A4.5).

Inversion Run	W_e	W_{rf}	W_a
IR1	0.0	0.85	0.15
IR2	0.30	0.60	0.10
IR3	0.60	0.30	0.10

Table A2: The weighting of the different data sets for three inversion runs using a 4LOH parameters space.

The inversion results show that the inversion of RF with a small contribution of the autocorrelation times (IR1, Fig. A4.4) does not provide an acceptable fit to ellipticity, especially for periods above 25 s, and there is more dispersion in the model parameters than in Fig. 3, particularly for Vs and Vp/Vs. The IR2 inversion run (Fig. A4.6), with a lower weight of the ellipticity than the RF in the inversion, presents similar results to the ones shown in Fig. 3 in the main text, so it could be considered as another good combination of weights. The other way around, when the ellipticity has a higher weight on the inversion than the RFs (IR3, Fig. A4.5), there is an underestimation of the amplitudes of the phases at 2.2 and 4.8 s in the RF and an overestimation of the amplitude of the phase at 7.2 s. A bimodal distribution of models is observed, particularly leading to different Moho depths, which is related to the fact that ellipticity cannot constrain the location of discontinuities. A larger scatter is observed for the predicted Ta. In all the cases, a low W_a provides reasonable estimates for both T_a.

In summary, the best inversion results are obtained when the weight of the RF data set is the same or slightly higher than the ellipticity data. On the other hand, a poorer fitting of all the data sets is obtained when $W_e > W_{rf}$.

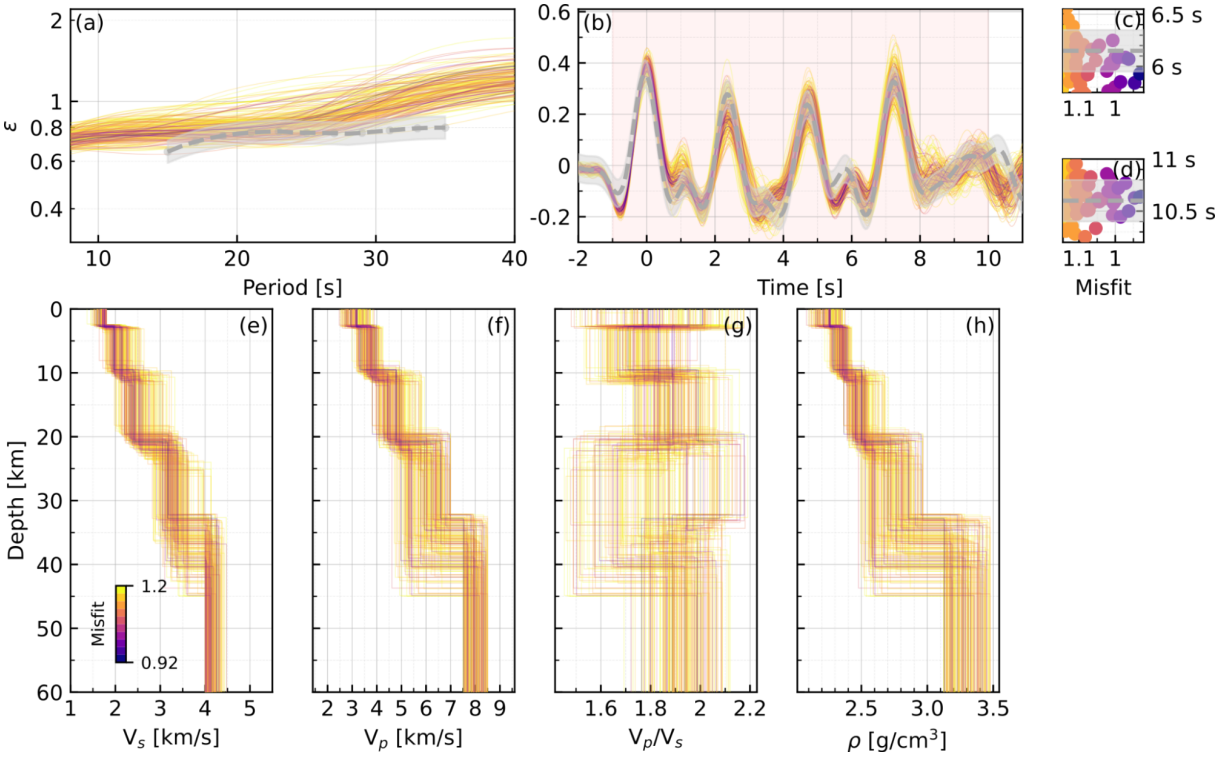


Figure A4.4: Same as Fig. A4.1, but for inversion run IR1 ($W_e = 0$, $W_{rf} = 0.85$, $W_a = 0.15$), using 4LOH.

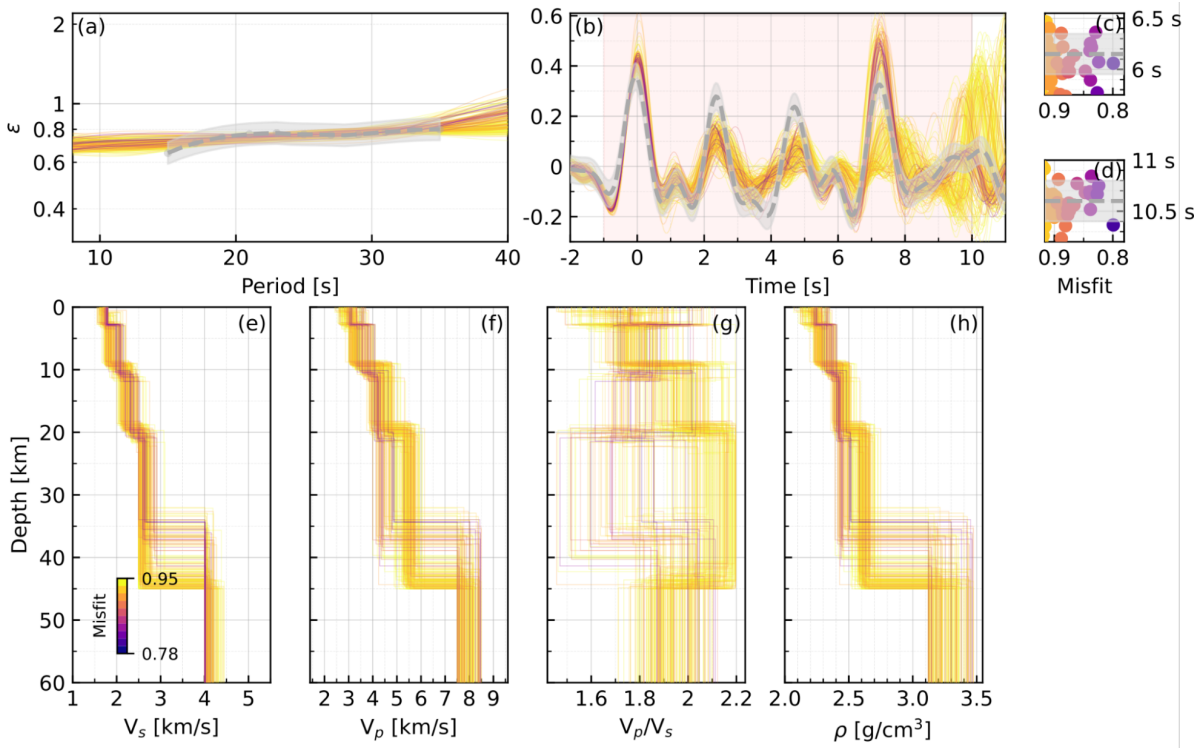


Figure A4.5: Same as Fig. A4.1, but for inversion run IR1 ($W_e = 0.30$, $W_{rf} = 0.60$, $W_a = 0.10$), using 4LOH.

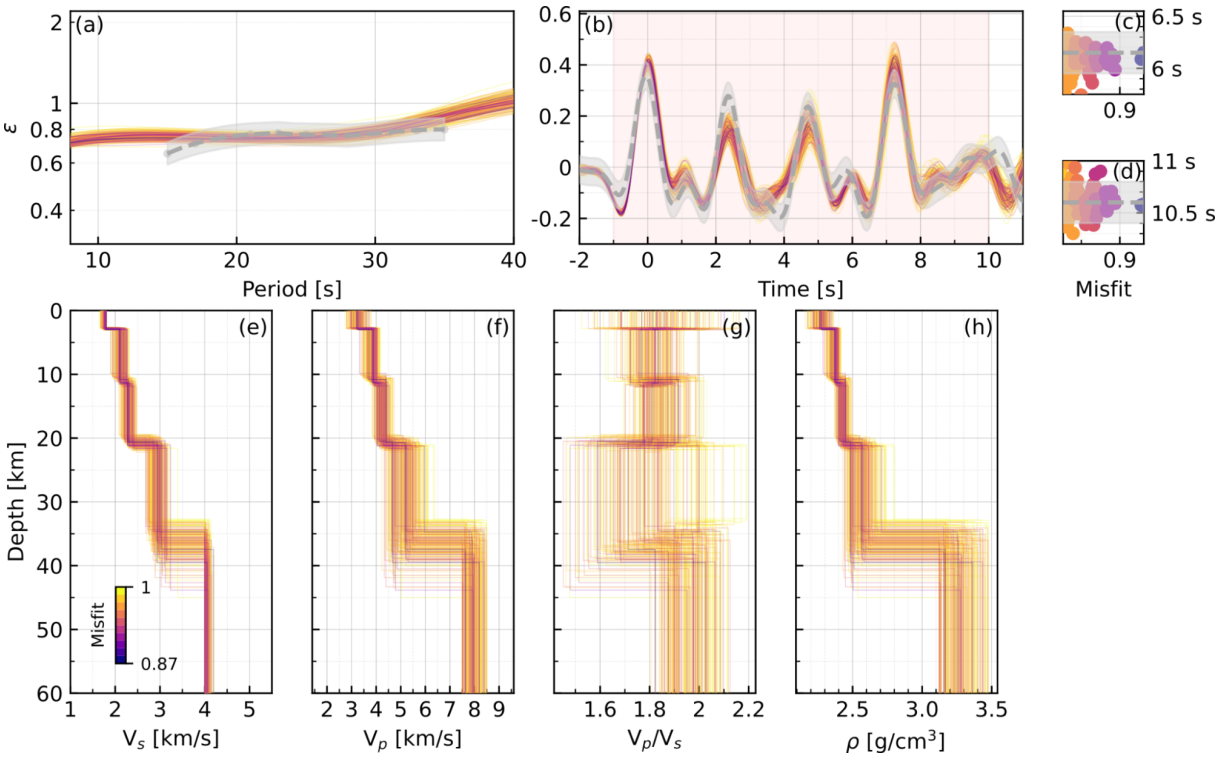


Figure A4.6: Same as Fig. A4.1, but for inversion run IR1 ($W_e = 0.60$, $W_{rf} = 0.30$, $W_a = 0.10$), using 4LOH.

A5 Density assessment

For the joint inversions in chapter 6, the density of each layer has been linked to the P-wave velocity by using the empirical relationship of Brocher (2005). Nevertheless, we do not provide conclusive interpretations of the resulting densities for two main reasons. First, the density-Vp relationship is based on Earth data, which are not necessarily comparable to the Martian case. In fact, the absolute density of the layers cannot be constrained as different models with the same density pattern result in the same ellipticity curve (Fig. A5.7).

Furthermore, density has some influence on the ellipticity data but is not as strong as the shear-wave velocity. In this sense, the perturbation of density produces small changes in the ellipticity curve (Fig. A5.8), so a proper assessment of the density variations through the crust is challenging unless strong variations are present.

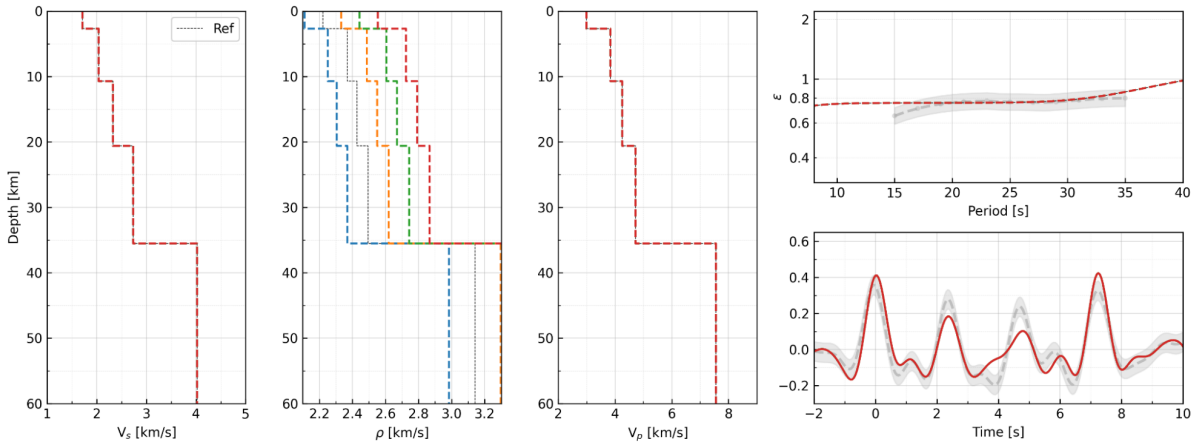


Figure A5.7: Synthetic modeling of ellipticity and P-to-s RFs using models with different absolute densities but same incremental pattern. Different colors correspond to different density models (while keeping the same Vs and Vp structure). The predicted ellipticity curves and RFs are exactly the same so they are overlapped.

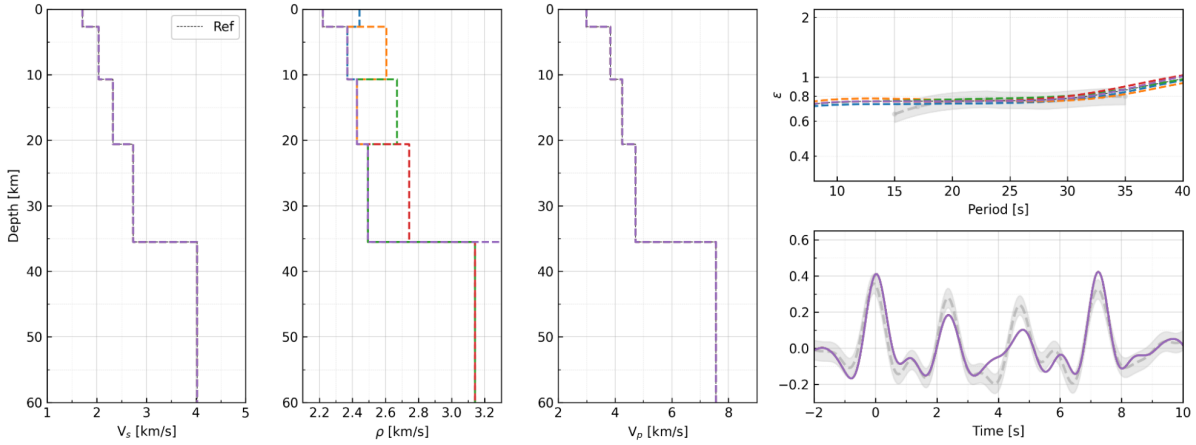


Figure A5.8: Synthetic modeling of ellipticity and P-to-s RFs using a four-layer model. Four new different models are generated based on this model, where the main difference is the perturbation of the density of each layer (the color indicates the perturbed layer).

A6 Comparison against further observations

The crustal models obtained from the joint inversion presented in this work can be compared to some other measurements representing the local structure. Among them, it is interesting to compare against the extra time windows in the P-to-s RFs used by Joshi et al. (2023). In their case, they included the signals observed between 14-16 s, 19-21 s and 23-25 s, which were interpreted as internal crustal reflections corresponding to P_2pPs, P_2pSs and P_3pPs phases, where the sub-scripted numeral in the phase name denotes the generating interface (see Fig. A6.9c and details in Fig. 3 in Joshi et al. (2023)). These time windows were not included in the joint inversion performed in this work due to their low amplitudes and unclear observation in the per-event P-to-s RFs. Another observation not utilized in this work is the apparent S-wave velocity (Fig. A6.9d), which was included in the joint inversion by Joshi et al. (2023).

As shown in Fig. A6.9c, some of the models generate anomalous signals between 20 and 27 s in the P-to-s RF time series, which are totally unobserved. The proposed models generate similar amplitude signals around 14 s (compared to the proposed P_2pPs between 14-16 s) and around 24 s (compared to the proposed P_2pPs between 14-16 s). The assumption of the wiggle between 19-21 s being a P_2pSs phase is doubtful due to its low amplitude. Some of the predicted P-to-s RFs present oscillations that might be comparable to it, but it is totally unclear.

Besides, the models proposed in this work fit relatively well in the error range of the apparent S-wave velocity at short periods (< 3 s), which represent the shallower depths, but they present a significant deviation from the measurements at longer periods (i.e., at larger depths). A joint inversion including all the available observations is encouraged.

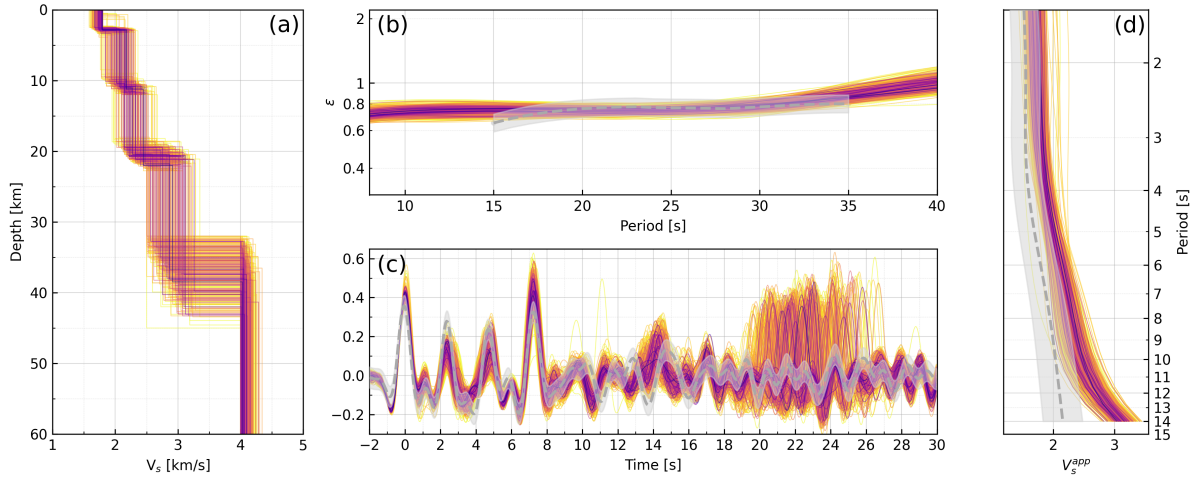


Figure A6.9: Crustal models proposed in this work and their synthetic response. **(a)** Best random 500 models from the inversion explained in chapter 6. **(b)** Predicted Rayleigh-wave ellipticity. **(c)** Predicted P-to-s RFs using the extended time window determined by Joshi et al. (2023). **(d)** Predicted apparent S-wave velocity compared to the measurements made by Joshi et al. (2023). The color of the models and curves is given by the fitting of the joint inversion of this work.

Acknowledgments

Sometimes, I have the feeling that I thank too much, but this time is completely necessary and worth it. With a pandemics, chaotic and uncertain times in between, finishing the PhD has been a whole challenge and, although only my name is there in front, this has been only possible thanks to many people "*behind the scenes*"!

First, I am deeply grateful to Brigitte for letting me be part of this interplanetary journey and the Bensberg Earthquake Station. Advancing our knowledge of Mars as we improve the performance of Bensberg has been an exciting and enormously enriching experience for me. Thanks for the opportunity to participate in such a diverse, interdisciplinary and novel project like InSight. It has been a unique experience! Thanks for all the discussions, all the questions and all the answers that helped to shape this work.

I also want to thank Prof. Bülent Tezkan for the conversations and the insightful discussions not only about subsurface mapping but also about football and daily PhD life.

Thanks to Prof. Thomas Meier for agreeing to review this work and giving valuable timely comments about it.

During this interplanetary mission (both the PhD and InSight by themselves), I also had the good fortune to collaborate and learn from great scientists, to whom I am very grateful. Special thanks to Ludovic Margerin, Martin Schimmel and Eleonore Stutzmann, who were always there, ready to help and contribute to this work. Also thanks to the InSight PhD fellows for sharing experiences, drinks, chats and meals when was possible: Niko, Cecilia, Sabrina, Marouchka, Rakshit, Keisuke and many others.

Special thanks to my family in Chile, for trusting in my abilities more than anyone else, since always, for encouraging me to take this step out of Chile without constraints or limitations and for being always there whenever I needed it. Mamá and Mami, thanks for all those video calls and your eternal smiles that helped me to stay always up!

This work would not have been possible without the permanent support and company of Barby. Thanks for always being there, in the high moments when everything was light and shiny, but especially in the low ones when everything was chaos and uncertainty, you were always there to support me and give me the motivation and drive I needed to keep going. Thanks for reviewing and for your help to improve this manuscript. Thanks for all your love, your patience, all the TV series, the beers, the *pancitos con palta* and the

countless good moments we have spent together during our PhDs in Germany. She won't read this, but also thanks to Geo, our lovely cat that was the piece of extra love and cuddles needed to finish this up.

Obviamente, my deep gratitude also goes to the Chilean crew in Cologne! A piece of home at such a long distance, who were always there to share a moment close to the Rhein. Thanks to Cata, Pipe, Anto, Maxi, Francisco, Mariana, Marco, Natascha, Maxi V., Cami R., Alex and Cami. Thanks for all the laughing, singing, dancing and chatting. Special thanks to Lucía and Cata for bringing the touch of Chilean flavors and food to every single gathering. You definitively made the cold days warmer!

Working at Bensberg is a little bit far away from "everything", but it has been my warmy second home during the last years and so the people I met there: thanks to Claus Fleischer, Peter Mora, Prof. Hinzen and Martin Zeckra for the scientific and not-so-scientific discussions that made the days easier. Thanks to Martin for helping with the Deutsch translations and for bringing some more Spanish to Bensberg!

Closer to the main campus, thanks to the IGM crew for the good moments: Wiebke, Stephan, Stefan, Shiva and Hannah. For more Delirium evenings to come: Cheers! Also thanks to the GSGS peers for making the PhD life more enjoyable and, of course, to Karin Boessenkool and Hannah Hartung for all the support during the course of this doctorate.

Last, but not least, thanks to my Chilean friends in Chile and around the world for being always there as well, despite the distance: Efra R., Javier O., Dani D., M. Jose, Carlitos R., Eric P., Jercko L., Miguel A. and the whole BH-crew and Pichi-friends! For more video calls to easily fix the world and *sacar la vuelta...* see you pretty soon!!

There have been many more people along this journey who contributed to make this PhD and daily life in Germany easier: thanks to all of you!!

Erklärung zur Dissertation

Hiermit versichere ich an Eides statt, dass ich die vorliegende Dissertation selbstständig und ohne die Benutzung anderer als der angegebenen Hilfsmittel und Literatur angefertigt habe. Alle Stellen, die wörtlich oder sinngemäß aus veröffentlichten und nicht veröffentlichten Werken dem Wortlaut oder dem Sinn nach entnommen wurden, sind als solche kenntlich gemacht. Ich versichere an Eides statt, dass diese Dissertation noch keiner anderen Fakultät oder Universität zur Prüfung vorgelegen hat; dass sie - abgesehen von unten angegebenen Teilpublikationen und eingebundenen Artikeln und Manuskripten - noch nicht veröffentlicht worden ist sowie, dass ich eine Veröffentlichung der Dissertation vor Abschluss der Promotion nicht ohne Genehmigung des Promotionsausschusses vornehmen werde. Die Bestimmungen dieser Ordnung sind mir bekannt. Darüber hinaus erkläre ich hiermit, dass ich die Ordnung zur Sicherung guter wissenschaftlicher Praxis und zum Umgang mit wissenschaftlichem Fehlverhalten der Universität zu Köln gelesen und sie bei der Durchführung der Dissertation zugrundeliegenden Arbeiten und der schriftlich verfassten Dissertation beachtet habe und verpflichte mich hiermit, die dort genannten Vorgaben bei allen wissenschaftlichen Tätigkeiten zu beachten und umzusetzen. Ich versichere, dass die eingereichte elektronische Fassung der eingereichten Druckfassung vollständig entspricht.

Teilpublikationen:

- **Carrasco, S.**, Knapmeyer-Endrun, B., Margerin, L., Schmelzbach, C., Onodera, K., Pan, L. *et al.* (2023). *Empirical HVSR spectral ratios at the InSight landing site and implications for the martian subsurface structure.* Geophysical Journal International, 232(2), 1293–1310. doi:10.1093/gji/ggac391.
- **Carrasco, S.**, Knapmeyer-Endrun, B., Margerin, L., Xu, Z., Joshi, R., Schimmel, M., *et al.* (2023). *Constraints for the Martian crustal structure from Rayleigh waves ellipticity of large seismic events.* Geophysical Research Letters, 50, e2023GL104816. doi:10.1029/2023GL104816

Köln, November 2023, Alejandro Sebastián Carrasco Morales